Geoforschungszentrum Potsdam (GFZ)
Sektion 2.6 „Erdbebengefährdung und Spannungsfeld"

Crustal stress variability across spatial scales – examples from Canada, Northern Switzerland and a South African gold mine

kumulative Dissertation

zur Erlangung des akademischen Grades

„doctor rerum naturalium" (Dr. rer. nat.)

in der Wissenschaftsdisziplin Geowissenschaften

eingereicht an der

Mathematisch-Naturwissenschaftlichen
Fakultät der Universität Potsdam

vorgelegt von

Diplom-Geologe Karsten Reiter

Potsdam, den 26. November 2014

Published online at the
Institutional Repository of the University of Potsdam:
URN urn:nbn:de:kobv:517-opus4-76762
http://nbn-resolving.de/urn:nbn:de:kobv:517-opus4-76762

"Essentially, all models are wrong, but some are useful."

(George E.P. Box (1919 - 2013) in 'Robustness in the strategy of scientific model building', 1987)

Abstract

The quantitative descriptions of the state of stress in the Earth's crust, and spatial-temporal stress changes are of great importance in terms of scientific questions as well as applied geotechnical issues. Human activities in the underground (boreholes, tunnels, caverns, reservoir management, etc.) have a large impact on the stress state. It is important to assess, whether these activities may lead to (unpredictable) hazards, such as induced seismicity. Equally important is the understanding of the in situ stress state in the Earth's crust, as it allows the determination of safe well paths, already during well planning. The same goes for the optimal configuration of the injection- and production wells, where stimulation for artificial fluid path ways is necessary.

The here presented cumulative dissertation consists of four separate manuscripts, which are already published, submitted or will be submitted for peer review within the next weeks. The main focus is on the investigation of the possible usage of geothermal energy in the province Alberta (Canada). A 3-D geomechanical–numerical model was designed to quantify the contemporary 3-D stress tensor in the upper crust. For the calibration of the regional model, 321 stress orientation data and 2714 stress magnitude data were collected, whereby the size and diversity of the database is unique. A calibration scheme was developed, where the model is calibrated versus the in situ stress data stepwise for each data type and gradually optimized using statistically test methods. The optimum displacement on the model boundaries can be determined by bivariate linear regression, based on only three model runs with varying deformation ratio. The best-fit model is able to predict most of the in situ stress data quite well. Thus, the model can provide the full stress tensor along any chosen virtual well paths. This can be used to optimize the orientation of horizontal wells, which e.g. can be used for reservoir stimulation. The model confirms regional deviations from the average stress orientation trend, such as in the region of the Peace River Arch and the Bow Island Arch.

In the context of data compilation for the Alberta stress model, the Canadian database of the World Stress Map (WSM) could be expanded by including 514 new data records. This publication of an update of the Canadian stress map after ~20 years with a specific focus on Alberta shows, that the maximum horizontal stress (S_{Hmax}) is oriented southwest to northeast over large areas in Northern America. The S_{Hmax} orientation in Alberta is very homogeneous, with an average of about 47°. In order to calculate the average S_{Hmax} orientation on a regular grid as well as to estimate the wave-length of stress orientation, an existing algorithm has been improved and is applied to the Canadian data. The newly introduced quasi interquartile range on the circle (QIROC) improves the variance estimation of periodic data, as it is less susceptible to its outliers.

Another geomechanical–numerical model was built to estimate the 3D stress tensor in the target area "Nördlich Lägern" in Northern Switzerland. This location, with Opalinus clay as a host rock, is a potential repository site for high-level radioactive waste. The performed modelling aims to investigate the sensitivity of the stress tensor on tectonic shortening, topography, faults and variable rock properties within the Mesozoic sedimentary stack, according to the required stability needed for a suitable radioactive waste disposal site. The majority of the tectonic stresses caused by the far-field shortening from the South are admitted by the competent rock units in the footwall and hanging wall of the argillaceous target horizon, the Upper Malm and Upper Muschelkalk. Thus, the differential stress within the host rock remains relatively low. East-west striking faults release stresses driven by tectonic shortening. The purely gravitational influence by the topography is low; higher S_{Hmax} magnitudes below topographical depression and lower values below hills are mainly observed near the surface. A complete calibration of the model is not possible, as no stress

magnitude data are available for calibration, yet. The collection of this data will begin in 2015; subsequently they will be used to adjust the geomechanical–numerical model again.

The third geomechanical–numerical model investigates the stress variation in an ultra-deep gold mine in South Africa. This reservoir model is spatially one order of magnitude smaller than the previous local model from Northern Switzerland. Here, the primary focus is to investigate the hypothesis that the M_w 1.9 earthquake on 27 December 2007 was induced by stress changes due to the mining process. The Coulomb failure stress change (ΔCFS) was used to analyse the stress change. It confirmed that the seismic event was induced by static stress transfer due to the mining progress. The rock was brought closer to failure on the derived rupture plane by stress changes of up to 1.5–15 MPa, in dependence of the ΔCFS analysis type. A forward modelling of a generic excavation scheme reveals that with decreasing distance to the dyke the ΔCFS values increase significantly. Hence, even small changes in the mining progress can have a significant impact on the seismic hazard risk, i.e. the change of the occurrence probability to induce a seismic event of economic concern.

Zusammenfassung

Die quantitative Beschreibung des Spannungszustandes in der Erdkruste sowie dessen räumlich-zeitliche Änderung ist von großer Bedeutung für wissenschaftliche Fragestellungen, sowie für industrielle Anwendung im geotechnischen Bereich. Bei jedem Eingriff des Menschen in den Untergrund (Bohrungen, Tunnel, Kavernen, Reservoirmanagement etc.) wird der Spannungszustand verändert. Entscheidend ist dabei, ob davon möglicherweise (unvorhersehbare) Gefahren, wie zum Beispiel induzierte Seismizität ausgehen können. Genauso wichtig ist auch ein Verständnis des ungestörten Spannungszustandes in der Erdkruste, um zum Beispiel sichere Bohrlochpfade bereits in der Planungsphase zu bestimmen. Selbiges gilt für eine optimale Konfiguration von Injektions- und Produktionsbohrung, wenn künstliche Fluidwegsamkeiten stimuliert werden müssen.

Die vorliegende kumulative Dissertation besteht aus vier Manuskripten, welche teilweise bereits publiziert sind. Fokus der beiden ersten Publikationen ist die potentielle Nutzung von Geothermie in der Provinz Alberta (Kanada). Dafür wurde ein 3-D-geomechanisch-numerisches Modell erstellt, das den kompletten gegenwärtigen 3-D-Spannungstensor in der oberen Erdkruste quantifiziert. Für die Kalibrierung des regionalen Modells wurde ein Datensatz von 321 Spannungsorientierungen und 2714 Spannungsmagnituden zusammengetragen, dessen Größe und Diversität einmalig ist. Aufgrund der vorhandenen Datenbasis wurde ein Kalibrierungsschema entwickelt, bei dem das Modell statistisch abgesichert an jedem einzelnen vorhandenen Datentyp schrittweise getestet und optimiert wird. Das optimale Verhältnis der Randbedingungen des Modells kann dabei durch bivariate lineare Regression, auf der Basis von nur drei Modellläufen bestimmt werden. Das Best-fit-Modell kann den Großteil der in situ Spannungsdaten sehr gut reproduzieren. So kann das Modell den 3-D-Spannungstensor entlang beliebiger virtueller Bohrlochpfade liefern, die zum Beispiel für die Planung der optimalen Orientierung horizontaler Stimulationsbohrungen genutzt werden können. Das Modell bestätigt regionale Abweichungen der Spannungsorientierung vom generellen Trend, wie z.B. in der Region des Peace River Bogens und des Bow Island Bogen.

Im Zusammenhang mit der Erstellung des Alberta-Spannungsmodells wurde die Datenbank der Weltspannungskarte (WSM) in der Region Kanada um 514 neue Datensätzen erweitert und alle bestehenden Datensätze überprüft. Dies ermöglichte es nach ca. 20 Jahren, eine aktualisierte Spannungskarte für Kanada mit einem vertiefenden Fokus auf die Provinz Alberta zu publizieren. Die maximale horizontale Spannung (S_{Hmax}) in weiten Teilen Nordamerikas ist Südwest nach Nordost orientiert. Die S_{Hmax} Orientierung in Alberta ist sehr homogen, im Mittel etwa 47°. Zur Berechnung der mittleren S_{Hmax}–Orientierung auf einem regelmäßigen Gitter und zur Ableitung des Spannungsmusters dieser Orientierung wurde ein existierender Algorithmus verbessert und auf den kanadischen Datensatz angewendet. Dabei wurde der Quasi Interquartilsabstand am Kreis (QIROC) neu eingeführt, um die Varianz eines periodischen Datensatzes besser abschätzen zu können. Der modifizierte Algorithmus ist weniger anfällig gegenüber Ausreißern in periodischen Datensätzen, als der Vorgänger.

Ein weiteres geomechanisch-numerisches Modell zur kontinuierlichen Beschreibung des 3-D-Spannungstensors wurde für das Gebiet „Nördlich Lägern" in der Nordschweiz erstellt. Diese Region ist ein potentieller Endlagerstandort für hochradioaktiven Abfall, eingelagert im Wirtsgestein Opalinuston. Der Fokus des Modells ist es, die Sensitivität des Spannungsfeldes von tektonischem Schub, Topographie, Störungen und den variablen Gesteinseigenschaften im mesozoischen Sedimentstapel auf den Spannungstensor zu untersuchen. Der Hauptanteil der tektonischen Spannungen, verursacht durch den Fernfeldschub von Süden, wird vor allem durch die mechanisch kompetenten Schichten im Liegenden und Hangenden des tonigen Zielhorizontes, dem Oberen Malm und dem Oberen

Muschelkalk aufgenommen. Dadurch bleiben die Differenzspannungen in den tonigen Formationen relativ gering. Ost-West streichende Störungen bauen zudem Spannungen des Fernfeldes ab. Der rein gravitative Einfluss der Topographie ist gering; höhere S_{Hmax}–Magnituden unterhalb topographischer Depressionen und geringere Werte unter Anhöhen sind vor allem oberflächennah zu beobachten. Eine Kalibrierung des Modells ist nicht abschließend möglich, da im Untersuchungsgebiet keine Spannungsmagnituden zur Verfügung stehen. Diese werden erst in der nächsten Etappe der Endlagersuche, die in 2015 beginnen wird erhoben, sodass das Modell dann gegebenenfalls angepasst werden muss.

Das dritte geomechanisch-numerische Modell eines Abschnitts einer tiefliegenden Goldmine in Südafrika ist räumlich gesehen nochmals eine Größenordnung kleiner als das vorherige lokale Modell in der Nordschweiz. Es wurde die Hypothese untersucht, ob das M_w 1.9 Erdbeben am 27. Dezember 2007 durch den Abbau verursacht wurde. Die Analyse der durch die Abbautätigkeit umgelagerten Spannungen unter Nutzung der Spannungsänderung des Coulomb Versagenskriteriums (ΔCFS) zeigt klar, dass das seismische Ereignis induziert wurde. Das Gestein wurde entlang der Bruchfläche um 1.5 bis 15 MPa dem Versagen näher gebracht, je nachdem welche ΔCFS Analysemethode angewendet wird und unter Berücksichtigung der Unsicherheiten in der Orientierung der Herdflächenlösung sowie der Modellparameter. Eine Vorwärtsmodellierung eines generischen Abbauprozesses zeigt exponentiell steigende ΔCFS–Werte mit abnehmender Distanz des Abbaus zu dem magmatischen Aufstiegskanal, in dem das Beben stattfand. Folglich haben geringe Änderungen des Abbauprozesses entscheidenden Einfluss auf die Eintretenswahrscheinlichkeit eines seismischen Ereignisses.

Contents

1 Overview

The upper Earth's crust is intensively used by humans for storage of waste, gas and CO_2 and a source of energy and raw materials as well. When using the underground, the fluid pressure, overburden load, tectonic forces and gravitational forces, all account for the in situ stress tensor, which defines the state of stress at a point inside a material. Understanding of the in situ stress tensor in the Earth's crust is crucial to a number of major scientific, economic and societal questions. Knowledge of the crustal stress tensor is also necessary to understand plate tectonics or the earthquake cycle (e.g. Richardson et al. 1976; Zoback and Zoback 1991; Harris and Simpson 1992; Coblentz and Sandiford 1994; Stein 1999; McCloskey et al. 2005; Hergert and Heidbach 2006). Such knowledge is as well essential for drilling projects because crustal stress influences borehole stability (Fuchs and Müller 2001; Bell 2003; Zoback 2007), reservoir operation and stimulation (Brown 2009; Henk 2009; Altmann et al. 2014), cap rock integrity (Konstantinovskaya et al. 2012), induced seismicity (Deichmann and Ernst 2009; Majer et al. 2007) and the long-term stability of underground constructions (Renner et al. 2000; Miller et al. 2000).

The first compilation of crustal stress data (Sbar and Sykes 1973; Zoback and Zoback 1980; Gough et al. 1983) lead to the initiation of the World Stress Map (WSM) database (Zoback et al. 1989; Zoback and Zoback 1991; Zoback 1992), later updated by Sperner et al. (2003) and Heidbach et al. (2009, 2010). They came to the conclusion, that the first order crustal stress pattern is governed by the plate tectonic forces (Fig. 1.1). These forces are the oceanic ridge push and the slab pull at subduction zones (Forsyth and Uyedaf 1975; Richardson and Reding 1991; Richardson 1992; Zoback and Zoback 1981; Zoback et al. 1989; Zoback 1992) in interaction with the mantle driving and resisting forces (e.g. Adams and Bell 1991; Becker and Faccenna 2011; Ghosh et al. 2013; Gough 1984; McGarr 1982), and resistance along transform faults. Another important source of stress in the lithosphere is the gravitational potential energy (GPE – Ghosh et al. 2009; Humphreys and Coblentz 2007; Naliboff et al. 2012). Second and third order stress sources (Heidbach et al. 2007, 2010; Müller et al. 1997; Tingay et al. 2005b; Zoback 1992; Zoback and Mooney 2003) disturb the observed general stress orientation trend from regional through local to reservoir scale (e.g. anthropogenic stress changes). Therefore, the stress tensor at a point is the sum of several stress sources, which act together on different scales (Fig. 1.1).

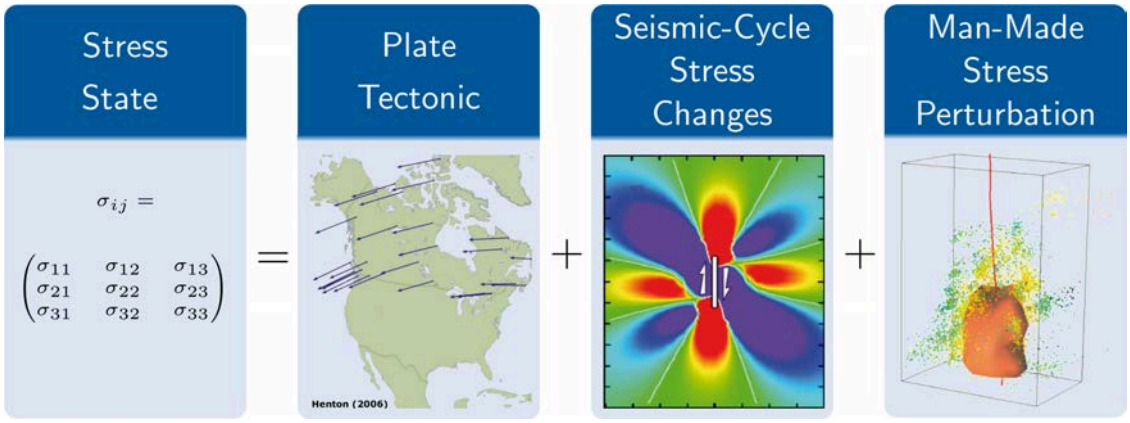

Figure 1.1: Stress tensor as a sum of several stress sources in the Earth's crust (incomplete).

However, there are large areas in highly prospected regions like Europe or Northern America where no stress data are available. Thus, it is a key challenge to estimate the 3-D stress state at an arbitrary chosen point in the crust based on the sparsely distributed in situ stress data. This can be done by interpolation methods but this approach becomes questionable in the case of structural inhomogeneities like faults, detachments (Bell and McLellan 1995; Röckel and Lempp 2003; Roth and Fleckenstein 2001; Yassir and Bell 1994), or varying material properties (Roche et al. 2013; Warpinski 1989). Furthermore, geothermal reservoir exploitation requires the knowledge of the stress state at greater depths than available stress data from hydrocarbon exploration. An alternative physics based approach to estimate the 3-D stress state is geomechanical–numerical modelling. This method has the advantage that it is able to incorporate structural and material inhomogeneities that impose local to regional changes of the stress field. There are several studies on tectonic plate scale stress orientation patterns in 2D (e.g. Coblentz and Richardson 1996; Dyksterhuis et al. 2005; Humphreys and Coblentz 2007; Jarosinski et al. 2006), large scale (regional) models in 3-D (Buchmann and Connolly 2007; Hergert and Heidbach 2011; Parsons 2006), and local (reservoir-scale) 3-D models (e.g. Fischer and Henk 2013; Heidbach et al. 2013; Henk 2005; Orlic and Wassing 2012; Van Wees et al. 2003). Modelling of the contemporary stress field mainly depends on the structural model, the material properties, the initial stress state and the applied displacement boundary conditions. However, the reliability of such models depends strongly on the model calibration with in situ stress data.

1.1 Structure of the thesis

This thesis is a "cumulative" dissertation and comprises four individual studies each estimating stresses in the Earth's upper crust. These studies focus on the analysis of stress orientation data, estimation of the contemporary and/or future in situ stress state, and static stress changes due to anthropogenic underground activities. Geomechanical–numerical methods are used for stress estimation.

Chapter 2 gives an introduction to the general motivation for this thesis and explains how much the exploitation of the underground depends on the magnitude and orientation of crustal stresses. It contains an overview of geothermal energy, subsurface construction, and stresses in the Earth's crust, applied stress concepts, the WSM database, and describes methods how to estimate the in situ stress.

Availability of in situ stress data is of great importance for the calibration of stress models. For the calibration of the Alberta stress model presented in Chapter 4, all WSM stress data were revised and 514 new data records of the maximum horizontal stress (S_{Hmax}) orientation data from Alberta and the whole of Canada could be added. This allowed publishing an updated Canadian stress map, see Chapter 3. Furthermore, an improved algorithm for computing an average stress orientation as well as the determination of the crustal stress orientation wavelengths is presented.

Chapter 4 presents the Alberta stress model using 3-D geomechanical–numerical modelling, which allows estimating the full stress tensor along any virtual well path before drilling. The study focuses on the calibration procedure, as the available amount and diversity of in situ stress data is large. For this new statistic calibration workflow, 2714 data records on stress magnitudes were compiled.

Chapter 5 presents a stress sensitivity analysis using 3-D geomechanical–numerical modelling in the geological target area "Nördlich Lägern". In the context of a possible final disposal site for radioactive waste in the host rock Opalinus Clay, the study focuses on the interacting effects of topography, tectonic shortening and the variable rock properties within the sedimentary stack.

In 2007, a M_w 1.9 earthquake occurred in the ultra-deep South African gold mine Mponeng. To assess whether or not the event was triggered by static stress transfer, a geomechanical–numerical

reservoir model was used. Chapter 6 presents this study, which investigates the static stress changes around the gold mine using the Coulomb failure criterion (ΔCFS).

In Chapter 7 the results of the four studies are debated, first independently and then as synthesis, where also some implications for Germany are discussed. A final conclusion is given in Chapter 8, which lists the major findings of the thesis.

1.2 Short overview of the presented papers

Paper No.:	1 — Chapter 3, page 23ff
Status:	published
Journal:	Tectonophysics, 2014, 636, 111–124, DOI: 10.1016/j.tecto.2014.08.006
Title:	A Revised Crustal Stress Orientation Database for Canada
Authors:	**Karsten Reiter**, Oliver Heidbach, Douglas Schmitt, Kristine Haug, Moritz Ziegler, Inga Moeck
Contribution:	I wrote the whole manuscript, supervised the compilation of new stress data and prepared all figures. The used smoothing algorithm for the hybrid stress map from Heidbach et al. (2010) was modified for a more robust statistical solution.

Paper No.:	2 — Chapter 4, page 43ff
Status:	published
Journal:	Solid Earth, 2014, 5, 1123–1149, DOI: 10.5194/se-5-1123-2014
Title:	3-D geomechanical–numerical model of the contemporary crustal stress state in the Alberta Basin (Canada)
Authors:	**Karsten Reiter**, Oliver Heidbach
Contribution:	I prepared the model, wrote the whole manuscript and prepared all figures. This paper represents the key part of this thesis.

Paper No.:	3 — Chapter 5, page 75ff
Status:	to be submitted
Journal:	Tectonophysics
Title:	Stress field sensitivity analysis in a sedimentary sequence of the Alpine foreland, Northern Switzerland
Authors:	Tobias Hergert, Oliver Heidbach, **Karsten Reiter**, Silvio B. Giger, Paul Marschall
Contribution:	I modified and adopted the provided geometry data, conceived the meshing strategy and produced the mesh for the geomechanical–numerical model. Furthermore, I contributed to the analysis and discussion of the model results.

Paper No.:	4 — Chapter 6, page 99ff
Status:	submitted on 13 October 2014
Journal:	Pure and Applied Geophysics
Title:	Mining-induced stress transfer and its relation to a M_w 1.9 seismic event in an ultra-deep South African gold mine
Authors:	Moritz Ziegler, **Karsten Reiter**, Oliver Heidbach, Arno Zang, Grzegorz Kwiatek, Dietrich Stromeyer, Torsten Dahm, Georg Dresen, Gerhard Hofmann
Contribution:	I co-supervised the first author during his master thesis that is presented in this manuscript, gave support during the mesh generation, prepared the geo-tectonical introduction, prepared Tab. 6.1 and contributed substantial parts of Fig. 6.1.

2 Introduction

2.1 Motivation

2.1.1 The Stress field of the Earth's crust and anthropogenic subsurface activity

The upper crust of the Earth is used by humans on a wide range of depth levels from a few 100 m to 6 km and even beyond. This include the utilisation of energy sources (crude oil, natural gas, heat, coal and uranium), mining of raw materials (minerals, construction materials and ashlar), but also interim storage sites for energy (natural gas, compressed air) as well as (final) disposal sites of anthropogenic and toxic waste (chemicals, radioactive waste). Due to the potentially hazardous nature of these applications, it requires a good knowledge of the target of exploitation. Apart from geology and rock properties, information on the stress field are important.

The stress field of the Earth's crust is mainly driven by the gravitational load of the overburden rocks and the forces which are propelling plate tectonics, overprinted by gravitational potential energy (GPE) and other stress sources during geological time (e.g. Richardson 1992; Zoback et al. 1989; Zoback 1992). In addition to this, humans reduce or increase fluid pressure due to the production of ground water and hydrocarbons or acid gas injection (H_2S and CO_2) as well as waste water grouting, respectively (e.g. Bachu et al. 2008; Bell and Grasby 2012; Woodland and Bell 1989). Furthermore, deep stress redistribution is observed by the removal of rock, such as in wells, caverns, tunnels or mines. The removal of rock masses, as well as modified load by buildings or dams, leads to stress redistribution even without a deep penetration of the crust (e.g. Fuchs and Müller 2001). These interventions can have a negative impact on the stability of underground constructions. Wider damage can have a negative impact on fauna (incl. humans), flora and other tangible goods. It is therefore important to understand the undisturbed stress field, but also the variation of the stresses due to anthropogenic activities. Since the stress field is driven or overprinted by different stress sources (Zoback et al. 1989; Zoback 1992; Heidbach et al. 2007, 2010), it is not possible to make simple predictions, by knowing the location or depth only. Direct measurement of the in situ stress state is not possible, but there are some methods used to estimate the different components of the stress field. Such in situ estimations are of course significant for the appropriate location, depth and lithology only. Inter- and extrapolation of stress data are helpful, but eventually limited, when material or structural inhomogeneities (stratigraphy, faults) are reached.

To estimate the 3D stress in the crust, it is essential to use geomechanical–numerical methods (e.g. Buchmann and Connolly 2007; Hergert and Heidbach 2011; Parsons 2006; Fischer and Henk 2013; Heidbach et al. 2013; Henk 2005; Orlic and Wassing 2012; Van Wees et al. 2003), which allow incorporating structural and material inhomogeneities. A good understanding of the structural interior in the crust is crucial for model design. However, model-independent in situ stress data are of key importance to calibrate stress models (e.g. Fischer and Henk 2013; Reiter and Heidbach 2014). The quality of such a calibration procedure dependent on data availability. Thus, it is of advantage to have a large number of data, but also have access to data from different components of the full stress tensor (e.g. S_{Hmax}, S_{hmin} or S_V). This shows that the model geometry and the in situ stress data are of great importance for the validity of a stress model. Usually, a few or no stress data are available for calibration of stress models of local- or reservoir-scale (e.g. Fischer and Henk 2013; Heidbach et al. 2013). Therefore, it is may be an advantage to generate a regional model that reproduces first- and second-order stress sources. At this scale significantly more stress data are available that allow to generate a well-calibrated model which can derive coarse estimations of the

full stress tensor. Additionally, in a subsequent step, the stress state of the regional model can be used to determine boundary conditions for a local– or reservoir model.

The Alberta stress model (Sec. 4) is such a regional model, which can provide boundary conditions for small scale models, depending on the desired location. But it can also be used to provide a rough estimate of the in situ stress state at any point in the model. Alternatively, the models of different scales can be coupled directly by nesting.

2.1.2 Geothermal Energy

Geothermal energy is the only renewable energy source, which is able to provide base load energy. The capacity factor (actual produced energy / potential produced energy) of 90% is very large compared to other renewable energies, like 20–30% for wind and 8–20% for solar photovoltaic (Chamorro et al. 2012). Usually geothermal energy is divided into shallow and deep geothermal energy. The shallow geothermal energy uses the superficial stored heat (~100 m depth), and is powered by the sun — this type of geothermal energy using ground source heat pumps (GSHP) is not further regarded here. Deep Geothermal energy technique is used also in some places in shallower depths (e.g. Iceland with a few hundred meters), where the heat is transported by ascending magmas at plate boundaries (rift zones) and/or hot spots (convection). In most areas the heat is mainly produced by radioactive decay in the lower Earth's crust and transported in the upper crust (conduction). For an overview of geothermal play types see Moeck (2014). Regional variations in the Earth's heat flow are described by the geothermal gradient into depth; the average is 25–30 K/km. In young rifting zones such as in Iceland, temperatures above 100°C are found in a few hundred meters depth (e.g. Arnórsson 1995; Flóvenz and Saemundsson 1993), which corresponds to a geothermal gradient of >100 K/km. In geological older regions, the geothermal gradient is significantly lower. For example, a well producing electrical currant in the province Alberta would go down to the base of the sedimentary basin and probably far beyond, in the crystalline basement due to a low geothermal gradient of about 15–30 K/km (e.g. Lam and Jones 1984; Majorowicz and Grasby 2010b; Majorowicz et al. 2012, 2014; Weides et al. 2013; Weides and Majorowicz 2014). This is of course associated with a much larger effort. However, it can be economically and especially ecologically meaningful to exploit this energy potential in the province Alberta too.

The question of whether, where and how this energy can be utilized in Albert is the task of Theme 4 of the international Helmholtz–Alberta Initiative (HAI). Canadas largest potential site for usage of geothermal energy are in the Province British Columbia, in the Yukon Territory as well as the large Western Canada Sedimentary Basin (WCSB), where the Alberta Basin is located (Thompson 2010). Geothermal energy can be utilized as thermal energy for greenhouse heating (>30°C), heating of houses (>40°C) or heat for technical processes (e.g. Pathak et al. 2013). To generate electricity, water with temperatures of 120–150 °C or more is needed. This requires well depths of 3000–6000 m in Alberta (Majorowicz and Grasby 2010a, c). Regardless of these issues such deep holes are of course very expensive; the loss or damage of the well due to lack of knowledge of the stress state would be fatal. The same stands for the well configuration, as the injection well pumps down cold water, which is heated in the porous or fractured reservoir, and the production well produces the hot water (Fig. 2.1). For low permeability reservoirs, stimulation by hydraulic fracturing is required to enhance permeabilities (enhanced geothermal systems – EGS, e.g. Huenges 2010). The artificial fluid pathways opens in orientation of the largest stress magnitude (Hubbert and Willis 1957; Scheidegger 1962; Haimson and Fairhurst 1969), as shown by Fig. 2.2. In the case of insufficient stress orientation information from the target area, the induced fractures cannot connect the wells; consequently the production rates are to small. Mistaken investments e.g. parts of the Fenton Hill project (Brown 2009; Duchane and Brown 2002) can potentially be avoided with a better pre-drilling understanding of the 3-D in situ stress state.

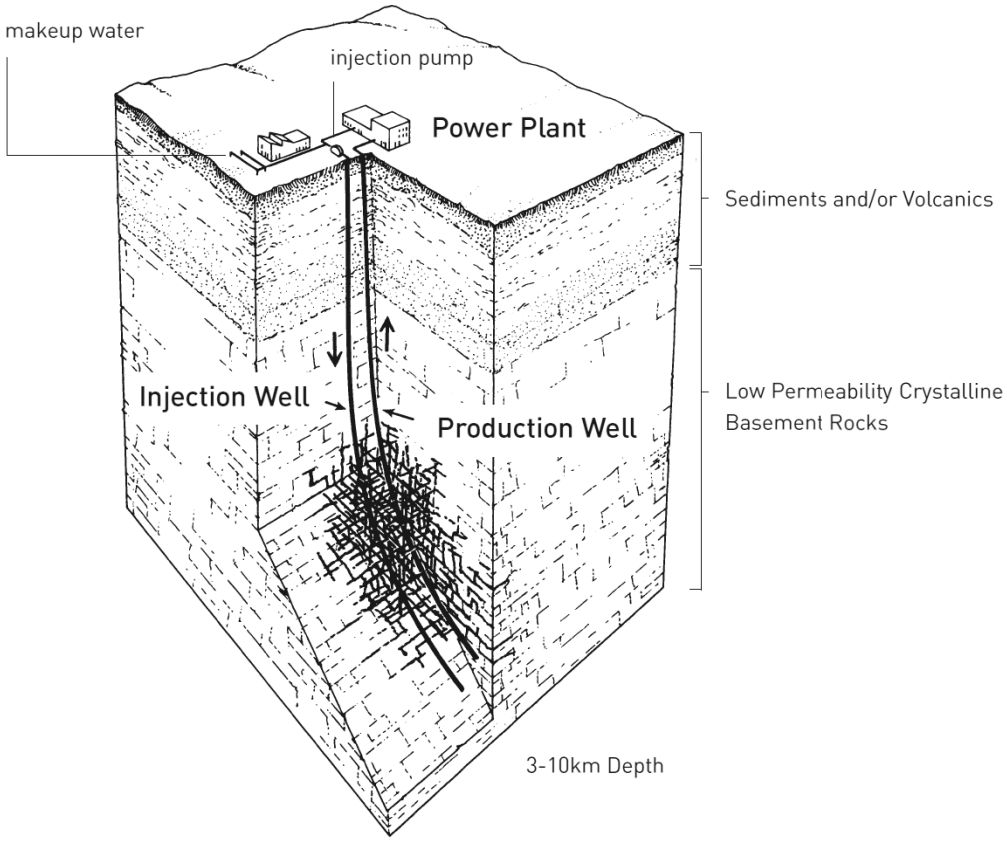

Figure 2.1: Sketch of a two-well Enhanced Geothermal System (EGS) in a low-permeability crystalline basement formation (Tester et al. 2006).

The investigation of the stress field in the province of Alberta is significant for the applied planning and use of geothermal energy, as well as for other energy resources in the region. Such research is of general academic interest and findings in a specific geo-tectonic region can also be transmitted to a similar geological setting. Such analogues for the Alberta foreland basin would be e.g. the Alpine Molasse Basin. Thus, experiences and findings are of interest for the applied investigation of the Alpine foreland basin in southern Germany, too.

Germany lacks high enthalpy resources at shallow depth (Ganz et al. 2013). However, aquifers with temperatures and hydraulic conductivities suitable for power generation can be expected particularly in the Upper Rhine Graben, in the south-eastern part of the Molasse Basin and in the North German Basin (Schellschmidt et al. 2010; Ganz et al. 2013). In 2012 the installed capacity in Germany reached 12.1 MW_e and produced 25.4 GWh (Ganz et al. 2013). Nevertheless, 95% of Germany's geothermal potential are in crystalline rock reservoirs (Paschen et al. 2003), where stimulation (EGS) is essential. They estimated the technical potential deliverable energy amount for geothermal power generation in Germany of about 300 TWh/a, which is about half of the gross electricity production. However, in a combined use of heat and power the entire demand for low-temperature heat and 25 % of gross electricity generation can be covered by geothermal energy in Germany.

2.1.3 Subsurface constructions (Mines and repository sites for radioactive waste)

For the exploitation of hydrocarbons or geothermal energy, only the transport ways for fluids with a few decimetres in diameter are essential. For underground constructions like mines or repository

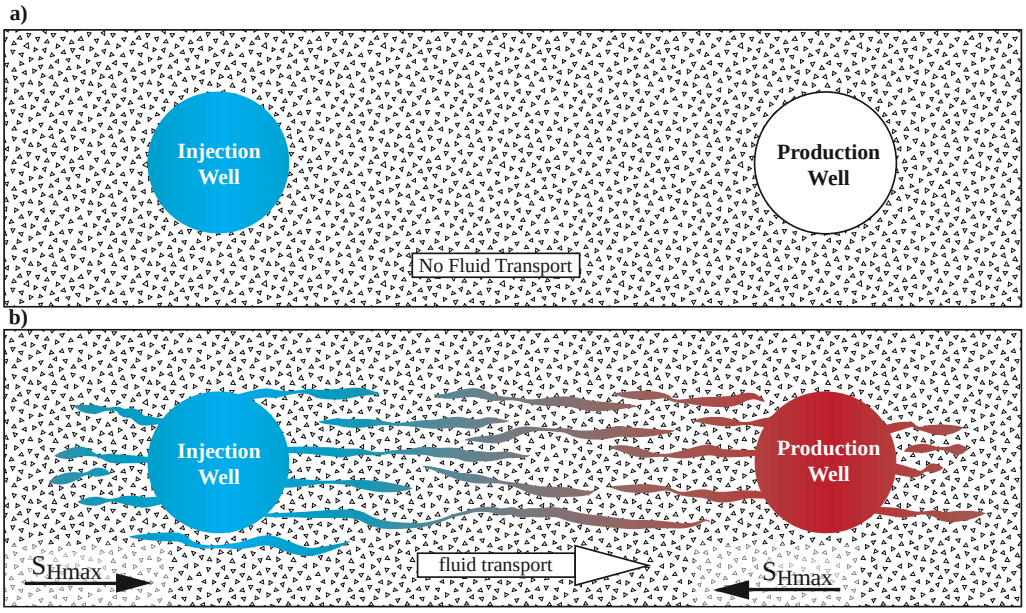

Figure 2.2: Sketch of hydraulic stimulation in a two well configuration. **(a)** The injected cold water cannot propagate from the injection well to the production well, because of the low permeable reservoir rock (e.g. crystalline rock). **(b)** After hydraulic stimulation, the cold water can propagate from the injection well to the production well. On the way, the water is heated by the hot and fractured reservoir rock.

sites, a much larger rock volume has to be removed. An additional risk is that mines and repositories are operated at depth by humans, which increases the risk in case of rock failure. For the planning of a final repository for nuclear waste, much more issues have to be respected. The geological barrier has to protect the radioactive waste in addition to the technical barrier (e.g. Chapman et al. 1987; Miller et al. 2000). This geological barrier must not be affected by the heat from the waste. Furthermore, the host rock has to restrain fluid transport or potentially leaking radiation. Such potentially emerging radiation should ideally be bound by the geological barrier, in case of failure. Any uprising minor fault should be closed quickly. In the long term it is expected that the repository is not affected by exogenous processes such as erosion or ice load over several hundred thousands of years. The same applies to endogenous processes such as tectonic processes in which the shortening is accumulated along fault zones. These complex questions can be investigated with the help of geomechanical–numerical models.

2.2 Stresses in the Earth crust

2.2.1 The Stress Tensor concept

2.2.1.1 Forces

The concept of force plays an important role in mechanical physics. Any force (F) is the product of the mass (m) of a body and the acceleration ($\vec{a}$), which consists of the magnitude and the direction, together called vector:

$$\vec{F} = m \cdot \vec{a} \tag{2.1}$$

Forces are subdivided into internal forces and external forces. External forces act from outside on a body, whereas internal forces are the mechanical properties like hardness or stiffness, which are in equivalence up to a certain point, where external forces leads to translation or deformation (failure). The internal forces are described by the rock attributes like elastic properties (Young's modulus E and Poisson's ration ν) or plastic properties (cohesion C and friction coefficient φ). Body forces act on the whole affected volume and are proportional to the density of the body; the most notable is gravity. A surface force describes action of two body's along a surface of one body along a thought or real (contact) surface.

2.2.1.2 Stress – directed pressure

When a force (F) act on a surface with a certain area (A), this force intensity is described as traction (Σ)

$$\Sigma = \frac{\vec{F}}{A} \tag{2.2}$$

Such a force ($\vec{F}$), acting on a surface is an oriented force; therefore traction is always a vector (magnitude and orientation). Traction has the same units as pressure, but traction has a certain orientation to a (thought) surface. When traction acts on a surface (Σ_{top}), but the surface does not move, which means the system is in equilibrium, an equal traction (Σ_{bottom}) act on the surface with an opposite orientation.

$$\Sigma_{top} = -\Sigma_{bottom} \quad ; \quad \Sigma_{top} + \Sigma_{bottom} = 0 \tag{2.3}$$

As the traction varies along a surface, the term stress ($\boldsymbol{\sigma}$) describes the intensity force at a point on a thought surface or within a infinitesimal cube in three dimensions, which act in opposite directions (surface stress). The stress which acts on a surface can be split into two perpendicular components, the normal stress (σ_n) acting upright to the surface and the shear stress ($\sigma_S = \tau$) acting parallel to the surface (Fig. 2.3a).

$$\sigma_n = \frac{\vec{F_n}}{A} \tag{2.4}$$

$$\sigma_s = \tau = \frac{\vec{F_S}}{A} \tag{2.5}$$

This convention is used for graphical representation in the Mohr Diagram, which is a very common tool in geosciences. Stresses which act on a body can be calculated for any arbitrary plane within a body. Therefore a normal stress (σ_n; $\sigma_s = 0$) on a body can be recalculated to a virtual plane within the body with a certain inclination (Θ). On such a virtual plane both, the normal stresses (σ'_n) as well the shear stresses (σ'_s) act.

$$\sigma'_n = \sigma_n \cdot \cos^2 \Theta \tag{2.6}$$

$$\sigma'_s = \sigma_n \cdot \sin \Theta \cdot \cos \Theta \tag{2.7}$$

In the two-dimensional case, the forces which act on a infinitesimal square can be described by the two stress tensors σ_{xx} and σ_{yy} which act normal to the surfaces, the normal stresses (Fig. 2.3a). The forces acting parallel to the surfaces are σ_{xy} and σ_{yx} are the shear stresses, which can be written as τ_{xy} and τ_{yx}. For the two-dimensional case the full stress tensor which acts on a infinitesimal square is defined by the following matrix:

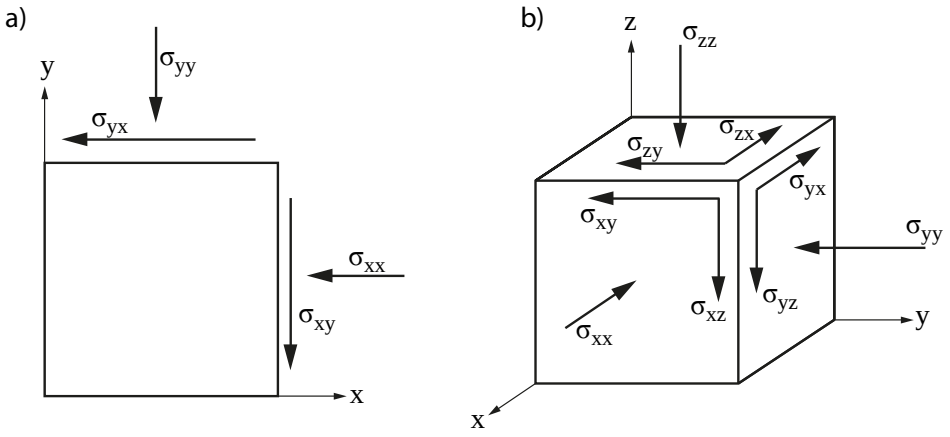

Figure 2.3: Visualisation of the stress components **(a)** in 2-d on a square and **(b)** in 3-d on a cube.

$$\boldsymbol{\sigma} = \begin{pmatrix} \sigma_{xx} & \sigma_{xy} \\ \sigma_{yx} & \sigma_{yy} \end{pmatrix} \quad or \quad \begin{pmatrix} \sigma_{xx} & \tau_{xy} \\ \tau_{yx} & \sigma_{yy} \end{pmatrix}. \tag{2.8}$$

In the context of Earth sciences, the extension of the theory into three dimensions is necessary. Therefore stress is described as a normalized force, acting on the three surfaces of an infinitesimal thought cube. Similar to the two-dimensional space, the normal stresses σ_{xx}, σ_{yy} and σ_{zz} act normal to the surfaces of the cube (Fig. 2.3b). Two parallel shear stresses act on each of the three principal surfaces. Therefore six shear stresses are combined with the three normal stresses, the three-dimensional stress tensor consists of nine components:

$$\boldsymbol{\sigma} = \begin{pmatrix} \sigma_{xx} & \sigma_{xy} & \sigma_{xz} \\ \sigma_{yx} & \sigma_{yy} & \sigma_{yz} \\ \sigma_{zx} & \sigma_{zy} & \sigma_{zz} \end{pmatrix} \quad or \quad \begin{pmatrix} \sigma_{xx} & \tau_{xy} & \tau_{xz} \\ \tau_{yx} & \sigma_{yy} & \tau_{yz} \\ \tau_{zx} & \tau_{zy} & \sigma_{zz} \end{pmatrix} \quad or \quad \begin{pmatrix} \sigma_{xx} & \tau_{xy} & \tau_{xz} \\ \tau_{xy} & \sigma_{yy} & \tau_{yz} \\ \tau_{xz} & \tau_{yz} & \sigma_{zz} \end{pmatrix}. \tag{2.9}$$

As the matrix of the 3-D stress tensor is a symmetrical matrix ($\boldsymbol{\sigma} = \boldsymbol{\sigma}^{\boldsymbol{T}}$), the full stress tensor consists of only six independent components since $\tau_{zx} = \tau_{xz}$ etc.

2.2.2 Principal stresses

Stress in geosciences are defined as compressive stress, in contrast to other fields e.g. engineering, it acts at a single point, visualized as a infinitesimal cube (Fig. 2.3b). The full stress tensor is described for an arbitrarily chosen reference frame by:

$$\boldsymbol{\sigma_{ij}} = \begin{pmatrix} \sigma_{11} & \sigma_{12} & \sigma_{13} \\ \sigma_{21} & \sigma_{22} & \sigma_{23} \\ \sigma_{31} & \sigma_{32} & \sigma_{33} \end{pmatrix}. \tag{2.10}$$

Each full stress tensor can be transformed by a rotation matrix (A, see Eq. 2.11) into a principal stress tensor ($\hat{\boldsymbol{\sigma}}$, Eq. 2.12), where only normal stresses act and all shear stresses disappear (Eq. 2.13).

$$A = \begin{pmatrix} a_{xx} & a_{xy} & a_{xz} \\ a_{yx} & a_{yy} & a_{yz} \\ a_{zx} & a_{zy} & a_{zz} \end{pmatrix} \tag{2.11}$$

$$\hat{\boldsymbol{\sigma}} = A\sigma A^T \tag{2.12}$$

The three principal stresses acts normal to the principal planes. Usually, the following convention is used: $\hat{\sigma}_1$ is the largest, $\hat{\sigma}_2$ the intermediate and $\hat{\sigma}_3$ the smallest stress ($\hat{\sigma}_1 \geq \hat{\sigma}_2 \geq \hat{\sigma}_3$).

$$\hat{\boldsymbol{\sigma}} = \begin{pmatrix} \hat{\sigma}_1 & 0 & 0 \\ 0 & \hat{\sigma}_2 & 0 \\ 0 & 0 & \hat{\sigma}_3 \end{pmatrix} \tag{2.13}$$

The Earth topography is a free surface, where shear stresses disappear. Thus the vertical stress (S_V) becomes one principal stress orientation. This is also the case in greater depth having a laterally homogeneous isotropic stratification. Such insights lead to the application of simplified crustal stress concepts.

2.2.3 Crustal Stress concepts

2.2.3.1 The stress concept of sedimentary basins

Most wells are drilled in sedimentary basins for the hydrocarbon industry, where the topographic gradient is typically low. The following assumption are made for analysing stress data from wells: The sedimentary column onto a certain point in the well is the vertical stress (S_V), which is oriented perpendicular to the surface (Fig. 2.4), directed to the centre of the Earth (Anderson 1951, cited in Zoback 1992). Perpendicular to the vertical stress are the minimum horizontal stress (S_{hmin}) and the maximum horizontal stress (S_{Hmax}) (e.g. Jaeger et al. 2009; McGarr and Gay 1978; Schmitt et al. 2012). Therefore, the full stress tensor ($\boldsymbol{S}$) is simplified to only three components:

$$\boldsymbol{S} = \begin{pmatrix} S_{\mathrm{Hmax}} & 0 & 0 \\ 0 & S_{\mathrm{hmin}} & 0 \\ 0 & 0 & S_{\mathrm{V}}. \end{pmatrix} \tag{2.14}$$

2.2.3.2 The stress regime

The magnitude of the three major stresses orientations controls the relative motion along faults in the crust (Anderson 1951, cited in Kanamori and Brodsky 2004). The tectonic stress regime (Fig. 2.5) is defined according to this simplification as follows:

$$\begin{aligned} \text{Normal Faulting} &= S_V > S_{Hmax} > S_{hmin} \\ \text{Strike Slip} &= S_{Hmax} > S_V > S_{hmin} \\ \text{Thrust Faulting} &= S_{Hmax} > S_{hmin} > S_V. \end{aligned}$$

2.2.4 Sources of crustal stress

The early plate wide compilations of crustal stress indicators helped researchers to estimate to what extend the plate boundary forces control the contemporary crustal stress field pattern on large continental crustal areas, such as the North American Plate (Adams 1987; Adams and Bell 1991; Fordjor et al. 1983; Gough et al. 1983; Sbar and Sykes 1973; Zoback and Zoback 1980, 1981, 1989, 1991). They came to the conclusion, that the crustal stress field is governed by the same forces driving plate tectonic motion, which are called first-order stress sources (Tab. 2.1). These are the oceanic ridge push, the slab pull at subduction zones (Forsyth and Uyedaf 1975; Richardson and Reding 1991; Richardson 1992; Zoback and Zoback 1981; Zoback et al. 1989; Zoback 1992) in interaction with the mantle driving and resisting forces (e.g. Adams and Bell 1991; Becker

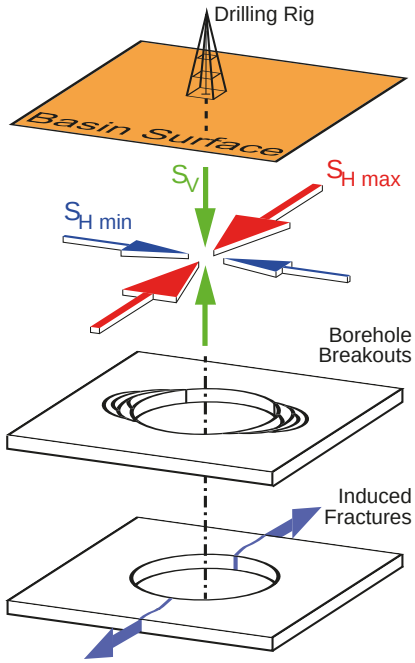

Figure 2.4: General assumption of stresses in sedimentary basins: The vertical stress (S_V) is a principal stress, thus perpendicular to the minimum and maximum horizontal stress (S_{hmin} and S_{Hmax}). Borehole breakouts occur in orientation of the S_{hmin} and induced tensile fractures occur in orientation of S_{Hmax}.

and Faccenna 2011; Ghosh et al. 2013; Gough 1984; McGarr 1982) and resistance along transform faults. Another important source of stress in the lithosphere is the gravitational potential energy (GPE — Ghosh et al. 2009; Humphreys and Coblentz 2007; Naliboff et al. 2012). A key challenge for regional and global compilation of crustal stress information is the combination of stress indicators that encompass a wide range of methods and sample very different rock volumes (Ljunggren et al. 2003).

2.2.5 The World Stress Map project (WSM)

The first comprehensive global compilation of stress data was initiated by the International Lithosphere Program with the World Stress Map (WSM) project that published after its first funding phase (1986-1992) a database with ~7,700 data records (Zoback 1992). In order to make the information comparable, a quality ranking scheme was developed for the World Stress Map project (Zoback et al. 1989; Zoback and Zoback 1991; Zoback 1992) and later updated by Sperner et al. (2003) and Heidbach et al. (2010). The WSM quality ranking scheme is based on the standard deviation on the individual stress indicator technique within a given suite. A-quality is the highest and E is the lowest quality. The WSM project website provides a guideline for the data analysis and quality assignment for the WSM database (http://world-stress-map.org). The latest update of the WSM in 2008 has 21,750 data records (Heidbach et al. 2009, 2010, – Fig. 2.6). Chapter 3 presents the recent update of the Canadian stress map.

2.3 Estimation of Stress Orientations

The full stress tensor consists of six independent components (Sec. 2.2.1.2) none of which can be measured directly. Most of our stress knowledge comes from stress indicators that are observed by the

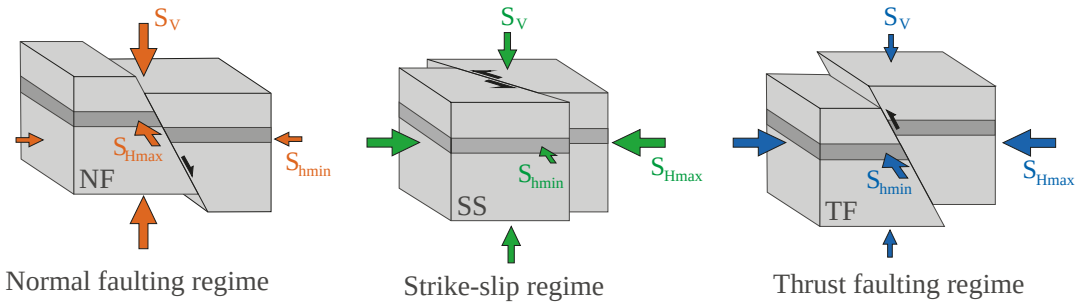

Figure 2.5: Anderson's theory of faulting – displayed are the ideal fault types and their relation between the orientations of the principal stresses. These stress proportions are used to identify the stress regime (Heidbach et al. 2009, modified).

Table 2.1: First, second and third order stress sources, modified after Zoback et al. (1989); Zoback (1992); Heidbach et al. (2007, 2010).

Order of stress source	Extent vs. lithosphere thickness	Extent [km]	Stress sources
First	$\gg$	>500	Plate boundary forces: ridge push, slab pull, trench suction; gravitational potential energy; basal tractions originating from density driven mantle convection
Second	$\sim$	$100-500$	lithospheric flexure (isostatic compensation, sediment loading on continental margins, seamount loading, upwarping oceanward of the trench), localized lateral density contrasts/buoyancy forces, lateral strength contrasts (anisotropy of material properties), topography, continental rifting, large fault zones, lateral contrasts of heat production, erosion
Third	$\ll$	<100	local density or strength contrasts, basin geometry, basal detachment, man-made excavation, man-made downhole pressure changes, impoundment dams, lowering of the water table, active faults, incised valleys

use of a variety of methods from boreholes. Only some important methods will be introduced here. These methods, for overview see Bell (1996a), Ljunggren et al. (2003), Schmitt et al. (2012), Stacey and Wesseloo (2002), Zang and Stephansson (2010) and Zoback et al. (2003) can be distinguished as they provide either data on crustal stress orientations only (this section), they give knowledge of the faulting regime, or they provide stress magnitudes (Sec. 2.4).

2.3.1 Borehole breakouts

Borehole breakouts (BO) are a failure of the borehole, which is observed in many wells (e.g. Babcock 1978; Cox 1972). Breakouts are borehole segments of several metres or more along which the borehole wall has spalled preferentially at diametrically opposed azimuths (Fig. 2.7). Bell and Gough (1979) and independently Hottman et al. (1979) recognized first that BO are an indicator of the orientation of stresses in the crust. As such, the diameter across the BO must be greater than that of the drill bit; and its major axis points in the orientation of S_{hmin} and perpendicular to S_{Hmax}). The breakouts occur due to concentration of the combined horizontal stresses at the borehole wall (e.g. Haimson and Song 1993; Schmitt et al. 2012; Zoback et al. 1985, 2003). The well

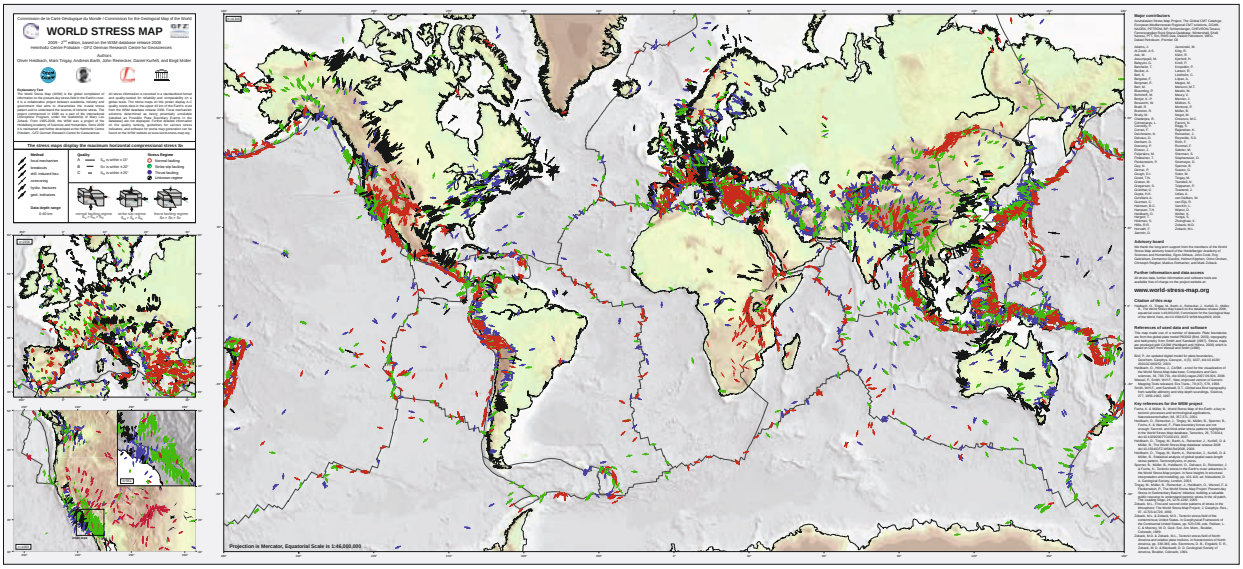

Figure 2.6: The World Stress Map provides a global database of stress orientation data (Heidbach et al. 2009). The symbols are colour codes according to the estimated stress regime; the symbols indicate the method of stress estimation.

is affected from the breakaway of small rock fragments in S_{hmin} orientation as well as horizontal shortening of the well in orientation of the maximum horizontal stress (S_{Hmax}). Finally the well has a symmetrical elliptical shape. The longer such a well deformation down well is observed, the more certain is the borehole breakout as an indicator of the orientation of the stress field. There are several geophysical logging methods to identify elliptical borehole sections. They include ultrasonic acoustic imaging as produced by the borehole televiewer (Zemanek et al. 1969, 1970), electrical resistivity imaging methods such as produced by micro-resistivity tools (Ekstrom et al. 1987), and simpler mechanical oriented-calliper logs like four-arm up to multi-finger dipmeter/calliper logs (e.g. Babcock 1978; Plumb and Hickman 1985; Reinecker et al. 2003). There are different problems which can lead to a misinterpretation of BO, as the following: wash-out, anisotropy within the rocks, or vertical faults or joints, which still exist or were induced during drilling. The least ones are often extensional fractures oriented in the orientation of S_{Hmax}. The mechanisms and the extent of the breakout vary depending on the lithology as well as in situ conditions like temperatures, pore pressure or drilling technology (Stacey and Wesseloo 2002).

2.3.2 Drilling induced (tensile) fractures (DIF)

Drilling induced tensile fractures (DIF) are also related to the superposition of the far-field tectonic stresses and the borehole fluid pressure at the borehole wall, and they result when the concentrated stresses become tensile. This occurs in the orientation of S_{Hmax}. Some care must be taken in their interpretation as the fractures are sometimes misinterpreted as borehole breakouts and vice versa (Brudy and Kjø rholt 2001; Barton and Moos 2010). But when carefully employed, DIF's are also reliable estimator of the stress orientation (Aadnø y and Bell 1998; Tingay et al. 2008; Zoback et al. 2003).

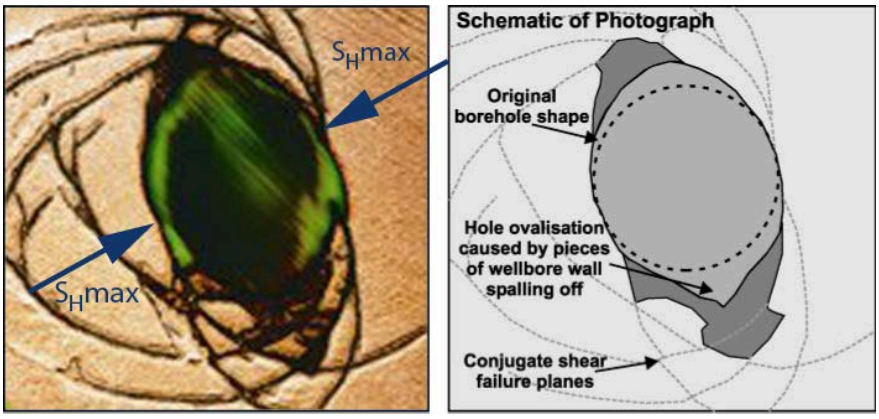

Figure 2.7: Borehole breakouts — results of laboratory tests on a hollow cylinder, which mimics the generation of borehole breakouts. Indicated is the S_{Hmax} orientation, which leads to spalling on the wellbore wall along the S_{hmin} azimuth. This broadens the initial circular borehole to an elliptical borehole (Tingay et al. 2005a, modified).

2.3.3 Geological indicators

Since the 19^{th} century, structural geologists have interpreted and quantified rock deformations on surface outcrops, excavations or tunnels under the assumption that ancient stress conditions lead to the observed deformation pattern in the rock mass. Therefore recent crustal deformation is interpreted to be caused by the recent stress field or remnant stresses such as those induced by glacio-isostatic rebound from Pleistocene glaciations (Sbar and Sykes 1973, and references therein). Precise dating of stress indicators helps to exclude palaeo-stress indicators. Stress- and strain markers in rock can be variable depending on rock type, deformation rate and stress regime potentially causing shear, shortening or extension. Among others, geological indicators include dykes or volcanic vent alignments (GVA) (Nakamura 1977; Nakamura et al. 1977), fault slip data (GF) (e.g. Angelier 1979, 1984) and pop-up structures or joint systems (Hancock and Engelder 1989; Hancock 1991).

2.3.4 Seismological methods – fault plain solutions and shear wave splitting

Earthquakes occur, when the elastically accumulated stress overcomes the internal friction of the rocks or the external friction along existing faults. This relative motion is used on the surface as geological indicators (Sec. 2.3.3). At remote depths, single focal mechanisms (FMS) are used as indicators for the S_{Hmax} azimuth (McKenzie 1969; Raleigh et al. 1972). Average or composite focal mechanisms (FMA) combine several single focal mechanism solutions. Due to the characteristics of a focal mechanism solution and the P-, B-, T-axes, the derived orientation of S_{Hmax} is subject to an uncertainty of about $20-25°$. Formal stress inversions of focal mechanisms (FMF) usually provide a better quality data than FMS or FMA (Arnold and Townend 2007; Célérier et al. 2012; Dziewonski and Woodhouse 1983; Gephart and Forsyth 1984; Michael 1987). Seismic data contributes further information about the stress field via the shear wave (SW) splitting method (shear wave velocity anisotropy – e.g. Buchbinder 1990, 1985; Li et al. 1988; Wahlstrom 1987).

2.3.5 Other methods to estimate S_{Hmax} orientation

There are some other methods to estimate the orientation of S_{Hmax} within the upper crust. Some methods provide besides the orientation the estimate of one or more stress components. These are

hydraulic fracturing (incl. leak-off tests) and the overcoring method, see Sections 2.4.2.1 and 2.4.2.2 respectively.

All these different methods cover a wide depth range. Geological indicators and overcoring provide near surface information. Borehole breakouts and hydraulic fracturing provide stress indicators from a depth of up to 6 km, and in a few scientific drilling projects to depths in excess of 8 km. Seismic data provide via focal mechanisms and shear wave splitting stress information throughout the brittle crust deeper than 40 km.

2.4 Estimation of Stress Magnitudes

2.4.1 Vertical stress (S_V)

The vertical stress S_V is estimated using density logs (e.g. Gardner and Dumanoir 1980) in a well. The density log (Fig. 2.8a) estimates precisely the density of the rocks along the borehole wall; the unlogged parts are estimated by inter- or extrapolation. The S_V at a certain point is the total weight of the overlaying rocks, based on the density (Fig. 2.8b). This can be described by the following equation:

$$S_V = \int_0^z \rho(z) g \, dz \approx \overline{\rho} g z. \tag{2.15}$$

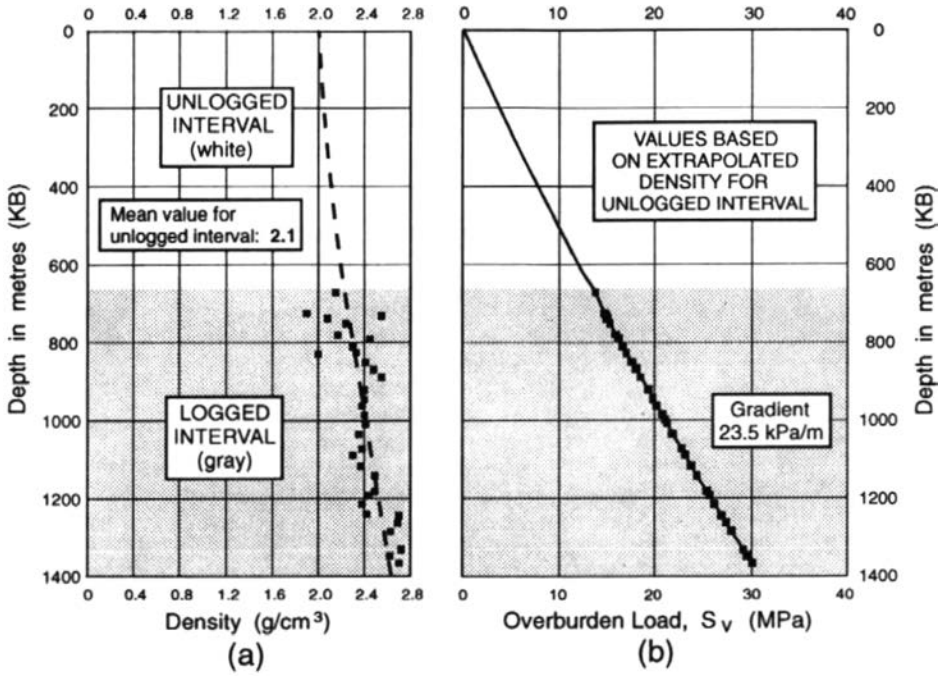

Figure 2.8: **(a)** The rock density is plotted versus depth; the unlogged interval is extrapolated up to the surface. **(b)** The plot of the overburden load against the depth estimates the S_V magnitude. The magnitude depends on the extrapolated values in the unlogged interval (Bell 1996a).

2.4.2 Magnitudes of minimum and maximum horizontal stress (S_{hmin} and S_{Hmax})

2.4.2.1 Hydro-fracturing / Leak-off tests

The method was developed by Clark (1949) for borehole stimulation, until Scheidegger (1962) and Fairhurst (1964) (cited in Stacey and Wesseloo 2002) suggested the method for the determination of the in situ stress magnitude (S_{hmin}). The S_{hmin} magnitudes are estimated by hydraulic fracturing or the similar leak-off test. During hydraulic fracturing (Bell 1996a; Haimson and Cornet 2003; Hubbert and Willis 1957; Zoback et al. 2003) and leak-off tests (e.g. Li et al. 2009; White et al. 2002; Zhou 1997), the down-hole pressure is increased up to a pressure loss due to fluid leakage in the rock mass (Fig. 2.9). This happens, when the hydraulic fracture splits apart the surrounding rock perpendicular to the least principal stress (σ_3), usually assumed to be S_{hmin} in sedimentary basins, and therefore the fracture opens in S_{Hmax} orientation (Fig. 2.10). The highest pressure is the fracture breakdown pressure (P_c, Haimson and Fairhurst 1969), which is S_{hmin} + rock resistance up to failure. When the pressure at which the fracture closes or re-opens is less than S_V, it is assumed that S_{hmin} is estimated (Haimson and Fairhurst 1969). The mini-frac test (e.g. McLellan 1987; Woodland and Bell 1989) and the micro-frac test (Gronseth and Kry 1983) as hydro-fracturing methods estimate the closure pressure by opening and closing the fracture several times, but differs by the injected fluid volume. The method is routinely applied by the hydrocarbon drilling industry, but uncertainties are quite large (Rutqvist et al. 2000).

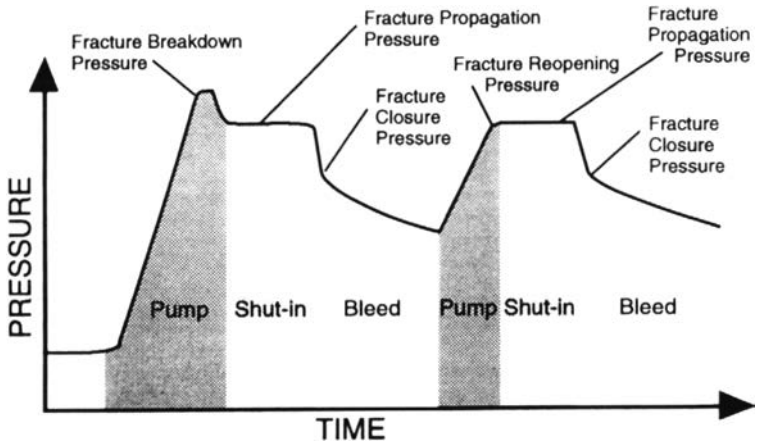

Figure 2.9: Schematic time versus pressure course during a hydraulic fracturing test with two pressurization cycles, the initiation cycle of the fracture and one reopening cycle (Bell 1996a).

The term "leak-off tests" is variably used and can be distinguished by their aim into formation integrity tests (FIT), "classic" leak-off tests (LOT) and extended leak-off tests (XLOT) (White et al. 2002). The general method is similar, but differs in pumping cycles and the point at which the pumping is stopped. In contrast to hydraulic fracturing, LOT are performed at the bottom of the borehole. Therefore, the LOT does not need the bottom hole packer (Fig. 2.10). Usually the term Leak-off test refers to LOT, which provide the upper limit of S_{hmin} and estimate the fracture closure pressure (FCP) or the instantaneous shut-in pressure (ISIP) (White et al. 2002). Extended leak-off tests (XLOT) allow measuring the fracture re-opening pressure, like originally hydro-fracturing tests.

If the pressurization records are appropriately made during LOT, they can be used to estimate the magnitude of the least compressive principal stress (σ_3). This is often interpreted to be the same as the magnitude of S_{hmin}, if the tensile fracture is vertical in strike–slip and normal faulting

stress regimes. If the induced fracture can be detected by the use of borehole image logging or by deformation of a rubber packer by intrusion, its azimuth indicates the orientation of S_{Hmax}.

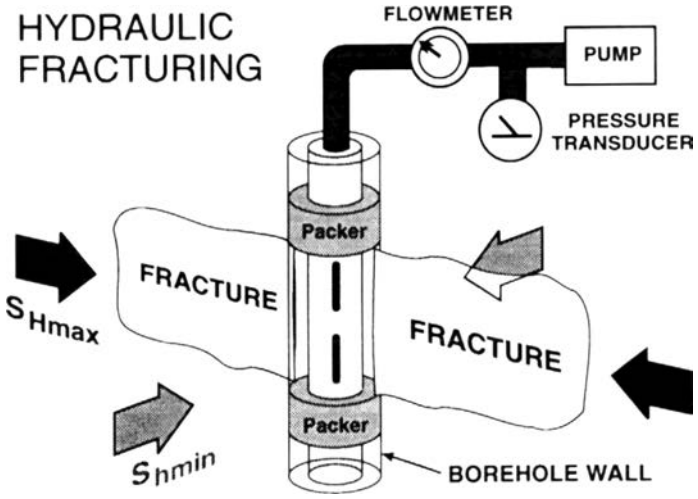

Figure 2.10: Sketch displaying how the S_{hmin} magnitude is estimated by hydraulic fracturing. The fractures will propagate in orientation of S_{Hmax} (Bell 1996a).

2.4.2.2 The overcoring method (OC)

The overcoring (OC) method (McGarr and Gay 1978; Obert 1962) in general isolates a rock cylinder with a diameter of about 3 cm and a length of about 30–60 cm from the surrounding rock. The measured elastic relaxation of the rock cylinder is assumed as equivalent to the stress magnitude as well as occurring in the direction of stress orientation, before removal of the surrounding rock. The method allows the three-dimensional estimation of strain relief, but is usually only applied close to the surface. A further drawback of strain relief estimation is the costs and the small amount of inspected rock mass. There are several similar methods measuring the elastic strain relief, see Zang and Stephansson (2010). However, the overcoring method is the only method to estimate in situ S_{Hmax}magnitudes.

2.4.2.3 Calculation of S_{Hmax}

As overcoring provides mainly data from the surface, some effort is made, to calculate S_{Hmax} based on S_{hmin} magnitude data and known rock properties (for overview see Schmitt et al. 2012). Warren and Smith (1985) provided the following equation to calculate S_{Hmax} based on hydraulic fracturing data:

$$S_{\mathrm{Hmax}} = 3 \cdot S_{\mathrm{hmin}} + T_0 - P_c, \tag{2.16}$$

where T_0 is the tensile strength of the rock an P_c is the breakdown pressure. Under the assumption that the fracture still exists, T_0 can be omitted, as demonstrated by Hickman and Zoback (1983); Stock et al. (1985); Healy and Zoback (1988). In such a case S_{Hmax} can be calculated by the following equation:

$$S_{\mathrm{Hmax}} = 3 \cdot S_{\mathrm{hmin}} - P_c. \tag{2.17}$$

However, the equations are revised or refused several times (Schmitt et al. 2012). Even if the accuracy of the S_{Hmax} magnitude estimation is poor, up to now there is no alternative method to

foresee. Thus such calculated S_{Hmax} magnitude data are the only data from greater depth, e.g. helping to calibrate geomechanical models.

2.5 Stress estimation using geomechanical–numerical models

2.5.1 Modelling workflow

In situ stress data from the Earth's crust are sparsely distributed; especially drilling down to a geothermal reservoir requires reaching great depths. Interpolation and extrapolation technique is widely used to estimate the stress tensor prior the first drilling. However, stress estimation via interpolation techniques becomes particularly questionable in the case of structural inhomogeneities like faults, detachments (Bell and McLellan 1995; Röckel and Lempp 2003; Roth and Fleckenstein 2001; Yassir and Bell 1994), or varying material properties (Roche et al. 2013; Smart et al. 2014; Warpinski 1989). Due to the complex structures and inhomogeneous materials properties, observed in the Earth's crust, an analytical solution cannot be estimated. The same stands for analogue modelling techniques, because of a bundle of problems related to scaling, resolution and stress measurement. Thus, discrete solutions like the finite element method (FEM) allow using unstructured meshes, for a good representation of the complex geometry.

Several steps are necessary to get a proper stress estimation using geomechanical–numerical modelling methods. First of all, the geometrical model is generated using a geological modelling software (e.g. GoCAD®), allowing incorporation of a great variety of geological data, well logs and geophysical date. These data are the model–depended data. Already in this step, the structural model needs to be simplified taking into account the possible number of elements, which determines the model resolution. In the second step, the model geometry is transferred to a grid-framework (mesh), which is generated using a mesh generator software (e.g. HyperMesh®). This mesh together with the material properties is the basis for the numerical modelling software (e.g. Abaqus®/Standard), which solves the partial differential equations of the equilibrium of forces. The solver allows testing initial body forces and different boundary conditions. Finally the visualization tool (e.g. Tecplot®) allows directly comparison between the model outcome and the in situ data (model–independent data). Therefore reasonable results are only achieved, when access exists to some in situ stress data, indicating the orientation and magnitude of crustal stresses. The model generation workflow is simplified:

Structural model		Mesh generation		Solving diff. Equations		Model validation
GoCAD®	→	HyperMesh®	→	Abaqus®/Standard	→	Tecplot®

2.5.2 Preparation of Model geometry

The structural–geological model is of major importance, prepared with a 3-D geomodelling system. Faults and lithological boundaries are defined as discrete triangulated surfaces (e.g. Van Wees et al. 2003). These are built based on points (stratigraphic borehole data and seismic data), curves (seismic and interpreted cross sections, lineaments from the geological map) or point clouds that describe surfaces (DEM). The ability to process this wide range of different data is the major advantage of a geomodelling software, compared to other CAD systems. Furthermore, data are honoured during surface generation as soft or hard constrained, depending on their quality (e.g. Ross et al. 2004). The roughness of the surfaces can be polished with the discrete smoothing interpolation (DSI) algorithm (Mallet 1992, 2002).

2.5.3 Finite Element Method (FEM)

The finite element method (FEM) is an approved numerical method to solve a wide range of continuum mechanical problems. It was developed in the 20^{th} century by the aerospace industry (Turner et al. 1956); the name FEM was introduced later by Clough (1960). In general, the FEM gives a discrete solution of a partial differential equation, describing the underlying physical problem, on a specific domain decomposition of the equation into finite elements. The finite elements form a polygonal grid (mesh) which completely exhausts the studied volume. The approximation of the solution being sought for a single element is controlled by a set of simple element equations. The method can be applied to complex structures with inhomogeneous materials properties, like the Earth's crust, where analytical solution are not available.

Due to the mainly slow processes in the crust it can be assumed, that most crustal parts are in equilibrium of forces. This state is described by the following partial differential equation (Eq. 2.18), where $\boldsymbol{\sigma}_{ij}$ is the effective stress, x are the spatial coordinates and f_i represents all body force, which are gravitationally forces (gravity $\vec{g}$ and density ρ) as well as forces generated by the initial stress conditions ($\boldsymbol{\sigma}^0_{ij}$).

$$\frac{\partial \boldsymbol{\sigma}_{ij}}{\partial x_j} + f_i = 0 \tag{2.18}$$

For estimation of contemporary crustal stresses, it is often assumed, that anisotropic linear elastic material properties are a proper approximation. This is the case as long as the applied forces or the acting deformations are small enough, that no failure occurs. Then, the stress σ_{ij} and the strain ϵ_{ijkl} are linear related and linkes by an elasticity tensor c_{ijkl}

$$\sigma_{ij} = \sum_{l=1}^{3} \sum_{k=1}^{3} c_{ijkl}\epsilon_{kl} \quad with \quad \epsilon_{kl} = \frac{1}{2}\left(\frac{\partial u_k}{\partial x_l} + \frac{\partial u_l}{\partial x_k}\right), \tag{2.19}$$

where u_k and u_l are appropriate components of the displacement vector $\vec{u}$. Eq. (2.18) and eq. (2.19) describe the stress state assuming furthermore that viscous rock deformation, acceleration, changing pore pressures or other thermal effects have marginal influence on the present day stress state. This is the case for tectonically calm regions, e.g. the Alberta Basin (Chapter 4). A further important issue is the definition of the boundary conditions, which defines the stable spatial position and/or a certain strain, in the same way, as the volume of interest is wedged in the Earth's crust. Using finite elements and taking into account the boundary conditions the partial differential equation system (Eq. 2.18) and (Eq. 2.19) can be replaced by a simple matrix equation (Eq. 2.20). The FEM software (solver) attempts to find an equilibrium between the acting forces $\mathbf{f}$, the stiffness matrix $\mathbf{K}$ and the displacement $\mathbf{u}$.

$$\mathbf{f} = \mathbf{K} \cdot \mathbf{u}. \tag{2.20}$$

The greatest advantage of the FE method is the possibility to use unstructured meshes, which favour the method for complex and non-rectangular structures, such as observed in the upper Earth crust. The method was fast introduced in geosciences to investigate crustal stress patterns (e.g. Stephansson and Berner 1971), later on continued with increasing element numbers. There are several studies on tectonic plate-scale stress models down to reservoir-scale models in the last two decades using 2-D models (e.g. Dyksterhuis et al. 2005; Humphreys and Coblentz 2007; Jarosinski et al. 2006), as well 3-D models (Buchmann and Connolly 2007; Hergert and Heidbach 2011; Parsons

2006; Fischer and Henk 2013; Heidbach et al. 2013; Henk 2005; Orlic and Wassing 2012; Van Wees et al. 2003).

Some of the FEM solver such as Abaqus®/Standard allows connecting separated meshes by contact surfaces. This allows incorporating faults in the model geometry having a certain friction coefficient. Furthermore, these contact surfaces can connect meshes with a different resolution.

2.5.4 Mesh optimisation

The fineness of the discretisation (mesh resolution) has a significant influence on the accuracy of the calculated model results. However, computational cost increases at the same time, using a finer mesh. Therefore, it is necessary to find a balance between resolution and element number. There are several element types available (Fig. 2.11) either in the 2-D or the 3-D case, which can reduce element number, when optimally chosen. The main element types are triangles and quadrilaterals for 2-D models as well as tetrahedrons and hexahedrons for 3-D models. Pyramid and prism elements are degenerated hexahedron elements. An variable mesh resolution allows to have very variable resolution within short distances within the model volume. This can be done in 3-D models with tetrahedrons only. In contrast a few tetrahedrons within a thin layer are very unstable, because of the small interior angle. This would be an issue e.g. for thin alternating stratigraphy units. In such a case thin hexahedrons are much more stable, finally more sparingly. However, complicated volumes cannot be meshed straight with hexahedrons. The problem can be reduced, by cutting down the volume into smaller pieces. Those can be filled with a hexahedron mesh directly, which is not possible for the complex bodies. However, an appropriate meshing strategy has to be adapted for each model.

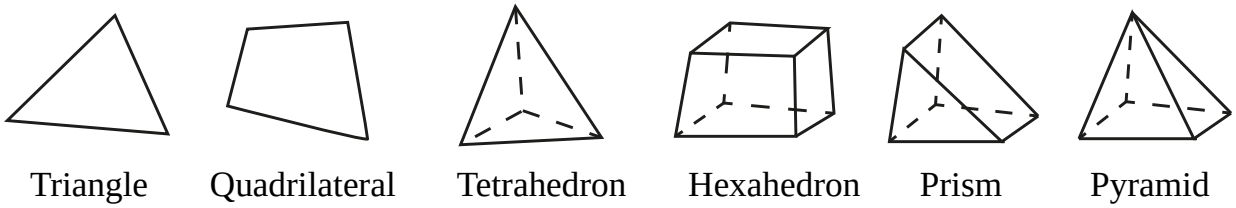

Figure 2.11: Major element types used for 2-D and 3-D FEM models.

3 A Revised Crustal Stress Orientation Database for Canada

Karsten Reiter[1,2], Oliver Heidbach[1], Douglas Schmitt[3], Kristine Haug[4], Moritz Ziegler[1,2], Inga Moeck[5]

[1] GFZ German Research Centre for Geosciences, Telegrafenberg, 14473 Potsdam, Germany
[2] University of Potsdam, Inst. of Earth and Environmental Science, Karl-Liebknecht-Straße 24 - 25, 14476 Potsdam–Golm, Germany
[3] Institute for Geophysical Research, CCIS 4-138, Dept. of Physics, University of Alberta, Edmonton, Alberta, T6G 2E1 Canada
[4] Alberta Energy Regulator, Alberta Geological Survey, 402 Twin Atria Building, 4999 - 98 Avenue, Edmonton, Alberta, T6B 2X3 Canada
[5] Technische Universität München, Dept. of Civil, Geo and Environmental Engineering, Arcisstraße 21, 80333 München, Germany

Journal: Tectonophysics, 636, 111–124, DOI: 10.1016/j.tecto.2014.08.006

Status: Received 8 May 2014, Revised 31 July 2014, Accepted 16 August 2014, Available online 27 August 2014

Abstract

The Canadian database on contemporary crustal stress has not been revised systematically in the past two decades. Here we present the results of our new compilation that contains 514 new data records for the orientation data of maximum compressive horizontal stress and 188 data records that were re-assessed. In total the Canadian stress database has now 1,667 data records, which is an increase of about 45%. From these data, a new Canadian Stress map as well as one for the Province of Alberta is presented.

To analyse the stress pattern, we use the quasi median on the circle as a smoothing algorithm that generates a smoothed stress map of the maximum compressive horizontal stress orientation on a regular grid. The newly introduced quasi interquartile range on the circle estimates the spreading of the data and is used as a measure for the wave-length of the stress pattern. The result of the hybrid wavelength analysis confirms that long spatial wavelength stress patterns ($\geq$1,000 km) exist in large areas in Canada. The observed stress pattern is transmitted through the intra-plate regions.

The results reveal that shorter spatial wave length variation of the maximum compressive horizontal stress orientation of less than 200 km, prevails particularly in south-eastern and western Canada. Regional stress sources such as density contrasts, active fault systems, crustal structures, etc. might have a significant impact in these regions. In contrast to these variations, the observed stress pattern in the Alberta Basin is very homogeneous and mainly controlled by plate boundary forces and body forces. The influence of curvature of the Rocky Mountains salient in southern Alberta is minimal. The present-day horizontal stress orientations determined herein have important implications for the production of hydrocarbons and geothermal energy in the Alberta Basin.

3.1 Introduction

Understanding of the in-situ stress tensor in the Earth's crust is of key importance to a number of major scientific, economic and societal issues. Knowledge of the crustal stress is key to understanding plate tectonics or earthquake cycles. Such knowledge is also crucial for drilling as crustal stresses influence well-bore stability, reservoir operation and stimulation, cap rock integrity, induced seismicity and the long-term stability of underground constructions. Consequently, knowledge of the contemporary crustal state of stress is of great importance to resource-rich nations such as Canada whose economies depend on the efficient and safe extraction of minerals and hydrocarbons and who is under pressure to do better at protection of the environment.

There are several methods used to estimate both stress orientation and magnitudes from borehole observations (e.g. Amadei and Stephansson 1997; Ljunggren et al. 2003; Schmitt et al. 2012; Zang and Stephansson 2010; Zoback et al. 2003). These methods include overcoring, analysis of the orientation of borehole breakouts and drilling induced tensile fractures, hydraulic fracturing (leak-off, mini-frac, micro-frac, etc.), earthquake focal mechanisms and geological indicators. The results from these methods may represent the stress state at scales of a few decimetres up to tens of kilometres (Ljunggren et al. 2003). However, obtaining the complete state of stress (i.e. the six independent components of the stress tensor) remains a challenging task. All techniques have in common that they can provide at least the maximum compressive horizontal stress (S_{Hmax}) orientation, or perpendicularly to it, the minimum horizontal stress (S_{hmin}) azimuth; only a few methods deliver further components of the stress tensor. Furthermore, the vertical stress magnitude (S_V) can be estimated from the weight of the overburden and the S_{hmin} magnitude from leak-off tests or hydraulic fracturing (e.g. Haimson and Fairhurst 1969; Hubbert and Willis 1957; White et al. 2002). However, in particular the reliable estimation of the S_{Hmax} magnitude remains difficult as the numerous assumptions to be made impose high uncertainties.

Consequently, stress maps have primarily focussed on illustrating the S_{Hmax} azimuth. The first systematic compilation of orientation data by Sbar and Sykes (1973) mapped the S_{Hmax} orientation over North America, by means of focal mechanisms, geological indicators, overcoring and hydraulic fracturing. Stress mapping accelerated significantly with the findings of Bell and Gough (1979) and Hottman et al. (1979) that the azimuth of borehole breakouts (Babcock 1978) indicates the S_{Hmax} orientation. The acquisition of such data is relatively easily found by means of oriented calliper log data as is provided, for example, by dipmeters (e.g. Plumb and Hickman 1985). The compilation of stress data in North America in the subsequent years by Adams (1987, 1989); Adams and Bell (1991); Bell et al. (1994); Fordjor et al. (1983); Gough et al. (1983); Zoback and Zoback (1980, 1981, 1989, 1991) showed, that the pattern of S_{Hmax} orientations is frequently uniform over thousands of kilometres. These observations were used as evidence that the tectonic stress field is controlled by plate boundary forces and body forces; these are first order stress sources (Zoback 1992). This hypothesis was studied globally by the continued compilation of stress data in the framework of the World Stress Map project (WSM) and is confirmed in first order (Richardson 1992; Zoback et al. 1989; Zoback 1992). Besides the first order main driving forces of plate tectonics, there are several stress perturbations of the second and third orders, which can strongly overprint the regional stress field in some areas (Heidbach et al. 2007; Zoback 1992). Such local or regional effects can be detected only in the case of the availability of dense stress observations of sufficient quality.

In the two decades after the initial phase of the WSM project (1986 - 1992), data entries in the recent global database have been tripled (Heidbach et al. 2010). Despite this global increase there has not to our knowledge been a substantial systematic revision nor extension on the Canadian stress database for about two decades (Adams and Bell 1991; Bell et al. 1994) with the exception of some additional work focussed on specific geological targets (e.g. Bachu et al. 2008; Bell and Bachu 2003, 2004; Bell and Grasby 2012). In the Western Canada Sedimentary Basin with more than 700,000 wells, a considerable amount of geophysical logging image and dipmeter has been collected, but most of this remains inaccessible. In principle, the extraordinary data density would allow a far more detailed study of second and third order stress deviations. A revised stress data compilation and analysis from the Alberta Basin which represents the foreland basin of Western Canadian Cordillera would allow the comparison of stress patterns in similar geologic settings as the Subalpine Molasse Basin, a foreland basin of the Alpine orogenic belt in Germany (Reinecker et al. 2010).

The first objective of this paper is to update and revise the stress map of Canada by adding all new stress orientation data to the existing data set. As much of the new data comes from the

portions of the Western Canada Sedimentary Basin in Alberta, the pattern analysis will focus on the overall stress there. All 1153 data records from the WSM 2008 database release (Heidbach et al. 2010) were cross-checked and state of the art quality ranking was applied. By adding 514 data records from new publications and a data set from the Alberta Geological Survey (AGS), the number of S_{Hmax} azimuth records in the research area is increased by 45 % to 1667.

The second objective of this work is the investigation of the S_{Hmax} orientation pattern in Canada and again in detail for Alberta, by means of the updated database. A hybrid wavelength analysis technique based on the algorithm from Heidbach et al. (2010) is developed further and presented here.

Furthermore, the data set showcases a more homogeneous stress pattern along the length of Alberta. In particular this new compilation appears to show that the S_{Hmax} orientations in the Alberta foreland basin are not always perpendicular to the front of the Rocky Mountains as had previously been believed (e.g. Bell and Gough 1979). That is the first and second order patterns dominate over Alberta despite the existence of large bounding geomorphological features such as the Rocky Mountains and the Rocky Mountains Trench further to the west. This is in contrast to other regions such as the St. Lawrence Lowland where a good observation density suggests a stress field dominated by the second and third order stress sources (e.g. fault zones).

3.2 Crustal stresses

3.2.1 Indicators of stress orientation

The full stress tensor consists of six independent components none of which can be measured directly. Most of our stress knowledge comes from stress indicators that are observed by the use of a variety of methods from boreholes. These methods (for overview see Ljunggren et al. 2003) may be distinguished as they provide either data on crustal stress orientations only or they give knowledge of the stress magnitudes and/or faulting regime. Here, we will focus only on those methods which allow for estimation of the stress orientation.

Since the 19^{th} century, structural geologists have interpreted and quantified rock deformations under the assumption that ancient stress conditions lead to the observed deformation pattern in the rock mass. Therefore recent crustal deformation is interpreted to be caused by the recent stress field or remnant stresses such as those induced by glacio-isostatic rebound from Pleistocene glaciations (Sbar and Sykes 1973, and references therein). Precise dating of stress indicators helps to exclude palaeo-stress indicators. Stress- and strain markers in rock can be variable depending on rock type, deformation rate and stress regime potentially causing shear, shortening or extension. Among others geological indicators include dykes or volcanic vent alignments (GVA) (Nakamura 1977; Nakamura et al. 1977), fault slip data (GF) (e.g. Angelier 1979, 1984) and pop-up structures or joint systems (Hancock and Engelder 1989; Hancock 1991).

Bell and Gough (1979) and independently Hottman et al. (1979) were the first to recognize that borehole breakouts (BO), which were known for some years (e.g. Babcock 1978; Cox 1972), are an indicator of the orientation of stresses in the crust. Breakouts are borehole segments of several metres or more along which the borehole wall has spalled preferentially at diametrically opposed azimuths. As such, the diameter across the BO must be greater than that for the drill bit; and this major axis points in the direction of S_{hmin}. The breakouts occur due to concentration of the combined horizontal stresses at the borehole wall (e.g. Haimson and Song 1993; Schmitt et al. 2012; Zoback et al. 1985, 2003). There are several geophysical logging methods to identify elliptical borehole sections that include ultrasonic acoustic imaging as produced by the borehole televiewer (Zemanek et al. 1969, 1970), electrical resistivity imaging methods such as produced by micro-resistivity tools (Ekstrom et al. 1987), and simpler mechanical oriented-calliper logs like

Table 3.1: Type and quality of the S_{Hmax} orientation data from Canada and surrounding (Latitude >41°N, Longitude 142°W to 46°W).

	complete dataset		new data only	
	A–E	A–C	A–E	A–C
Data type	quality		quality	
Focal mechanisms (FMF, FMS, FMA)	767	516	212	132
Borehole breakouts (BO, BOT)	657	389	181	38
Drilling-induced tensile fractures (DIF)	42	38	42	38
Geological: fault–slip (GFM, GFS)	6	6		
Hydraulic fracturing (HF, HFG, HFM)	43	13	20	4
Overcoring (OC)	91	12	53	4
Geological: volcanic alignment (GVA)	53	3		
Petal centreline fractures (PC)	4	4	4	4
Shear wave splitting (SW)	4		2	
Total	1667	981	514	220

four-arm up to multi-finger dipmeter/calliper logs (e.g. Babcock 1978; Plumb and Hickman 1985; Reinecker et al. 2003).

Drilling induced (tensile) fractures (DIF) also provide stress orientation data. They are also related to the superposition of the far-field tectonic stresses and the borehole fluid pressure at the borehole wall, and they result when the concentrated stresses become tensile. This occurs in the direction of the greatest horizontal compressive stress — the orientation of the DIF indicates that for S_{Hmax}. Some care must be taken in their interpretation as the fractures are sometimes misinterpreted as borehole breakouts (Brudy and Kjø rholt 2001; Barton and Moos 2010). When carefully employed, however, the DIF are also reliable estimator of the stress orientation (Aadnø y and Bell 1998; Tingay et al. 2008; Zoback et al. 2003).

Leak-off methods are very commonly used to test borehole integrity, and are similar to the hydraulic fracturing method (HF) (e.g. Haimson and Fairhurst 1969; Hubbert and Willis 1957; Schmitt et al. 2012; White et al. 2002; Zoback et al. 2003). If the pressurization records are appropriately made, they can be used to measure the magnitude of the least compressive principal stress (σ_3). This is often interpreted to be the same as the magnitude of S_{hmin}, if the tensile fracture is vertical in strike–slip and normal faulting environments. If the induced fracture can be detected by the use of borehole image logging or by deformation of a rubber packer by intrusion, its azimuth indicates the orientation of S_{Hmax}.

The overcoring (OC) method (McGarr and Gay 1978; Obert 1962) in general isolates a rock cylinder with a diameter of about 3 cm and a length of about 30 – 60 cm from the surrounding rock. The measured elastic relaxation of the rock cylinder is assumed as equivalent to the stress magnitude as well as occurring in the direction of stress orientation, before removal of the surrounding rock. The method allows the three-dimensional measurement of strain relief, but is usually only applied close to the surface. A further drawback of strain relief measurements is the costs and the small amount of measured rock mass.

Earthquakes occur, when the elastically accumulated stress overcomes the internal friction of the rocks or the external friction along existing faults. This relative motion is used on the surface as geological indicators. At remote depths, single focal mechanisms (FMS) are used as indicators for the S_{Hmax} azimuth (McKenzie 1969; Raleigh et al. 1972). Average or composite focal mechanisms (FMA) combine several single focal mechanism solutions. Due to the characteristics of a focal mechanism solution and the P-, B-, T-axes, the derived orientation of S_{Hmax} is subject to an uncertainty of about 20 – 25°. Formal stress inversions of focal mechanisms (FMF) usually provide a better quality

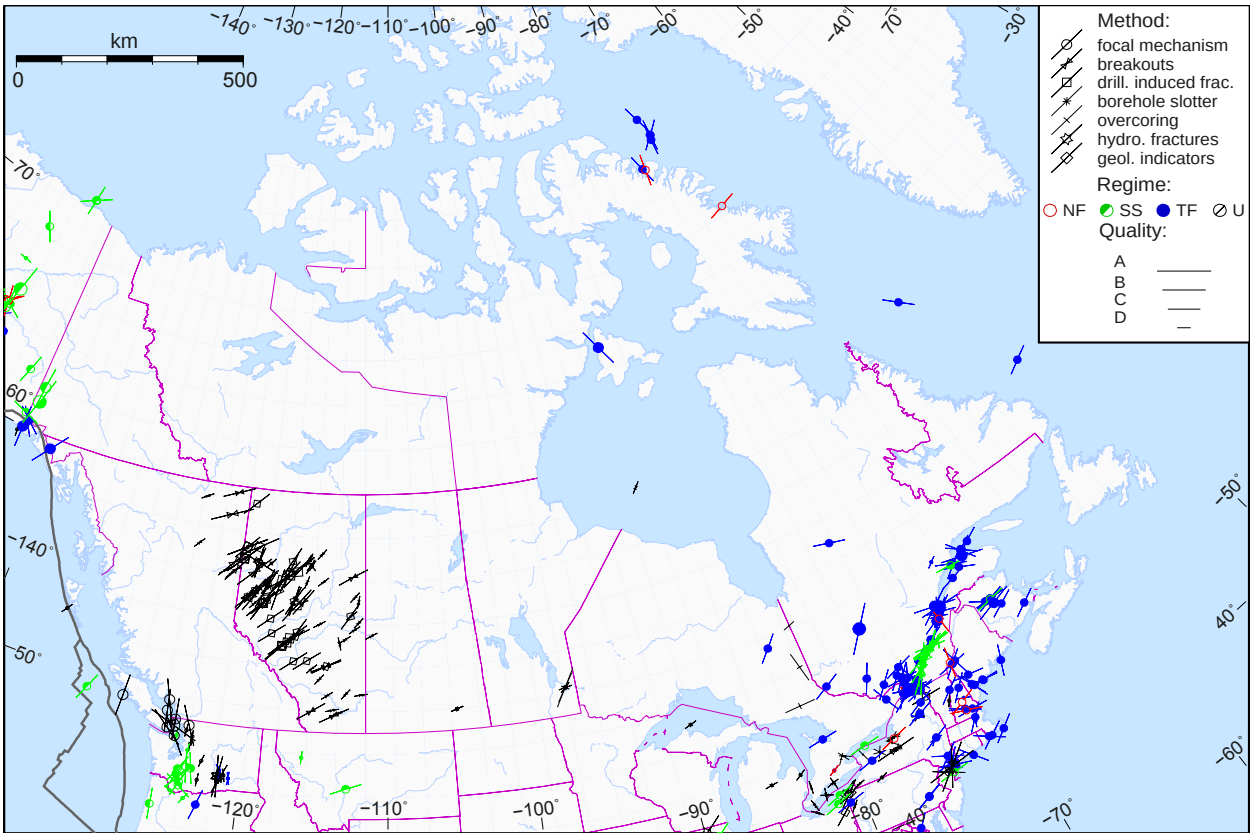

Figure 3.1: New data in the Canadian database, added since the 2008 World Stress Map update (Heidbach et al. 2009, 2010). Lines represent orientations of maximum horizontal compressional stress (S_{Hmax}), line length is proportional to quality. Colours indicate stress regimes, with red for normal faulting (NF), green for strike–slip faulting (SS), blue for thrust faulting (TF), and black for unknown regime (U). Plate boundaries are taken from the global model PB2002 of Bird (2003).

data (Arnold and Townend 2007; Célérier et al. 2012; Dziewonski and Woodhouse 1983; Gephart and Forsyth 1984; Michael 1987) . Seismic data contributes further information about the stress field via the shear wave (SW) splitting method (e.g. Buchbinder 1990, 1985; Li et al. 1988; Wahlstrom 1987).

These different methods cover a wide depth range. Geological indicators and overcoring provide near surface information. Borehole breakouts and hydraulic fracturing provide stress indicators from a depth of up to 6 km, and in a few scientific drilling projects to depths in excess of 8 km. Seismic data provide via focal mechanisms and shear wave splitting stress information throughout the brittle crust deeper than 40 km. Borehole breakouts are the major contributor beyond focal mechanisms in the Canadian database (Tab. 3.1).

3.2.2 Stress data compilation

The early plate wide compilations of crustal stress indicators helped researchers to recognize the impact of plate boundary forces on large continental crustal areas, such as the North American Plate (Adams 1987; Adams and Bell 1991; Fordjor et al. 1983; Gough et al. 1983; Sbar and Sykes 1973; Zoback and Zoback 1980, 1981, 1989, 1991). They came to the conclusion, that the crustal stress field is governed by the same forces driving plate tectonic motion, which are called first

Table 3.2: First, second and third order stress sources, modified after Zoback et al. (1989); Zoback (1992); Heidbach et al. (2007, 2010).

Order of stress source	Extent vs. lithosphere thickness	Extent [km]	Stress sources
First	$\gg$	>500	Plate boundary forces: ridge push, slab pull, trench suction; gravitational potential energy; basal tractions originating from density driven mantle convection
Second	$\sim$	$100-500$	lithospheric flexure (isostatic compensation, sediment loading on continental margins, seamount loading, upwarping oceanward of the trench), localized lateral density contrasts/buoyancy forces, lateral strength contrasts (anisotropy of material properties), topography, continental rifting, large fault zones, lateral contrasts of heat production, erosion
Third	$\ll$	<100	local density or strength contrasts, basin geometry, basal detachment, man-made excavation, man-made downhole pressure changes, impoundment dams, lowering of the water table, active faults, incised valleys

order stress sources (Tab. 3.2). These are the oceanic ridge push, the slab pull at subduction zones (Forsyth and Uyedaf 1975; Richardson and Reding 1991; Richardson 1992; Zoback and Zoback 1981; Zoback et al. 1989; Zoback 1992) in interaction with the mantle driving and resisting forces (e.g. Adams and Bell 1991; Becker and Faccenna 2011; Ghosh et al. 2013; Gough 1984; McGarr 1982) and resistance along transform faults. Another important source of stress in the lithosphere is the gravitational potential energy (GPE — Ghosh et al. 2009; Humphreys and Coblentz 2007; Naliboff et al. 2012).

Second and third order stress sources (Heidbach et al. 2007, 2010; Müller et al. 1997; Tingay et al. 2005b; Zoback 1992; Zoback and Mooney 2003) disturb the observed general stress orientation trend from regional through local to reservoir scale (Tab. 3.2). They are in a range of about 100 - 500 km, for second and <100 km for third order stress sources.

3.2.3 World Stress Map project

A key challenge for regional and global compilation of crustal stress information is the combination of stress indicators that encompass a wide range of methods and sample very different rock volumes (Ljunggren et al. 2003). In order to make the information comparable, a quality ranking scheme was developed for the World Stress Map project (Zoback et al. 1989; Zoback and Zoback 1991; Zoback 1992) and later updated by Sperner et al. (2003) and Heidbach et al. (2009, 2010). The WSM quality ranking scheme is based on the standard deviation on the individual measurements within a given suite. A-quality is the highest and E is the lowest quality. The WSM project website provides a guideline for the data analysis and quality assignment for the WSM database (http://world-stress-map.org).

The first comprehensive global compilation of stress data was initiated by the International Lithosphere Program with the WSM project that published after its first funding phase a database with ∼7,700 data records (Zoback 1992). The latest update of the WSM in 2008 has ∼21,750 data records (Heidbach et al. 2009, 2010). Nevertheless, data are irregularly distributed across the world with the highest densities coming from sedimentary basins penetrated by many logged boreholes and zones of active seismicity with frequent earthquakes. This unfortunately occurs even in North America, a region with generally many entries, that has large areas with no data due to a lack of oil or gas or mineral exploration or low seismicity. Whatever the application of the data is: analysis of

the stress distribution or numerical modelling, the high volume of data in the database reduces uncertainties as well as it allows a better understanding of the local stress field pattern.

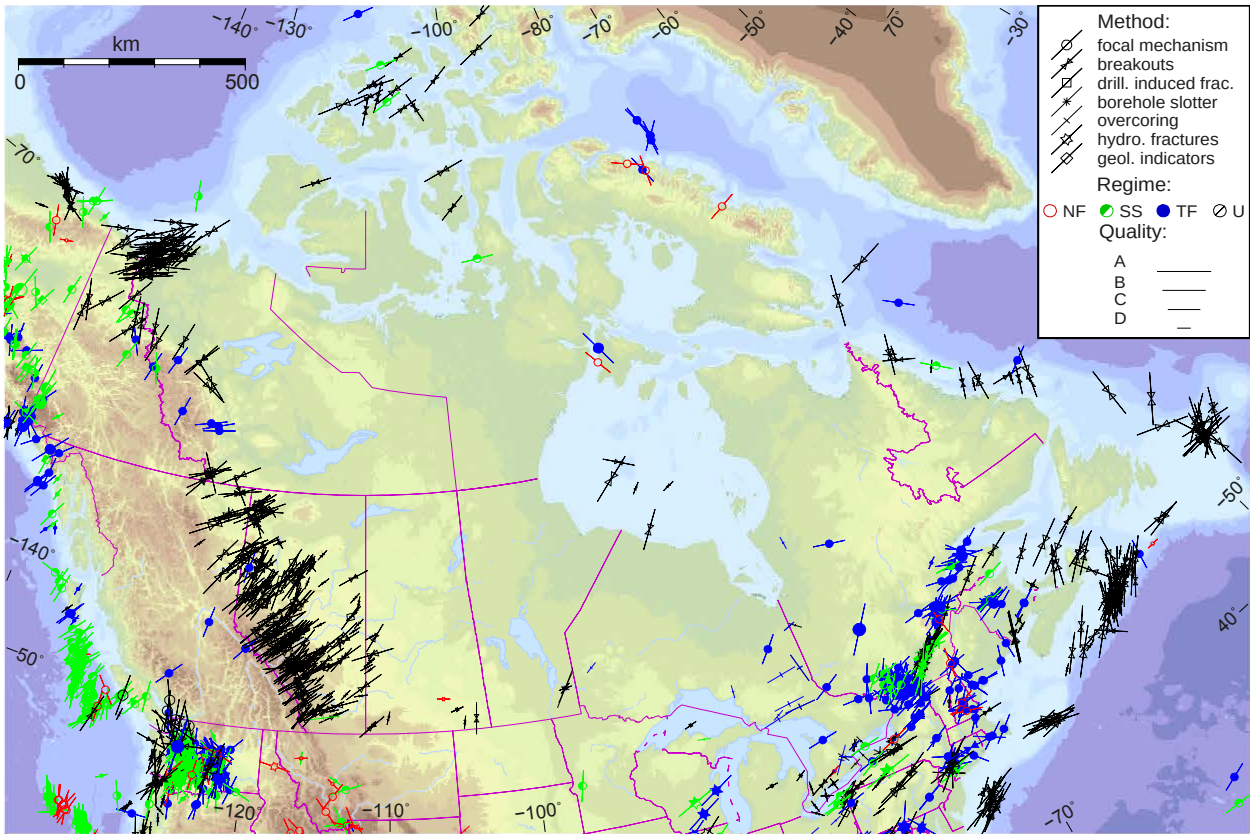

Figure 3.2: Stress map of Canada including topography with the complete compiled dataset. Lines represent orientations of maximum horizontal compressional stress (S_{Hmax}), line length is proportional to the quality. Colours indicate stress regimes, with red for normal faulting (NF), green for strike–slip faulting (SS), blue for thrust faulting (TF), and black for unknown regime (U). Plate boundaries are taken from the global model PB2002 of Bird (2003).

3.2.4 Update of the Canadian Stress Map

As crustal stress is not impacted by political boundaries, this update of the Canadian stress map includes data from the northern US and offshore measurements. An artificial boundary is used to compare the amount of existing and updated data records in the database. It is restricted to latitudes $\geq$41°N as the southern boundary and the longitudes ranging from 142°W to 46°W.

At the beginning of this study, it was first necessary to revise the existing data records according to rigorous application of the latest revision of the WSM quality ranking (Heidbach et al. 2010), correct of typographical errors, and remove of poor quality data. Data published in the open literature in the 20 years since the first version of the stress map (see below) provided additional information to allow for completion of some of the data records with changes in their quality ranking. In total, 188 data records from the old WSM database were updated.

New data are also added since data published elsewhere and from a previously unavailable dataset that had been maintained by the Alberta Geological Survey (AGS). The published data are compiled from a literature investigation of the following articles by Adams (1987); Balfour et al. (2011); Bell

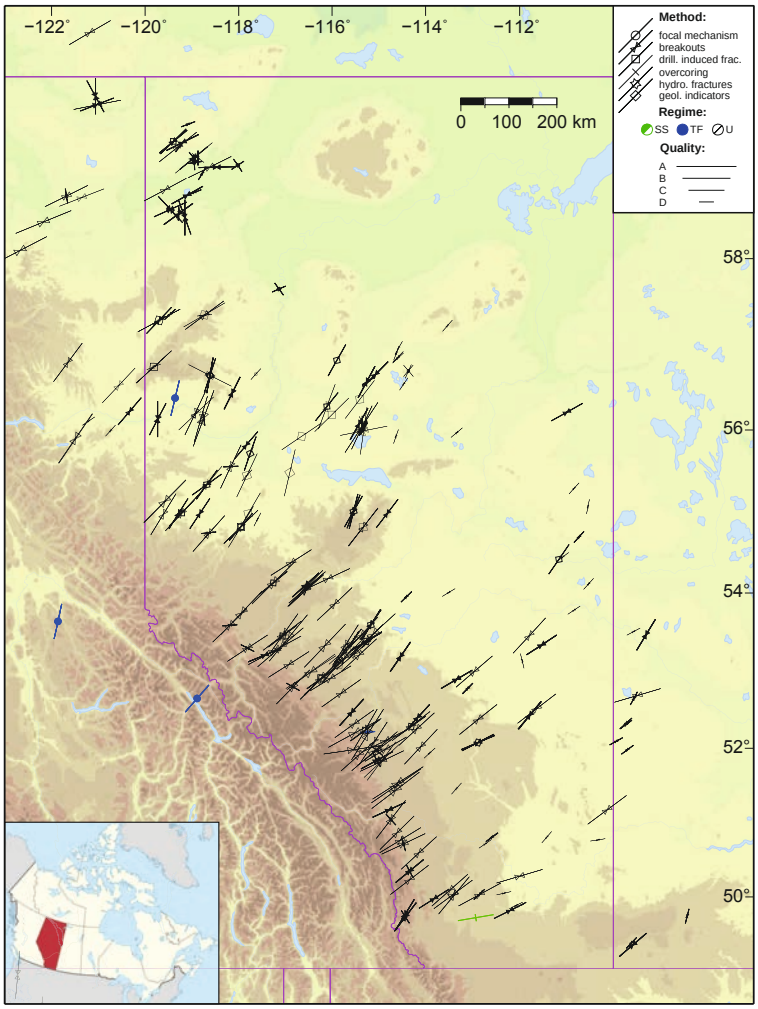

Figure 3.3: New stress map of Alberta. Lines represent orientations of maximum horizontal compressional stress (S_{Hmax}), line length is proportional to quality. Colours indicate tectonic stress regimes, with green for strike–slip faulting (SS), blue for thrust faulting (TF), and black for unknown regime (U). The tectonic regime is mostly unknown due to the fact, that only focal mechanisms and overcoring have the potential to derive this information.

et al. (1994); Bell and Bachu (2003); Buchbinder (1990); Du et al. (2003); Eisbacher and Bielenstein (1971); Hamid (2008); Hurd and Zoback (2012); Konstantinovskaya et al. (2012); Kim (2003); Kim et al. (2006); Ma et al. (2008); Mazzotti and Townend (2010); Michael and Buschkuehle (2008); Ruppert (2008); Steffen et al. (2012); StLouisEQcenter (2010); Yassir and Dusseault (1992) and Zakharova and Goldberg (2014). The update adds up to 514 new records in Canada (Fig. 3.1) with a grand total of 1667 entries (Fig. 3.2, Tab. 3.1). In Alberta, 78 records were modified and 142 new ones are added to the WSM database; nearly doubling the data set to 297 entries (Fig. 3.3). This is highly advantageous because it allows for a refinement of the grid and for increased confidence in the application of statistical analysis than before.

3.3 Statistical analysis of the Canadian stress data

3.3.1 Mean orientation and wavelength analysis

It is assumed that large intra-plate regions, such as much of Northern America have a uniform S_{Hmax} orientation that is governed by plate boundary- and body forces (Adams 1987, 1989; Adams and Bell 1991; Zoback and Zoback 1980; Fordjor et al. 1983; Gough et al. 1983; Zoback and Zoback 1981, 1989, 1991). That said, several intra-plate regions are influenced or disturbed by the second and third order stress sources. As such, it can be difficult to separate the first from the higher order stress.

To better understand such regions, interpolation and smoothing algorithms have been applied in local studies (Bird and Li 1996; Hansen and Mount 1990; Heidbach and Ben-Avraham 2007; Müller et al. 2003; Rebaï et al. 1992). A further motivation of such studies is to fill gaps in the distribution of the data record, which allows estimations of the stress orientation.

The first global statistical stress pattern analysis was carried out by the use of 4,527 A – C quality entries from the WSM 1992 database by Coblentz and Richardson (1995). Their statistical test on S_{Hmax} orientations separated the data into $5 \times 5°$ bins. They determined the bins, in which the S_{Hmax} orientation is not randomly distributed based on a circular confidence level (Mardia 1972). Depending on different confidence levels, the orientation of the mean S_{Hmax} ($\widehat{S}_{Hmax}$) was plotted. Their results suggested a strong correlation between the ridge push and the absolute plate velocity azimuths with the average S_{Hmax} orientation.

A similar analysis is presented by Heidbach et al. (2010) by means of nearly four times the number of data records (16,969 A – C quality data). In contrast to Coblentz and Richardson (1995), they used a reticular node geometry with a spatial resolution of $0.5 \times 0.5°$, with a variable area around the nodes with radii ranging from 100 to 1,000 km. The radius of a given area was successively varied. The $\widehat{S}_{Hmax}$ orientation was estimated with a circular standard deviation (SD) (Mardia 1972) of $\sigma \leq 25°$ thus providing a smoothed global stress map. Their colour coded maps indicate the largest diameter which fulfils the criterion (SD$\leq 25°$); these diameters are interpreted as wavelength of a homogeneous stress orientation. Their map confirmed regions with long wavelength pattern ($\geq$ 1,000 km) in North America. The $\widehat{S}_{Hmax}$ orientations were also compared to the ridge push and absolute plate velocity azimuths.

3.3.2 Median and quartiles on periodic data

The major problems of circular statistics on stress orientation data are the following: 1. usually there are just a few data records in a certain area, 2. all of these stress indicators have large uncertainties and variation, and 3. the data sets are contaminated with incorrect data (outliers). For example tensile fractures are often misinterpreted as borehole breakouts (e.g. Barton and Moos 2010; Brudy and Kjø rholt 2001), which results in a 90° rotation in S_{Hmax}. These outliers (3.) in combination with less data (1.) could disturb the calculation of the mean drastically.

Therefore, the median is preferred as estimator of the average, because of its robustness in terms of outliers. Based on the Mardia Median (Mardia 1972) for circular data, and the linear quasi median (Hodges and Lehmann 1967), Ratanaruamkarn et al. (2009) introduced the quasi median on the circle ($\widetilde{\theta}$):

$$\widetilde{\theta} = \theta_{.50} = \begin{cases} \arctan\left(\frac{sin\theta_{m+1}}{cos\theta_{m+1}}\right) & \text{if } n = 2m+1 \\ \\ \arctan\left(\frac{sin\theta_m + sin\theta_{m+1}}{cos\theta_m + cos\theta_{m+1}}\right) & \text{if } n = 2m. \end{cases} \tag{3.1}$$

where $\theta_1 < \theta_2 < \cdot \cdot \cdot < \theta_n$ are the ordered circular data. This circular quasi median is a better estimator of the average than the median, especially when the sample size (n) is small.

To quantify the spread of the data, neither the variance nor standard deviation is a good estimator for possibly contaminated data sets. In such a case the interquartiles range (IQR):

$$IQR = Q_{.75} - Q_{.25} \tag{3.2}$$

is a good estimator of data spreading in the linear case ($Q_{.25}$ = lower quartile and $Q_{.75}$ = upper quartile — Upton and Cook 1996). Based on the method, to calculate the quasi median on circular data (Ratanaruamkarn et al. 2009), the lower ($\theta_{.25}$) and the upper quartile ($\theta_{.75}$) on circular data are now calculated as follows:

$$\theta_{.25} = \begin{cases} \arctan\left(\frac{sin\theta_{m+1}}{cos\theta_{m+1}}\right) & \text{if } n = 4m \\ \arctan\left(\frac{3\,sin\theta_m + sin\theta_{m+1}}{3\,cos\theta_m + cos\theta_{m+1}}\right) & \text{if } n = 4m+1 \\ \arctan\left(\frac{sin\theta_m + sin\theta_{m+1}}{cos\theta_m + cos\theta_{m+1}}\right) & \text{if } n = 4m+2 \\ \arctan\left(\frac{sin\theta_m + 3\,sin\theta_{m+1}}{cos\theta_m + 3\,cos\theta_{m+1}}\right) & \text{if } n = 4m+3 \end{cases} \tag{3.3}$$

$$\theta_{.75} = \begin{cases} \arctan\left(\frac{sin\theta_{3m+1}}{cos\theta_{3m+1}}\right) & \text{if } n = 4m \\ \arctan\left(\frac{3\,sin\theta_{3m} + sin\theta_{3m+1}}{3\,cos\theta_{3m} + cos\theta_{3m+1}}\right) & \text{if } n = 4m+1 \\ \arctan\left(\frac{sin\theta_{3m} + sin\theta_{3m+1}}{cos\theta_{3m} + cos\theta_{3m+1}}\right) & \text{if } n = 4m+2 \\ \arctan\left(\frac{sin\theta_{3m} + 3\,sin\theta_{3m+1}}{cos\theta_{3m} + 3\,cos\theta_{3m+1}}\right) & \text{if } n = 4m+3. \end{cases} \tag{3.4}$$

The newly introduced quasi interquartile range on the circle (QIROC) is now calculated:

$$QIROC = \theta_{.75} - \theta_{.25}, \tag{3.5}$$

which is an even better estimator of data spreading for circular data, robust towards outliers, especially for small data sets.

3.3.3 Applied statistic method

The quasi circular median (Mardia 1972; Ratanaruamkarn et al. 2009) of S_{Hmax} ($\widetilde{S}_{Hmax}$) and the new quasi interquartile range in the circle (QIROC), which estimates the variability, are calculated, by means of the A – D quality data records in the updated Canadian stress database (Tab. 3.1, Fig. 3.2) on a 0.75, 0.25 and 0.1° square grid of Canada and surrounding. When calculating $\widetilde{S}_{Hmax}$ and the QIROC, the distance and the quality of the measured data were weighted by a quality index according to the scheme of Heidbach et al. (2010). The quality weighting is $w_Q = 1/15$ for A quality, 1/20 for B quality, 1/25 for C quality, and 1/40 for D quality. Distance (D) weighting $w_D = 1/D$ (D = 25 km when D < 25 km) is applied, where D is the distance from the measured location to the grid point. The largest allowed variability of used data records on a single grid point is limited with a QIROC of ≤20°. The lower limit of data records is n ≥ 5, where n is the number of reliable data records within the search radius.

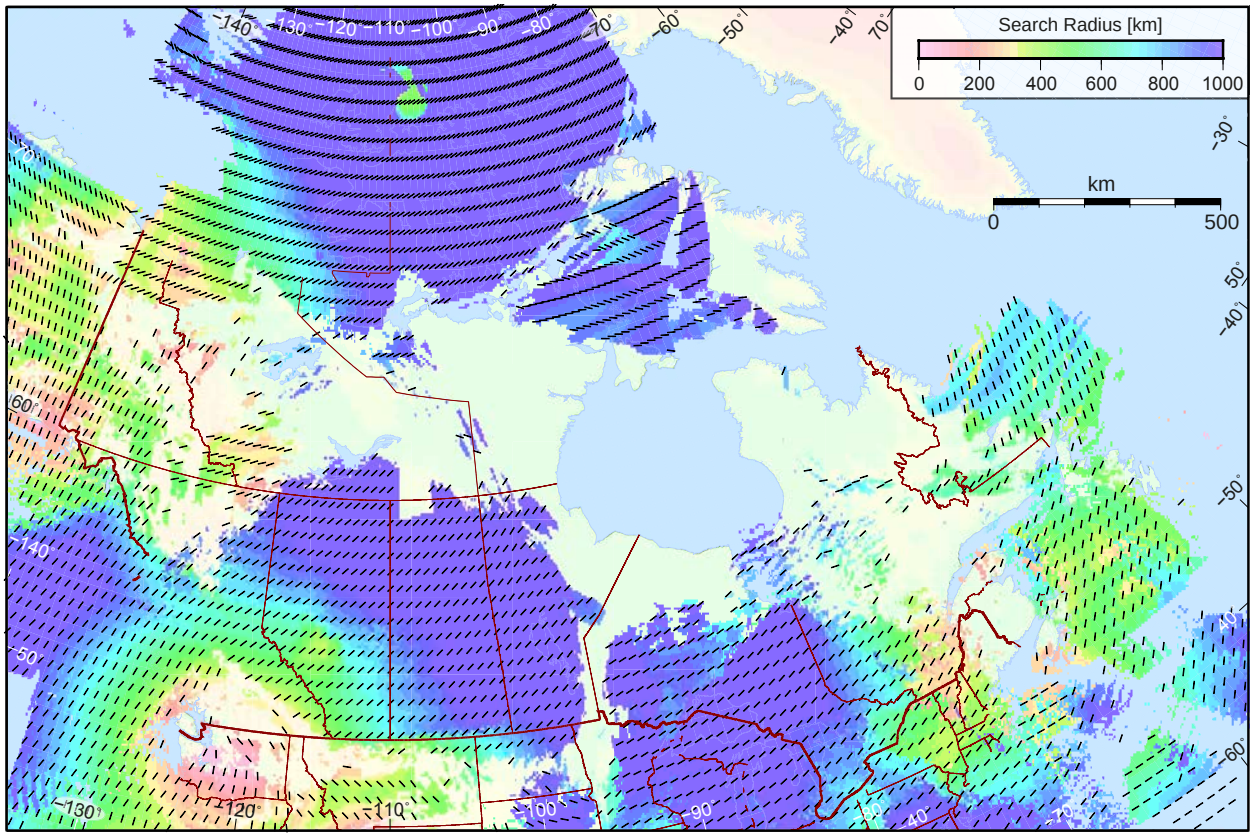

Figure 3.4: Wavelength map of Canada and surrounding, results of the statistic stress pattern analysis are displayed. The smoothed S_{Hmax} orientation is visualised by the black strokes, indicating the $\widetilde{S}_{Hmax}$ azimuths on an $0.75 \times 0.75°$ grid. The largest radii (r_{max}), which fulfil the confidence criteria (QIROC $\leq 20°$) and data records $n \geq 5$ are colour coded, which is interpreted as the wavelength of the crustal stress pattern.

Beginning with a search radius (r) of 1,000 km around each grid point, the radius is reduced stepwise by 100 km down to 200 km, then in 50 km steps down to 50 km and finally 25 km is the smallest search radius. The largest radius, which fulfils all criteria (QIROC $\leq 20°$, $n \geq 5$) is r_{max}. All data within the largest radii around the grid point are used to calculate $\widetilde{S}_{Hmax}$orientation. The $\widetilde{S}_{Hmax}$ azimuths are plotted based on the 0.75° grid for Canada (Fig. 3.4) and with the 0.25° grid for Alberta (Fig. 3.5).

To visualise the wavelength of homogeneous stress orientations in the maps, r_{max} is plotted colour coded, based on a $0.1 \times 0.1°$ grid for both maps (Fig. 3.4 and 3.5). Pink indicates small wavelength < 200 km, green indicates intermediate 400 - 600 km, and blue indicates long wavelength areas > 800 km.

3.4 Geologic and tectonic setting

For the interpretation of the resulting stress pattern displayed in Figures 3.2, 3.3, 3.4 and 3.5, we summarize in the following section the main geological and tectonic setting of Canada and in particular for Alberta.

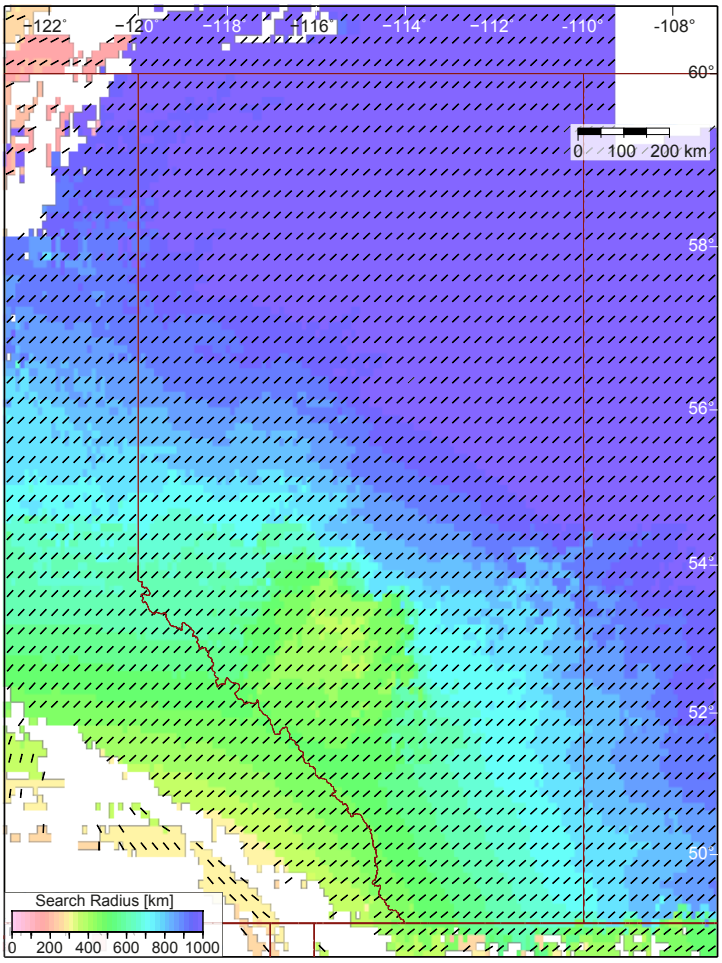

Figure 3.5: Wavelength map of Alberta, the average S_{Hmax} orientation is visualised by the black strokes, indicating the $\widetilde{S}_{Hmax}$ azimuths on a $0.25 \times 0.25°$ grid. The largest radii (r_{max}), which fulfil the confidence criteria (QIROC $\leq 20°$) and data records n ≥ 5 are colour coded, which is interpreted as the wavelength of the crustal stress pattern. An increasing wavelength, orthogonal to the Rocky Mountains in direction to the Canadian Shield is observed.

3.4.1 Canada

The geological units of Canada (Fig. 3.6) range from one of the oldest rocks worldwide on the Canadian Archean Shield to young glacial sediments. The main structural unit is the Canadian Shield: a vast composite cratonic region assembled during the late Palaeo-proterozoic (e.g. Hoffman 1989). It is exposed in the north-central part of North America, mainly to the east and to the west of the Hudson Bay area. The craton is covered by four sedimentary basins. These are the Interior Platform or Western Canadian Sedimentary Basin (WCSB), including the Alberta Basin and the Williston Basin (Porter et al. 1982; Wright et al. 1994), the Arctic Platform to the north and the St. Lawrence Platform to the east. Additionally, the Hudson Bay Platform is located in the centre of the Canadian Shield (e.g. Norris 1986).

Except the Hudson Bay Platform, each of these platforms is in contact with a Phanerozoic orogenic belt surrounding the Canadian Shield. The oldest is the Palaeozoic Appalachian Orogen on the south-east coast (e.g. Pollock et al. 2012). The Innuitian Orogen (e.g. Oakey and Stephenson

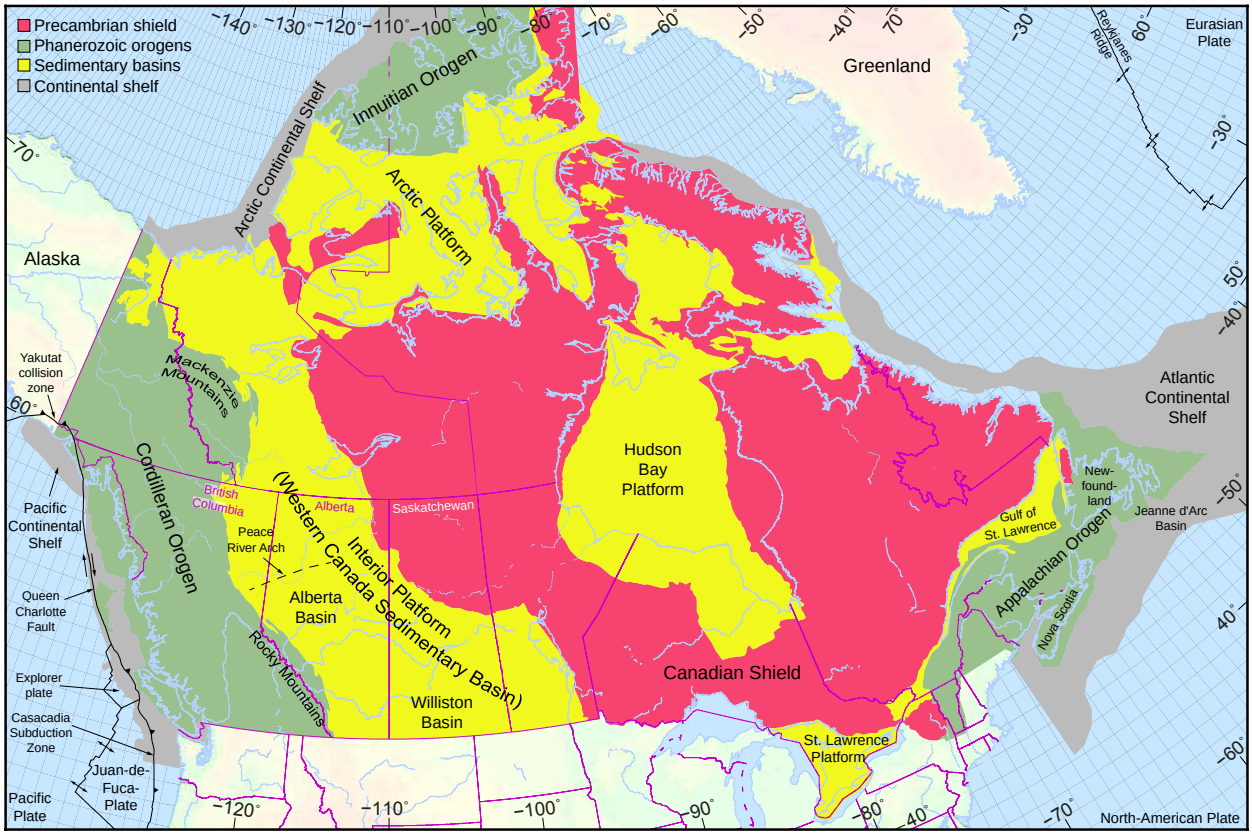

Figure 3.6: Map of the Canadian geological provinces, with the main tectonic features. The Canadian Shield (incorporating seven geological provinces) is in red, the platform-sedimentary basins onto the Canadian Shield in yellow, building together the consolidated craton. The Phanerozoic orogens are in green, continental shelf areas in grey. Plate boundaries are taken from the global model PB2002 of Bird (2003), modified and indicated by black, administrative borders by pink lines. The Map is redrawn and modified after NRCan (2009).

2008) developed in the north of the Arctic Platform, from Cretaceous to Palaeocene. To the west of the WCSB is a wide Mesozoic to recent mountain chain of the Canadian Cordillera with the front-ranges of the Rocky Mountains riding upwards over the craton (Gabrielse and Yorath 1989; Monger et al. 1972; Monger and Price 2002; Price 1981a, 1986, 1994; Sigloch and Mihalynuk 2013). Off-shore are the Pacific-, the Arctic- and the Atlantic Continental shelves as transition regions to the oceanic crust.

There are two major plate boundaries, which could influence the present stress field in Canada. To the west, the boundary between the North American Plate and the Pacific Plate near the latitude of the Canada–U.S. border is represented by the Cascadian subduction zone. At this contact the Juan-de-Fuca-Plate is subducting eastward under the North American Plate. To the north and nearly parallel to the western shoreline the plate boundary is marked by the south–south-east trending Queen Charlotte transform fault, whereas south of the Cascadian subduction zone, the plate boundary is represented by the San Andreas fault zone. To the East, the Reykjanes Ridge (Mid-Atlantic rift zone) is about 1,500 km outboard and sub-parallel to the eastern Canada shoreline.

3.4.2 Alberta

The Alberta Basin, occupies a portion of the much larger WCSB (Fig. 3.6) and was formed as a foreland basin during the Middle Jurassic to early Eocene development of Rocky Mountains portion of the Cordilleran foreland fold-and- thrust belt (e.g. Porter et al. 1982; Price 1981b; Wright et al. 1994). Sediments settled partly discontinuous during the whole Phanerozoic (Mossop and Shetsen 1994a, Chapter 6 - 26). The crystalline basement of the WCSB, and implicitly that of the superposed Alberta Basin is the North American craton, which is exposed by erosion to the north-east where it is more commonly called the Canadian Shield. Jurassic to Palaeocene strata deposited in the western part of the Alberta Basin have been incorporated in the Rocky Mountains fold-and-thrust belt, which is bound farther west in British Columbia by the Rocky Mountain Trench. The Alberta Basin consists of an undeformed sedimentary wedge that increases in thickness from zero at the Canadian Shield to approximately 5,500 m near the fold-and-thrust belt.

The final shape of the Alberta Basin developed by downward flexing of the Canadian Shield due to lithospheric loading and isostatic flexure in a retro-arc setting (English and Johnston 2004), together with the sediment derived from the developing Canadian Cordillera. The fold-and-thrust belt documents the deformation history and is curved convexly towards the foreland sedimentary basin. The axis of the fold-and-thrust belt changes orientation from southerly in the northern segment between 60°and 55°N, to south-easterly between 55°and 49°N, and again to southerly close to the U.S. border. These orientation changes of about 30°, includes the peculiar convex curvature of the fold-and-thrust belt in southern Canada was variously assigned to either changing stresses at the plate boundary, or a re-entrant in the ancestral margin of north America (north of the "Montania" promontory, see McMechan and Price 1982).

3.5 Results and Discussion

3.5.1 $\widetilde{S}_{Hmax}$ orientation and QIROC as new statistical methods

Statistical methods, to determine a grid with average S_{Hmax} orientations are further developed in this paper, based on Coblentz and Richardson (1995) and Heidbach et al. (2010). A circular median S_{Hmax} ($\widetilde{S}_{Hmax}$) is a better estimator of the S_{Hmax} orientation than the circular mean S_{Hmax} ($\widehat{S}_{Hmax}$), because $\widetilde{S}_{Hmax}$ is more robust to outliers. The allowed deviation criteria, a standard deviation of $\leq 25°$, used from Heidbach et al. (2010) is replaced by the quasi interquartile range on the circle (QIROC $\leq 20°$), which is more strict. This may exclude some data records, but in general it gives a more precise and robust estimator, which is justified by the increasing amount of available data. However, despite the fact, that orientation data are weighted according the quality ranking scheme, uncertainties are not eliminated. Especially systematic errors are reproduced by the method, whereas random errors are balanced.

The resolution of the used rectangular grid (0.75°) of smoothed S_{Hmax} orientation in Canada (Fig. 3.4) is slightly coarser then the grid used by Heidbach et al. (2010) and seven times finer than the grid used by Coblentz and Richardson (1995). For the Alberta map (Fig. 3.5), the grid resolution (0.25°) is two times and 20 times finer, respectively. The colour coded grid of the wavelength (0.1°) has a five times higher resolution than that one used by Heidbach et al. (2010). The general $\widetilde{S}_{Hmax}$ orientation is similar to the previously found $\widehat{S}_{Hmax}$ orientation (Coblentz and Richardson 1995; Heidbach et al. 2010), but with a higher resolution, a better coverage and smaller confidence level.

3.5.2 Stress pattern in Canada

It is assumed that first order stress sources like ridge push, slab pull, mantle tractions and gravitational potential energy (GPE) are the main drivers of the stress field in the North American crust (Adams 1987, 1989; Adams and Bell 1991; Flesch et al. 2007; Fordjor et al. 1983; Gough et al.

1983; Gough 1984; Ghosh et al. 2013; Humphreys and Coblentz 2007; McGarr 1982; Richardson and Reding 1991; Sbar and Sykes 1973; Zoback and Zoback 1980, 1981, 1989; Zoback 1992). The overall observed S_{Hmax} orientation is about north-east. According to the assumed second order stress sources (Adams 1989; Adams and Bell 1991; Zoback 1992), the following influences are suggested to act in Canada: isostatic rebound as reaction to the load of thick ice sheets during ice age, margin-normal extensional stresses on the continental shelf and margin-normal compressional stresses in the adjacent oceanic part. The latter two influences could be the case for the Atlantic margin. Proterozoic or Palaeozoic suture zones as well other structures should not or only slightly disturb the recent plate driven stress field (Zoback 1992). According to Camelbeeck et al. (2013), the orientation of the stress field could be estimated as perpendicular to the slope of the geoid high. Comparison of the geoid heights (Huang and Véronneau 2005) with the stresses fit for the Rocky Mountains in Alberta. But for whole Canada (Véronneau 1997), the correlation of the observed stress pattern vs. geoid high is not convincing. But the stress pattern is consistent with estimations of crustal stress by GPE models (Flesch et al. 2007) in western Canada.

The Stress Map of Canada (Fig. 3.2) displays several regions with a very dense net of in-situ stress data but still has wide regions with no or just a few observations. The majority of the data records are focal mechanisms (46%, n = 767) and from borehole breakouts (39%, n = 657), see Tab. 3.1. Focal mechanisms are concentrated on the east coast at the St. Lawrence Platform and along the Appalachian Orogen as well as off-shore of the west coast, along the Cascadian subduction zone and the Queen Charlotte fault (Fig. 3.2). Borehole breakouts in contrast are mainly eastward of the Canadian Cordillera and in the Atlantic continental shelf area along the east coast. Substantial portions of the data are from the Alberta Basin to the east of the Rocky Mountain trench.

There is a general trend of the S_{Hmax} orientation east of the Cordillera towards northeast–southwest, visible in Fig. 3.2. A similar pattern is visible for $\widetilde{S}_{Hmax}$ (Fig. 3.4); the smoothed S_{Hmax} is also preferentially oriented northeast–southwest in most regions. The strong correlation of S_{Hmax} orientation in the mid-plate crust of North America with plate motion (Henton et al. 2006) has been interpreted to be due to resistive drag at the base of the plate (Adams 1989; Adams and Bell 1991; Gough et al. 1983; Gough 1984; Zoback et al. 1989). This orientation is also in the expected orientation based on Mid-Atlantic push (Zoback et al. 1989, and references therein).

The wavelength map of Canada (Fig. 3.4) displays long wavelengths in the area of the Canadian Shield (Fig. 3.6) and a transition to intermediate wavelengths in the areas of the sedimentary basins onto the Canadian Shield. On the east coast, the foothills of the Appalachian Mountains as well as the continental shelf areas are characterized by intermediate to small wavelengths. In the most parts of the Canadian Cordillera, short wavelengths are observed. There are some regions where the wavelength map displays long wavelengths, for example in Saskatchewan, where only a few stress orientation indicators are measured. This is due to the homogeneous stress data, when large search radii fulfil the pass criteria. On the other hand some regions with a few measurements display no wavelength, as the pass criteria are not fulfilled. The data points from the Hudson Bay for example illustrates this perfectly: there are five data points (Fig. 3.2), but one of them have clearly a larger deviation than the defined QIROC of $\leq 20°$ for at least necessarily data points ($n \geq 5$), to fulfil the criteria.

The stress orientation is different in the north-western Canadian Cordilleras, where $\widetilde{S}_{Hmax}$ points to the north. This is associated to the transform plate boundary between the North American Plate and the Pacific Plate. This trend continues but rotates to a south-east orientation of S_{Hmax} in northern Alaska, as discussed in Adams (1989); Adams and Bell (1991).

Only in the Mackenzie Mountains, north of the Rocky Mountains, the $\widetilde{S}_{Hmax}$ orientation changes from north-east to north; this rotation has also been observed by Ristau et al. (2007). The majority of the S_{Hmax} azimuth data are oriented perpendicular to the topography of the Mackenzie Mountains and follow nicely the curved shape of those mountains with a rotation of nearly 90°. Besides the

topographic effect, this also may be caused by a north to south oriented strike slip zone and a proposed strain transfer from the Yakutat collision zone by a lower crustal detachment (Mazzotti and Hyndman 2002).

Within the Hudson Bay, Bell and Wu (1997) observed S_{Hmax} orientation to the north-east, according the overall trend, which is observed in both sub-salinary and supra-salinary sediments. North of the Hudson Bay area S_{Hmax} orientations are towards south-east. These orientations are derived from only a few focal mechanisms. These deviations from the overall stress pattern can be possibly explained by post-glacial isostatic rebound (Adams 1989; Adams and Bell 1991). However, elastic thickness in the centre of the Canadian Shield is 80 km (Kirby and Swain 2014), but the inner part of the Canadian Shield has V_S velocities constantly lower than in the outer rim (Kao et al. 2013). Perhaps these structures explain even better that several of the S_{Hmax} data are oriented towards the centre of the Canadian Shield, even for northward oriented data in the south of the Hudson Bay.

Along the St. Lawrence Platform up to the Gulf of St. Lawrence and in the northern part of the Appalachian Mountains, the S_{Hmax} orientations are inhomogeneous and the wavelengths are short, partly <50 km. A possible reason for this may be that the earthquakes, from which the S_{Hmax} orientations are derived, occurred on a fault system that is not optimally oriented in the contemporary stress field. Following Heidbach et al. (2010), FMS data always have the potential to inherit larger uncertainties on the derived S_{Hmax} orientation than indicated by the C-quality assigned by default (Célérier et al. 2012). Another explanation is a low velocity anomaly, observed in shallow depth (<20 km) (Kao et al. 2013). However, stress orientations in this region are most probably perturbed by the second or third order stress sources such as low friction faults and less from isostatic rebound (Mazzotti and Townend 2010).

The orientation of S_{Hmax} along the south-eastern coast is sub-parallel to the shore line, which indicates that neither sedimentary load on the shelf nor buoyancy contrast on the continental slope disturbs the overall stress pattern. Some irregularities are observed south-east of Nova Scotia. In this region a ductile salt layer and an over-pressured zone are accused to affect the general stress pattern (Yassir and Bell 1994). Bell (1996b) interprets the irregular stress pattern in the Jeanne d'Arc Basin offshore Newfoundland by the same overprint mechanism.

The stress pattern in the shelf area to the north of the Gulf of St. Lawrence is more irregular. S_{Hmax} orientations in the region between Alaska and Greenland are north–northeast oriented, which neither fits to the overall stress pattern (north-east) nor to the orientation of the continental slope, which is also north-east. Zoback et al. (1989) and Zoback (1992) suggest, that some regions seems to be partly superimposed by local stress perturbation due to the sedimentary load, loading flexure or other sediment related effects along the continental shelf.

3.5.3 Stress pattern in the Alberta Basin

The stress field over much of Alberta has been studied for more than 30 years (e.g. Fordjor et al. 1983; Gough et al. 1983; Bell et al. 1994) with stress orientations obtained from nearly all of Alberta except for the north-east (Fig. 3.3). There are some zones of clustered data that come from areas where appropriate borehole log data was available. Visual inspection of the map indicates a rather homogeneous pattern of north-east directed stress orientations that are approximately perpendicular to the Rocky Mountain orogenic belt. A slight change of the orientation may follow the large scale curvature of the Rocky Mountain range in southern Alberta and is in agreement to the previous studies (e.g. Bell et al. 1994; Fordjor et al. 1983; Gough et al. 1983). The stress orientations in the Alberta Basin are consistent within single stratigraphic units (Bell and Bachu 2003) and down across several stratigraphic levels to the Precambrian basement (Bell 1996b; Bell and Grasby 2012; Fordjor et al. 1983). This average stress orientation (north-east) is concurrent to the observed overall pattern in Canada.

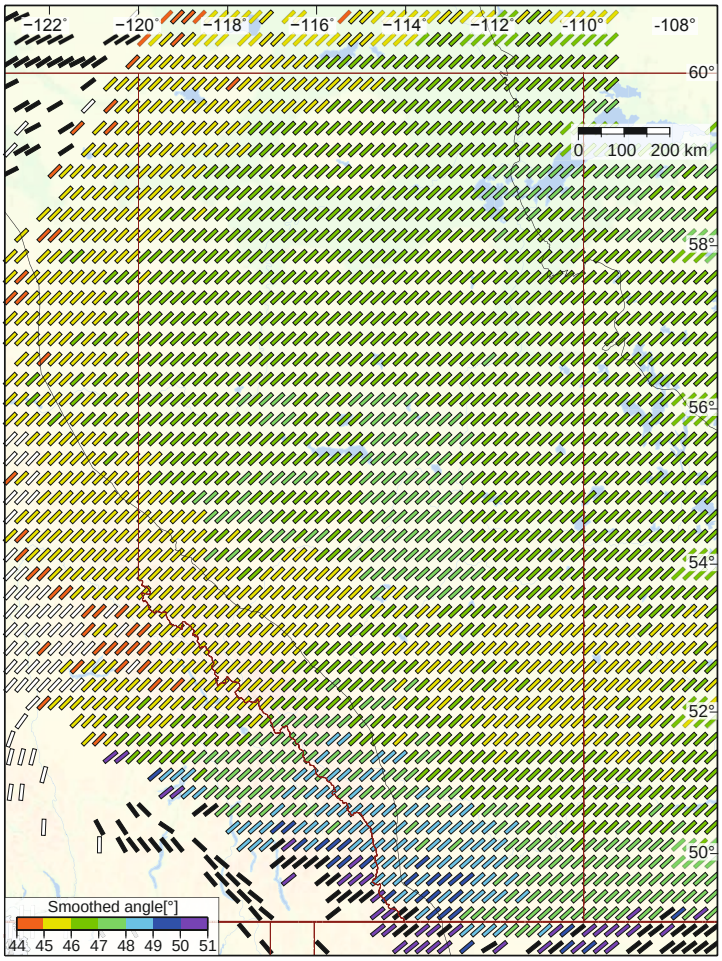

Figure 3.7: Map of Alberta, displaying the smoothed S_{Hmax} orientation ($\widetilde{S}_{Hmax}$) grid from Figure 3.5 is colour coded depending on the azimuth angle. The border to the Canadian Shield and to the foreland belt is indicated by a black line. The very small change of the orientation in contrast to the change of topography as well the curvature or the front of the Rocky Mountains fold-and-thrust belt in the southern area is obvious.

The median S_{Hmax} ($\widetilde{S}_{Hmax}$) orientation (Fig. 3.5) in Alberta is very uniform and on casual inspection appears constant everywhere. To highlight more subtle variations of the $\widetilde{S}_{Hmax}$ azimuth in Alberta the angle of the $\widetilde{S}_{Hmax}$ orientations is colour coded in Fig. 3.7. These orientations range from only $45-47°$ over most of Alberta, and deviate from this trend only in the south-west where the angle rotates to 51°. Therefore the $\widetilde{S}_{Hmax}$ orientation varies only a few degrees.

Figure 3.8 displays the S_{Hmax} orientation in the southern Alberta Basin. In the very south at 50°N of the Rocky Mountains it is convexly curved, but the stress orientation in the foothills and the Alberta Basin do not follow this trend, This is in contrast to the assumption from Bell and Gough (1979) and to comparable tectonic settings like the Molasse Basin of Germany, immediately north of the European Alps (Fig. 3.9). In the curved Molasse foreland basin, the S_{Hmax} orientations are consistently perpendicular to the topography (Reinecker et al. 2010). The S_{Hmax} orientation there follows nicely the basin geometry and the crustal thickness. The cause could be the different age of the foreland basin's development. The younger Molasse basin developed in the Cenozoic whereas the Alberta Basin is a result of Mesozoic deformation. An end-member in such a train of

thought is the Palaeozoic Appalachian Mountains (Fig. 3.2), where S_{Hmax} neither shows any context to past orogenic shortening nor to recent topography.

In southern Alberta, the influence of the topography and the curved fold-and-thrust belt are limited on the stress orientations. This suggests that deeper effects such as the influence of basal tractions from density driven mantle convection (e.g. Becker and Faccenna 2011) or the influence of lithospheric thickness and density variations may predominate (e.g. Camelbeeck et al. 2013; Flesch et al. 2007; Naliboff et al. 2012). Recent modelling of upper crustal stress orientation and magnitude in the Alberta Basin demonstrates less influence of Mohorovičić depth-variation below the Rocky Mountains (Reiter and Heidbach 2014).

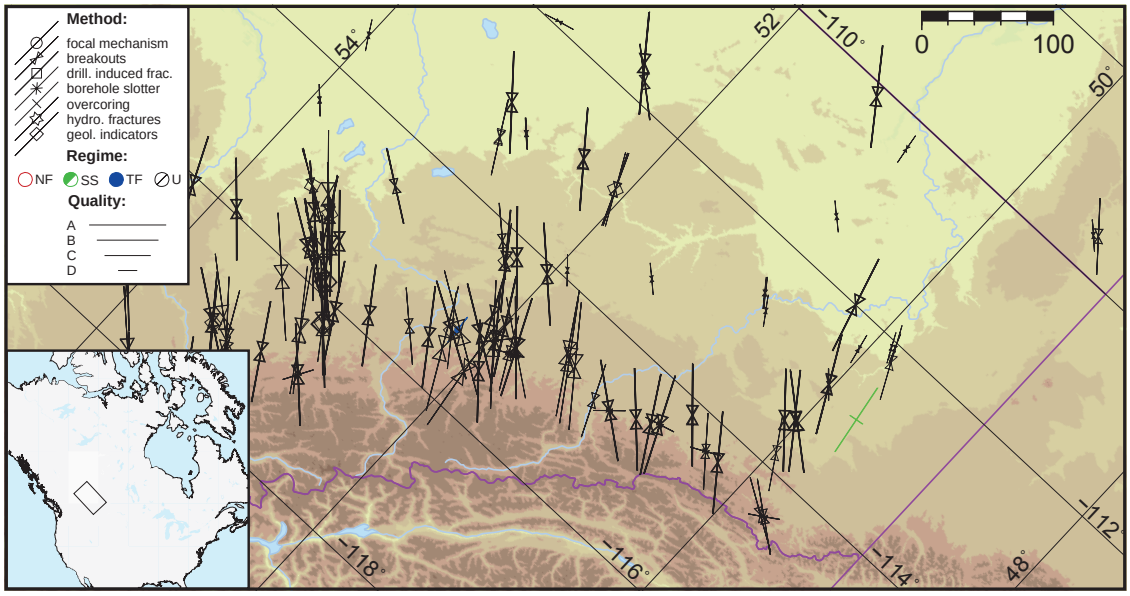

Figure 3.8: Part of the Alberta Stress Map, rotated about 47° counter-clockwise. The map displays, that S_{Hmax} orientation does not always follow perpendicular the topographic trend, which is in contrast to the S_{Hmax} orientation, which is to observe in the Alpine Molasse basin (Fig. 3.9).

In contrast to the Canadian map, the colour coded wave-length map of Alberta (Fig. 3.5) displays no gaps. It changes from intermediate wavelengths (∼400 km) in the Rocky Mountains region (with only three focal mechanisms) and ingresses perpendicular to Rocky Mountains up to large wavelengths (>1,000 km) in the area of the Canadian Shield, but also in the northern part of the Alberta Basin. Small wavelengths in the Rocky Mountains are caused by the variable orientation of focal mechanisms in Washington State in the US due to the subduction of the Juan-de-Fuca-Plate below the North America Plate.

There are just a few orientation data, differing from the main trend like those close to the Peace River Arch, (about 56°N in Fig. 3.3), where a counter-clockwise rotation of about 20° is observed. The Peace River Arch has an elevated Precambrian basement (Bell and Grasby 2012; Halchuk and Mereu 1990), which could be interpreted as a buried contractional duplex. The other explanations for the locally perturbed stress field in the Peace River region are mafic sills, which intruded in the upper crust (Eaton et al. 1999) and/or lateral heterogeneities (transfer zone or local rheological properties), according to Bell and McCallum (1990). Dusseault and Yassir (1994) modelled successfully the stress perturbation in the Peace River Arch with an anisotropic softer inclusion.

The variation of S_{Hmax} azimuths in Alberta (e.g Bell and Babcock 1986; Bell et al. 1994) or the last WSM update by Heidbach et al. (2010), when comparing visually with this update (Fig. 3.3),

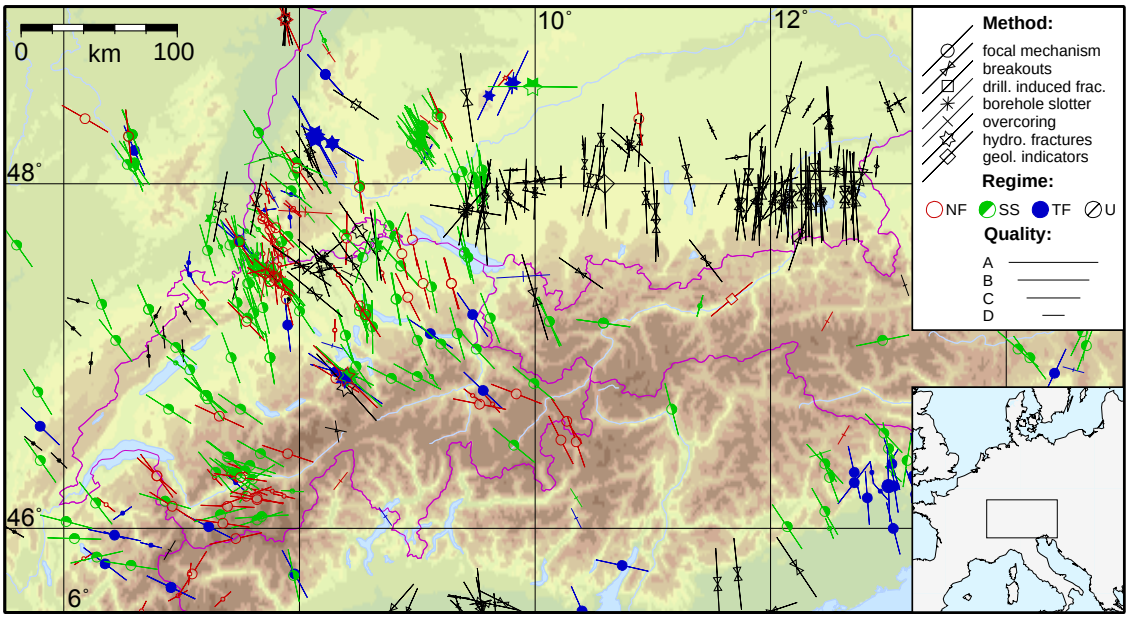

Figure 3.9: Stress map of the Alpine Molasse basin. S_{Hmax} orientation follows perpendicular the topographic trend of the Alpine Mountain chain.

seems to be decreasing. This is confirmed by a change of the circular (non-rated) standard deviation (Mardia 1972) from 9.2°, for the old Alberta WSM dataset to a standard deviation of 8.7° for the new complete Alberta dataset. This shows that an increasing amount of available data records and the stringent application of common quality criteria reduce uncertainties, at least for Alberta.

3.6 Conclusion

The maximum horizontal crustal stress (S_{Hmax}) is oriented south-west to north-east over wide areas in Northern America. However, there was no systematic revision or extension on the Canadian stress database for about two decades (Adams and Bell 1991; Bell et al. 1994); the data records in the WSM 2008 release (Heidbach et al. 2010) included 1153 S_{Hmax} orientation data. The WSM database for Canada has now been completely revised and 514 new data records were added, with a special emphasis on Alberta. The data are from intra-plate regions as well as from plate boundaries and sedimentary basins. The new Canadian stress database with now 1667 data records is more reliable since all data records are cross checked with common modern WSM quality criteria. The largest accession occurred in Alberta and in the south-eastern region (St. Lawrence Platform and Appalachian Orogen). Furthermore, the high data density allows a robust assessment and interpretation of the S_{Hmax} orientation. This is important for the data application for statistic smoothing algorithms or for the validation of geomechanical models.

The Alberta region displays a uniform S_{Hmax} orientation (~47°N) with a clear increase of wavelength in the same orientation, towards the Canadian Shield. In contrast, the region of the Gulf of St. Lawrence Platform and Appalachian Orogen have short to very short wavelengths.

The quasi median on the circle ($\widetilde{S}_{Hmax}$) from Ratanaruamkarn et al. (2009) that we use to estimate the average S_{Hmax} orientation and the newly introduced equation, to calculate the quasi interquartile range on the circle (QIROC), which estimates the variance of the data, is more robust to outliers within small datasets of periodic data than previously applied techniques. The general smoothed S_{Hmax} orientation is similar to the previously found orientation by Coblentz and Richardson (1995); Heidbach et al. (2010), but with a higher resolution, a better coverage and larger confidence level.

Acknowledgement

This study was conducted under the Helmholtz-Alberta-Initiative (HAI), the first author is grateful for the financial support (SO-061). We also want to thank the Alberta Geological Survey (AGS), which provided the S_{Hmax} data set and allowed us to publish these data in the World Stress Map. Finally we thank two anonymous reviewers, who improved the paper's quality. Maps were generated by means of GMT software (Wessel et al. 2013).

4 3-D-geomechanical-numerical model of the contemporary crustal stress state in the Alberta Basin (Canada)

Karsten Reiter[1,2], Oliver Heidbach[1]

[1] GFZ German Research Centre for Geosciences, Telegrafenberg, 14473 Potsdam, Germany
[2] University of Potsdam, Inst. of Earth and Environmental Science, Karl-Liebknecht-Straße 24 – 25, 14476 Potsdam–Golm, Germany

Journal: Solid Earth, 2014, 5, 1123–1149, DOI: 10.5194/se-5-1123-2014

Status: Received: 31 July 2014, Accepted: 19 October 2014, Published: 25 November 2014

Abstract

In the context of examining the potential usage of safe and sustainable geothermal energy in the Alberta Basin whether in deep sediments or crystalline rock, the understanding of the in situ stress state is crucial. It is a key challenge to estimate the 3-D stress state at an arbitrarily chosen point in the crust, based on sparsely distributed in situ stress data.

To address this challenge, we present a large-scale 3-D geomechanical–numerical model (700 km × 1200 km × 80 km) from a large portion of the Alberta Basin, to provide a 3-D continuous quantification of the contemporary stress orientations and stress magnitudes. To calibrate the model, we use a large database of in situ stress orientation (321 S_{Hmax}) as well as stress magnitude data (981 S_V, 1720 S_{hmin} and 2 (+11) S_{Hmax}) from the Alberta Basin. To find the best-fit model we vary the material properties and primarily the displacement boundary conditions of the model. This study focusses in detail on the statistical calibration procedure, because of the large amount of available data, the diversity of data types, and the importance of the order of data tests.

The best-fit model provides the total 3-D stress tensor for nearly the whole Alberta Basin and allows estimation of stress orientation and stress magnitudes in advance of any well. First-order implications for the well design and configuration of enhanced geothermal systems are revealed. Systematic deviations of the modelled stress from the in situ data are found for stress orientations in the Peace River Arch and the Bow Island Arch as well as for leak-off test magnitudes.

4.1 Motivation

The estimation of the in situ stress state in the upper crust in addition to the understanding of earthquake cycles and plate tectonics is crucial for exploration and production of energy resources. These include geothermal energy, hydrocarbons, CO_2 sequestration (carbon capture storage – CCS) and geotechnical subsurface constructions such as mines, tunnels, interim storage sites for natural gas and nuclear waste deposits. Reliable estimates of orientation and magnitude of the crustal stress field are desired before drilling. This is important in terms of well stability (e.g. Bell and McLellan 1995; Peska and Zoback 1995), but is also related to the well configuration of several corresponding wells (e.g. Bell and McLellan 1995), in the case of reservoir stimulation by hydraulic fracturing. This is important in geothermal reservoirs (enhanced geothermal systems – EGS) (Legarth et al. 2005; Wessling et al. 2009) and issues of inadequate understanding of the spatial stress pattern (e.g. Brown 2009; Duchane and Brown 2002). This is also true for hydrocarbon reservoirs or the evaluation of nuclear waste repositories (e.g. Fuchs and Müller 2001; Gunzburger and Magnenet 2014; Heidbach et al. 2013).

The stress tensor and its components are not to be measured directly, but there are several stress indicators, which allow estimation of several components of the stress tensor (e.g. Ljunggren et al. 2003; Schmitt et al. 2012; Zang and Stephansson 2010). The following components of the stress tensor are potentially available: the azimuth of the maximum (or minimum) horizontal stress (S_{Hmax}), the vertical stress magnitude (S_V) as well as the magnitudes of the maximum and minimum horizontal stress (S_{hmin} and S_{Hmax}). However, reliable estimation of the S_{Hmax} magnitude remains difficult as only shallow in situ stress estimations are available or numerous assumptions have to be made that impose high uncertainties. Furthermore, stress information is sparse and extra- or inter-polation of a few data records to the area or depth of interest is necessary.

However, stress estimation via interpolation techniques becomes particularly questionable in the case of structural inhomogeneities like faults, detachments (Bell and McLellan 1995; Röckel and Lempp 2003; Roth and Fleckenstein 2001; Yassir and Bell 1994), or varying material properties (Roche et al. 2013; Warpinski 1989). Furthermore, drilling down to a geothermal reservoir requires reaching greater depths, as available measurements are delivered in the context of hydrocarbon production. For example in Alberta, deeper parts of the basin or the upper basement are the target depths for EGS (e.g. Hofmann et al. 2014; Majorowicz and Grasby 2010a, c; Weides et al. 2013, 2014a). Therefore, estimation of the stress state, especially at greater depths, is a challenge prior to drilling.

An alternative approach to estimating the 3-D stress state is geomechanical–numerical modelling. This method has the advantage of incorporating structural and material inhomogeneities that impose local to regional changes on the stress field. There are several studies on tectonic plate scale stress orientation patterns in 2-D (e.g. Coblentz and Richardson 1996; Dyksterhuis et al. 2005; Humphreys and Coblentz 2007; Jarosinski et al. 2006), large scale (regional) models in 3-D (Buchmann and Connolly 2007; Hergert and Heidbach 2011; Parsons 2006), as well as local (reservoir-scale) 3-D models (e.g. Fischer and Henk 2013; Heidbach et al. 2013; Henk 2005; Orlic and Wassing 2012; Van Wees et al. 2003). Modelling of the contemporary stress field mainly depends on the structural model, the material properties, the initial stress state and the applied displacement boundary conditions. However, the reliability of such models depends strongly on the model calibration towards in situ stress data. Usually there are little in situ stress data available for model calibration in published studies (e.g. Buchmann and Connolly 2007; Fischer and Henk 2013; Heidbach et al. 2013; Hergert and Heidbach 2011), which rules out any statistical validation.

The Alberta Basin is a study area with well-understood structures and material properties, and a large collection of in situ stress data. We use this information to build a 3-D geomechanical–numerical model of the Alberta Basin and surroundings with an extent of 1200 km×700 km down to a depth of 80 km. The goal is to get the full tensor of the contemporary undisturbed stress state, called stress model in the following. These are 981 S_V magnitude data, 321 S_{Hmax} azimuth data, 1720 S_{hmin} magnitudes, and 2 measured (overcoring) and 11 calculated S_{Hmax} magnitudes within the model region. There is no other basin with a comparable range of available in situ stress data (Bell and Grasby 2012). The availability of very good stress data allows for the calibration of the stress model vs. a never-reached diversity, and a number of in situ stress indicators.

The model calibration will be done in three consecutive steps: (1) density of basin infill, using S_V magnitude data, (2) orientation of displacement boundary conditions using S_{Hmax} azimuth data, and (3) magnitudes of displacement boundary conditions (strain) using S_{hmin} and S_{Hmax} magnitude data. As linear elastic rheology is used for the model, the linear dependency between the two applied strain magnitudes (push and pull) along the outer edges of the model is calculated. This allows, via planar regressions the calculation of the optimal strain magnitudes, providing the best-fit model. The application of the model would be for exploitation of hydrocarbons and more for exploration and design of a geothermal plant in the Alberta Basin. Additionally it may be used in crystalline rocks, mainly in case of necessary hydraulic stimulation. Mistaken investments e.g. parts of the

Fenton Hill project (Brown 2009; Duchane and Brown 2002) could potentially be avoided with a better previous understanding of the 3-D in situ stress state.

4.2 Modelling concept

4.2.1 Model assumptions

The compilation of stress data in North America by Adams (1987, 1989), Adams and Bell (1991), Bell et al. (1994), Fordjor et al. (1983), Gough et al. (1983), Sbar and Sykes (1973), Zoback and Zoback (1980, 1981, 1989, 1991) and recently by Reiter et al. (2014) resolved that the pattern of S_{Hmax} orientations is largely uniform over thousands of kilometres. An assumption was that the same forces driving plate tectonics are the major control on the stress field, which is confirmed in first order (e.g. Richardson 1992; Zoback et al. 1989; Zoback 1992).

The stress pattern is driven and altered by several stress sources; they are discriminated depending on the scales into first order (>500 km), second-order (100–500 km) and third-order stress sources (<100 km) (Heidbach et al. 2007, 2010; Müller et al. 1997; Tingay et al. 2005b; Zoback 1992; Zoback and Mooney 2003). First-order stress sources as the main driving forces are summarized as plate boundary forces, which are ridge push, slab pull, and trench suction, gravity and basal drag by mantle convection. Second-order stress sources are lithospheric flexure, localized lateral density, stiffness and strength contrasts, topography, large fault zones, and lateral contrasts of heat production. Third-order stress sources are local density, stiffness or strength contrasts, basin geometry, basal detachment, incised valleys, and anthropogenic stress changes.

Under the parameters to reproduce the crustal stress field of the Alberta Basin, the model has to be large enough to portray the first- and second-order stress sources. Whereas the first-order stresses sources, which control plate tectonic motion, are represented by the displacement boundary conditions, the second- and third-order stress sources are represented by the model geometry. This is possible when structures are known and convertible to the model. As inhomogeneous topography and mass distribution within the lithosphere have a major impact on the stress orientation (Camelbeeck et al. 2013; Ghosh et al. 2009; Humphreys and Coblentz 2007; Naliboff et al. 2012), it is crucial to incorporate the major structural units in the crust and upper mantle into the model geometry.

Linear elastic material properties are an accurate approximation as long as the strain ($\boldsymbol{\epsilon}$) is small enough, and no failure occurs. This might be assumed for the Alberta Basin, which is seismically relatively quiescent. Documented earthquakes are usually restricted to the Rocky Mountains, foothills, and suspected man-made clustered events (e.g. Baranova et al. 1999; Schultz et al. 2014).

Our focus is the Alberta Basin and the uppermost basement below the basin due to our key interest in the investigation of the potential usability of deep geothermal energy (EGS). Furthermore, the calibration data are from the sediments up to a depth of about 5 km when no deeper stress indicators are available. Exceptions to this are three S_{Hmax} azimuths, derived from focal mechanism solutions.

Viscous rock deformation, acceleration, changing pore pressures as well as other thermal effects influence the stress state, but as we strive to model the contemporary undisturbed total stress tensor (stress model) these processes are assumed to have only marginal influence and are disregarded in the model. We assume that the following model assumptions are sufficient to estimate the contemporary 3-D stress state within the Alberta Basin and upper basement:

- large-scale geometry of the model down to the upper mantle is crucial (main structural units only).
- linear elastic material properties are used.
- gravity as the body force.

- the lateral displacement boundary conditions of the model are a parameterization of ongoing plate tectonic motion, effects of lateral density contrasts (gravitational potential energy) of outside of the model, and remnant stresses from terminated tectonic processes.

Due to the complex structures and inhomogeneous materials properties, an analytical solution cannot be estimated. Thus, we use for the discrete solution the finite element method (FEM), as it allows us to use unstructured meshes, for a good representation of the 3-D model structure. With these assumptions the model is described with the partial differential equations of the equilibrium of forces:

$$\frac{\partial \boldsymbol{\sigma}_{ij}}{\partial x_j} + \rho x_i = 0, \tag{4.1}$$

where $\partial \boldsymbol{\sigma}_{ij}$ is the change in total stress, ∂x the change in length and ρx represents the weight of the rock section (ρ = density).

After model design (structural model) and definition of material properties (Poisson's ratio, Young's modulus and density), the partial differential equation (Eq. 4.1) can be calculated within given displacement boundary conditions. The latter will be varied to find the best-fit model. This is the stress model together with material properties and displacement boundary conditions, which deliver the best-fit for all in situ stress data.

4.2.2 General workflow of model calibration

Generally a model has to be calibrated before application or interpretation. The general concept, independent of the technical context, is to test the model's outcome vs. in situ data. Such data are called model-independent data in contrast to model-dependent data, which are used to generate the model.

In this study, the lithological and tectonic structures, the rheology, the body force, the initial stress state, and the displacement boundary conditions are the model-dependent data (Fig. 4.1). Based on these data the structural model is defined, which is discretized to a (unstructured) mesh and assembled together with the material properties, body forces, the boundary conditions, and the initial stress state. Available in situ stress data are the model-independent data. These are the S_V magnitudes, the S_{Hmax} azimuth data, and S_{hmin} and S_{Hmax} magnitudes. The modelled stress tensor is tested against the in situ data. When one data set is tested successfully, the next dataset is used in the next calibration step. Otherwise the material properties or boundary conditions are optimized as long as the test is successful.

First, the stress model is tested vs. in situ S_V magnitudes, to conclude estimation of density (material properties and body force). In the second step the S_{Hmax} orientation is tested to determine the orientation of applied displacement boundary conditions. In the final step, S_{hmin} and S_{Hmax} magnitudes are used to calibrate the applied magnitudes of the displacement boundary conditions. When all model-independent data sets are tested successfully, the best-fit model is found and is a subject of further use (interpretation and application).

The model-depended data, construction and compilation process of the geomechanical model are described in Sect. 4.3, whereas the model-independent data are introduced in Sect. 4.4. The calibration procedure is presented in detail in Sect. 4.5. Finally, the discussion can be found in Sect. 4.6.

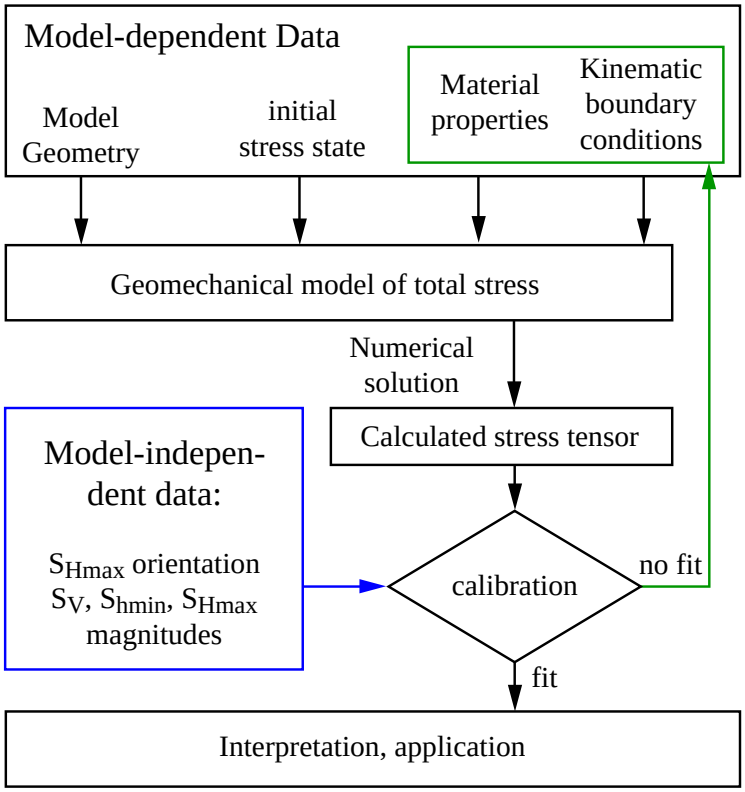

Figure 4.1: Sketch of the general workflow. The geomechanical model is prepared based on the model geometry, the material properties, the variable displacement boundary conditions and the initial stress state. The numerically modelled total stress tensor is calibrated on model-independent in situ stress data until the model fits the calibration data.

4.3 Model setup

4.3.1 Geometry of the Alberta Basin

4.3.1.1 Tectonic and sedimentary history of the Alberta Basin

The Alberta Basin (Fig. 4.2) occupies a large portion of the much larger Western Canada Sedimentary Basin (WCSB). Starting from the northeast clockwise it is bounded by the Canadian Shield, the Bow Island Arch, the Rocky Mountains and the Tathlina High in the north. The crystalline basement of the WCSB and implicitly of the superposed Alberta Basin, is the North American craton exposed by erosion to the northeast as the Canadian Shield (Boerner et al. 2000; Flowers et al. 2012; Hoffman 1989; Ross et al. 1994, 2000). The main structural units of the Alberta basement are the Buffalo Head Terrane (Aulbach et al. 2004), the Taltson Magmatic Zone (e.g. Chacko et al. 2000), the Hearne Province (Hajnal et al. 2005) and the Trans-Hudson Orogen (e.g. Corrigan et al. 2005; Németh et al. 2005) and other smaller units, which welded together between 1.8 and 2.0 Ga. There are two important lineaments, the Snowbird Tectonic Zone (STZ – Ross et al. 2000, and references therein) and the Great Slave Lake Shear Zone (GLS – Sami and James 1993), and their continuation (Hay River fault zone).

Sediments were deposited in the basin, interrupted by a few discontinuities during the whole Phanerozoic (Mossop and Shetsen 1994a, Chapter 6–26). Mainly shelf sediments deposited onto the craton as recently as the Upper Jurassic. At that time, sedimentation character changed, and the basin developed to a rapidly subsiding fore-deep trough (Poulton et al. 1994). Mature

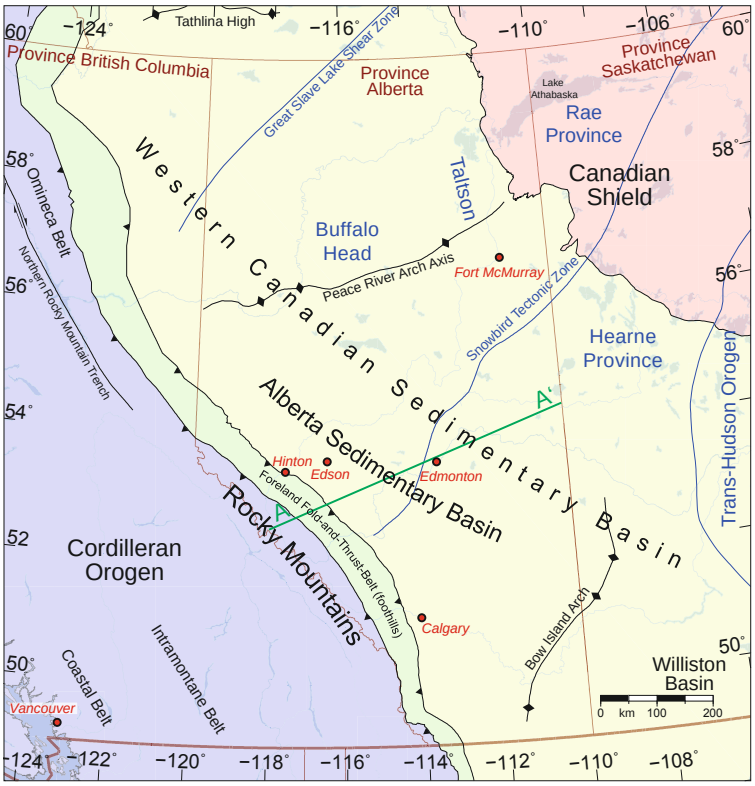

Figure 4.2: Tectonic map of Alberta and surroundings displaying the important structural features. Blue lines and labels indicate Precambrian structures in the basement. Provincial boundaries and areas are indicated by reddish-brown colours, and tectonic features are labelled in black. The trace of the cross section in Fig. 4.3 is indicated by a green line. The map is modified and redrawn after Wright et al. (1994).

sediments were previously derived from northeast, and changed to less mature sediments derived from the west. The change to terrestrial deposits in Early Cretaceous (Smith 1994) coincides with first the Ominicean Orogeny, and later the Lamariden Orogeny (Porter et al. 1982; Price 1981b; Wright et al. 1994). Jurassic to Palaeocene strata mainly deposited in the western part of the Alberta Basin and have been incorporated in the Rocky Mountains fold-and-thrust belt (foothills and front ranges – Fig. 4.3). This is bound farther west (main ranges) in British Columbia by the Rocky Mountain Trench. The final shape of the Alberta foreland basin developed by downward flexing of the Canadian Shield due to lithospheric loading and isostatic flexure in a retro-arc setting (Leckie and Smith 1992; English and Johnston 2004), together with the sediments derived from the developing Canadian Cordillera (Gabrielse and Yorath 1989). The Alberta Basin consists of a nearly undeformed sedimentary wedge (Fig. 4.3) that increases in thickness from zero at the Canadian Shield to approximately 5500 m near the fold-and-thrust belt. The overall wedge shape in the Alberta Basin, perpendicular to the Rocky Mountains, is quite homogeneous from northwest to southeast.

Only the Peace River Arch close to the Rocky Mountains is striking within the homogeneous wedge, which is indicated by several geophysical investigations. There are several explanations: elevated Precambrian basement (Bell and Babcock 1986; Bell 1996b; Bell and Grasby 2012; Halchuk and Mereu 1990), the occurrence of mafic sills which intruded in the upper crust of the Peace River Arch (Eaton et al. 1999) and/or lateral heterogeneities (transfer zone or local rheological properties

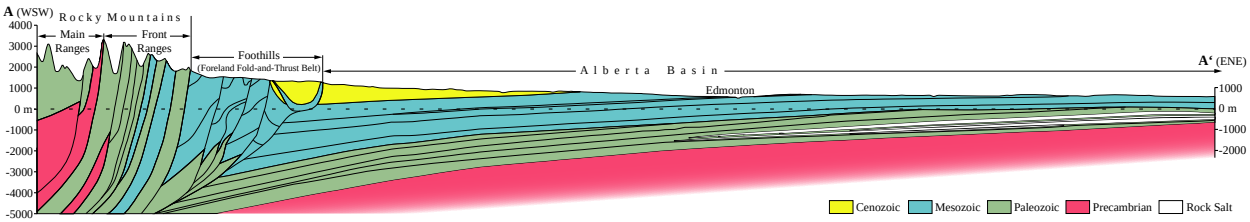

Figure 4.3: Cross section across Alberta in west–southwest to east–northeast orientation; the trace is highlighted in Figs. 4.2 and 4.4. Visible is the Alberta Basin as a wedge-shaped retro-arc foreland basin, together with parts of the Rocky Mountains and the foreland fold-and-thrust belt (foothills) in between. The rock units are roughly indicated by the stratigraphic age. Additional thick rock salt units are indicated separately, because of their potential to detach the stress field. The vertical exaggeration is 10 times, redrawn after Hamilton et al. (1999).

in Bell and McCallum 1990), a softer inclusion (Dusseault and Yassir 1994), or crustal thinning caused by extension Bouzidi et al. (2002).

4.3.1.2 Model geometry

The structural–geological model is of major importance, and is prepared with the GOCAD® 3-D geomodelling system. Faults and lithological boundaries are defined as discrete triangulated surfaces. These are built based on points (stratigraphic borehole data and seismic data), curves (seismic and interpreted cross sections, lineaments from the geological map) or point clouds that describe surfaces (DEM). During surface generation, data are honoured as soft or hard constrained, depending on their quality (e.g. Ross et al. 2004). The roughnesses of the surfaces are polished with the discrete smoothing interpolation (DSI) algorithm (Mallet 1992, 2002).

The model box of Alberta, indicated in Fig. 4.4, is oriented parallel or perpendicular to the observed basin structure (Fig. 4.2), the orientation of S_{Hmax} (e.g. Bell et al. 1994; Reiter et al. 2014, see rose diagram in Fig. 4.4), the wedge shape of the Alberta Basin (Fig. 4.3), the thermallly defined Cordillera–Craton boundary (Hyndman et al. 2009) and the overall plate motion of the North American Craton, measured by GPS (Henton et al. 2006; Mazzotti et al. 2011).

The model has a southwest-to-northeast striking extent of 700 km, 1200 km in northwest-to-southeast direction (Fig. 4.4), and 80 km in depth. For the definition of the model geometry, it was necessary to choose the geometrically relevant structures, strength contrasts or density variations. These can potentially affect the stress field, while considering limitations of the possible number of finite elements. The main structural units are the mantle, the crustal basement, the sedimentary basin, the foothills, the Rocky Mountains and the Elk Point evaporates within the basin due to their potential to detach the stresses of the supra-salt units from the sub-salt units. Furthermore, the Snowbird tectonic zone and the Great Slave shear zone are incorporated, and cut the basement and the sediments.

The deepest implemented boundary is the Mohorovičić discontinuity (Moho) as the crust–mantle transition. We use various geophysical data to define the Moho topography (Fig. 4.5) by directional kriging. These are data from seismic refraction studies (Bouzidi et al. 2002; Burianyk et al. 1997; Clowes et al. 2002; Fernández-Viejo and Clowes 2003; Halchuk and Mereu 1990; Németh et al. 1996, 2005; Spence and McLean 1998; Welford et al. 2001; Zelt and White 1995) and from teleseismic studies (Gu et al. 2011; Shragge et al. 2002).

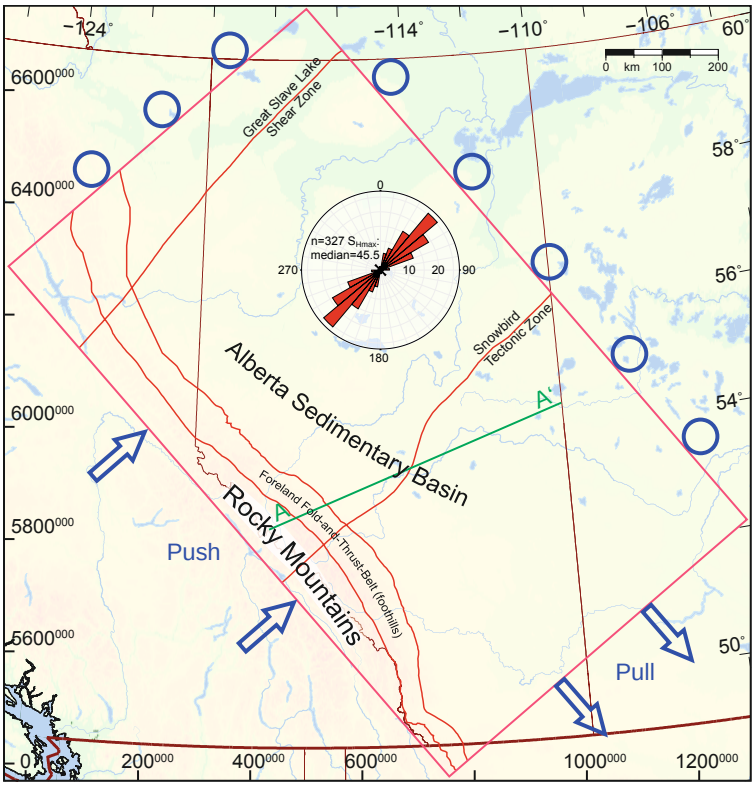

Figure 4.4: Map of Alberta with the model extent (red box) combined with the model features. Implemented are the main structural features (red lines), which are the front of the Rocky Mountains and the foothills, respectively, as well as the Snowbird Tectonic Zone and the Great Slave Lake Shear Zone. For comparison, see the tectonic map (Fig. 4.2). Push and pull along model sides and the allowed lateral motion are indicated by blue arrows and circles, respectively. The mean orientation of S_{Hmax} is indicated by a rose diagram; note that stress orientation is parallel and orthogonal, respectively, to the model box. The trace of the cross section in Fig. 4.3 is indicated by the green line.

The basement top (Fig. 4.6) is defined as the boundary between the basement (south-western continuation of the Canadian Shield) and the sedimentary basin. It is constructed by DSI, based on 7257 well data available from the Alberta Geological Survey (AGS).

The strata overlying the Precambrian basement are subdivided into the Rocky Mountains, the foreland fold-and-trust belt (foothills) and the sediments within the basin (Fig. 4.7). The first set consists of allochthonous Palaeozoic strata, whereas the foothills consist of the same stack of sediments from the entire Phanerozoic, deposited in the Western Canadian Sedimentary Basin. For a definition of the boundary between these parts, geological maps and interpreted cross sections were used (Mossop and Shetsen 1994b; Price 1994; Wright et al. 1994).

Salt deposits within the sedimentary column have the possibility to geomechanically detach the stresses in the upper rock units from the long wave-length stresses at depth (Bell 1993; Roth and Fleckenstein 2001; Röckel and Lempp 2003; Tingay et al. 2005b). The Devonian Elk Point Group contains several salt deposits (Grobe 2000; Meijer Drees 1994). These up to 380 m thick deposits (Figs. 4.3 and 4.7) have been recognized within five stratigraphic formations. They are ordered from oldest to youngest: Lower Lotsberg, Upper Lotsberg, Cold Lake, Prairie Evaporate and Hubbard Evaporate salts. The Elk Point evaporates are separated from the other basin sediments (Mossop and Shetsen 1994a, Chapter 8–26) as an independent unit; evaporate strata with a thickness of

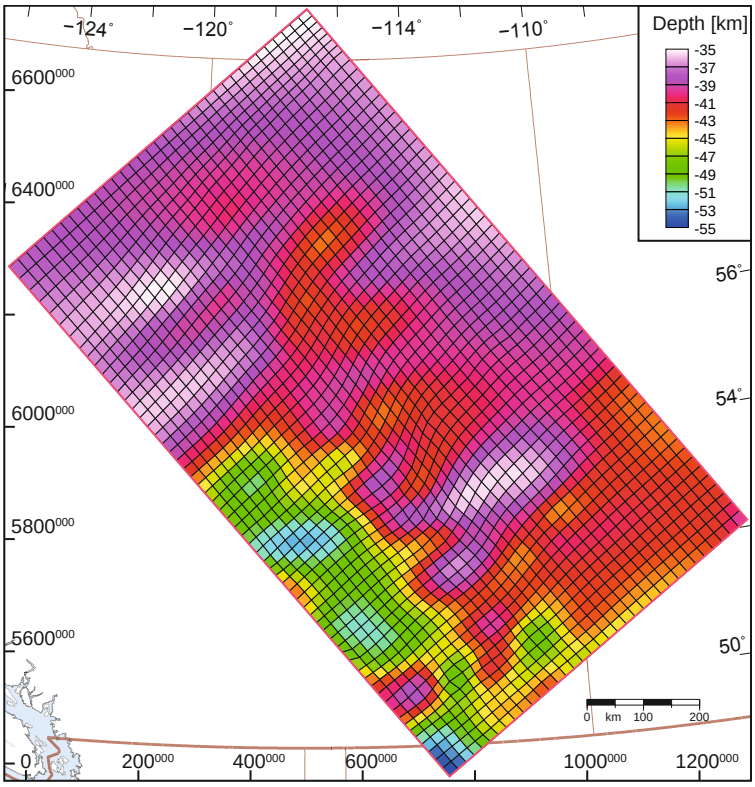

Figure 4.5: Topography of the Mohorovičić discontinuity (Moho) within the model box. The map extent is indicated by geographical coordinates (top and right) and by UTM coordinates from zone 11 (left and bottom). The mesh size (~ 20 km) at that depth is indicated by black lines.

≥ 100 m are used based on data from Grobe (2000). All these interfaces are also generated with the DSI algorithm. Finally the model box is completed with the digital elevation model (DEM) from the USGS (2008).

4.3.1.3 Model discretization into finite elements

Our key goal is to model the contemporary 3-D stress state within the basin and in the upper part of the basement. To reproduce the thin rock salt layer within the basin, it was necessary to have a minimum element amount of six elements within the basin in the z direction. This results in a vertical resolution of about 200 to 800 m for the upper model parts (Fig. 4.8). In the x and y directions, the resolution within the basin and the upper basement is about 5000 m. The element thickness increases with depth within the basement. In deeper parts (-25 to -80 km), the resolution is approximately 20 km in all directions (Fig. 4.5). The whole model is discretized into 349 690 hexahedrons, 4188 tetrahedrons, 552 pyramids and 474 prism elements with linear approximation functions. The partial differential equation of the equilibrium of forces is solved numerically using the Abaqus®/Standard v.6.11 finite element software.

4.3.2 Rock properties

To calculate the stresses, Young's modulus (E) and Poisson's ratio (ν) are the essential geomechanical material properties. The body forces of the rock units are represented by the density (ρ). Mantle density below Alberta ranges from 3346 to 3366 kg m^{-3} according to White et al. (2005). For this

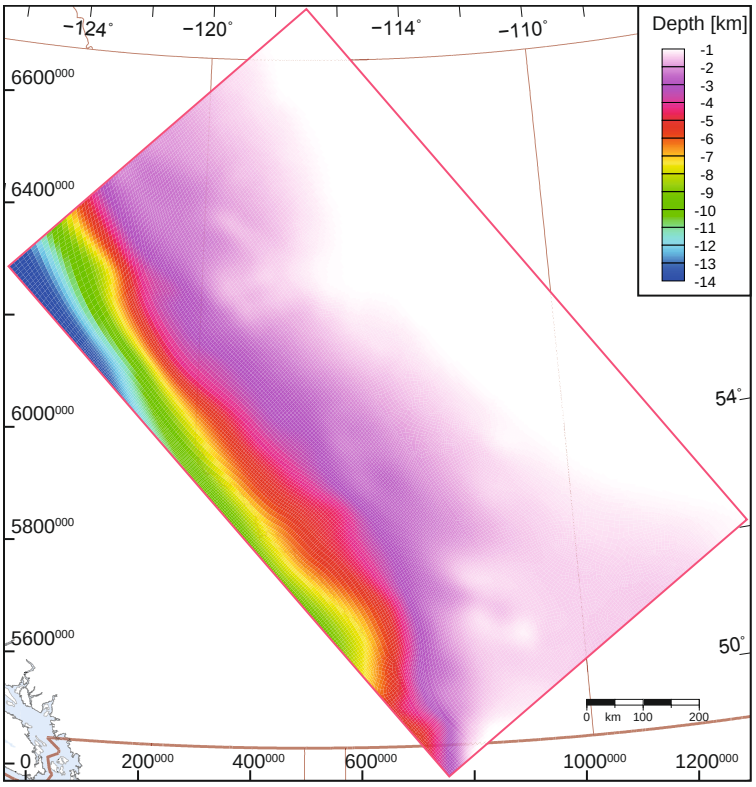

Figure 4.6: Topography of the basement top is shown within the model box. The map extent is indicated by geographical coordinates (top and right) and by UTM coordinates from zone 11 (left and bottom).

model, a density of 3350 kg m^{-3} for the mantle is used (Table 4.1). The density of the Canadian Shield ranges from 2640 to 2830 kg m^{-3} (White et al. 2005), with this model using a value of 2800 kg m^{-3}. Young's modulus and Poisson's ratio of the basement are calculated based on the V_p and V_s data from northern Alberta (Dalton et al. 2011). The dynamic Young's modulus and the Poisson's ratio (0.21–0.22) are calculated according to Mavko et al. (2009). Based on the dynamic Young's modulus, the static Young's modulus is calculated according to King (1983) and Wang et al. (2000) with a range of 1.02×10^{10} to 8.56×10^{10} Pa. In the model, 0.21 and 7.0×10^{10} are used as Poisson's ratio and Young's modulus respectively for the basement, which is in agreement with data from Turcotte and Schubert (2002). Most Phanerozoic sediments overlying the basement, including the foothills and the Rocky Mountains, are mainly clastic sediments (e.g. sandstone or shale) and limestone with the exception of the separated evaporates. These material properties are estimated based on Fossen (2010), (Okrusch and Matthes 2005) and Turcotte and Schubert (2002); see Table 4.1.

4.3.3 Initial stress state

Deformation of the model due to gravity-driven subsidence is not desired. Therefore, an initial stress state of the model is derived, which is in equilibrium with the body forces (gravity). For the initial stress state uniaxial strain conditions (Eq. 4.2) or lithostatic stress conditions for greater

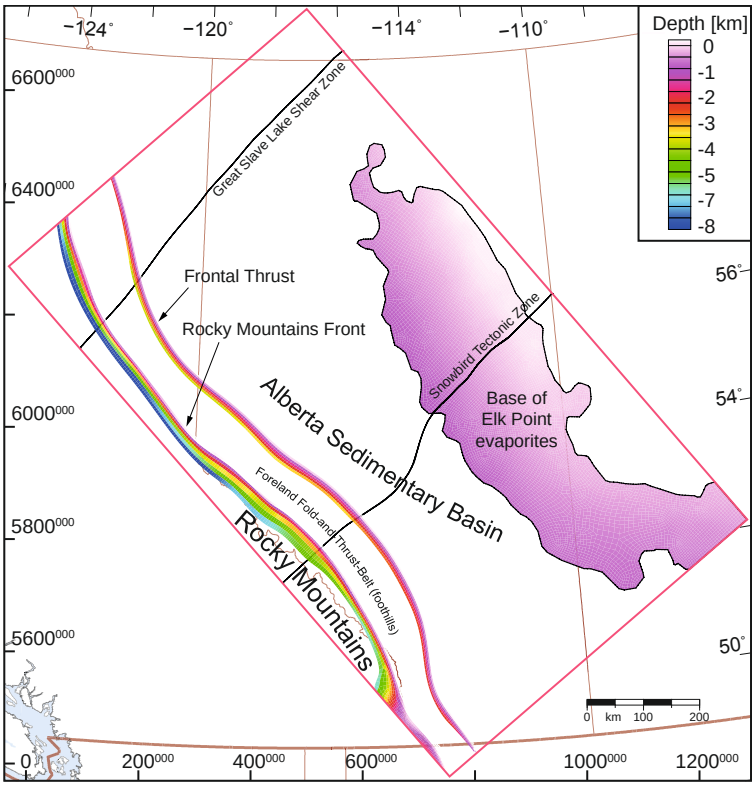

Figure 4.7: Upper crustal structures used in the model. The units above the basement are separated in the basin, the foothills and the Rocky Mountains. The basin also contains a thin rock salt layer from the Elk Point group. Within the basement, the Great Slave Lake Shear Zone and the Snowbird Tectonic Zone are incorporated. The map extent is indicated by geographical coordinates (top and right) and by UTM coordinates from zone 11 (left and bottom).

depths (Heim 1878, Eq. 4.3) are often assumed.

$$S_{\mathrm{Hmean}} = \frac{S_{\mathrm{Hmax}} + S_{\mathrm{hmin}}}{2} = S_{\mathrm{V}} \left(\frac{\nu}{1-\nu} \right) \tag{4.2}$$

$$S_{\mathrm{Hmax}} = S_{\mathrm{hmin}} = S_{\mathrm{V}} \tag{4.3}$$

$$k = \frac{S_{\mathrm{Hmean}}}{S_{\mathrm{V}}} = \frac{S_{\mathrm{Hmax}} + S_{\mathrm{hmin}}}{2S_{\mathrm{V}}}. \tag{4.4}$$

Using uniaxial strain conditions ($k = 1/3$ when ν is 0.25, Eq. 4.2) or lithostatic conditions ($k = 1$, Eq. 4.3), the stress ratio k (Eq. 4.4) is constant for both, when plotting vs. depth, but when k is plotted vs. depth, based on in situ data, the discrepancy is obvious (e.g. Brown and Hoek 1978; Gay 1975, Fig. 4.9a). Visible are increasing k values close to the surface. Thus, assuming lithostatic or uniaxial conditions is apparently insufficient for appropriate initial stress conditions.

Sheorey (1994) provides a simple spherical earth model for tectonically calm regions with no significant lateral density and strength contrasts. In this model, k is a function (Eq. 4.5) of Young's modulus (E in GPa) and depth (z in m). This was confirmed by later published in situ stress magnitudes from the KTB borehole (Brudy et al. 1997, see Fig. 4.9a).

$$k = 0.25 + 7E \left(0.001 + \frac{1}{z} \right) \tag{4.5}$$

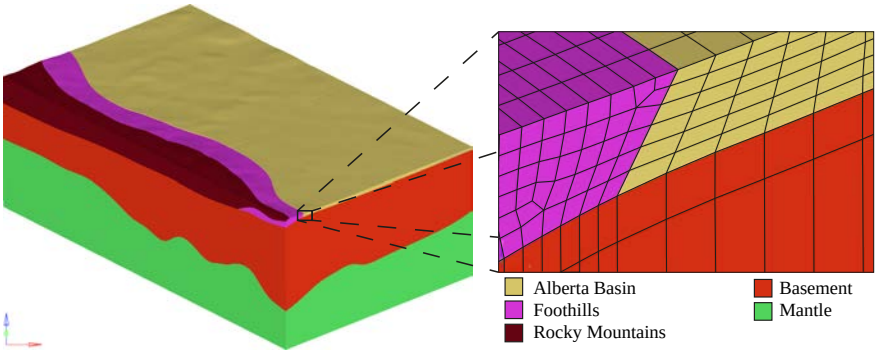

Figure 4.8: 3-D view of the Alberta model, view from south to north – rock units are indicated by colours. A small cut-out is zoomed in to see the mesh in detail. The vertical exaggeration is 5 times.

Table 4.1: Material properties of the Alberta model.

Lithology	Density ($\mathrm{kg\,m^{-3}}$)	Young's modulus (Pa)	Poisson's ratio
Sediments	2200[a]	6.0×10^{10}[b]	0.15[b]
Rock salt	2100[c]	4.0×10^{10}[d]	0.38[d]
Foothills	2400[b]	6.0×10^{10}[b]	0.20[b]
Rocky Mtns.	2500[b]	6.0×10^{10}[b]	0.20[b]
Basement	2800[e]	7.0×10^{10}[f]	0.21[f]
Mantle	3350[e]	1.5×10^{11}[b]	0.25[b]

[a] best-fit (tested during calibration), [b] estimated based on Turcotte and Schubert (2002), [c] Okrusch and Matthes (2005), [d] Fossen (2010), [e] White et al. (2005), [f] calculated based on Dalton et al. (2011)

When the model is embedded in an extended model with inclined edges, it is possible to find a fit of the k values vs. depth from the model. This is in comparison to a synthetic depth distribution, based on the Sheorey equation (Eq. 4.5). This technique has so far been used only occasionally (Buchmann and Connolly 2007; Hergert and Heidbach 2011). By generating the initial stress model, settlement due to the gravitational load occurs. Using the initial stress condition in the stress model, settlement in the model (<1 m) can be neglected in relation to the model size.

For comparison, the calculated k ratio, Eq. (4.5) from Sheorey (1994), and the initial k ratio from the model of Alberta, are plotted vs. depth. Material properties are adjusted for the initial model only until good agreement is obtained. Exemplarily, two of them are plotted for illustration (Fig. 4.9b and c). From a purely technical point of view, the initial stress conditions were determined after calibration of the used sediment density.

4.3.4 Boundary conditions

Henton et al. (2006) and Mazzotti et al. (2011) showed that surface strain measured by GPS indicates strain rates are below the measurement error within Alberta and the Rocky Mountains. More to the west, in the Intramontane Belt the values are also very low, yet in the coastal cordilleras, rates of about 10–15 $\mathrm{mm\,yr^{-1}}$ in the northeasterly direction with respect to stable North America are

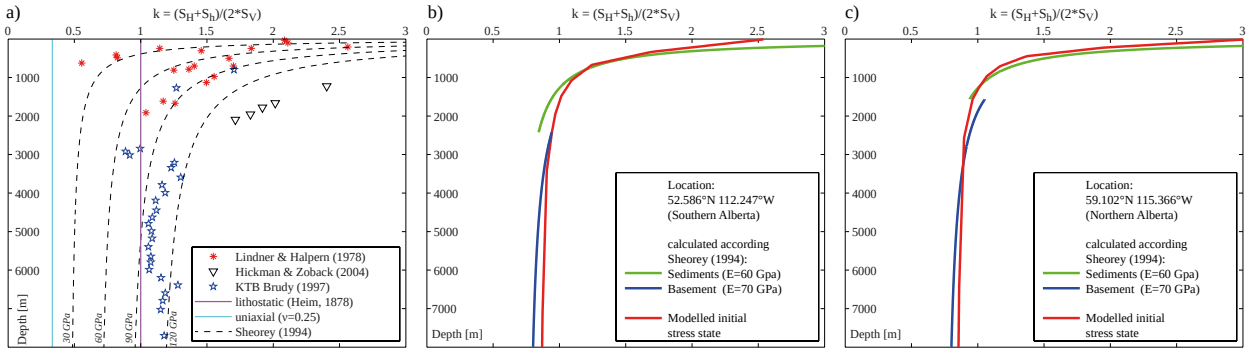

Figure 4.9: **(a)** Compilation of k ratios from North America (Lindner and Halpern 1978), the SAFOD pilot hole (Hickman and Zoback 2004) and from the KTB (Brudy et al. 1997). Theoretical k ratios based on the assumption of lithostatic load at greater depths (Heim 1878, $k = 1$), uniaxial strain conditions (Eq. 4.2) and the distribution according to Sheorey (1994, Eq. 4.5) for Young's modulus $E = 30$, 60, 90 and 120 GPa are plotted. **(b)** and **(c)** Depth profile of the initial and calculated k values for two test sites within the model. Blue and green line indicates calculated k profiles based on Sheorey (1994, Eq. 4.5) and the associated Young's modulus. The red lines indicate the k profiles from the model with the initial stress state.

observed. The North American Eulerian rotation pole is located southwest of Ecuador, resulting in a anticlockwise rotation of about 20 mm yr^{-1} in the southwesterly direction in Alberta (Henton et al. 2006). Flesch et al. (2007) found that (deviatoric) stresses associated with the accommodation of relative plate motion are of the same order of magnitude as buoyancy forces (gravitational potential energy – GPE). The orientation of observed North American rotation, shortening in the Canadian Cordillera (Henton et al. 2006; Mazzotti et al. 2011), and GPE gradient orientation (Flesch et al. 2007) correspond to the observed average S_{Hmax} azimuths in Alberta (see the rose diagram in Fig. 4.4).

As the model edges are parallel and perpendicular, respectively, to the observed plate motion, GPE and horizontal stress azimuth, displacement at the model boundaries will be applied orthogonally to the side walls of the model box. Horizontal and vertical motion is allowed along the side walls (Fig. 4.4). The applied amount and orientation of push (towards the northeast) and pull (towards the southeast) along the model will be tested during the calibration phase of the model. The bottom of the model is fixed in the z direction lateral motion within the extent of the model box is allowed.

4.4 In situ stress

This section presents a short introduction to the terminology used for the stress data during the model calibration procedure.

4.4.1 Orientation and magnitudes of stresses in sedimentary basins

The 3-D stress in rock ($\boldsymbol{\sigma}$) is described with a second-order tensor. By choosing an principal coordinate system, the stress tensor ($\boldsymbol{\sigma_{ij}}$)

$$\boldsymbol{\sigma_{ij}} = \begin{pmatrix} \sigma_{11} & \sigma_{12} & \sigma_{13} \\ \sigma_{21} & \sigma_{22} & \sigma_{23} \\ \sigma_{31} & \sigma_{32} & \sigma_{33} \end{pmatrix} \text{ or } \begin{pmatrix} \sigma_{xx} & \sigma_{xy} & \sigma_{xz} \\ \sigma_{yx} & \sigma_{yy} & \sigma_{yz} \\ \sigma_{zx} & \sigma_{zy} & \sigma_{zz} \end{pmatrix}, \tag{4.6}$$

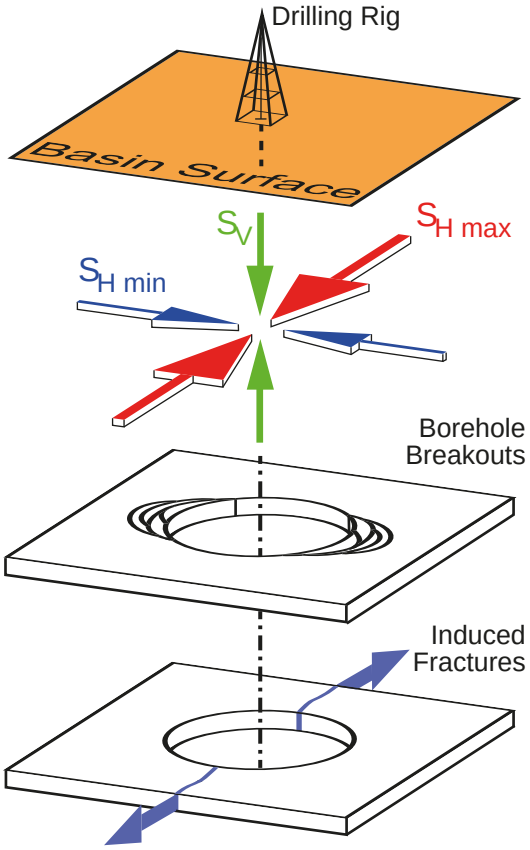

Figure 4.10: General assumption of stresses in sedimentary basins: the vertical stress (S_V) is a principal stress, thus perpendicular to the minimum and maximum horizontal stress (S_{hmin} and S_{Hmax}). Borehole breakouts occur in orientation of the S_{hmin} and induced tensile fractures occur in orientation of S_{Hmax}.

can be expressed with the three principal stresses:

$$\hat{\boldsymbol{\sigma}}_{ij} = \begin{pmatrix} \sigma_1 & 0 & 0 \\ 0 & \sigma_2 & 0 \\ 0 & 0 & \sigma_3 \end{pmatrix}. \tag{4.7}$$

These act normally to the principal planes and are the following: $\sigma_1 > \sigma_2 > \sigma_3$, in the order of magnitude. As the earth's surface is a free surface and sedimentary basins are roughly flat at the top, it is often assumed that the vertical stress (S_V) is a principal stress. With this assumption the minimum horizontal stress (S_{hmin}) and the maximum horizontal stress (S_{Hmax}) (e.g. Jaeger et al. 2009; McGarr and Gay 1978; Schmitt et al. 2012) are also principal stresses that are orthogonal to each other (Fig. 4.10). Their relative magnitudes determine the stress regime (Anderson 1951, cited in Kanamori and Brodsky 2004):

- normal faulting: $S_V > S_{Hmax} > S_{hmin}$
- strike slip: $S_{Hmax} > S_V > S_{hmin}$
- reverse faulting: $S_{Hmax} > S_{hmin} > S_V$.

More details can be found in Amadei and Stephansson (1997), Jaeger et al. (2009), Schmitt et al. (2012), Zang and Stephansson (2010) and Zoback (2007).

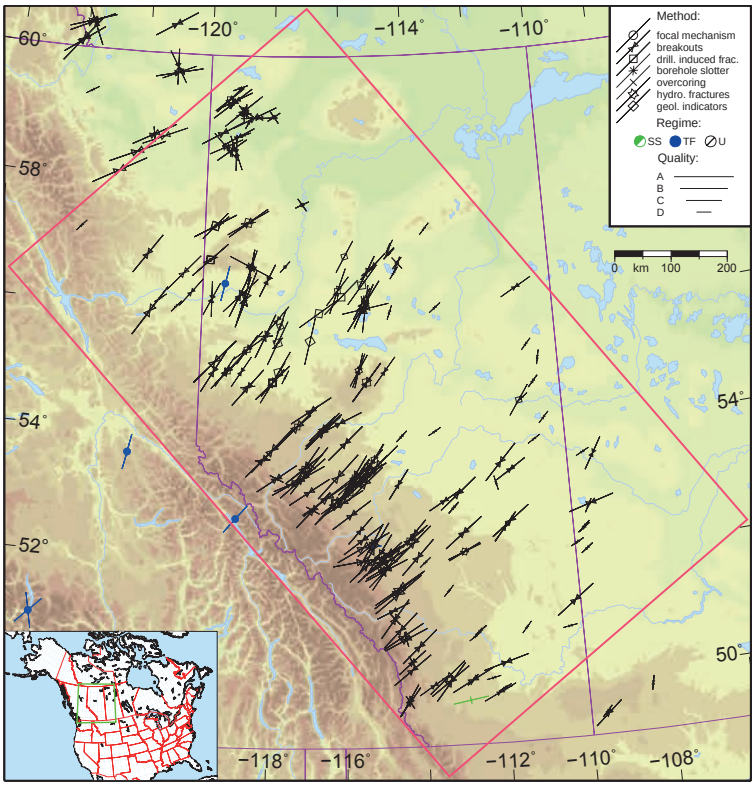

Figure 4.11: Crustal stress map of Alberta. Lines represent orientations of maximum horizontal compressional stress S_{Hmax}; line length is proportional to the data quality. Colours indicate stress regimes, with green for strike-slip faulting (SS), blue for thrust faulting (TF), and black for unknown regime (U). In summary, there are 321 S_{Hmax} azimuth data available within the modelled region. Data are from the latest update of the Canadian stress map (Reiter et al. 2014).

4.4.2 Contemporary stress field in the Alberta Basin

The present-day stress field in Alberta has been the subject of several studies. It started with Bell and Gough (1979) recognizing in the Alberta Basin that borehole breakouts are an indicator of crustal stress orientation (Fig. 4.10). They found that the S_{Hmax} azimuth is uniformly oriented southwest to northeast in substantial parts of the Alberta Basin (Fig. 4.11). This observed orientation is perpendicular to the Rocky Mountain trench, which was confirmed by Adams and Bell (1991), Bell and Gough (1981), Bell et al. (1994), Fordjor et al. (1983) and recently by Reiter et al. (2014). Orientation data are derived from a large variety of rock types, depths, and different indicators. These are borehole breakouts at a depth range of 113–5485 m (e.g. Bell et al. 1994), geological indicators (Bell 1985), and drilling-induced tensile fractures (Fordjor et al. 1983), and seismological studies in the Canadian Cordillera (Ristau et al. 2007), confirmed the overall orientation pattern (Fordjor et al. 1983). Only an anticlockwise rotation of about 10–20° is observed in northern Alberta over the Peace River Arch.

The same homogeneous stress orientation is observed over wide areas of the North American plate (Bell and Gough 1979; Adams and Bell 1991; Fordjor et al. 1983; Gough et al. 1983; Reiter et al. 2014; Sbar and Sykes 1973; Zoback and Zoback 1980), which indicates that southwest-to-northeast stress orientation is present over the whole lithosphere rather than sediments only (Fordjor et al. 1983). This implies also that the sediments are attached to the basement (Bell 1996b). The S_{Hmax} orientation is at a right angle to the Rocky Mountains fold axis. Therefore, the stress field

responsible for thrust faulting in Mesozoic time is still present (Bell and Gough 1979). The driving force of the observed stress pattern is plate tectonics, either by drag resistance of the lithosphere sliding over asthenosphere (Bell and McLellan 1995; Zoback and Zoback 1980) or mantle convection propelling the lithosphere (Bell and Gough 1979; Fordjor et al. 1983; Gough 1984).

The depth gradients of S_V and S_{hmin} increase from the basin centre towards the foothills and the Rocky Mountains (Baranova et al. 1999; Bell 1996b; Bell and Bachu 2004; Bell and Grasby 2012). This trend coincides with higher organic maturity (England and Bustin 1986; Nurkowski 1984) and larger compaction (Bell and Bachu 2004) in that direction, which is related to the depth of present and past burial. The maximum erosion of basin sediments is by about 1400 m (Woodland and Bell 1989), uplift occurring since the mid-Cenozoic time, mainly in the foothills (Bell and McLellan 1995).

The stress regime in the basin sediments changes from thrust faulting in the foothills to strike slip within the basin, up to a normal faulting regime further east in Saskatchewan (Bell and Gough 1979; Bell et al. 1994; Bell and McLellan 1995; Bell and Bachu 2003; Bell and Grasby 2012; Woodland and Bell 1989). A similar change from surface to depth is observed: from thrust faulting at <350–600 m in depth, strike slip in a depth range of about 500–2500 m, down to normal faulting at greater depths >2500 m (Bell and Babcock 1986; Fordjor et al. 1983; Jenkins and Kirkpatrick 1979). There is also a varying S_{hmin} gradient discussed (Bachu et al. 2008; Bell and Grasby 2012; Hawkes et al. 2005), but this is may be due to different measurement methods (Bell et al. 1994) or man-made stress changes. The S_{Hmax}/S_{hmin} ratio in the Alberta Basin is about 1.3–1.6 (Fordjor et al. 1983).

Man-made stress perturbation due to hydrocarbon production or acid gas injections (e.g. Bachu et al. 2008; Bell and Grasby 2012; Woodland and Bell 1989) reduces or increases reservoir fluid pressure respectively, but has likely only local effects (e.g. Altmann et al. 2010). Furthermore, Baranova et al. (1999) found a strong correlation between rates of gas production and the number of seismic events, which is reasonable because production lead to decrease of S_V and increase of S_{Hmax} – consequentially increasing differential stresses. The stress change due to the gas extraction point to a regime which favours thrust faulting (Baranova et al. 1999). Hydraulic fractures applied for hydrocarbon industry or for enhanced geothermal systems deeper than 350 m will open parallel to southwest- to northeast-oriented S_{Hmax} orientations, except that in the Peace River Arch, they will tend to south–soutwest to north–northeast (Bell et al. 1994; Bell and Grasby 2012). Close to the Rocky Mountain foothills, northwest- to southeast-oriented hydraulic fractures are possible parallel to the thrust planes and the fold axes (Bell and Babcock 1986). However, horizontal wells e.g. for EGS should be designed parallel to the S_{hmin} orientation (Bell and Grasby 2012).

4.4.3 In situ stress data

4.4.3.1 Vertical stress (S_V)

The vertical stress (S_V) is the overburden load, which is estimated using density logs (e.g. Gardner and Dumanoir 1980) in a well:

$$S_V = \int_0^z \rho(z) g \, \mathrm{d}z \approx \overline{\rho} g z. \tag{4.8}$$

For the Alberta model region 981 S_V magnitude data sets are available (provided by the AGS), these are indicated by black points in Fig. 4.12. S_V magnitude data vary only slightly, even in greater depths, the lateral variation is less than 5 MPa.

4.4.3.2 Orientation of maximum horizontal stress (S_{Hmax})

The orientation of S_{Hmax} is indicated by borehole breakouts, focal mechanisms, hydraulic fracturing, overcoring, and drilling-induced fractured and geological indicators (for overview, see Bell 1996a; Ljunggren et al. 2003; Schmitt et al. 2012; Zang and Stephansson 2010; Zoback et al. 2003). 321 S_{Hmax} azimuth data sets are available for the modelled region in Alberta; these are indicated in Fig. 4.11, based on the latest update of the Canadian stress database (Reiter et al. 2014).

4.4.3.3 Magnitude of minimum horizontal stress (S_{hmin})

The S_{hmin} magnitudes are measured by hydraulic fracturing or the similar leak-off test. During hydraulic fracturing (Bell 1996a; Haimson and Cornet 2003; Hubbert and Willis 1957; Zoback et al. 2003) and leak-off tests (e.g. Li et al. 2009; White et al. 2002; Zhou 1997), the down-hole pressure is increased up to pressure loss due to fluid leakage in the rock mass. This happens, when the hydraulic fracture splits apart the surrounding rock perpendicular to the least principal stress (σ_3), usually assumed to be S_{hmin} in sedimentary basins, and therefore the fracture opens in S_{Hmax} orientation (Fig. 4.10). The highest pressure is the fracture breakdown pressure (FBP, Haimson and Fairhurst 1969), which is S_{hmin} + rock resistance up to failure. When the pressure at which the fracture closes or re-opens is less than S_V, it is assumed that S_{hmin} is measured (Haimson and Fairhurst 1969). The mini-frac test (e.g. McLellan 1987; Woodland and Bell 1989) and the micro-frac test (Gronseth and Kry 1983) as hydro-fracturing methods estimate the closure pressure by opening and closing the fracture several times, but differ by the injected fluid volume.

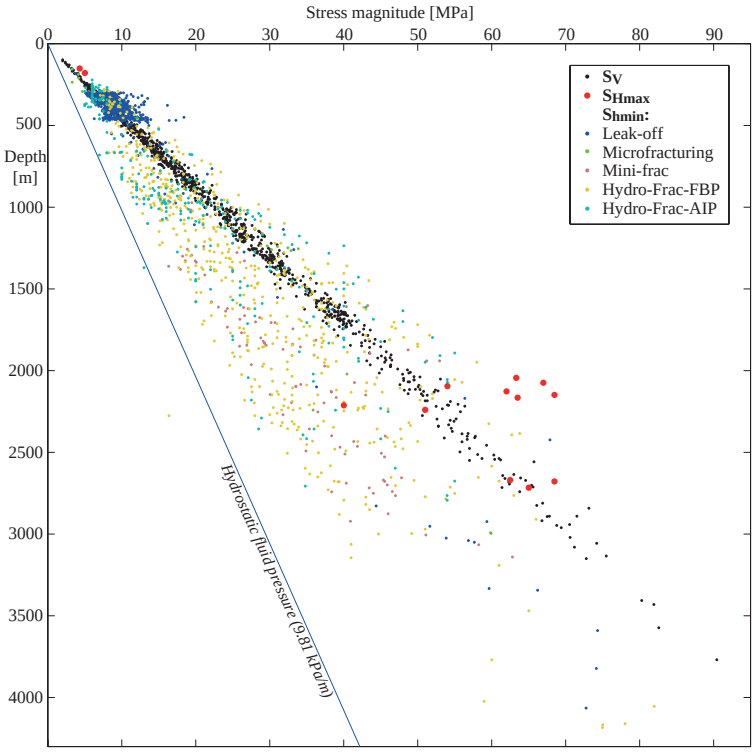

Figure 4.12: Depth plot of the in situ stress magnitudes. These are 981 S_V magnitude data (black), 1720 S_{hmin} magnitudes (several colours), and 2 measured as well as 11 calculated S_{Hmax} magnitudes (highlighted red points). S_{hmin} data are colour coded depending on the test type, which is taken over from the original database.

The term "leak-off tests" is used variably and can be distinguished by their aim into formation integrity tests (FIT), "classic" leak-off tests (LOT) and extended leak-off tests (XLOT) (White et al. 2002). The general method is similar, but differs in pumping cycles and the point at which the pumping is stopped. Usually, leak-off tests (LOT) are meant, which provide the upper limit of S_{hmin} and measure the fracture closure pressure (FCP) or the instantaneous shut-in pressure (ISIP) (White et al. 2002). XLOT allow measurement of the fracture re-opening pressure, like the original hydro-fracture tests.

For the model region, 1720 S_{hmin} magnitudes data are available, provided by the AGS; see Fig. 4.12. These are 784 leak-off magnitude data and 936 magnitude data from hydraulic fracturing. The different hydraulic fracturing methods are 14 Micro-frac, 91 Mini-frac, 250 Hydro-Frac-AIP, and 581 Hydro-Frac-FBP data. The data scatter strongly, independently from the test method or lithology. Further detailed information about the measurements are not available; that would allow whether the data represents the undisturbed stress state or not. The scatter either reflects the spatial anisotropy of the in situ stress, or that the data set is noisy, i.e. a mix of in situ stress information and data from areas with a disturbed stress field.

4.4.3.4 Magnitude of maximum horizontal stress (S_{Hmax})

The magnitude of S_{Hmax} is measured via the overcoring method (McGarr and Gay 1978; Obert 1962), which isolates a rock cylinder from the surrounding rock and measures the elastic relaxation of the rock cylinder. This is equivalent to the stress magnitude as well as the stress orientation, before removal of the surrounding rock. The drawbacks are the small quantity of inspected rock mass and the fact that the application is usually close to the surface. Furthermore, there are several methods used to calculate S_{Hmax}, based on S_{hmin} magnitudes and known rock properties (e.g. Schmitt et al. 2012). For the model region, 11 calculated data (Bell et al. 1994) and 2 shallow measured data (overcoring from Kaiser et al. 1982) are available (see Fig. 4.12).

4.5 Model calibrations

4.5.1 General comparison technique

The 3-D geomechanical–numerical model (with the initial stress state) from Alberta will be calibrated in the following according to the work flow scheme (Fig. 4.1). Each type of in situ stress data will be used step by step to calibrate the model. We first use the S_V data to calibrate the density (technically, the initial stress state is found after this step); then, we use the S_{Hmax} azimuth data to calibrate the orientation of applied displacement boundary conditions. Finally, the S_{hmin} and S_{Hmax} magnitudes are used to calibrate the magnitude of applied displacement boundary conditions, i.e. push and pull at the edges of the model box.

In each step, the modelled stress tensor is interpolated via inverse distance interpolation onto each point, where in situ stress data are available. The difference (ΔS) between measured stress ($S_{measured}$) and the modelled stress (S_{model}) is calculated in the following way:

$$\Delta S = S_{\text{measured}} - S_{\text{model}}, \tag{4.9}$$

which means that negative values indicate an overestimation by the model and vice versa. A value close to zero indicates a good approximation of the in situ stresses by the model. To compare magnitude data independently of the range, the deviation is normalized by the modelled stress value:

$$n\Delta S = \frac{S_{\text{measured}} - S_{\text{model}}}{S_{\text{model}}}. \tag{4.10}$$

To evaluate the differences between each in situ data set and the model as a whole, the median of ΔS ($\widetilde{\Delta S}$) is calculated as a single value for each model. In the case of the best-fit model, the $\widetilde{\Delta S}$ shall be close to zero. To estimate the influence of outliers and the variation of the data, the mean ($\overline{\Delta S}$) and the standard deviation (SD) is also calculated. The linear correlation between the in situ data and the model data is represented by the Pearson product-moment correlation coefficient (r), where $r = 1$ indicates total positive correlation, $r = -1$ total negative correlation and $r = 0$ no correlation.

The data sets are contaminated with unlikely in situ data; such data are often sorted out (e.g. Bell and Bachu 2004; Bell and Grasby 2012) for interpolation. As statistical tests are used in this study, data weed out is not required.

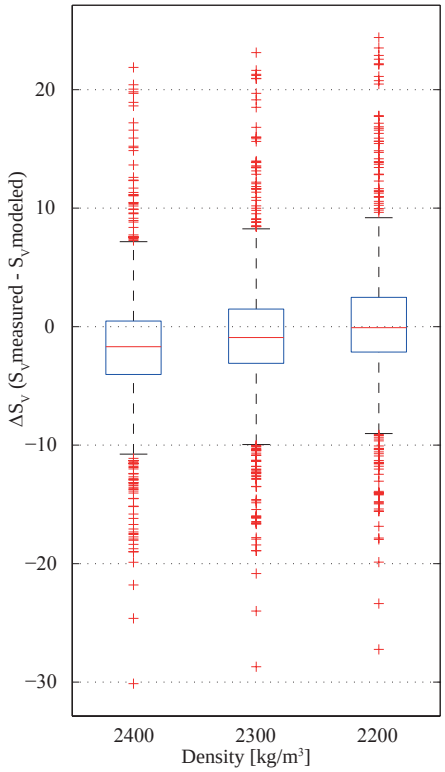

Figure 4.13: Boxplot of the varied density of the basin sediments – plotted is the ΔS_{V}. The median ΔS_{V} of the model with a density of 2200 kg m^{-3} is close to 0 MPa and therefore the best-fit density to the available $\mathrm{S_V}$ data, in contrast to the models with a higher basin density, where ΔS_{V} is negative (see Eq. 4.11).

4.5.2 Calibration of material density on $\mathrm{S_V}$ data

The density of the sedimentary basin is calibrated based on $\mathrm{S_V}$ magnitudes ($n = 981$, Fig. 4.12); all other material properties are defined in Sect. 4.3.2. The overall density of the modelled basin sediments is tested with 2200, 2300 and 2400 kg m^{-3}. According to Eq. (4.9), the difference between the measured and modelled $\mathrm{S_V}$ ($\Delta \mathrm{S_V}$), as well as the normalized $\Delta \mathrm{S_V}$ ($n\Delta \mathrm{S_V}$) are calculated:

$$\Delta S_{\mathrm{V}} = S_{\mathrm{V\ measured}} - S_{\mathrm{V\ model}}. \tag{4.11}$$

$$n\Delta S_{\mathrm{V}} = \frac{S_{\mathrm{V\ measured}} - S_{\mathrm{V\ model}}}{S_{\mathrm{V\ model}}}. \tag{4.12}$$

The model with a density of 2200 kg m^{-3} has a $\widetilde{\Delta S}_{\mathrm{V}}$ which is close to zero (−0.09 MPa) and a $\overline{\Delta S}_{\mathrm{V}}$ of 0.28 MPa, which is also close to zero (Fig. 4.13). A standard deviation of 5.58 MPa as well as the Gaussian distribution in the normalized histogram (Fig. 4.14a) indicates that there is no large data drift. The correlation coefficient of $r = 0.935$ indicates a good fit.

4.5.3 Calibration of the orientation of displacement boundary conditions based on S_{Hmax} azimuth data

The S_{Hmax} orientation is controlled by the applied displacement boundary conditions. Within the model region, 321 S_{Hmax} orientation data are available. They are displayed together with the data aside of the model in the stress map from Alberta (Fig. 4.11). The observed stress pattern is quite homogeneous.

The displacement boundary conditions act orthogonally to the model margins, in a horizontal direction. Whereas shortening is applied in a northeasterly direction to the model, extension is applied in a southeasterly direction (Fig. 4.4). According to Eq. (4.9), the difference between the measured and modelled S_{Hmax} azimuth is calculated. Eq. (4.13) is expanded with two additional lines, due to the fact that S_{Hmax} orientation data are circular data (0–180°, and 0°=180°) and therefore $\Delta S_{\mathrm{Hmax\,Azi}}$ have to range from −90° to +90°:

$$\begin{aligned}\Delta S_{\mathrm{Hmax\,Azi}} = {} & S_{\mathrm{Hmax\,Azi\ Meas}} - S_{\mathrm{Hmax\,Azi\ Model}} \\ & - 90(\mathrm{sgn}(S_{\mathrm{Hmax\,Azi\ Meas}} - S_{\mathrm{Hmax\,Azi\ Model}} - 90) \\ & + \mathrm{sgn}(S_{\mathrm{Hmax\,Azi\ Meas}} - S_{\mathrm{Hmax\,Azi\ Model}} + 90)).\end{aligned} \tag{4.13}$$

The histogram of the ΔS_{Hmax} azimuths (Fig. 4.14b) displays a main cluster around zero with a $\widetilde{\Delta S}_{\mathrm{Hmax}}$ azimuth of −3.44°. The main cluster ranges from −40° to 40°; a second (smaller) cluster ranges from −50° over ±90° to 60°, with a slight peak around ±90°. This is exactly orthogonal to the main cluster and explains the large SD of 26.9°; the mean ($\overline{\Delta S}_{\mathrm{Hmax}}$=3.42°) is similar to the median. The best-fit orientation is found for a large range of push and pulls magnitudes. Therefore, different oriented boundary conditions are not further tested.

Table 4.2: Overview of major push-and-pull experiments. The orientation of the displacement boundary condition is indicated in Fig. 4.4. Four test scenarios with different push and pull magnitudes are displayed, same as in Fig. 4.15a and b. The displacement boundary conditions for the best-fit model (last line) are calculated based on bivariate linear regression; see text.

Models	Push from SW (m)	Pull to SE (m)	median ΔS_{hmin} (MPa)	median ΔS_{Hmax} (MPa)
Test scenarios	0.00	150.00	−1.120	7.246
	200.00	100.00	−6.424	−10.800
	200.00	250.00	1.264	−9.561
	−50.00	−280.00	6.273	12.705
best-fit	86.24	194.52	−0.005	0.018

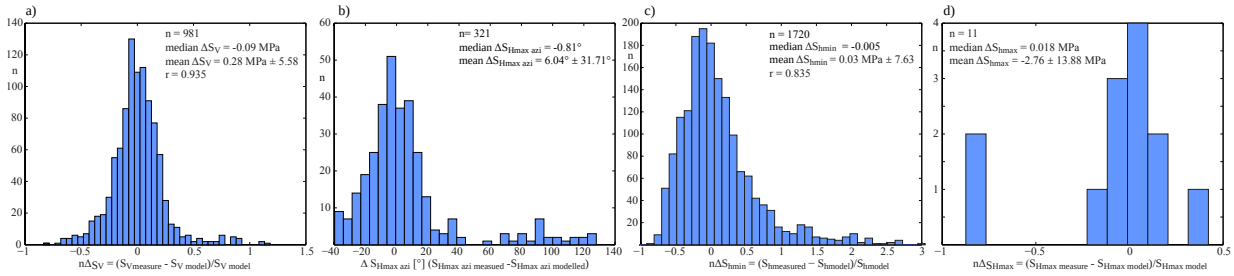

Figure 4.14: Distribution plots of the best-fit model, the number of data, the median, the mean, the standard deviation (SD) and the Pearson product-moment correlation coefficient (r) for the most $n\Delta S$ or ΔS are indicated in the histograms. **(a)** The histogram of the normalized ΔS_{V} displays a nice Gaussian distribution. **(b)** The histogram of the ΔS_{Hmax} azimuth data displays one major cluster around zero, with a range from -40 to 40°; a second smaller cluster ranges in orientations between -50°over ± 90° to 60°, with the highest peak by about $\pm$ 90°. **(c)** The normalized ΔS_{hmin} magnitudes display a positive screwed distribution. **(d)** The normalized ΔS_{Hmax} magnitude histogram for the 13 available data displays two negative outliers (the two shallow (overcoring) data). However, the 11 calculated data are arranged around zero.

4.5.4 Calibration of the magnitude of displacement boundary conditions by S_{hmin} and S_{Hmax} magnitude data

The S_{hmin} (n=1720) and S_{Hmax} (n=13: 2 measured and 11 calculated) magnitude data (Fig. 4.12) are used to calibrate the magnitude of applied push and pull along the model edges (Fig. 4.4). The aim is a model, which mimics the S_{hmin} and S_{Hmax} in situ magnitude data quite well. Several scenarios with different amount of push and pull are calculated, to estimate the range of push and pull, close to the best-fit model. In the following we focus in only four scenarios with a different amount of push and pull (Table 4.2). According to Eqs. (4.9) and (4.10) the difference between the measured and modelled S_{hmin} and S_{Hmax} magnitudes is calculated as well as the normalized difference.

$$\Delta S_{\mathrm{hmin}} = S_{\mathrm{hmin\ Measured}} - S_{\mathrm{hmin\ Model}}, \tag{4.14}$$

$$\Delta S_{\mathrm{Hmax}} = S_{\mathrm{Hmax\ Measured}} - S_{\mathrm{Hmax\ Model}}, \tag{4.15}$$

$$n\Delta S_{\mathrm{hmin}} = \frac{S_{\mathrm{hmin\ Measured}} - S_{\mathrm{hmin\ Model}}}{S_{\mathrm{hmin\ Model}}}, \tag{4.16}$$

$$n\Delta S_{\mathrm{Hmax}} = \frac{S_{\mathrm{Hmax\ Measured}} - S_{\mathrm{Hmax\ Model}}}{S_{\mathrm{Hmax\ Model}}}. \tag{4.17}$$

The calculated $\widetilde{\Delta \mathrm{S}}_{\mathrm{hmin}}$ and $\widetilde{\Delta \mathrm{S}}_{\mathrm{Hmax}}$ of four model runs (Table 4.2) are plotted in the push vs. pull diagram (Fig. 4.15a and b). To highlight the linear dependency between push and pull in an elastic model, colour coded isolines are plotted. Each model along the light blue line (Fig. 4.15a) would derive a model, which fits well with the in situ S_{hmin} data. The same stands for the light blue line in Figs. 4.15b and S_{Hmax} data. As the determination of the best-fit model is intended, the intersection of both light blue lines from Fig. 4.15a and b would derive such a model. This is done with a bivariate linear regression based on the spatial distribution of the $\widetilde{\Delta S}_{\mathrm{hmin}}$ and $\widetilde{\Delta S}_{\mathrm{Hmax}}$ (Fig. 4.15c). This method provides the following equations, which describes the zero isoline (light

blue line) as a linear function. These are for median $\Delta S_{\mathrm{hmin}} = 0$:

$$y = -0.2709 \cdot x - 171.1586, \tag{4.18}$$

and for the $\widetilde{\Delta S}_{\mathrm{Hmax}}$ zero isoline:

$$y = -10.6642 \cdot x + 725.1380. \tag{4.19}$$

By equalizing Eqs. (4.18) and (4.19):

$$x = \frac{725.1380 + 171.1586}{10.6642 - 0.2709}, \tag{4.20}$$

the best-fit model has a push from southwest of 86.24 m and a pull in southeasterly direction of 194.52 m (Table 4.2, last line).

The median values ($\widetilde{\Delta S}_{\mathrm{hmin}} = -0.005$ and $\widetilde{\Delta S}_{\mathrm{Hmax}} = 0.018$) fits quite well, the same stands for the mean values ($\overline{\Delta S}_{\mathrm{hmin}}$ =0.03 and $\overline{\Delta S}_{\mathrm{Hmax}} = -2.76$). The distribution of the normalized S_{hmin} (Fig. 4.14c) displays a positive screwed distribution. The correlation coefficient of the in situ S_{hmin} magnitude data and the modelled S_{hmin} is $r = 0.835$. The normalized best-fit of S_{Hmax} (Fig. 4.14d) displays two outliers; these are the only two measured S_{Hmax} magnitudes, measured at a depth of 152 m.

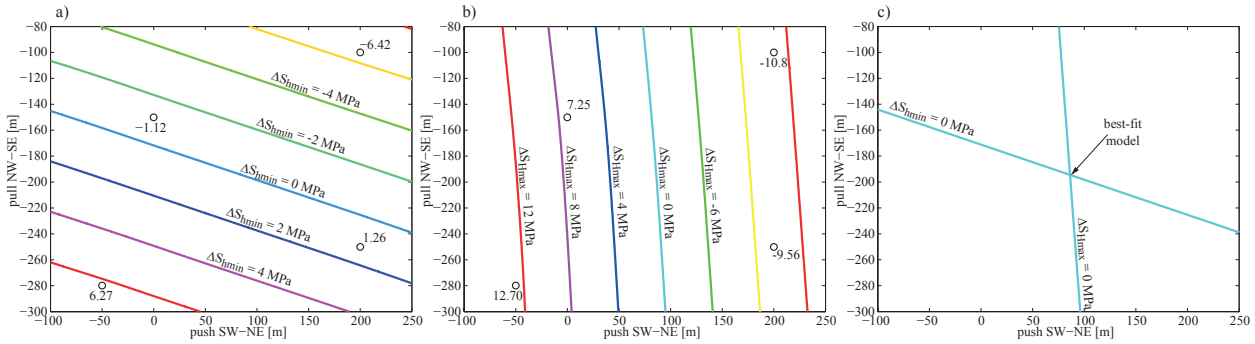

Figure 4.15: Plot of four models with different shortening or extension at the model boundary; see Table 4.2 for details. **(a)** and **(b)**: the median S_{hmin} and the median S_{Hmax} are plotted depending on the northwest to southeast extension (pull) and the southwest to northeast shortening (push) The isolines of the median ΔS_{hmin} and ΔS_{Hmax} are colour coded. **(c)** The isolines, where the median ΔS_{hmin} and ΔS_{Hmax} are zero are plotted alone. The intersection of both isolines indicated the push-pull values where the best-fit model can be found.

4.6 Discussions

4.6.1 Workflow and calibration

The general workflow of model calibration (Fig. 4.1) is similar to other studies on numerical stress field modelling (e.g. Buchmann and Connolly 2007; Fischer and Henk 2013; Heidbach et al. 2013; Hergert and Heidbach 2011). However, in contrast to former studies, the number of in situ stress data from the Alberta Basin allows a statistical comparison with the model results.

4.6.1.1 S_V calibration

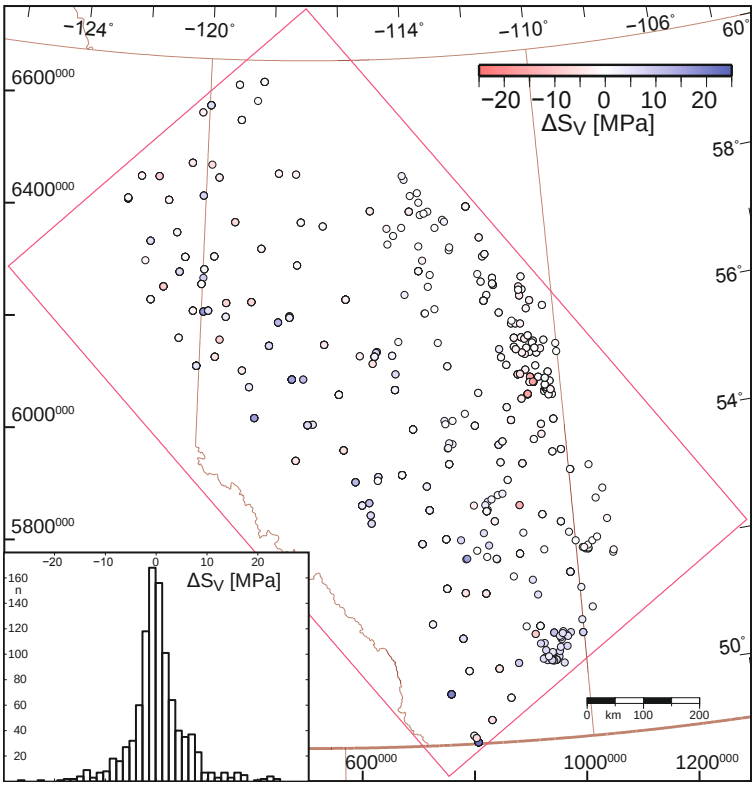

Figure 4.16: Spatial distribution of ΔS_V differences are plotted colour coded. The map extent is indicated by geographical coordinates (top and right) and by UTM coordinates from zone 11 (left and bottom).

Given the large model size ($1200\,km \times 700\,km \times 80\,km$), the Alberta Basin infill is considered to be one material type only, except for the Elk Point evaporates. The available data set of 981 S_V magnitude data points (Fig. 4.12) could be used via linear regression to calculate the overall density of the sedimentary basin, but, to incorporate the (minor) lateral effects of topography, the overall density is determined in the calibration process. Plotting the distribution of the normalized deviation ($n\Delta S_V$) in histogram Fig. 4.14a demonstrates a Gaussian distribution, which implies there is no process affecting data drift. As data spreading does not depend on the vertical depth, a slightly higher lithological resolution with linearly increasing density into depth would most likely not deliver a much better data fit. This could be solved by incorporation of all stratigraphic units, which would go far beyond the goals of this study. The spatial plot of ΔS_V (Fig. 4.16) shows that in situ S_V magnitudes are slightly higher close to the foothills. This is expected from former studies, showing S_V increases in southwesterly direction (e.g. Bell and Bachu 2004; Bell and Grasby 2012).

4.6.1.2 Calibration of S_{Hmax} orientation

The 321 data records of the S_{Hmax} azimuth (Fig. 4.11) are used to test the orientation of the applied displacement boundary conditions. As long as a certain push to northeast and a pull in southeasterly direction are applied orthogonally to the model box (Fig. 4.4), a good fit of the stress orientation (Fig. 4.14b and 4.17) is achieved. No variation of the boundary conditions (orientation of push and pull) was necessary, due to the appropriately chosen model orientation.

The histogram of the ΔS_{Hmax} azimuth (Fig. 4.14b) displays two data clusters. The larger cluster displays a normal distribution around zero, which is confirmed by a $\widetilde{\Delta S}_{Hmax}$ azimuth of $-3.44°$. A second data cluster is distributed around $\pm 90°$, which explains the high SD of 26.9°. The second cluster with a deviation of around $\pm 90°$ is the orientation of S_{hmin} indicating that some of the used in situ S_{Hmax} azimuth data are likely miss-interpreted S_{hmin} orientations. Such incorrect interpretations are sometimes observed in borehole breakout data (Brudy and Kjø rholt 2001; Barton and Moos 2010); in such cases drilling induced tensile fractures, originated during drilling, are misinterpreted as borehole breakouts. Other reasons for orientation of data with right angles to the major population (S_{hmin}) are mud cake padding along caved zones and the collapse of pre-existing open fractures, again parallel to S_{Hmax} (Bell and Babcock 1986; Bell and Grasby 2012). Therefore, this second (smaller) cluster around $\pm 90°$ rather confirms then disproves the good data fit by the model.

The alternative explanation would be a horizontal stress state close to isotropic. This would allow large stress rotation due to small local stress sources (Heidbach et al. 2007). However, from the provided data this explanation can be ruled out, and the previously stated explanation is much more likely.

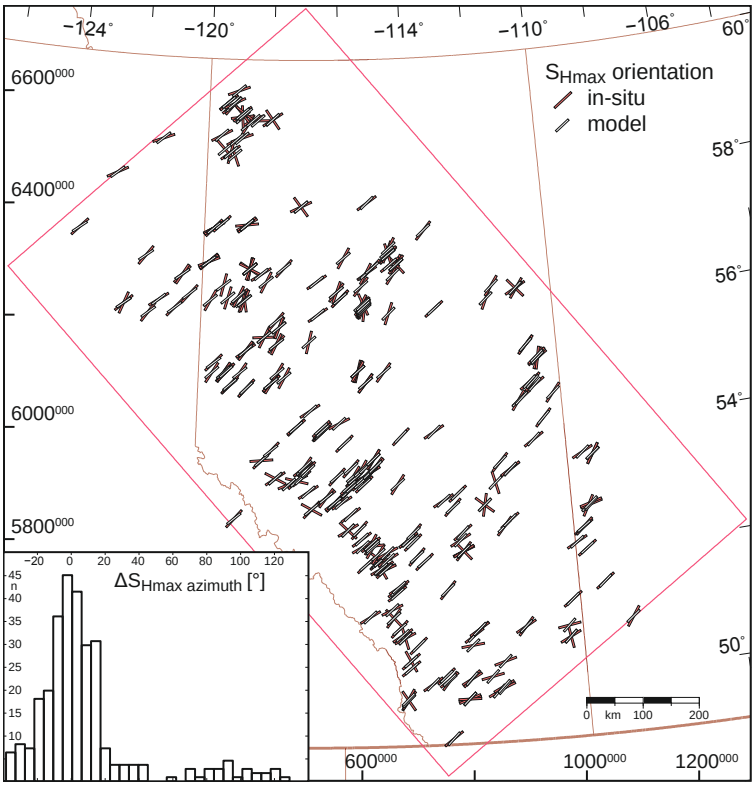

Figure 4.17: Spatial distribution of the modelled and in situ S_{Hmax} azimuth data. A good fit of the modelled data is reached, except for some suggested misinterpreted data ($\pm 90°$) and systematic rotations close to the Peace River Arch (56° N, 118° W) and close to the Bow Island Arch (50° N, 114° W). The map extent is indicated by geographical coordinates (top and right) and by UTM coordinates from zone 11 (left and bottom).

There are two areas in the modelled region, where a systematic difference of the S_{Hmax} azimuth between the in situ data and the model is visible (Fig. 4.17). These are the western Peace River arch (56° N, 118° W) and the Sweetgrass arch in the very south, close to the southern Bow Island Arch (50° N, 114° W). In the Peace River arch, in situ S_{Hmax} is rotated by about 20–30° anticlockwise

(Bell et al. 1994; Bell and Grasby 2012). The causes of this rotation, (see discussion in Bell and Babcock 1986; Bell and McCallum 1990; Bell 1996b; Bell and Grasby 2012; Bouzidi et al. 2002; Dusseault and Yassir 1994; Eaton et al. 1999; Halchuk and Mereu 1990), are not well represented by the model.

Bell and Gough (1979) suggested that the S_{Hmax} orientation is orthogonal to the topography of the Rocky Mountains, but a comparison close to the topography in the very south of Alberta displays a good fit between the in situ data and the model. They appear more influenced by the overall orientation than by the topography, which is also found by Reiter et al. (2014).

In contrast, the clockwise rotation of about 25° with respect to the regional trend is obvious close to the Bow Island arch. Likely this systematic rotation is caused by structural features along the Bow Island arch which are not incorporated into the model, then by the Rocky Mountain topography.

The Bow Island Arch separates the Alberta Basin and the Walliston Basin. It is a northeastward plunging Precambrian basement feature, which was activated during the Laramiden orogeny and may be associated with intrusions, similar to Eocene intrusions, about 200 km to the south in Montana (Podruski 1988). The systematic S_{Hmax} rotation in that region is most likely affected by these basement features along the Bow Island Arch.

4.6.1.3 S_{hmin} calibration

The largest number of stress data are the S_{hmin} magnitudes ($n = 1720$, Fig. 4.12). These, with a few S_{Hmax} magnitudes ($n = 13$: 2 measure and 11 calculated, Fig. 4.12), are used to find the best-fit magnitudes of the utilized boundary conditions.

A large number of models were tested, but only four of these are shown here (Table 4.2 and Fig. 4.15a and b). Based on these four test scenarios with different strain magnitudes, the best-fit model is determined via bivariate regression. Calculated is the intersection of zero-isolines of $\widetilde{\Delta S}_{Hmax}$ and $\widetilde{\Delta S}_{Hmin}$ (Fig. 4.15c) based on a plot of push vs. pull (Table 4.2, Fig. 4.15a and b). This is possible as linear elastic rheology is used in the model.

An evaluation as to whether the measured S_{hmin} magnitudes really represent S_{hmin} or only σ_3, because hydraulic fracturing tests provide the information on the smallest principal stress. The correlation between the in situ S_{hmin} magnitudes vs. modelled σ_3 ($r = 0.837$) is negligible higher then vs. modelled S_{hmin} ($r = 0.835$). This indicates that in situ S_{hmin} measurements in the Alberta Basin likely represent the magnitude of S_{hmin} and confirms the assumptions for sedimentary basins, being that S_{hmin} is the smallest principal stress (e.g. Jaeger et al. 2009; McGarr and Gay 1978; Schmitt et al. 2012).

The spatial distribution of the ΔS_{hmin} (Fig. 4.18) indicates that larger differences between the in situ and modelled magnitudes mainly occur in regions with clustered data. Slightly higher in situ magnitudes are observed in the region 56° N, 121° W, in contrast to the slightly lower in situ S_{hmin} magnitudes in region 55° N, 119° W.

The $n\Delta S_{hmin}$ histogram in Fig. 4.14c displays a positive screwed distribution. This indicates that the model underestimates a larger portion of the S_{hmin} magnitudes, in contrast to the in situ data.

To examine deviation reasons, Fig. 4.19 plots $n\Delta S_{hmin}$ depending on depth with the measuring method is indicated. in situ S_{hmin} LOT data provide rather positive $n\Delta S_{hmin}$ values in shallow depths (< 500 m) and negative values in depth > 500 m relative to the modelled S_{hmin} magnitudes. This implies that the model derives smaller magnitudes compared to shallow LOT magnitudes and larger ones with respect to deeper LOT magnitudes. In contrast hydraulic fracturing data did not indicate systematic deviations.

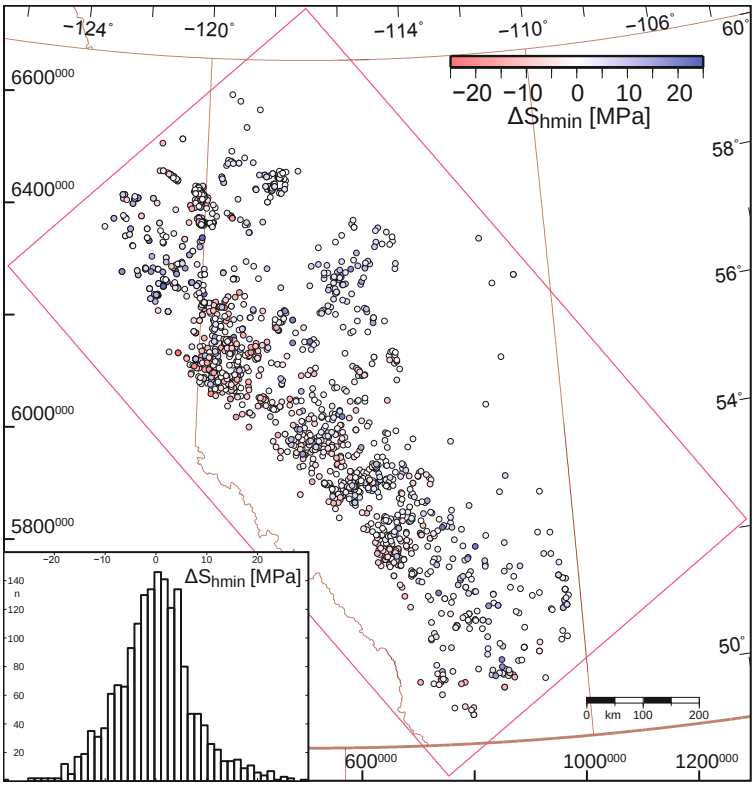

Figure 4.18: Comparison of the modelled and the in situ S_{hmin} magnitudes, plotted as ΔS_{hmin}. The map extent is indicated by geographical coordinates (top and right) and by UTM coordinates from zone 11 (left and bottom).

4.6.1.4 Deviation of Leak-off test (LOT) data vs. stress model

There are several reasons for the discrepancy in S_{hmin} in the in situ LOT data vs. stress model; they are

- the thrust faulting regime ($S_{hmin} > \sigma_3$),
- systematic measurement errors,
- systematic model errors, and
- disturbed in situ measurements.

Thrust faulting regime ($S_{hmin} > \sigma_3$)

Hydraulic fracturing (HF) and leak-off tests (LOT) measure the smallest principal stress (σ_3), which is expected as S_{hmin} in sedimentary basins with normal faulting or strike slip stress regime. In a thrust faulting stress regime, in situ data would underestimate S_{hmin}, as S_V is measured. However, the thrust faulting stress regime is expected in the Rocky Mountains, as well as in and close by the foothills (Bell and Gough 1979; Bell et al. 1994; Bell and McLellan 1995; Bell and Bachu 2003; Bell and Grasby 2012; Woodland and Bell 1989) and in shallow depths (up to 600 m) (Bell and Babcock 1986; Fordjor et al. 1983; Jenkins and Kirkpatrick 1979). Measuring $S_V = \sigma_3$ at shallow depth (<500 m) instead of S_{hmin} would indicate a thrust faulting regime for some regions, but shallow LOT magnitudes are systematically larger than expected by the stress model, which excludes this attempt at explanation.

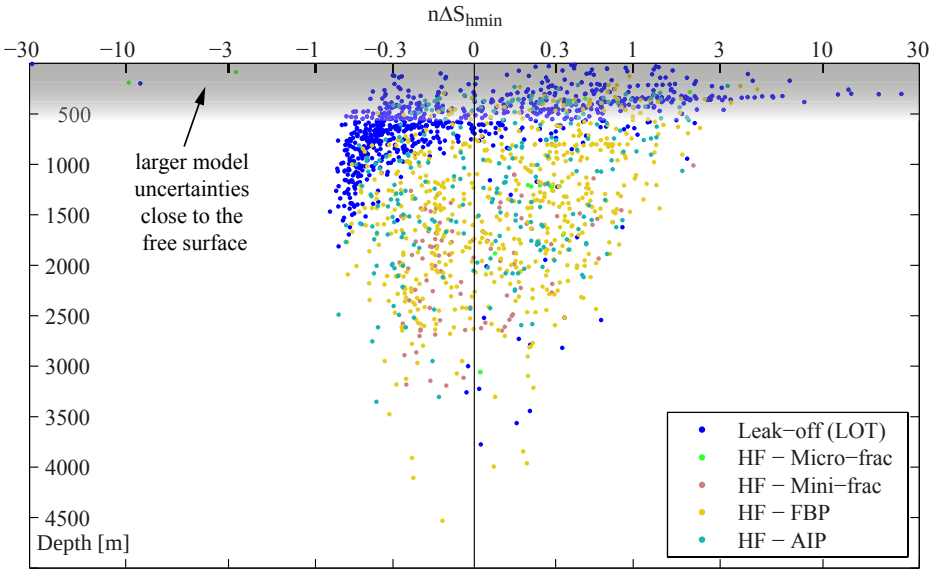

Figure 4.19: The distribution of the normalized ΔS_{hmin} vs. depth, the measurement method is colour coded. Results close to the surface up to about $-500\,\text{m}$ (indicated by greyish haze) have to be interpreted with care, as interpolation of the integration points to the nodes of the finite elements at the surface is problematic. Note that shallow ($< -500\,\text{m}$) leak-off tests (LOT) deliver systematic higher magnitudes than the stress model. In contrast to that are deeper ($> -500\,\text{m}$) LOT data, which have systematically smaller magnitudes as the model. Hydraulic fracturing (HF) data are unconcerned from such systematic drift.

Systematic measurement errors

Alternatively, an overestimation of S_{hmin} by LOT could be explained when the formation breakdown pressure (FBP) or leak-off pressure (LOP) (White et al. 2002) is measured. Additionally, LOT performed at shallow depths ($<300\,\text{m}$) are less reliable, because the tensile strength of the rock plays a more significant role for the measured pressure (Bachu et al. 2008). These reasons would explain larger S_{hmin} magnitudes from LOT, compared to the model at shallow depths ($<500\,\text{m}$).

LOT are also used as formation integrity tests (FIT) to determine whether the well bore can sustain the stresses expected during drilling and production, and then to determine stress magnitudes (e.g. White et al. 2002). Such FIT data derives smaller magnitudes then the formation S_{hmin} magnitude. Furthermore, poor cement seal between the well bore and the casing close to the LOT can reduce measured magnitude (Edwards et al. 1998). Both reasons could explain smaller S_{hmin} measurements in greater depth ($> 500\,\text{m}$), derived from LOT magnitudes.

Systematic model errors

In situ stresses are affected by the lithology at the locality (Roche et al. 2013; Warpinski 1989). This is observed in the Alberta Basin where sandstone exhibits lower in situ S_{hmin} magnitudes than shale (Bell and Grasby 2012; Kry and Gronseth 1983). As the modelled basin has only one material property, likely the evaporate layer, the modelled stresses represent stress conditions from rocks where in situ stress data are derived. These are mainly sandstone and limestone, whereas leak-off tests are usually conducted in shale (Bell and Grasby 2012). Therefore, the drift could be explained by shallow shale and deeper sandstone or limestone. Furthermore, extrapolation drift close to a free surface of an FEM model are sometimes observed.

Disturbed in situ measurements

Man-made stress changes perturb the juvenile in situ stress due to production (Bell and Grasby 2012) and injection of fluids (Bachu et al. 2008), besides other mining activity. This is obvious where induced seismicity has been reported (e.g. Baranova et al. 1999; Schultz et al. 2014). Such effects are not restricted to the reservoir alone; the country rock is affected too, in various styles, depending on the relative position (e.g. Segall 1989).

4.6.1.5 S_{Hmax} calibration

The quantity and quality of the S_{Hmax} magnitude data are rather poor compared to the S_{hmin} magnitude data, but are very helpful for constraining the best-fit model. Otherwise only a linear best-fit function could be estimated. The two outliers (Fig. 4.14d) are the only two measured S_{Hmax} magnitude data from Kaiser et al. (1982) at a depth of 152 m in clay shale. As the measured in situ data are more reasonable then the modelled magnitudes, the reasons for the large deviation are most likely extrapolation problems close to the model surface, as discussed in the previous chapter.

4.6.2 Reliability of the predicted 3-D stress field

The calibration procedure presented in Sect. 4.5 ensures that the resulting stress field is from a statistically point of view the best-fit model. Nevertheless, there are three main issues that limit the reliability of the model output: (1) The size of the model limits the local resolution. Local structural features such as small faults, material inhomogeneities or stratigraphy are not represented in the model. Thus the predicted stress field in particular close to local structures cannot resolve potential local stress field variations. However, the objective of the large-scale model is to provide boundary and/or initial conditions of regional to local stress field model that address the local stress field variations (e.g. Heidbach et al. 2013). (2) The predicted S_{Hmax} orientations as well as the S_V magnitudes are quite reliable given that density is quite well known (on the level of the resolution of the model) and due to the fact that the wave-length of the S_{Hmax} orientation is high and only minor affected by local features (Reiter et al. 2014). Also, the reliability of the predicted S_{hmin} magnitudes is high due to the large number of available data in the model volume. However, to what extend the S_{hmin} magnitudes that we use for the calibration of the undisturbed in situ stress are unaffected by production is not clear. Nevertheless, assuming that the majority of these data reflect the in situ stress, the outliers of S_{hmin} magnitude data that are affected by production are weeded out by the statistic tests. (3) The least reliable stress component of the predicted stress field is the S_{Hmax} magnitude. Only 13 S_{Hmax} magnitude data were available for the model calibration and these data have much higher inherent uncertainties in comparison with the S_{hmin} magnitude data. Given this, the statistical fit to the S_{Hmax} magnitude presented in Figs. 4.14 and 4.15 is not well constrained. In particular in areas where S_{Hmax} is close to the S_V magnitude the stress regime is not resolved and might change from strike-slip to normal faulting. This is critical for e.g. borehole stability or for the assessment of potential fault reactivation (Fuchs and Müller 2001; Moeck and Backers 2011). This is not a problem of the presented model in particular, but is a key challenge in general as this stress tensor component is hardly constrained from model-independent data.

4.6.3 Model variation

4.6.3.1 Impact of fault activation

The Great Slave Lake Shear Zone (GLS) and the Snowbird Tectonic Zone (STZ) are incorporated within the basement and the basin as vertical contact surfaces. The contact between the Alberta Basin and the foothills (foothill front), as well as the contact of the foothills to the Rocky Mountains (Rock Mountain front), are defined in the model as contact surfaces too. During the model calibration

all these contact surfaces are handled as locked faults with a high friction coefficient. To test the impact of fault re-activation on the stress field, we use in a model variant friction coefficients of 0.3 for STZ and GLS within the deeper basement. For the activation of the basement tectonic zones, the found correlation coefficient for S_{hmin} has been lowered only slightly: STZ alone ($r = 0.808$), GLS alone ($r = 0.828$) and STZ together with GLS ($r = 0.801$), compared to the best-fit model ($r = 0.835$). When the friction is lowered at the foothill front ($r = 0.836$) and the Rocky Mountains front ($r = 0.835$) alone, the correlation coefficient did not change. Only when both, the foothill and the Rocky Mountains front are active, the correlation declines ($r = 0.701$).

The S_{Hmax} orientation changes slightly (up to 2°) for all the fault activation. The exception is the Rocky Mountains front, where the $\widetilde{\Delta S}_{Hmax}$ orientation is equal to the best-fit model. This is expected, as only a few S_{Hmax} indicators are derived close to the Rocky Mountains front.

4.6.3.2 Impact of Moho depth variation

To test the influence of the Moho topography (Fig. 4.5) on the stress state within the Alberta Basin, the best-fit model is modified. The Moho depth is uniform ($z = -50\,\text{km}$) over the entire model region. The results of ΔS_{hmin} magnitudes show that this model fits all data, similar to the best-fit model ($r = 0.835$ for both model runs). S_{Hmax} orientation did not change between the models. Probably, stress magnitudes and orientations are only slightly influenced by the Moho topography in this region.

4.6.4 Model application for deep geothermal reservoirs

To generate electricity, water with temperatures of 120–150 °C is needed. This requires well depths of 4000–6000 m in Alberta (Majorowicz and Grasby 2010a, c). However, stimulation is required to enhance permeabilities (enhanced geothermal systems – EGS) at such depths. Furthermore, less hot water has potential as a domestic heat source.

Three major issues for application of EGS are related to the crustal stresses. These are (1) the orientation of S_{Hmax}, as induced fractures open parallel to S_{Hmax}. This is important for configuration of injection and production wells. (2) The tectonic stress regime determines whether fractures open horizontally (thrust faulting) or vertically (strike slip and normal faulting regime). Furthermore, well stability is a major issue for deep and of course very expensive wells; thus, (3) stress orientation and magnitude as well as differential stresses are important parameters for safe drilling.

S_{Hmax} orientations have been well understood in the Alberta Basin for decades (e.g. Bell and Gough 1979; Bell et al. 1994; Fordjor et al. 1983; Reiter et al. 2014), mainly homogeneous in southwest-to-northeast orientation, with the exception of the Peace River Arch and close to the Bow Island Arch.

Horizontal wells, oriented parallel to S_{hmin} (southeast to northwest) (Bell and Grasby 2012) with multiple fractures, open in the S_{Hmax} direction. This creates several fluid propagation paths, which has the potential to provide cost-efficient energy Hofmann et al. (2014).

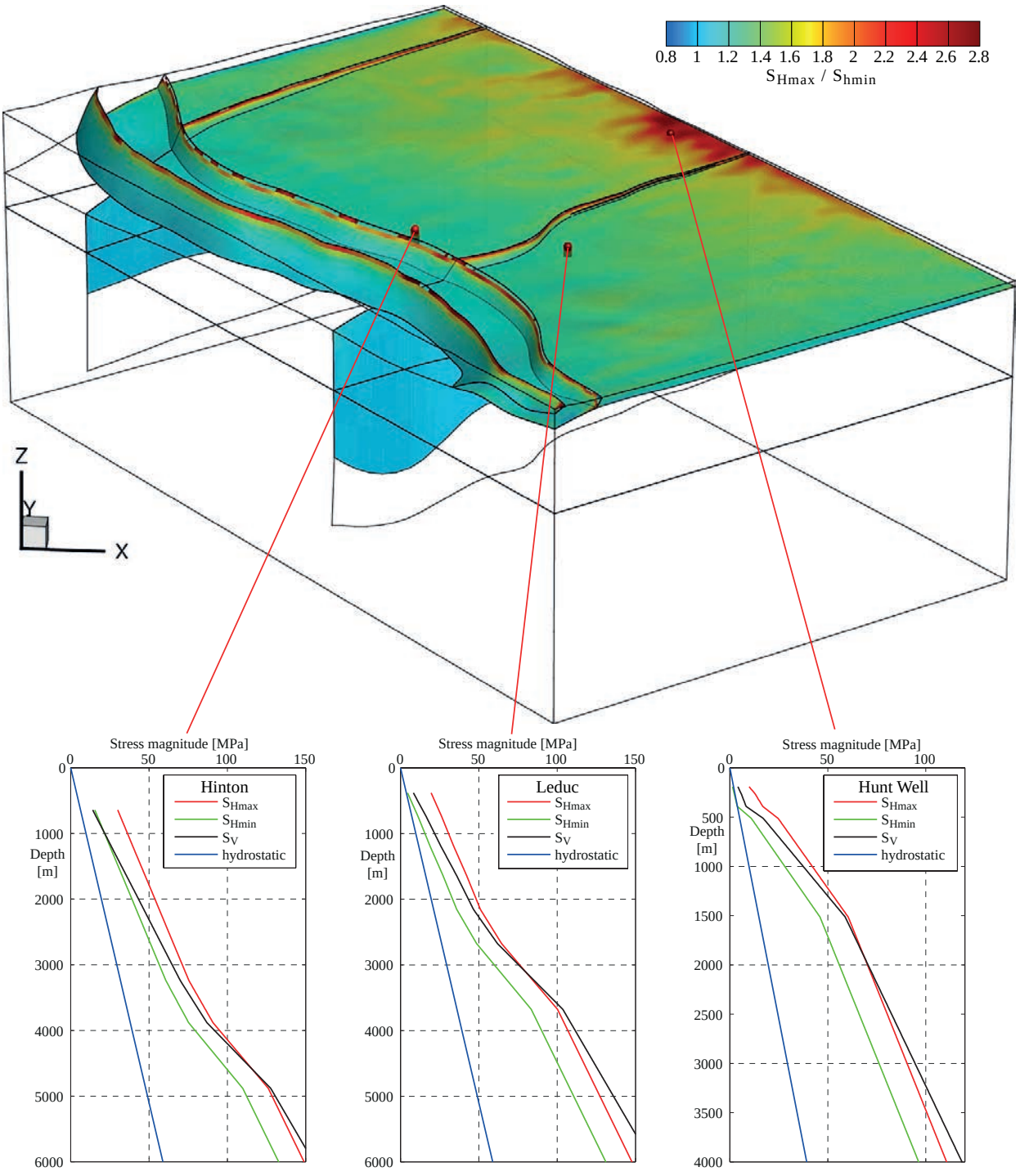

Figure 4.20: 3-D view of the best-fit model. Displayed is the S_{Hmax}/S_{hmin} ratio, plotted at the basement top, along the Snowbird- and the Great Slave Tectonic Shear Zone, the Rocky Mountains front and the front of the foothills. Three virtual wells from the surface down into the basement are indicated in the model. The stress growth into depth is illustrated in the lower part. These are virtual wells in Hinton, in Leduc (30 km south of Edmonton) and the location of the Hunt well (15 km west of Fort McMurray). The shallowest part is not shown in the plots due to free surface effects.

We chose three locations in Alberta that have been identified as possible geothermal sites (Weides and Majorowicz 2014; Pathak et al. 2013), and show S_V, S_{hmin} and S_{Hmax} along the virtual well path (Fig. 4.20). They are (1) the Edson–Hinton region, with sediment thicknesses of 4000–6000 m and potential temperatures of 100–150 °C, (2) the village of Leduc, 30 km south of Edmonton, with the potential to heat houses (Weides and Majorowicz 2014) and (3) the Hunt well site (e.g. Majorowicz et al. 2012) close to the town of Fort McMurray, where heat is needed for industrial application (Pathak et al. 2013).

The virtual wells in Fig. 4.20 shows that thrust faulting regimes occur close to the Rocky Mountains and foothills at shallow depths. A strike-slip regime is common within the basin from the surface to about 1500 to 3000 m in depth and along the foothills from about 1000 to 4000 m in depth. At greater depths, from about 4500 m in depth for the foothills, 3000 m in depth for Edmonton, and 2000 m in depth for Fort McMurray, a normal faulting regime is expected. This confirms Bell and Gough (1979), Bell et al. (1994), Bell and McLellan (1995), Bell and Babcock (1986), Bell and Bachu (2003), Bell and Grasby (2012), Woodland and Bell (1989), Fordjor et al. (1983) and Jenkins and Kirkpatrick (1979). Therefore opening of induced fractures horizontally can be expected only close to the foothills, at depths less than 1000 m.

4.7 Conclusion

A large data set of stress orientation and stress magnitude data is used to calibrate a 3-D geomechanical–numerical model of the Alberta Basin, which provides a good first-order estimation of the contemporary stress tensor. During calibration procedure, the density of the sediments, the orientation of the displacement boundary conditions, and the magnitude of applied shortening of the model along the model boundaries are calibrated. As linear elastic material properties are used, the magnitude of applied displacement boundary conditions for the best-fit model can be determined by bivariate linear regression. This is based on only three (or more) models with variable boundary conditions. The stochastic verified calibration allows the evaluation of measurement outlier and systematic uncertainties. Variations of the best-fit model suggest that main faults have only local effects on the stresses and that the Moho topography has only a negligible impact on the model results. A systematic drift of S_{hmin} magnitudes from leak-off tests against the stress model is obvious, but may be affected by multiple reasons.

The best-fit model applies for potential EGS reservoir horizontal wells, oriented northwest to southeast. A virtual well path or cross estimation of the full contemporary stress tensors can be provided by the model in advance of any drilling. The model has the potential to derive boundary conditions for local or reservoir models (e.g. Reiter et al. 2013), where petrological and tectonic inhomogeneities could be respected in more detail.

Acknowledgements

This study was conducted under the Helmholtz-Alberta Initiative (HAI), to which the first author is grateful for the financial support. We also want to thank the Alberta Geological Survey (AGS), in particular Kristine Haug, who allowed us to use the in situ stress database. We thank Douglas Schmitt, Inga Moek, Dietrich Stromeyer and Tobias Hergert for fruitful discussions about stresses in the Alberta Basin, the modelling approach and technical support. Furthermore, we thank Nathaniel Walsh for spelling and grammar correction. Maps were generated using GMT software (Wessel et al. 2013). The service charges for this open access publication have been covered by a Research Centre of the Helmholtz Association.

5 Stress field sensitivity analysis in a sedimentary sequence of the Alpine foreland, Northern Switzerland

Tobias Hergert[1], Oliver Heidbach[2], Karsten Reiter[2,3], Silvio B. Giger[4], Paul Marshall[4],

[1] Karlsruhe Institute of Technology, Institute of Applied Geosciences, Adenauerring 20b, 76131 Karlsruhe, Germany
[2] GFZ German Research Centre for Geosciences, Telegrafenberg, 14473 Potsdam, Germany
[3] University of Potsdam, Institute of Earth and Environmental Science, Karl-Liebknecht-Straße 24–25, 14476 Potsdam–Golm, Germany
[4] National Cooperative for the Disposal of Radioactive Waste (NAGRA), Hardstrasse 73, Postfach 280, 5430 Wettingen, Switzerland

Journal: Tectonophysics

Status: to be submitted in December 2014

Abstract

The stress field in the upper Earth's crust is an important parameter for the design of subsurface constructions and reservoir management. However, the distortion of the regional stress field due to local-scale features such as sedimentary and tectonic structures or topography is often poorly constrained. We conduct a stress sensitivity analysis using 3-D geomechanical–numerical modelling with an elasto-plastic material law to explore the impact of such site specific features on the stress field in a sedimentary sequence of the Alpine foreland. The stress model covers a volume of 14×14×3 km^3 and contains ten geomechanical units with different mechanical properties and two regional fault zones. The initial state of stress is established by introducing a semi-empirical relationship between the stress ratio and the overconsolidation ratio of argillaceous sediments. The results of the model indicate that local topography can significantly affect the stress field down to depths greater than the relief contrasts at the surface, especially in connection with horizontal tectonic loading. The complexity and frictional properties of faults are also relevant for the stresses. The greatest variability of the stress field is observed across the different geomechanical units of the sedimentary rocks. Stress magnitudes and stress anisotropies are much larger in stiffer formations such as massive limestone than in the softer argillaceous formations. The more rigid formations support to carry the load of the far-field stresses and therefore the stress field in these formations is more sensitive to changes in the boundary conditions compared to the softer formations. This relative difference of stress magnitudes between stiffer and softer formations is broadly maintained with progressive loading towards the plastic limit. However, the differences are less pronounced and partly vanish with regards for the fracture potential. The stress field in argillaceous sediments within a stack of rock formations with strongly contrasting mechanical properties as in the Swiss Alpine foreland basin appears to be relatively insensitive to changes in the tectonic boundary conditions, and is largely controlled by the maximum stiffness contrast with respect to the load-bearing formations.

5.1 Introduction

Knowledge of the in situ stress in the subsurface and its local variability is of importance both, for research questions and for applications in industry (e.g. Fuchs and Müller 2001; Tingay et al. 2005b). In particular for geotechnical projects such as tunnelling, drilling or reservoir management, knowledge of the stress state is required prior to operations in order to plan a safe and sustainable underground operation (Moeck et al. 2009; Zoback 2010).

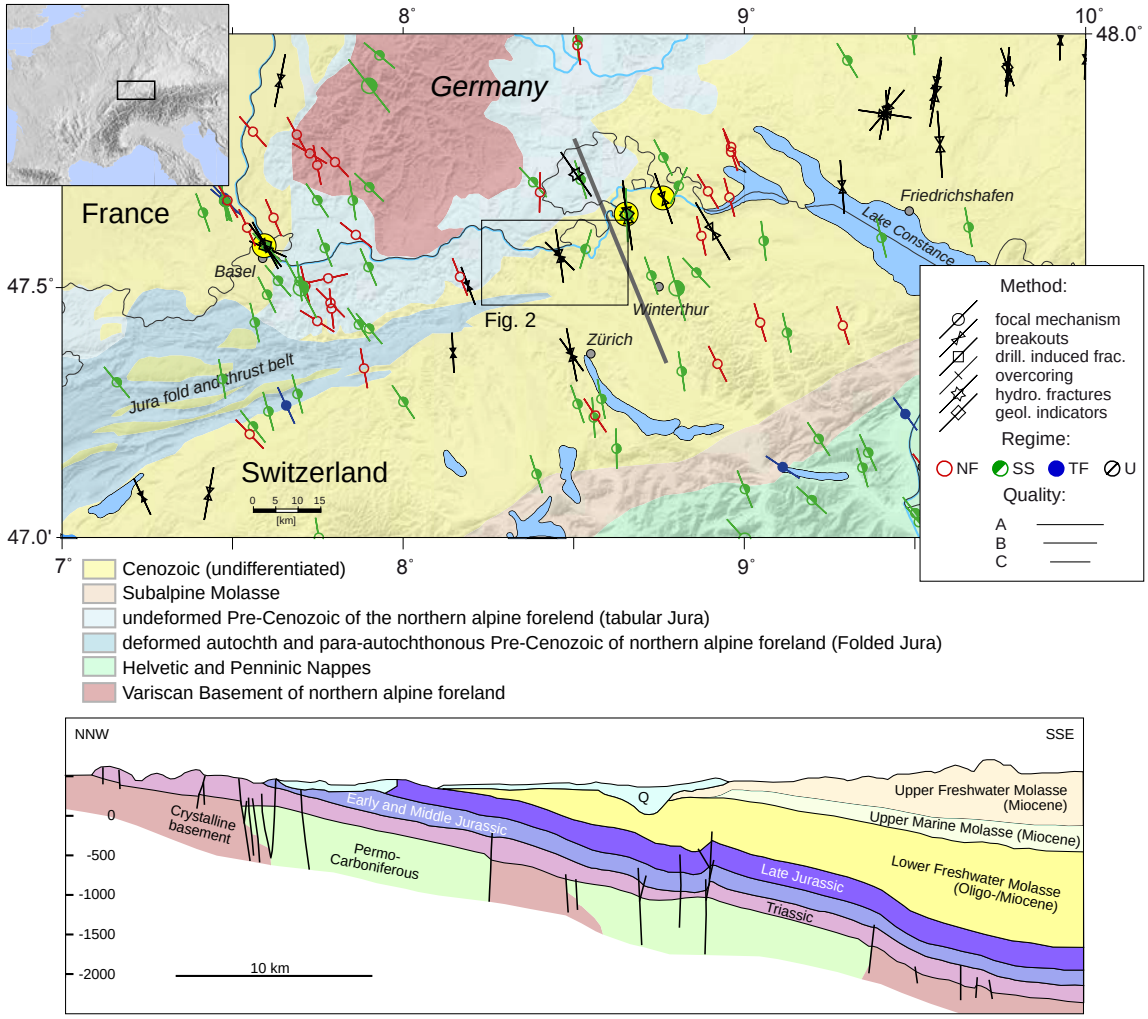

Figure 5.1: General geological setting of the model area in Northern Switzerland. **Top:** Main geological units and stress map with A–C quality data records of the revised WSM database release 2008 (Heidbach and Reinecker 2013; Heidbach et al. 2010). Bars indicate the orientation of maximum horizontal stress (S_{Hmax}), symbols in the legend show the stress indicator, and colours give the tectonic regime, with red for normal faulting (NF), green for strike-slip faulting (SS), blue for thrust faulting (TF), and black for an unknown regime (U). Yellow circles show the three locations where stress magnitude data are available (Basel, Benken, Schlattingen). Thick Black line show the location of the cross section below. **Bottom:** Generalized cross section through the main lithological units in the northern Alpine foreland (modified after Mazurek et al. (2006)).

The stress field in the Earth's crust can vary strongly on a local scale due to topography, faults and variable properties of rock formations. Savage and Morin (2002) showed that topography can cause a largely variable stress field up to polarity reversals of the principal stresses. Examples for stress perturbations due to faults have been compiled by Barton and Zoback (1994) and Yale (2003). Warpinski (1989) showed on the basis of a large number of hydraulic fracturing data that linear interpolation of stress magnitudes across different lithologies can result in erroneous estimates. Using a generic geomechanical–numerical model, Roche et al. (2013) showed that the influence of the mechanical properties of rock formations on the stress field can be significant.

Constraining the stress field at a local scale in Northern Switzerland is of particular interest for the evaluation of geological target area in the context of radioactive waste disposal (NAGRA 2008). The target area is characterized by moderate local topography (~300 to 400 m of difference in altitude). The proposed host rocks are Mesozoic argillaceous sediments, which alternate with Mesozoic clastics, marls, carbonates, and evaporates. For high-level radioactive waste, the lower Dogger Opalinus Clay is the suggested host rock. At the potential repository level, the absence of a regional fault zone is also required.

Information on the stress field is often very sparse and incomplete, especially at depths relevant for energy resources or subsurface construction works under challenging conditions (i.e. a few hundred meters to kilometres). Stress magnitude data for these depths are only available in exceptional cases. The orientation of the maximum horizontal stress (S_{Hmax}) and the stress regime may only be constrained at a few localities within the area of interest. Such data are systematically compiled from various stress indicators in the database of the World Stress Map project (Heidbach et al. 2010; Sperner et al. 2003; Zoback 1992).

The role of topography, faults and layered sedimentary formations on local stress variability can hardly be assessed based on available stress data alone. To investigate these effects on the in situ stress conditions at the scale of a geological target area, we perform a geomechanical–numerical sensitivity analysis based on semi-generic and simplified geological models. The study focuses on the variability of the stress state within the Opalinus Clay of the lower Dogger. The aim of this study is to explore the relative impact of parameter variations on the local stress field rather than a precise estimation of the absolute stress state.

5.2 Model setup

5.2.1 Tectonic setting and stress field of Northern Switzerland

In the northern Alpine foreland, the gently to the south dipping Mesozoic units below the Molasse sediments spread out on the surface in Northern Switzerland and overlays to the crystalline basement, exposed in the Black Forest (Fig. 5.1). Northward shift and shortening of these units resulted in the formation of the Jura fold-and-thrust belt. North of this belt, the North Swiss Permo-Carboniferous Trough strikes WNW-ESE buried below the Mesozoic units. Approximately above the northern and southern boundaries of the trough, compressional structures exist in the sedimentary cover with the Siglistorf Anticline (SA) in the north and the Stadel-Irchel Anticline (SIA) in the south (Fig. 5.2).

The stress map of Northern Switzerland (Fig. 5.1) shows 128 data records with a mean S_{Hmax} orientation of 160±20° (Heidbach and Reinecker 2013). The S_{Hmax} orientation rotates anticlockwise by ~40° from north-southerly oriented in the Lake Constance area to a northwest to southeast orientation in western Switzerland which is in agreement with the trend reported by Reinecker et al. (2010). The S_{Hmax} orientation pattern is rather uniform and perpendicular to the Alpine chain and to the isobaths of the Moho (Waldhauser et al. 2002). Fig. 5.1 also shows the location of the three boreholes Basel, Benken and Schlattingen, where minimum horizontal stress magnitude data (S_{hmin}) exist. However, measurements are only available for a few of the lithological horizons (NAGRA

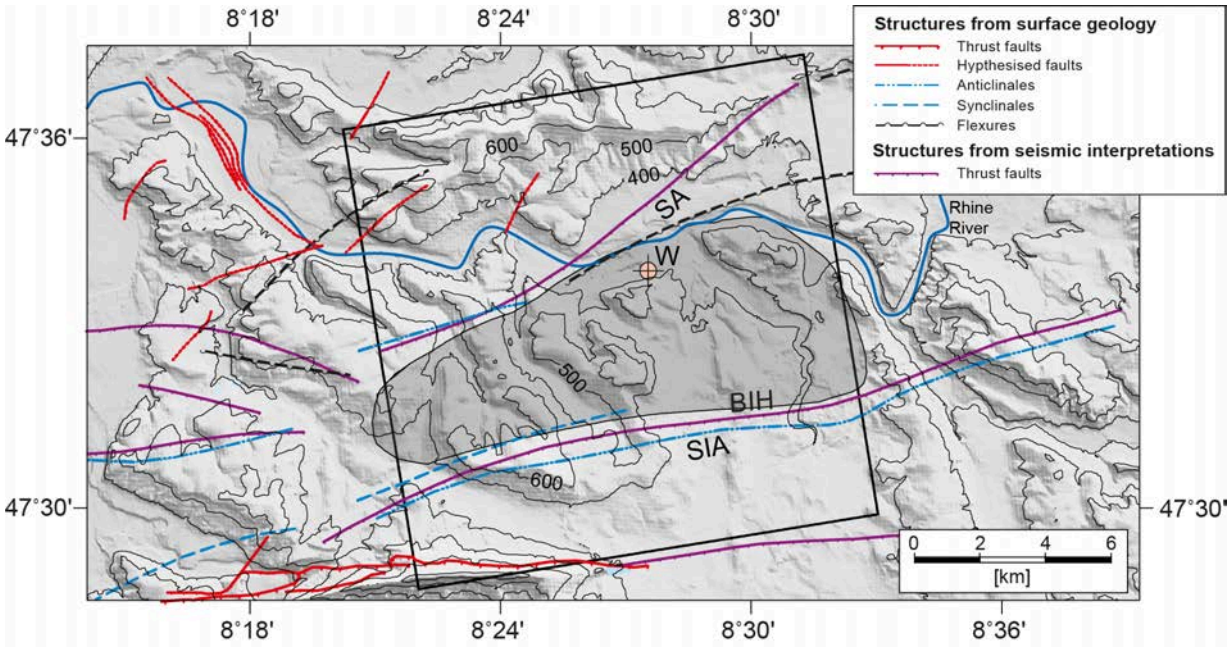

Figure 5.2: The black box indicates the location and extent of the model area ($14\times14\,km^2$). The Stadel-Irchel Anticline (SIA), the Baden-Ircher-Herden Lineament (BIH) and the Siglistorf Anticline (SA) cut through the whole model. Indicated are the Borehole Weiach (W, black square) and the target area Nördlich Lägern (grey shaded area) are indicated. Topography contours (thin black lines) are in meters above sea level. The variation of the elevation the model area is of ~300 m.

2001; Sikaneta and Evans 2012) and thus, the variability of the in situ stress caused by stiffness and strength contrasts, faults and topography is not well understood.

5.2.2 Location of the model area

The geological target area Nördlich Lägern (Fig. 5.2) was declared by the Swiss National Cooperative for the Disposal of Radioactive Waste (NAGRA) as a candidate site for a repository (NAGRA 2008). The model which investigates the target area covers an area of $14\times14\,km^2$ and is situated approximately 20 km north of Zürich (Fig. 5.1). Mesozoic formations gently dip to the south-east. In combination with local topography variations of more than 300 m (Fig. 5.2), this leads to variable burial depths for Mesozoic sediments. The centre of the 100 to 120 m thick Opalinus Clay formation is between 500 and 860 m below ground level in the model area.

Miocene shortening in the model area was moderate and is estimated to a maximum of 200 m from balanced cross sections. The dominant compressive structures in the area which accommodated the north-south directed shortening are the SA and the SIA (Fig. 5.2). Horizontal shortening is much larger in the Jura fold-and-thrust belt, situated to the south-west of the model area (Fig. 5.1). The formation of the SIA appears to be closely related to the Baden-Irchel-Herdern lineament (BIH), a Pre-Cenozoic fault structure which is also considered to represent the southern boundary of the east-northeast to west-southwest striking Permo-Carboniferous trough system.

The Weiach borehole is located roughly in the centre of the model (Fig. 5.2) and the only direct source of stress information at greater depth. From analysis of borehole breakouts down to a depth of approximately 2500 m below ground level the S_{Hmax} was interpreted to strike ~172°(Heidbach and Reinecker 2013), which is in good agreement with the observations at nearby wells (Fig. 5.1 top). Over a much shorter interval limited to the Upper Dogger and Lower Malm units at the Weiach

borehole, the S_{Hmax} azimuth was found to deviate from the dominant value in the Mesozoic and Paleozoic formations with a strike of 134°. From earthquake focal mechanisms, the dominant stress regime in the larger area around the model appears to be strike-slip faulting (Fig. 5.1 top). The eastern and western model boundaries are oriented 350°(Fig. 5.2), which is approximately parallel to the dominant orientation of S_{Hmax} and approximately perpendicular to the east-northeast to west-southwest trending major fault structures.

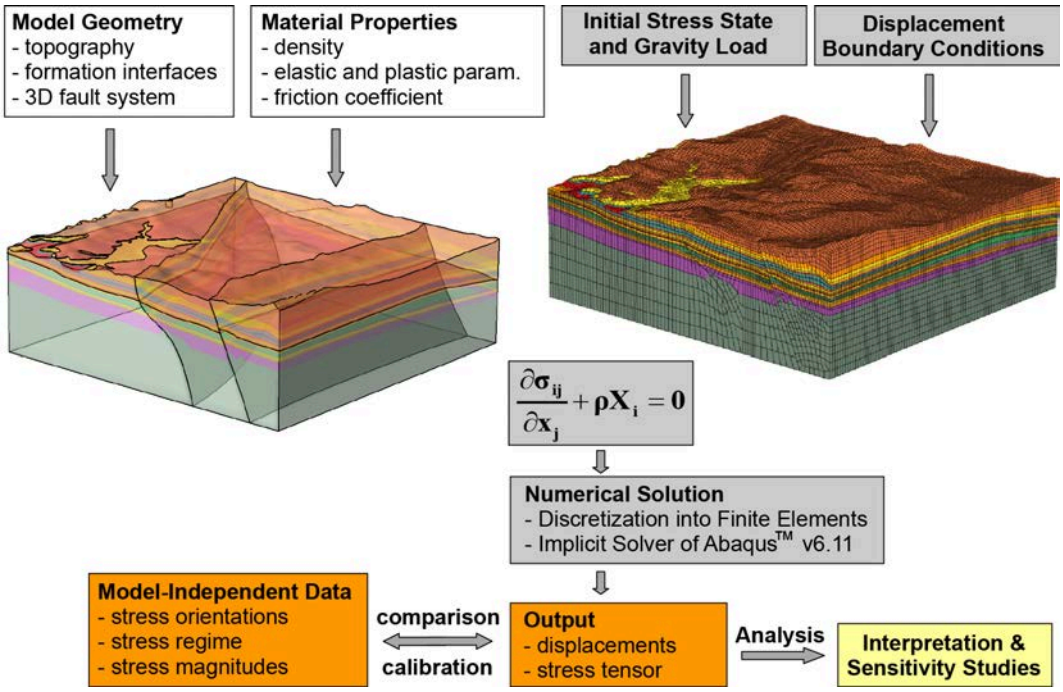

Figure 5.3: General modelling workflow. White boxes: Assembly of model geometry, rock properties and the 3-D fault system. Left figure: 3-D view of the model structure. Grey boxes: Gravity, initial stress field and displacement boundary conditions are determined and applied; numerical solution. Right figure: Discretised model volume. The partial differential equations of the equilibrium of forces in 3-D are solved using the finite element method (σ_{ij} stress tensor, x_j Cartesian coordinates, ρ density, and X_i body forces). Orange boxes: Model results are calibrated against model-independent data. Yellow box: Once the fit to the model-independent observations is acceptable the model results are interpreted and analysed. This should include a sensitivity analysis with respect to the uncertainties of the model parameters.

5.2.3 Model assumptions and workflow

Fig. 5.3 gives an overview of the model setup and workflow. The model includes structural information such as the geometry of faults and lithological units. Ten individual rock formations are considered in the model, these are characterized by their respective rock properties (density, elastic and plastic parameters; Tab. 5.1). Each geomechanical formation (Tab. 5.1) is considered as homogeneous with isotropic mechanical properties. Fault behaviour is controlled by the coefficient of friction. An initial stress state representing a reference stress state is established using semi-empirical relationships between the vertical to horizontal stress ratio and the overconsolidation ratio (OCR - Jáky 1944; Brooker and Ireland 1965; Mayne and Kulhawy 1982) of argillaceous sediments, namely for the Opalinus Clay (section 5.2.5). Displacement boundary conditions introduce tectonic stresses

from the far field and control deformation and stress in the model's interior in addition to the gravitational forces. The equilibrium of forces is computed numerically using the finite element solver Simulia/Abaqus®. The basic output of the model is the 3-D displacement and stress field, which has to be compared to model-independent data.

5.2.4 Model geometry and rock properties

The geological model used as a basis for the stress model is generated from field mapping, shallow and deep boreholes and depth-converted 2D seismic sections in Northern Switzerland (NAGRA 2008). The lithostratigraphic formations of the geological model are grouped into ten model units with different geomechanical properties (Tab. 5.1). Criteria to group lithological units into geomechanical units are sufficiently large thickness for numerical feasibility, and sufficiently large contrast of the mechanical properties to adjacent lithostratigraphic formations. Thick Permo-Carboniferous sediments (~1000 m) was encountered at the Weiach borehole in excess of 1000 m (cf. Fig. 5.2). The geometry of the Permo-Carboniferous Trough is not well constrained, because of poor seismic reflectivity below the Mesozoic sediments. Therefore, no distinction is made between Permo-Carboniferous sediments and the crystalline basement. Complex fault structures as interpreted in geological cross sections are strongly simplified when used in 3-D geological model. They are further simplified for the finite element model of this study due to uncertainties in the structural information and resolvable mesh size. The northern boundary fault of the SA in the north of the model area and the SIA in the south are incorporated as the two major, east-west striking features. The northern boundary fault of the SA is generally interpreted to root in the evaporates of the Middle Muschelkalk, which acts as a décollement for the detached Mesozoic sediments (Laubscher 1992). However, a direct relationship to the Permo-Carboniferous horst-and-graben structure cannot be excluded. Therefore, the SA is implemented as a basement fault in the finite element model (Fig. 5.4). To investigate the effect of a more complex fault structure on the local stress field, an antithetic back-thrust (model BT) to the SA, dipping 50° to the north, is also implemented and investigated by model GR (Tab. 5.2). It is assumed that this subsidiary fault strikes parallel to SA and roots at the Keuper-Gipskeuper interface (Fig. 5.4).

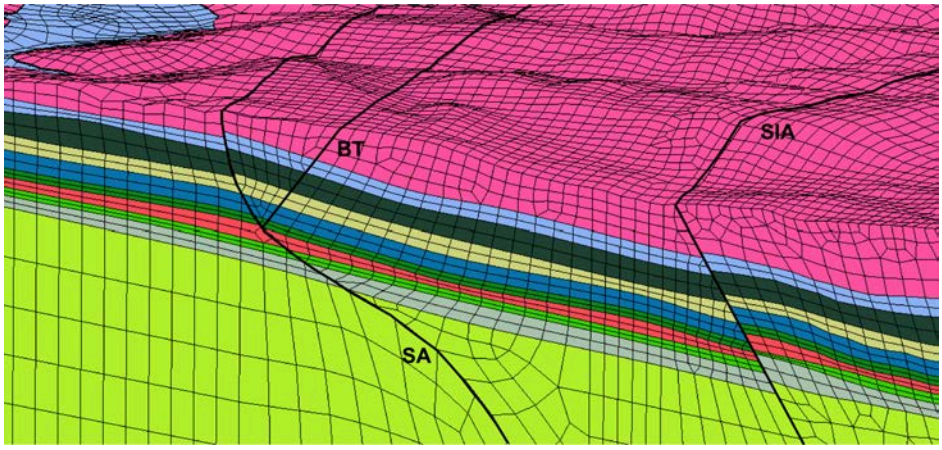

Figure 5.4: Discretised model volume, view to north-east. Thick black lines indicate the Siglistorf Anticline (SA), the Stadel-Irchel Anticline (SIA) and a supposed back thrust (BT) that are implemented as contact surfaces with Coulomb friction. The individual formations are colour-coded, the basement is in green and the Cenozoic in purple, for stratigraphic details see Tab. 5.1.

The SIA consists of a number of compressive, mainly south-dipping fault structures and is geometrically related to the prominent Baden-Irchel-Herdern Lineament, a mainly north-dipping Permo-Carboniferous trough boundary fault. For the stress model, this complex structure is highly simplified as a single south-dipping fault with a net reverse faulting offset (Fig. 5.4). Both the SA and the SIA faults are extended to the base of the stress model (2.5 km depth). In a case study, the basement-parts of the two faults are effectively eliminated by assigning a very high coefficient of friction ($\mu' = 100$) to those parts of the faults (model GB).

The geomechanical model units are characterised by their mechanical rock properties. Representative values for density ρ and elasto-plastic parameters (Young's Modulus E, Poisson's ratio ν, friction angle φ and cohesion C) are assigned to each of the units (Tab. 5.1). A homogeneous model (model EO, Tab. 5.2), where the elastic material properties are the same for all units, is tested in order to assess the influence of topography and faults in absence of the stress perturbations arising from variable rock properties. The effective coefficient of friction at the faults is assumed to be ($\mu' = 0.2$). This low value even it represents a case in which the stress perturbing influence of the faults is maximised and the blocks are widely decoupled from each other. Additionally, a coefficient of friction of $\mu' = 1.0$ is tested to consider the case of strong coupling of the blocks.

The model volume is discretised into ~272 000 linear hexahedron elements. Each of the formations comprises at least two element layers. The spatial resolution (element size) is ~100 to 200 m in the horizontal and ~20 to 80 m in the vertical direction (Fig. 5.4).

Table 5.1: Lithological and geomechanical units along with their thickness and rock properties.

Lithostratigraphy		Thickness at Weiach [m]	Model unit	ρ [g/cm^3]	E [GPa]	ν [ ]	φ [°]	C [MPa]
Cenozoic	Quaternary	37	Quaternary (11)	2.35	15	0.29	38	10
	OSM/OMM USM/Bohnerz Fm.	- 149	Molasse (10)	2.35	15	0.29	38	10
Malm	Felsenkalke to Villigen Fm.	202	Upper Malm (9)	2.68	40	0.25	50	20
	Wildegg-Fm. (incl. Effingen Member)	87	Wildegg Fm. (8)	2.65	15	0.29	40	8
Dogger	Wutach Fm. to Murchisonae Oolith Fm.	77	Upper Dogger (7)	2.55	15	0.27	30	8
	Opalinus Clay	112	Opalinus Clay (6)	2.50	10	0.29	23	4
Lias	Upper and Lower Lias Upper Mittelkeuper	64	Lias and Upper Mittelkeuper (5)	2.45	15	0.25	30	8
Keuper	Gipskeuper (incl. Lettenkohle)	83	Gipskeuper (4)	2.70	20	0.25	34	28
Muschel-kalk	Upper Muschelkalk	69	Upper Muschelkalk (3)	2.65	40	0.25	45	23
	Middle Muschelkalk	57	Middle and lower Muschelkalk (2)	2.65	20	0.25	40	20
	Lower Muschelkalk	37						
Buntsandstein		10						
Paleozoic	Permo-Carboniferous/ Pre-Mesozoic basement	>1490	Pre-Mesozoic Basement (1)	2.60	30	0.25	40	30

Table 5.2: Properties of the model variants with respect to the base model (BM)

Model	Rock property changes with respect to Tab. 5.1	friction coefficient of the faults $\mu^{'}$ [ ]	boundary conditions: compression [m] north-south	east-west
BM	-	0.2	9	-0.8
E0	$r = 2.6\,\mathrm{g/cm^3}$, $\nu = 0.26$, $E = 25\,\mathrm{GPa}$	0.2	0 and 9	0 and -0.8
E1	Upper Dogger: $E = 20\,\mathrm{GPa}$ Lias and Upper Keuper: $E = 20\,\mathrm{GPa}$	0.2	9	-0.8
E2	Upper Dogger: $E = 20\,\mathrm{GPa}$ Lias and Upper Keuper: $E = 10\,\mathrm{GPa}$	0.2	9	-0.8
E3	Upper Dogger: $E = 10\,\mathrm{GPa}$ Lias and Upper Keuper: $E = 20\,\mathrm{GPa}$	0.2	9	-0.8
E4	Upper Dogger: $E = 10\,\mathrm{GPa}$ Lias and Upper Keuper: $E = 10\,\mathrm{GPa}$	0.2	9	-0.8
G10	-	1	9	-0.8
GB	-	0.2 (sediments), 100 (basement)	9	-0.8
GR	-	0.2 (+ generic back thrust)	9	-0.8
P2	-	0.2	9 to 30	-0.8 to -3

5.2.5 Initial stress state, gravity and boundary conditions

5.2.5.1 Definition of initial stress

The initial stress state of the model considers no lateral tectonic loading and is in equilibrium with gravity forces. For normally consolidated clays or clay-rich soils, the horizontal to vertical effective stress ratio ($K^{'}$) is generally approximated by:

$$K^{'} = \frac{S^{'}_{hmin}}{S^{'}_{V}} \approx 1 - sin\varphi, \tag{5.1}$$

as introduced by Jáky (1944), where S_V is the vertical stress and φ is the effective friction angle. Empirical correlations have shown that the $K^{'}$ ratio of overconsolidated clays or shales during unloading (e.g. exhumation) is elevated with respect to values at identical depth during initial or normal loading (e.g. Brooker and Ireland 1965). Mayne and Kulhawy (1982) suggested to extend the stress ratio relationship of normally consolidated clays to overconsolidated clays or shales by taking the overconsolidation ratio (OCR) into account, that the effective stress ratio $K^{'}$ becomes:

$$K^{'} = (1 - sin\varphi) \cdot OCR^{sin\varphi}, \tag{5.2}$$

where the OCR is the ratio of the maximum effective overburden stress experienced during its geologic history ($S^{'}_{VC}$) and the present effective overburden stress ($S^{'}_{V}$). $S^{'}_{VC}$ can be estimated e.g. by one-dimensional compression tests. Applying Eq. (5.2) to the Opalinus Clay by using $\varphi = 25°$ and OCR values from three locations in Northern Switzerland, the depth-dependent effective stress ratio $K^{'}$ may then be approximated as:

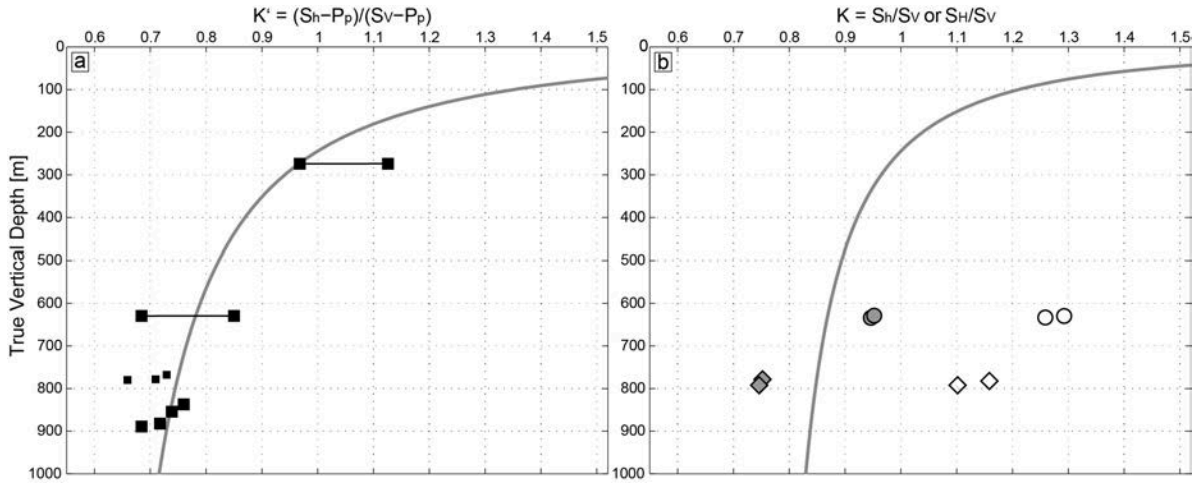

Figure 5.5: Depth-dependent stress ratio in Opalinus Clay in Northern Switzerland. **(a)** Effective stress ratio $K^{'}$ without tectonic loading. Black line shows calculated $K^{'}$ ratio for Opalinus Clay based on Eq. (5.3) with overconsolidation ratios from the underground lab Mont Terri (present depth ~280 m, OCR ≈ 4), and the boreholes Benken (~630 m, OCR ≈ 2) and Schlattingen (~900 m, OCR ≈ 1.7) (large black squares) and with $\varphi = 25°$. The small black squares represent data from Upper Dogger samples from Schlattingen with comparable clay mineral content as the Opalinus Clay. **(b)** Calculated total stress ratio K based on Eq. (5.5), which is used to calibrate the initial stress state for the Opalinus Clay in the model. Symbols are hydraulic fracturing data and represents the in situ stress state including tectonic loading (diamonds = Schlattingen (Klee 2012), circle = Benken (NAGRA 2001); filled symbols = S_{hmin}/S_V, open symbols = S_{Hmax}/S_V).

$$K^{'} = 0.58 \cdot \left(1 + \frac{650}{z}\right)^{0.42}. \tag{5.3}$$

where z is the present depth in metres (Fig. 5.5a). Since the numerical modelling of this study is looks at total stresses, the effective stress ratio $K^{'}$ has to be converted into the total stress ratio K:

$$K = \frac{K^{'}(S_V - P_P) + P_P}{S_V} \tag{5.4}$$

Assuming hydrostatic pore fluid pressure (P_P) and a constant density of $\rho = 2.5\, g/cm^3$, Eq. (5.4) simplifies to:

$$K = 0.6 \cdot K^{'} + 0.4 \tag{5.5}$$

The resulting curve in Fig. 5.5 b represents the total stress ratio K for the calibration of the initial stress state in the Opalinus Clay. Hydraulic fracturing data indicates in situ stress, i.e. the stress state including tectonic loading. Both the S_{hmin} and derived S_{Hmax} magnitudes at the Benken site plot to the right of the grey curve (Fig. 5.5b), indicating that tectonic loading has led to horizontal stresses which are greater than expected by simple burial and unloading from the empirical relationship. Conversely, the S_{hmin} magnitude of hydraulic fracturing plots to the left of the grey line, indicating that tectonic unloading may have decreased the expected magnitude derived from empirical relationship. This is consistent with the tectonic setting as the borehole Schlattingen was drilled in the border zone of the Hegau-Bodensee Graben.

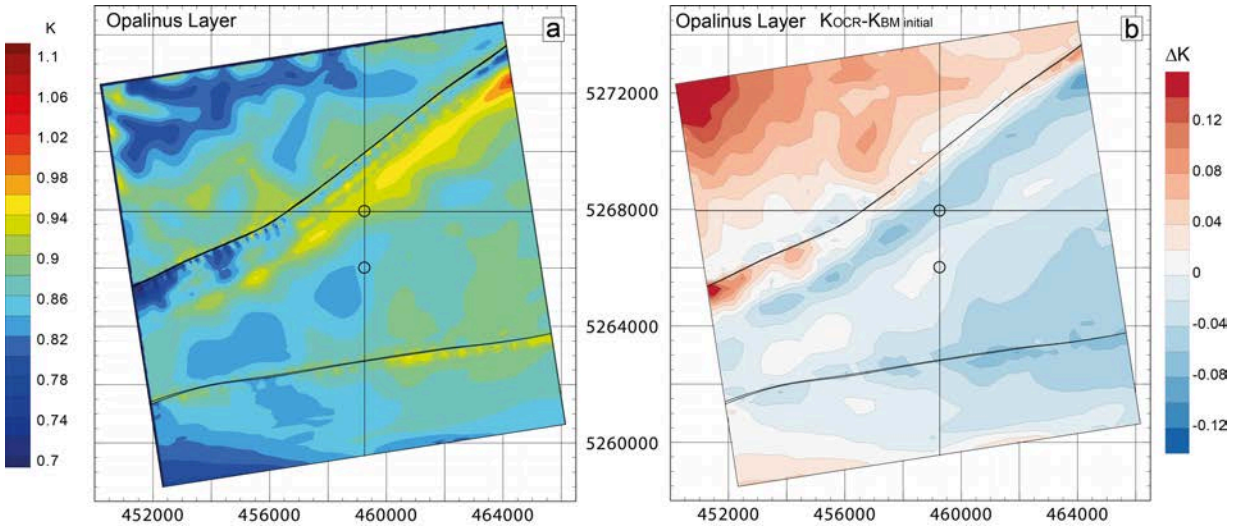

Figure 5.6: S_{hmin}/S_V ratios from initial stress field of the base model (BM) at the mean thickness of the Opalinus Clay formation. **(a)** Initial K-ratios at the middle of the Opalinus Clay formation in BM without tectonic loading. **(b)** Difference between the theoretical K-ratio from Eq. (5.5) and the initial stress state in the BM. Small circles indicate the location of the two depth profiles displayed in Fig. 5.8; the northern one is the location of the Weiach borehole.

5.2.5.2 Technical realisation of initial stress conditions

Technically, the initial state of the stress in the model is established by applying the force of gravity on the model volume and its boundaries at the bottom and at the sides fixed for displacement perpendicular to the model boundaries. During uniaxial compaction, the Poisson's ratio (ν) controls the horizontal stress and this mechanism is used to establish the stress state as defined in section 5.2.5.1. Values for the Young's modulus E are used as defined in Tab. 5.1. However, for the Poisson's ratio values are $\nu = 0.46$ for the argillaceous Opalinus Clay and Gipskeuper, $\nu = 0.43$ for the Pre-Mesozoic basement and $\nu = 0.40$ for all other formations are used. In an iterative approach the resulting stress state is used as an initial stress state in an undeformed model with the real Poisson's ratios applied as stated in Tab. 5.1 to allow for rebalancing displacements and to eventually obtain the initial stress state of the model that is in equilibrium with gravity.

It is tested whether the obtained stress state agrees with the initial stress state to be matched. The modelled K-ratio at the level of the Opalinus Clay (Fig. 5.6a) and the difference between the modelled K-ratio and the theoretical K-ratio (Fig. 5.6b) from Eq. (5.5) in shown map view. The K-ratio in the Opalinus Clay shows relatively small spatial variation between values of 0.8 and 0.95 in most of the model area, except for regions near the model boundaries, right to the south of the SA and in the north, where the Opalinus Clay comes close to the surface. The deviations of the modelled and theoretical K-ratio with respect to the values of Eq. (5.5) are small except in the north-west of the model area, where the Opalinus Clay is located between 150 to 250 m below the surface and thus strongly influenced by the prominent topographic gradient in that area (Fig. 5.2). To the south of the SA, the K-ratio is influenced by this fault and thus there is no undisturbed, purely gravity-controlled stress state. The modelled stress state fits the theoretical one in areas not influenced by faults or topography and is therefore taken as the initial stress state for the models.

The initial stress state of the model was also obtained for two vertical profiles (Fig. 5.7). The K-ratio increases when approaching the surface. Over the depth range of the model, several jumps in K-ratio appear, which are due to the different Poisson's ratios used in the compaction step.

The argillaceous formations, which have high Poisson's ratios, show larger K-ratios than the other formations, which have lower Poisson's ratios. The two profiles were taken at the location of the Weiach borehole and 2 km south of it (Fig. 5.6). At the location of the Weiach borehole, the centre of the Opalinus Clay is encountered at ~600 m below ground level. At that depth, K should be 0.875, according to Eq. (5.5). However, this site is in the zone affected by the SA and therefore, no perfect match with the theoretical value that is expected. The other profile 2 km to the south, is located between the SA and the SIA and seems to be relatively unaffected by these faults. Here, the center of the Opalinus Clay is at ~800 m depth and K should be 0.845 after Eq. (5.5). At this site, good agreement is obtained between the modelled and theoretical K-ratio.

5.2.5.3 Final stress state and displacement boundary conditions

After the initial stress state is obtained and in equilibrium with gravity, displacement boundary conditions are applied at the lateral boundaries of the model to incorporate the tectonic stresses of the far-field. These boundary conditions cannot be derived from geodetic observations as their uncertainties are greater than displacement rates. Thus, in order to integrate the available knowledge of south-north compression in the cause of the Alpine orogenesis, the model is shortened in south-north direction and dilated in east-west direction. To calibrate the amount of displacement, we fit the model results to the observed S_{Hmax} orientation from borehole in Weiach (Heidbach and Reinecker 2013), to the overall transtensional tectonic stress regime in Northern Switzerland (Heidbach and Reinecker 2013) and to the measured stress ratio $K = S_{hmin}/S_V = 0.94$ from hydraulic fracturing in the Opalinus Clay from the wellbore Benken (NAGRA 2001). For the K-value, it is assumed that the stress magnitude at the level of the Opalinus Clay at the Benken borehole is a good proxy for the model area some 10 km to the south-west of this location.

The best-fit boundary conditions are applied in the base model (BM, see Tab 5.2): a displacement of 9 m to the north perpendicular to the model boundaries are used The boundaries in the west and east are pulled outward by 0.4 m each; the northern model boundary is fixed for displacements perpendicular to the boundary. Displacements parallel to the model boundaries are allowed everywhere. Displacements at the bottom of the model are not allowed in vertical direction while horizontal displacements are permitted. The surface of the model is not fixed and are allowed to move freely. Due to the slightly rotated boundaries of the model with respect to north-south and east-west, the direction of the exerted push is perpendicular to the compressive structures in the sedimentary cover. The detailed results of the model calibration for the basic model BM are presented in the next section.

5.2.5.4 Calibration results for the base model (BM)

The prevailing S_{Hmax} orientation of the initial stress field in model BM is 170–175° (Fig. 5.7 top left). In the vicinity of the SA, S_{Hmax} is slightly rotated anticlockwise to 165–170° with some very local rotations to ~140°. No depth dependence of the S_{Hmax} orientation is detectable. The modelled S_{Hmax} orientation agrees very well with the dominant data record from the Weiach borehole with a S_{Hmax} orientation of 172° between 560–2276 m drilled depth derived from 772 m borehole breakout length (Heidbach and Reinecker 2013). The lower-quality data record from the Weiach borehole with a S_{Hmax} orientation of 134° represents the depth section 408–558 m drilled depth, derived from 42 m borehole breakout length (a few in the Wildegg Formation (Lower Malm) and most of them in the Upper Dogger). This S_{Hmax} orientation is not represented in the model results.

The modelled tectonic regime of the final BM shows transpression to compression close to the surface, visualised in terms of the regime stress ratio (RSR) (Simpson 1997, Fig. 5.7 bottom). In the deeper sedimentary formations including the Opalinus Clay, a strike-slip regime prevails with a tendency towards transpression. For the 1999 $M = 3.1$ earthquake near Eglisau at the eastern

model boundary with a hypo-centre at 1000–2000 m depth, a strike-slip focal mechanism solution was reported (Deichmann et al. 2000). The stratification of the sedimentary pile is reflected by the tectonic regime with stiffer formations showing more compressive stress than softer formations. Below the sedimentary column, the tectonic regime develops gradually towards extension and reaches almost transtension near the bottom of the model.

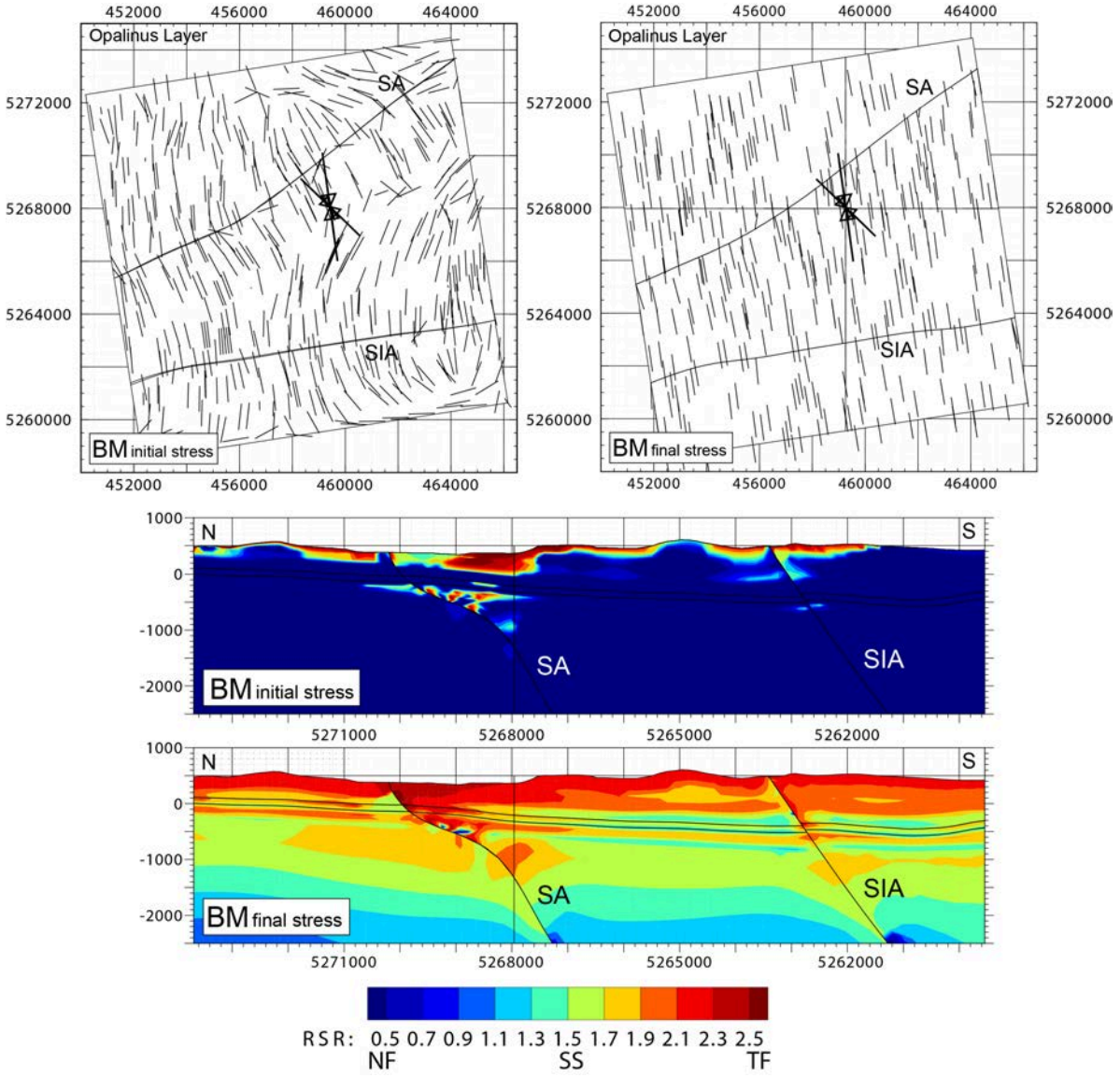

Figure 5.7: **Top:** S_{Hmax} orientation at the center of the Opalinus Clay layer for the initial stress field of model BM (left) and its final stress state (right). **Bottom:** The tectonic regime in terms of regime stress ratio (RSR) on a north-south cross sections through the Weiach borehole for the initial stress field of model BM and its final stress state are shown. The RSR provides a continuous range of the tectonic regime with NF=Normal Faulting, SS=Strike-Slip, TF=Thrust Faulting.

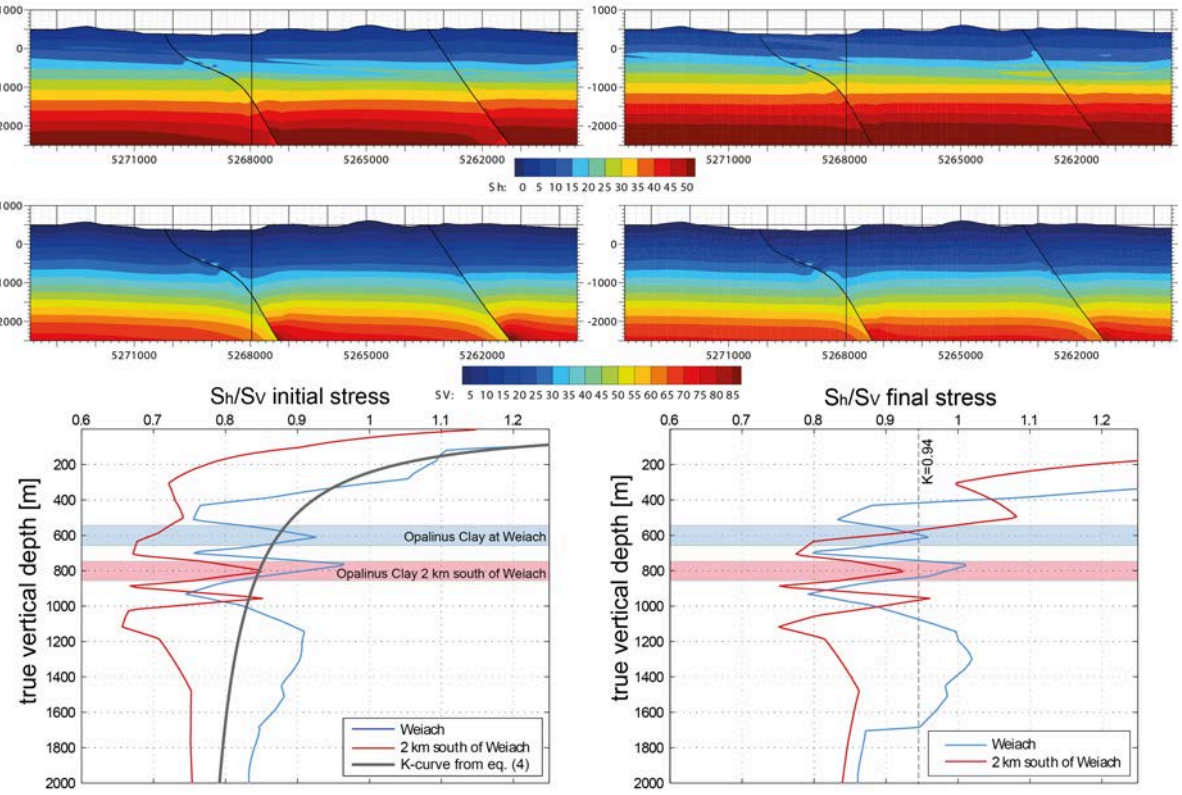

Figure 5.8: Stress values and ratios of the initial stress model (left) and the final stress model (right). **Top:** Magnitude of S_V and S_{hmin} on a north-south cross section through Weiach. **Bottom:** Depth profiles of S_{hmin}/S_V ratio from model BM at Weiach and 2 km south of it. Left: K-ratio of the initial stress field of the model BM. The grey line corresponds to the line in Fig. 5.5b. Right: K-ratios from model BM with tectonic boundary conditions applied. $K = 0.94$ is derived from hydraulic fracturing at Benken.

Fig. 5.8 top shows the magnitudes of S_V and S_{hmin} on a north-south cross section and the K-ratio at the two depth profiles at the Weiach borehole and 2000 m south of it. At Weiach at 600 m true vertical depth, $K \cong 0.95$ and $K \cong 0.934$ is at 800 m true vertical depth at the location 2000 m south of Weiach. The increase of the S_{hmin} magnitude value from the initial stress to the final stress, i.e. the one with displacement boundary conditions is larger than the increase of the S_V magnitude. Thus, the K-ratio is higher in the final stress model due to the lateral tectonic stresses imposed by the boundary conditions.

5.3 Results of the base model (BM)

5.3.1 Differential stresses

The competent formations Upper Malm and Upper Muschelkalk are characterised by high differential stresses $S_1 - S_3$ of up to 20 MPa compared to low values in the weaker formations, e.g. 4 to 7 MPa in the Opalinus Clay (Fig. 5.9). Similarly, the horizontal differential stress $S_{Hmax} - S_{hmin}$ is about 3 to 6 MPa in the Opalinus Clay. The vertical changes of the differential stress are therefore very pronounced (factor of about four), whereas differential stress is rather uniform within a formation (factor of about two at most), at least within the deeper formations (Fig. 5.9).

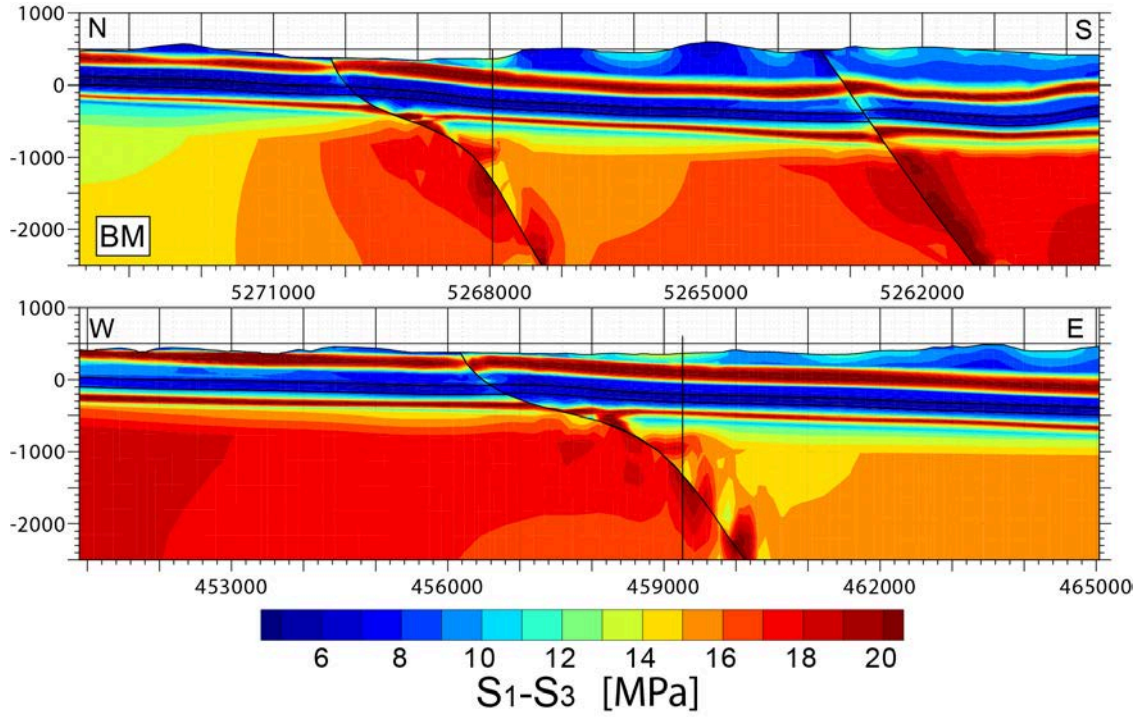

Figure 5.9: Differential stress $S_1 - S_3$ in north-south (top) and east-west (bottom) cross sections through the Weiach borehole. Thin black lines in the lower blue area indicate top and bottom of the Opalinus Clay.

5.3.2 Stress ratios

The ratio S_{Hmax}/S_{hmin} ranges between 1.2 and 1.4 in the Opalinus Clay, except in the north-west, where it is higher (Fig. 5.10 top). In the other formations S_{Hmax}/S_{hmin} is clearly higher than in the Opalinus Clay except for the Pre-Mesozoic basement. Furthermore, S_{Hmax}/S_{hmin} generally increases towards the surface. S_{Hmax}/S_{hmin} is higher in competent formations than in weak formations.

The ratio S_{Hmax}/S_V show very high values >2 in the uppermost Molasse formation but strongly decreases to 1.5 and less below the Upper Malm (Fig. 5.10 centre left). S_{Hmax}/S_V is about 1 at the base of the model and generally increases towards the surface. In the Opalinus Clay, S_{Hmax}/S_V ranges between about 1.1 and 1.3 in most of the model area, with an increase to >1.3 in a narrow stretch 1–2 km wide south of the SA and north of it (Fig. 5.10 centre right).

The ratio S_{hmin}/S_V varies between 0.8 and 1.1 in the Opalinus Clay and is slightly less than 1 in most of the model area (Fig. 5.10 bottom). S_{hmin}/S_V increases towards surface and than approaching the SA. However, differences in S_{Hmax}/S_V among the individual Mesozoic formations are smaller than for S_{Hmax}/S_{hmin} and S_{Hmax}/S_V. All stress ratios S_{Hmax}/S_{hmin} S_{Hmax}/S_V and S_{hmin}/S_V show reduced values within the Opalinus Clay compared to the stiffer formations above and below it (Fig. 5.10). Further, all stress ratios tend to increase beneath topographic depressions, e.g. below the Rhine valley.

5.4 Results of model variants

In this section, changing model parameters with respect to topography, rock properties, fault geometry and fault friction are presented. Most of the applied changes show only minor changes with respect to BM. Tab. 5.2 gives an overview of the model variants.

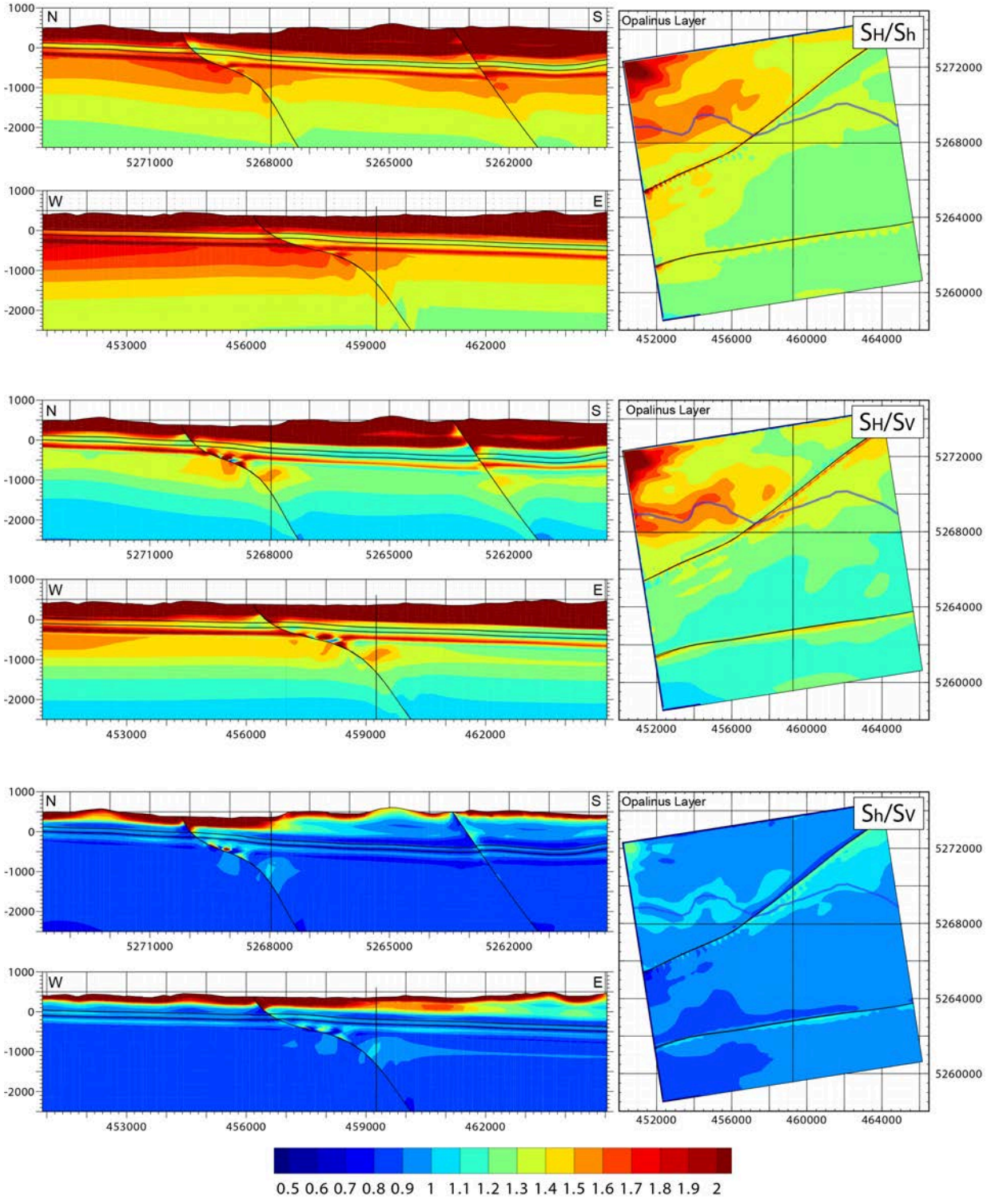

Figure 5.10: Base model (BM) stress ratios S_{Hmax}/S_{hmin} (top), S_{Hmax}/S_V (middle) and S_{hmin}/S_V (bottom) in north-south and east-west cross sections through the Weiach borehole (left) and at the centre of the Opalinus Clay formation (right). Colour scale is identical for all figures. Thin black lines indicate top and bottom of the Opalinus Clay. Blue line in the map views of the Opalinus Clay shows the river Rhine; thin lines denote location of the cross sections.

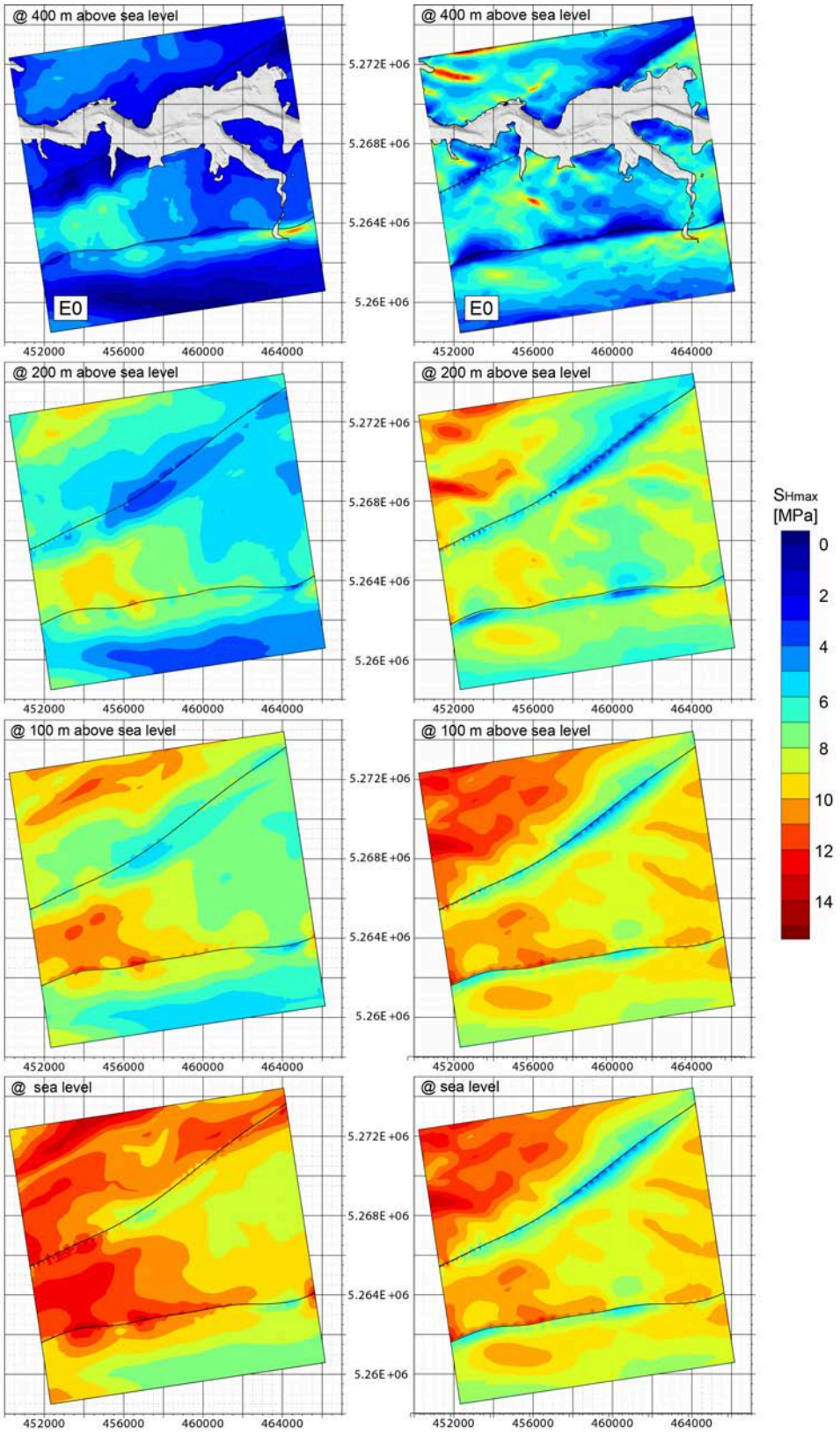

Figure 5.11: S_{Hmax} magnitude from the homogeneous model (E0) at different elevations. **Left:** without kinematic boundary conditions, i.e. without tectonic stress. **Right:** with kinematic boundary conditions.

5.4.1 Influence of topography

To investigate the influence of topography, a homogeneous model (E0, see Tab. 5.2) is designed. In such a model, the effect of topography on the stress state can be observed without the influence of the different rock properties of the individual formations. The pattern of the topography is hardly recognisable in initial S_{Hmax} magnitudes (i.e. without displacement boundary conditions) at levels of constant elevation (Fig. 5.11 left). Contrarily, the pattern of topography is clearly mimicked in S_{Hmax} magnitudes, once tectonic boundary conditions are applied in the model (Fig. 5.11 right). In this case, S_{Hmax} corresponds roughly to the north-south component of stress. Stress is increased below valleys, particularly below east-west elongated ones, while stress is reduced below mountains. The topographical influence on the stress state can be traced down to a depth of several hundred metres. High gradients of topography are expressed in the stress pattern. However, the effect of small wave-length gradients in the topography disappears at shallow depth, whereas elevation changes of greater lateral extent.

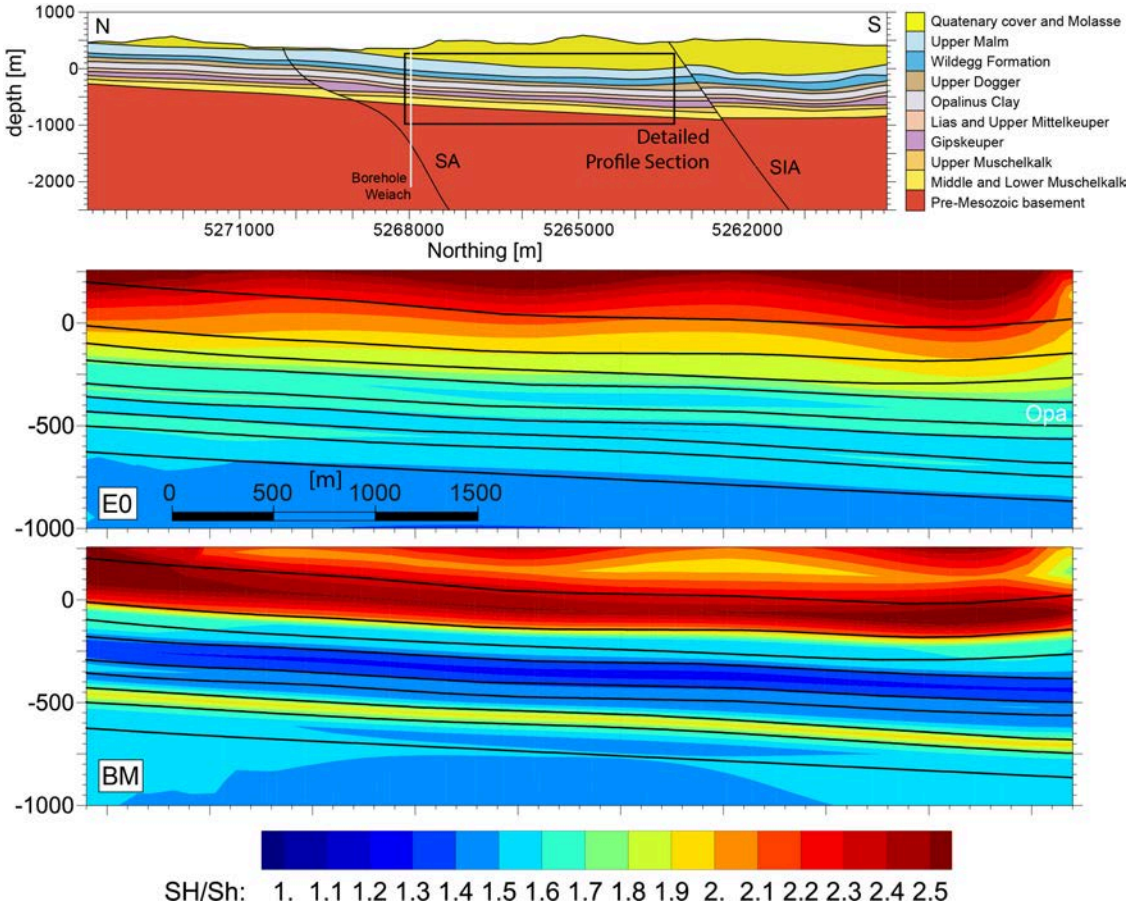

Figure 5.12: Detailed view of S_{Hmax}/S_{hmin} in north-south cross sections through the Weiach well for different Young's moduli. Geomechanical stratification for reference (top), homogeneous model (E0 – middle) and base model (BM – bottom) with rock properties as defined in Tabs. 5.1 and 5.2. Box in the upper figure shows location of the cross sections.

5.4.2 Influence of rock properties

Increased or decreased Young's moduli (models E1–E4, Tab. 5.2) of the Keuper and Upper Dogger formations below and above the Opalinus Clay , respectively, hardly affect S_{Hmax}/S_{hmin}, S_{Hmax}/S_V and S_{hmin}/S_V in the Opalinus Clay (Fig. 5.12 middle). Increasing the Young's modulus of the Keuper and Upper Dogger by 33% to 20 GPa results in slightly increased stress ratios in the Opalinus Clay, whereas a smaller Young's modulus of the Keuper and the Upper Dogger (33% less 10 GPa) results in slightly lower stress ratios in the Opalinus Clay. However, changes in stress ratios are always smaller than 0.1. Plastic rock behaviour does not result in any significant changes of stress ratios compared to an elastic model. This is because the strength of rock is not reached throughout most of the model volume. Plastic strain only occurs at some locations at the bottom or at the edges of the model, particularly, where the edges of the model are intersected by faults.

5.4.3 Influence of fault geometry and coefficient of friction

The model G10 has an increased effective coefficient of friction on the faults with $\mu' = 1.0$. The results (Fig. 5.13) show an overall increase of the ratios S_{Hmax}/S_{hmin} and S_{Hmax}/S_Vbut a decreased ratio of S_{hmin}/S_V in the Opalinus Clay. An exception is in the western and southern part of the block between SIA and SA, where S_{hmin}/S_V increases. Changes are mostly smaller than 0.1, and 0.2 south of the SA in the eastern half of the model. From about half a kilometre north of the SA to about 2 km south of the SA, S_{Hmax}/S_{hmin} increases by about 50% in the Upper Malm (S_{Hmax}/S_{hmin} up to 2.5) compared to the BM. The ratio S_{Hmax}/S_{hmin} increases slightly south of the SA, too.

In the model variant GB, the faults were deactivated below the Middle Muschelkalk in the basement by using a very high coefficient of friction ($\mu' = 100$), which means that faults essentially become locked. This reduces the stress ratios S_{Hmax}/S_{hmin}, S_{Hmax}/S_V and S_{hmin}/S_V within the Opalinus Clay in most of the model area, particularly immediately south of the fault (Fig. 5.13). However, changes with respect to the base model are smaller than 0.1. The stress ratios increase below the Opalinus Clay.

Incorporation of a back thrust adjacent to the SA (model GR in Fig. 5.13) reduces the stresses outside the wedge formed by the back thrust and the SA. The decrease of the stress ratios S_{Hmax}/S_{hmin}, S_{Hmax}/S_V and S_{hmin}/S_V within the Opalinus Clay compared to the base model occurs right beside the wedge. The decreased ratios are also found north of the wedge at the northern model boundary, however the decrease of stress ratios is <0.1 at greater distance from the wedge. The uplift of the wedge decrease stresses which lowers horizontal stress in the individual formations. In the Opalinus Clay the effect of the back thrust is smaller than at shallower depth because the wedge terminates just below the Opalinus Clay and becomes broader towards the surface. Particularly, the horizontal stress anisotropy is reduced by the back thrust in the Upper Malm south of the SA.

5.4.4 Plastic limit

In the previous model runs (e.g BM), the southern model boundary was displaced by 9 m to the north (perpendicular to the boundary) to account for the tectonic boundary conditions, i.e. to generate the desired horizontal in situ stress magnitudes. This rather moderate amount of shortening did not lead to failure in any of the geomechanical units. In this section, the effect of further north-south shortening (model P2) is assessed by starting with the model BM and sequentially adding up to 21 m of additional shortening (9–30 m in total) and allowing for additional extension both at the western and eastern model boundaries of up to 1.1 m (0.8–3 m in total). Assuming that the overall north-south shortening between the central Alps and the southern Black Forest north of the geological target area is 1 mm/a, the north-south shortening within the model area is approximately 0.1 mm/a. Thus 21 m of additional shortening may broadly represent a time span of ~210 000 years.

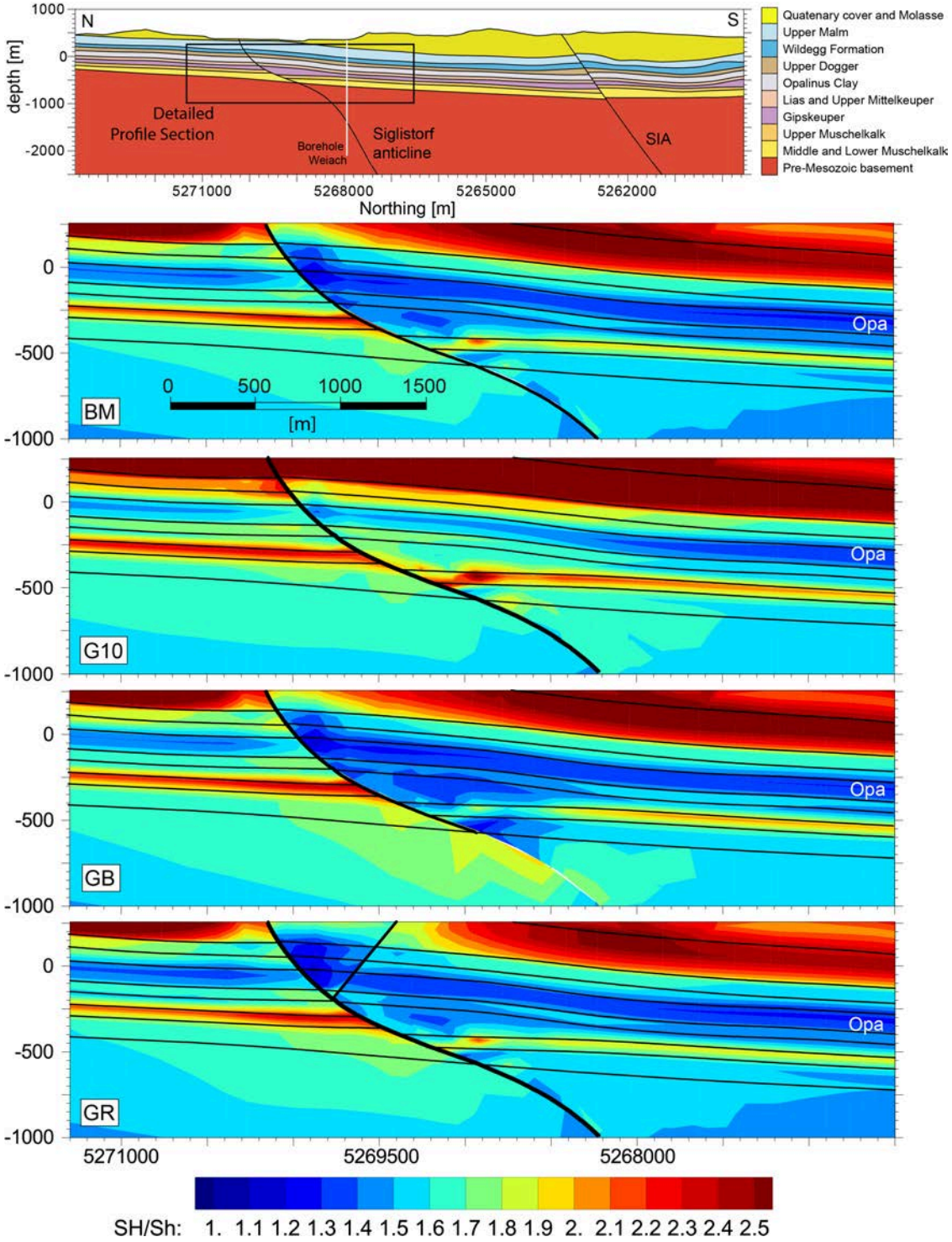

Figure 5.13: S_{Hmax}/S_{hmin} in north-south cross section through the Weiach well for different fault geometries. BM is the base model, G10 is the model with $\mu' = 1.0$, GB the model where the SA is inactive in the Pre-Mesozoic basement and GR the model with the generic back thrust, see Tab. 5.2. Box in the upper figure shows location of the cross sections.

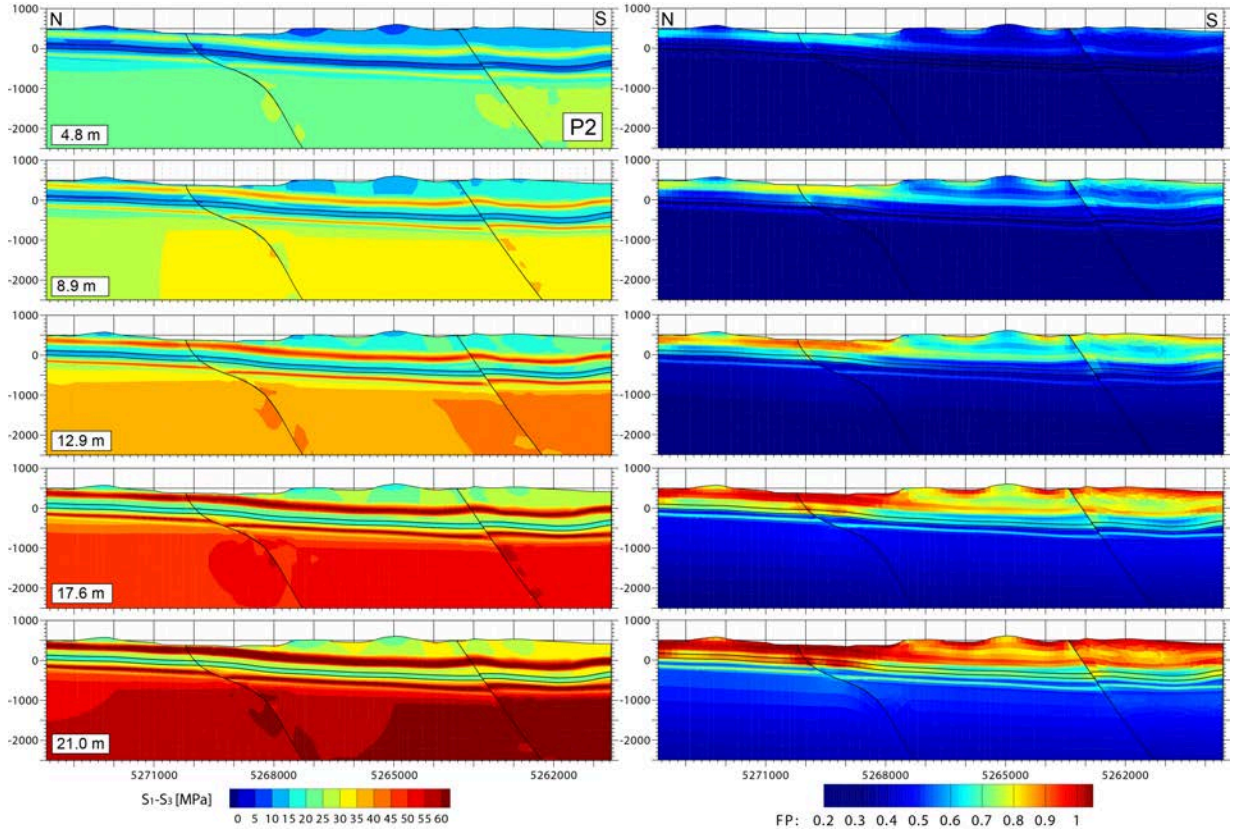

Figure 5.14: Further 21 m (9–30 m) of north-south push and 2.2 m (0.8–3 m) pull of the P2 model with respect to BM in consecutive steps displayed on north-south cross sections through borehole Weiach. Thin black lines indicate top and bottom of the Opalinus Clay. Left column shows the gradual increase of the differential stress; right column shows the increase of the Fracture Potential (FP), which is the normalised ratio of actual stress to the yield stress.

The evolution of the differential stress at different time steps (left column of Fig. 5.14) show that the stiff formations of the Upper Malm and the Upper Muschelkalk bear most of the differential stress accumulation. The maximum horizontal differential stress in the Opalinus Clay is <20 MPa whereas in the stiffer formations it is partly >60 MPa. In order to assess which formations will most likely undergo plastic deformation at additional shortening the fracture potential $FP = \sigma_d/\sigma_{dcrit}$ for each geomechanical unit is calculated. σ_d is the differential stress and σ_{dcrit} the critical differential stress at which the failure envelope is reached. The values of the friction angle and the cohesion are given in Tab. 5.1. Plastification starts when $FP = 1$. Results show that this plastic limit is only reached after approximately 15 m of additional shortening when FP reaches values close to or equal to one (right column of Fig. 5.14). The stiff formations that are close to the surface are most prone to failure. In the Opalinus Clay, FP values are below 0.8 except near the Siglistorf anticline where FP values are close to one at the final stage with 21 m of additional north-south shortening. The stiff Upper Muschelkalk below the Opalinus Clay has slightly lower FP values compared to the supposedly softer clay-rich units.

5.5 Discussion

5.5.1 Model results

5.5.1.1 Role of topography

The direct effect of the topography on the stress state due to the laterally varying weight acting on the subsurface and the associated increase of stress below mountains and decrease below valleys is visible in the results. However, topographic affects stress at most in an indirect way. The northward directed push induces stress that is determined by the shape of the surface. Stress increases below valleys and decreases below mountains, thus this induced stress is opposite to the stress that originates from the weight of the overburden (Fig. 5.11).

S_V is reduced below valleys due to the lower weight of the overburden. Below valleys, the horizontal stresses S_{Hmax} and S_{hmin} increases due to interaction between topography and far-field push (see section 5.4.1). In the north of the model area stress ratios are generally higher in the Opalinus Clay than in the south. This is because stress ratios generally increase towards the surface and the Opalinus Clay is found at shallower depth from south to north in the model. The vertical stress becomes zero at the surface, while the horizontal stresses S_{Hmax} and S_{hmin} do not.

5.5.1.2 Role of individual formations

Deformation in the model is roughly the same in the individual Mesozoic formations due to the uni-formly applied displacement at the southern model boundary over the whole depth extent of the model. Therefore, the stress regime (RSR) and the stress ratios S_{Hmax}/S_{hmin}, S_{Hmax}/S_V and S_{hmin}/S_V as well as the horizontal differential stress S_{Hmax}-S_{hmin} only depends on material properties and are higher in the competent formations than in the weak formations. This can be interpreted in a way that the northward directed push at the southern boundary is carried predominantly by the formations with high stiffness values. The stiff Upper Malm and Upper Muschelkalk formations embracing the clay bearing formations in between and shield those weaker formations, providing a stress shadow for them.

The stiffness of the Upper Dogger and Keuper formations located right above and below the Opalinus Clay affects stress ratios in the Opalinus Clay. With reduced stiffness of both, Upper Dogger and Keuper, the stress ratios within the Opalinus Clay are reduced with S_{Hmax}/S_{hmin} approaching 1.1. This is because the formations of reduced stiffness above and below accommodate deviation stress from the formations further above and below by deformation, thus reducing stress anisotropy in the Opalinus Clay. In turn, stiffer Upper Dogger and Keuper formations result in increased stress ratios in the Opalinus Clay. However, changes of S_{Hmax}/S_{hmin} among the different cases considered only account for up to 0.1 at most.

A uniform S_{Hmax} orientation for all formations indicates relatively high horizontal differential stress. This does not imply, that there is no stress decoupling in any of the formations, because the boundary conditions are uniformly applied over the whole depth extent of the model.

5.5.1.3 Role of faults on stress

The role of the semi-generic east-west striking SA and the SIA fault is revealed by comparing models with different coefficient of friction on the faults. The end-member case of infinite friction would indicate that a fault is absent because a faults' ability to slip at a given stress state is reduced at higher friction. The model with high friction of $\nu' = 1.0$ (G10) shows higher S_{Hmax}/S_{hmin} ratios in the Mesozoic sediments than BM ($\nu' = 0.2$), particularly in the uppermost 20 to 300 m up to 2 km south of the SA. This is an expression of higher horizontal stress anisotropy. Higher stress

ratios S_{Hmax}/S_V and differential stresses at higher fault friction indicate that the faults weaken the northward directed horizontal push within the sedimentary cover.

Several mechanisms can be identified for the weakening of the push and the associated reduction of horizontal stress anisotropy in the Mesozoic formations. (1.) The faults are reactivated by thrust faulting. The shortening as a result of thrust faulting reduces south-north directed compressional stress. (2.) The thrust faulting results in vertical offset of the Mesozoic formations at the faults. If a competent and a weak formation now come to lie at opposite sides of the fault, the efficiency of the south-north directed push is diminished because the push is governed by the competent formations. (3.) The faults are also laterally reactivated. The lateral reactivation of faults, with right-lateral slip on the SIA and left-lateral slip on the SA, results in an eastward directed extrusion of the block between the SA and the SIA, thereby also weakening the south-north directed push.

An important question is at what distance from the faults the state of stress can be assumed to be undisturbed by the faults. The role of the faults lowering the overall compression exerted by the push from the far field was outlined already. This effect is appreciable throughout the whole area of the model. In addition, there is a near field discernible in which stress is altered by the pressure of the faults. This near-field extends latterally to approximately 1–2 km from the faults in the models considered. Generally, the distance at which a fault affects stress in its surrounding depends on the coefficient of friction, on the total fault displacement and on the radius of bends and the curvature of the fault (Saucier et al. 1992; Yale 2003).

Stress concentrations, if present, predominantly occur nearby faults and are induced by fault geometry. The implemented generic back thrust (model GR) reduces horizontal stress anisotropy. However, the influence of the back thrust is very small at the depth of the host rock (Opalinus Clay) and increases towards the surface (Fig. 5.13).

5.5.1.4 Pushing the model into the plastic limit

The stiffer formations essentially carry the load of the far-field and therefore the stress field of these formations is more sensitive to changes in the boundary conditions then the stress field of the softer formations. This relative difference of stress distributions between stiffer and softer formations is broadly maintained with progressive loading towards the plastic limit. The increase of differential stresses in the stiff formation is higher compared to the softer argillaceous formations. However, in terms of FP, the differences are clearly less pronounced and for the deeper stiff formations even reverse (Fig. 5.14). Due to the high strength of the stiff formations, they are further away from failure with FP values in the range of 0.5 in the final stage of model P2. In contrast the Opalinus Clay has values of approximately 0.75.

The additional shortening of model P2 alters the tectonic regime to a compressional stress state where S_{Hmax} and S_{hmin} are larger than S_V. Plastic failure under a compressional tectonic regime would lead to the formation of a thrust fault. Thrust faults tend to propagate towards the surface where the normal stress decreases. Comparably low FP values in the Upper Muschelkalk, despite high differential stress makes the generation of a thrust fault propagating through the Opalinus Clay unlikely.

5.5.2 Discussion of assumptions

The presented model includes a number of assumptions and simplifications to maintain practicability and due to the lack of information about the subsurface. These assumptions and simplifications may pose limitations regarding the applicability and reliability of the model.

The simplifications concern the model boundaries and the conditions applied there. The model does not include the Jura main thrust. Therefore, the influence of the geometrical peculiarities of

this thrust altering the far field push, are not considered. Potentially existing Hercynian faults extending from the Black Forest down to below the Molasse Basin are neglected.

Below the Mesozoic sediments, it was assumed that there are uniform Permo-Carboniferous sediments down to the model boundary at 2500 m depth. Thus, the crystalline basement is not in the model, although in the Weiach borehole the contact between Permo-Carboniferous sediments and the crystalline basement was encountered at 2020 m depth. The boundaries of the Permo-Carboniferous Trough are not known precisely and it is possible that the thickness of the Permo-Carboniferous sediments varies strongly over the model area and may even be absent at some parts of the area.

The boundaries of the model are rather close to the target area. Therefore, boundary effects might affect the results. In particular, boundary conditions at the eastern and western model boundaries are difficult to define at the intersections of the faults with the model boundaries. As the SA and SIA are reactivated left- and right-laterally, respectively, the boundaries should be defined accordingly, allowing fault slip at the boundaries. However, once fault slip is defined at the boundaries, fault slip is no longer an independent result of the model and it is unclear what amount of slip should be imposed. In turn, if no boundary-perpendicular fault slip is allowed at the model boundaries, which is the case for the model presented, an artefact comes into the model: artificial east-west compression is generated at the eastern model boundary south of the SA and extension at the western model boundary south of the SA due to the left-lateral displacement at this fault.

The absence of data on stress magnitudes within the model area limits the reliability of the absolute stresses resulting from the model. The assumption made that the reference stress and the tectonic load are the same in Weiach as in Benken, where stress magnitude data are available, is to simple. While Benken is located above crystalline basement, Weiach is situated over Permo-Carboniferous sediments and an influence of the Permo-Carboniferous Trough is likely.

Model assumptions, chosen rock properties, interpreted fault geometries, remnant stress from the geological history, appropriate initial stress and boundary conditions are factors that are difficult to assess. The reliability of the model results may be increased if more detailed information on the fault geometries would be available, if the interface between the Permo-Carboniferous sediments and the crystalline basement would be better resolved, if details on the deformation occurring in the area would be known and most of all, if information on stress magnitudes were available in the target area "Nördlich Lägern".

5.6 Conclusion

A stress sensitivity analysis using geomechanical–numerical modelling was performed to assess the influence of topography, faults and the mechanical properties of a sedimentary sequence on the state of stress in the geological target area Nördlich Lägern, particularly in the Opalinus Clay. The effect of topography on the state of stress can be attributed predominantly to the interaction between the topography and the north-south shortening rather than to the gravitational effect of the topography alone. This results in increased S_{Hmax} magnitudes below topographic depressions and decreased values below mountains. These altered S_{Hmax}magnitudes are detected down to several hundred meters depth. East-west striking faults such as the SA, the SIA and a back-thrust adjacent to the SA reduce horizontal stresses which are exerted on the model area from the far-field. However, in the vicinity of these faults stresses increase. The stiff formations Upper Malm and Upper Muschelkalk take up the majority of tectonic stresses associated with the far-field push from the south, while differential stresses remain relatively small in the clay-rich formations. Stiff formations close to the surface are most prone to reach the plastic limit. Differential stress in the Opalinus Clay are below critical values except in the vicinity of the SA in a long-term scenario of persistent shortening.

Acknowledgement

This study was conducted under supported of the National Cooperative for the Disposal of Radioactive Waste (NAGRA). Maps were generated with the help of the GMT software (Wessel et al. 2013).

6 Mining-induced stress transfer and its relation to a M_w 1.9 seismic event in an ultra-deep South African gold mine

Moritz Ziegler[1,2], Karsten Reiter[1,2], Oliver Heidbach[1], Arno Zang[1,2], Grzegorz Kwiatek[1], Dietrich Stromeyer[1], Torsten Dahm[1,2], Georg Dresen[1,2], Gerhard Hofmann[3]

[1] GFZ German Research Centre for Geosciences, Telegrafenberg, 14473 Potsdam, Germany
[2] University of Potsdam, Inst. of Earth and Environmental Science, Karl-Liebknecht-Straße 24–25, 14476 Potsdam–Golm, Germany
[3] Anglogold Ashanti, 76 Jeppe Street, Newtown, Johannesburg, 2001, South Africa

Journal: Pure and Applied Geophysics

Status: Received 13 October 2014

Abstract

On 27 December 2007 a M_w 1.9 seismic event occurred in the deep level Mponeng gold mine, South Africa, within a dyke. From the network of the mine and the one from the JAGUARS group the hypocentral depth (3509 m), focal mechanism and aftershocks location was estimated. As no mining activity took place in the days before the event, dynamic triggering due to blasting can be ruled out as the cause. To investigate the hypothesis that stress transfer due to excavation of the gold reef induced the event, we set up a small scale ($450\times300\times310\,m^3$) high resolution 3D geomechanical-numerical model. The model consists of the four different rock units present in the mine: quartzite (footwall), hard lava (hanging wall), conglomerate (gold reef), and diorite (dykes). For the numerical solution we use the finite element method, with a discretised mesh of approximately 10^6 elements. The initial stress state of the model is in agreement with in situ data from a neighbouring mine and the step-wise excavation is simulated by mass removal in the gold reef. The resulting 3D stress tensor and its changes due to mining is analysed with the Coulomb failure stress changes on the fault plane of the event. The results show that the seismic event was induced regardless of how the Coulomb failure stress changes are calculated and of the uncertainties in the fault plane solution. We also use the model to assess the seismic hazard due to the excavation towards the dyke. The resulting curve of stress changes shows a significant increase in the last ~50 m in front of the dyke indicating that little changes in the mining progress towards the dyke have a substantial impact on the stress transfer.

6.1 Introduction

Seismicity in mining environments can cause large damages (McGarr 1971; Ortlepp 1992, 2001; Brady and Brown 2004; Orlecka-Sikora et al. 2012; Hasegawa et al. 1989; Pytel 2003). Especially in deep-level high-stress environments, such as the South African Gauteng mining district, seismicity induced by mining excavations is a high risk (Prinsloo 2011; Pretorius 1976; Gay and Ortlepp 1979; Hofmann et al. 2013). The vertical stress due to the overburden reaches values of 80–100 MPa (Lucier et al. 2009) which is equal to 800–1000 kg/cm^2. Furthermore, inhomogeneities like variable rock strength, paleo-surfaces, inherited fault zones or intrusions can act as promoter for violent failure of rocks (Pretorius 1976; Gay and Ortlepp 1979).

On 27 December 2007, an M_w 1.9 seismic event occurred in the ultra-deep levels of Mponeng tabular gold mine, Carletonville, South Africa (Yabe et al. 2009; Plenkers et al. 2010; Naoi et al. 2011; Kwiatek et al. 2010; Kwiatek and Ben-Zion 2013). The hypocentre and its aftershocks were

located within a dyke around a depth of 3509 m in direct proximity (<50 m) to access tunnels and recently mined-out areas of the gold bearing target horizon (Kwiatek et al. 2010; Naoi et al. 2011; Kwiatek and Ben-Zion 2013). As the seismic event occurred on the fifth day of the Christmas closure of the mine, the level of background noise due to excavation work was low, which allowed a precise detection and location of the aftershocks (Plenkers et al. 2010). Furthermore, dynamic triggering of the event by blasting activities can be ruled out and the event was most likely induced by stress transfer due to the excavation towards the dyke in the preceding months. Hofmann et al. (2012) investigated whether the event was induced by stress changes by means of a homogeneous elastic boundary element model. From their model they estimated the Excess Shear Stress (ESS), which is defined as the difference between normal stress multiplied with the internal friction coefficient and the absolute value of the shear stress prior to slip for a given fault orientation (Ryder 1988). Hofmann et al. (2012) estimated the plane which is optimally oriented in the stress field after excavation from a grid search and found that its orientation is similar to the rupture plane of the event estimated by Naoi et al. (2011) and the aftershock distribution. From these results they concluded that the event was induced by the excavation of the gold reef.

In this paper, we also investigate whether the event was induced by stress transfer, but instead of the EES value we use two variants of the change of Coulomb Failure Stress (ΔCFS) analysis to investigate in detail which component of the stress transfer is the potential key driver for the event. The ΔCFS is defined as the difference between the normal stress multiplied with the friction coefficient and the shear stress component in slip direction (rake) of the seismic event prior to slip for a given fault (e.g. King et al. 1994; Harris 1998; Stein 1999; Heidbach et al. 2007). In addition to this definition we also calculate the ΔCFS using the maximum shear stress and the ΔCFS values for both nodal planes of the fault plane solution. To simulate the stress changes we use a 3D geomechanical-numerical model that estimates the stress transfer due to step-wise mining excavations immediately before the occurrence of this seismic event. In extension to the model of Hofmann et al. (2012) the model area consists of the complex topology of the dyke and the different rock properties of the lithologies are considered.

Since dykes are known to be promoters for failure (Gay and Ortlepp 1979; McGarr et al. 1975), we also calculate in a forward approach the ΔCFS at the hypocentre of the event for the orientation of the rupture plane for the step-wise excavation towards the dyke. We also estimate the variability of the resulting ΔCFS values as a function of excavation distance to the dyke. By varying the orientation of the rupture plane we account for the uncertainties of the fault plane solution. The resulting function can serve as a first-order seismic hazard assessment.

6.2 Data

6.2.1 Geological Setting

The Mponeng gold mine represents a typical ultra-deep tabular mining environment (e.g. Hofmann et al. 2013; Plenkers et al. 2010; Roberts and Schweitzer 1999). It is located in the north-western part of the Witwatersrand Basin, South Africa (Fig. 6.1) at the centre of the Kaapvaal Craton, which is one of the world's largest gold mining districts (Coward et al. 1995). Mining activity at Mponeng reaches down to about 3900 m (AngloGold Ashanti Limited 2013) and is thus one of the deepest mines in the world.

Sedimentation in the Witwatersrand Basin started 3086 Ma ago onto 3120 Ma old basement granites and gneiss (Robb et al. 1992; Armstrong et al. 1991). Over a period of about 1000 Ma, the Witwatersrand-, the Ventersdorp- and the Transvaal Supergroup were deposited (Tab. 6.1)(Coward et al. 1995; Frimmel and Minter 2002). The meta-sediments of the Mandeor Formation form the footwall. They are argillaceous to siliceous quartzites and conglomerates (Roberts and Schweitzer 1999) as well as shale (Jolley et al. 2004). In the research area the Mandeor Formation consists

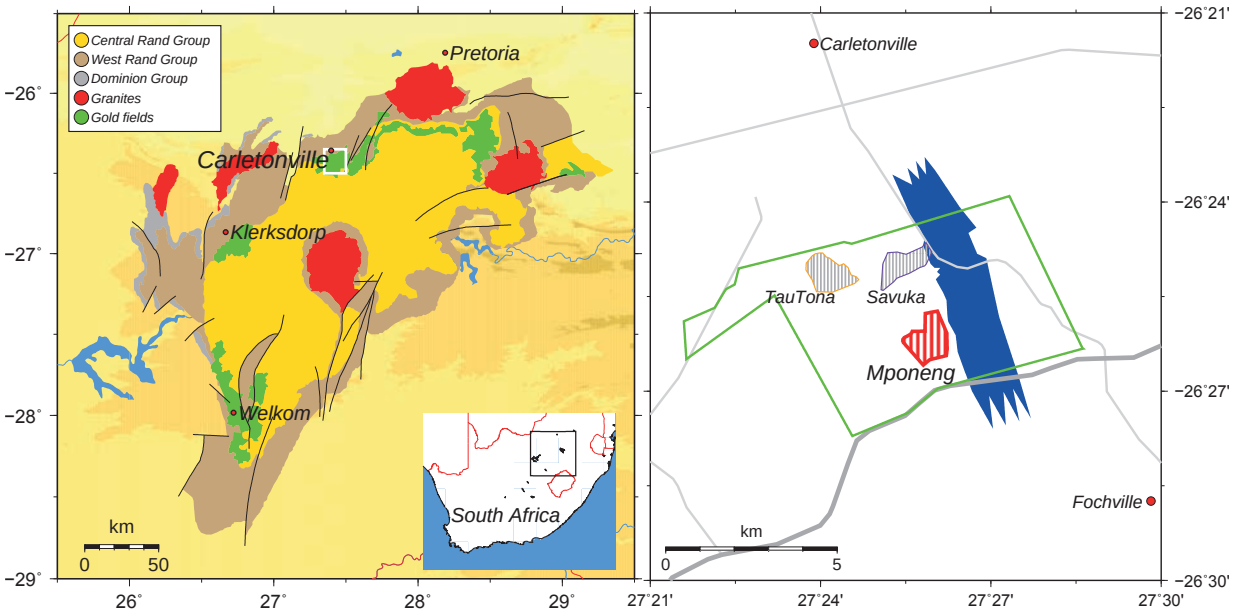

Figure 6.1: Left: The Witwatersrand Basin and its geological units. The white box indicates the location of the right map section. Right: The mining area around Carletonville. The borders of Anglogold Ashanti's claim (green), known occurrence of Booysens shale of the Mandeor Formation (blue), major roads (grey), and the surface operations of the three mines.

of quartzite. The top of Mandeor Formation is a paleosurface, which has locally meter-scale slope-terrace relief (Jolley et al. 2004). These areas (so called rolls) are frequently subject to violent deformation and fatal mining accidents (Roberts and Schweitzer 1999). The target horizon of the gold exploitation in Mponeng mine is the lowest unit of the Ventersdorp Supergroup, the conglomerate Ventersdorp Contact Reef (VCR)(AngloGold Ashanti Limited 2013). It is made of 1–2 m alluvial coarse conglomerates and quartzites, which lie unconformable above the Mandeor Formation (as a part of the Central Rand Group)(Roberts and Schweitzer 1999). The reef is internally structured in complex terraces and fluvial channels (Frimmel and Minter 2002; Jolley et al. 2004) and it dips with ~22° to the SSE (e.g. Hofmann et al. 2013; Plenkers et al. 2010. The enrichment of the gold took place during fluvial transport and eolian upgrading (deflation) as well as due to post-sedimentary hydrothermal displacement (Frimmel and Minter 2002). Large mafic to komatiitic flood basalts with mantle origin (Alberton metabasalts/hard lava) were deposited above the VCR with thicknesses of up to 2000 m (Van der Westhuizen et al. 1991). After the deposition of the Transvaal Supergroup, two events overprinted the region. First, the Bushveld Igneous Complex which is related to thermal metamorphism due to mafic underplating of lower crust and second the Vredefort impact event, which lead to the formation of the Vredeford Dome (Coward et al. 1995; Frimmel and Minter 2002). Both are believed to be responsible for hydrothermal alteration (e.g. gold enrichment within the reef) and many intrusions (e.g. the Pink-Green and Great-Green Dyke) in Witwatersrand Basin (Coward et al. 1995; Frimmel and Minter 2002).

Fault ramps are restricted to the footwall, forming fault-bend folds and imbricated zones close to the VCR and detach the footwall from the hanging wall below or within the VCR (Jolley et al. 2004). This is mainly observed in the eastern part of the mine, where Booysens Shale (Fig. 6.1) underlies the reef (Jolley et al. 2004), hence not in the model area. Highest gold contents are observed along such imbrications and associated with transfer faults, which have Klipriviersberg ages (Jolley et al. 2004). Two subvertical intrusions, the mafic Pink Green and Great Green dyke,

Table 6.1: Stratigraphic table of the units and area of interest for the model of the Mponeng gold mine in Witwatersrand Basin, South Africa.

Supergroup	Group	Formation	age [Ma]	Relevance for the model
Vredefort impact			2023[a]	Peak metamorphism & hydrothermal alteration of VCR, dyke intrusion?
Bushveld Igneous Complex			2054[b]	
Transvaal			2250[a] 2642[c]	
Ventersdorp	Pniel Sequence Platberg		2709[d]	
	Klipriviersberg	Alberton Venterpost	2714[d] 2714[e]	hard lava (hanging wall) Ventersdorp Contact reef (VCR)
Witwatersrand	Central Rand	Mandeor	2837[a]	quartzite (footwall)
			<2894[f]	
	West Rand		2914[d] <2970[a]	
	Dominion		3074[d] 3086[g]	
Basement			3120[d]	

[a]Frimmel and Minter (2002), [b]Scoates and Friedman (2008), [c]Eriksson et al. (1995), [d]Armstrong et al. (1991),[e]Hall et al. (1997), [f]Poujol et al. (1999), [g]Robb et al. (1992)

cross the research area in NNW and NNE direction (Kwiatek et al. 2010). They probably intruded in post Transvaal time (Pretorius 1976). The hypocentre of the M_w 1.9 seismic event is located within the Pink-Green dyke (Fig. 6.2)(Yabe et al. 2009; Plenkers et al. 2010; Kwiatek and Ben-Zion 2013; Hofmann et al. 2012, 2013).

6.2.2 The M_w 1.9 seismic event

On 27 December 2007 an M_w 1.9 seismic event occurred in the deep level of Mponeng gold mine at ~3509 m during the mine's Christmas holidays (Plenkers et al. 2010; Naoi et al. 2011; Kwiatek and Ben-Zion 2013). The Christmas closure of the mine results in a low level of background noise (no blasting or movement of heavy equipment). These circumstances rule out dynamic triggering and allowed undisturbed recording of the aftershock sequence which proved to contain valuable information (Kwiatek et al. 2010; Plenkers et al. 2010).

For the estimation of the focal mechanism solution only 9 out of 27 stations from the mine's seismological network could be used due to wrong polarity of the seismometer's channels and maintenance issues (Naoi et al. 2011). The focal mechanism solution displayed in Fig. 6.2 shows as expected a normal faulting regime with the two nodal planes N1: 125|46|-129 (strike|dip|rake) and N2: 348|56|-59 (Naoi et al. 2011; Kwiatek and Ben-Zion 2013). The aftershocks of the main event were recorded in a distance of ~30 m to the hypocentre by the high frequency acoustic emission sensor JAGUARS-network (Japanese-German Underground Acoustic Emission Research in South Africa)(Naoi et al. 2008; Nakatani et al. 2008; Plenkers et al. 2010). This network registered more than 20 000 aftershocks with magnitudes down to -4.4 (Fig. 6.2)(Kwiatek et al. 2010; Plenkers et al. 2010; Naoi et al. 2011). The distribution of aftershocks presented in Fig. 6.3 indicates that the nodal plane N2 (348|56|-59) is the rupture plane (Naoi et al. 2011; Kwiatek and Ben-Zion 2013). Furthermore, the normal faulting mechanism of the event is in agreement with the in situ stress

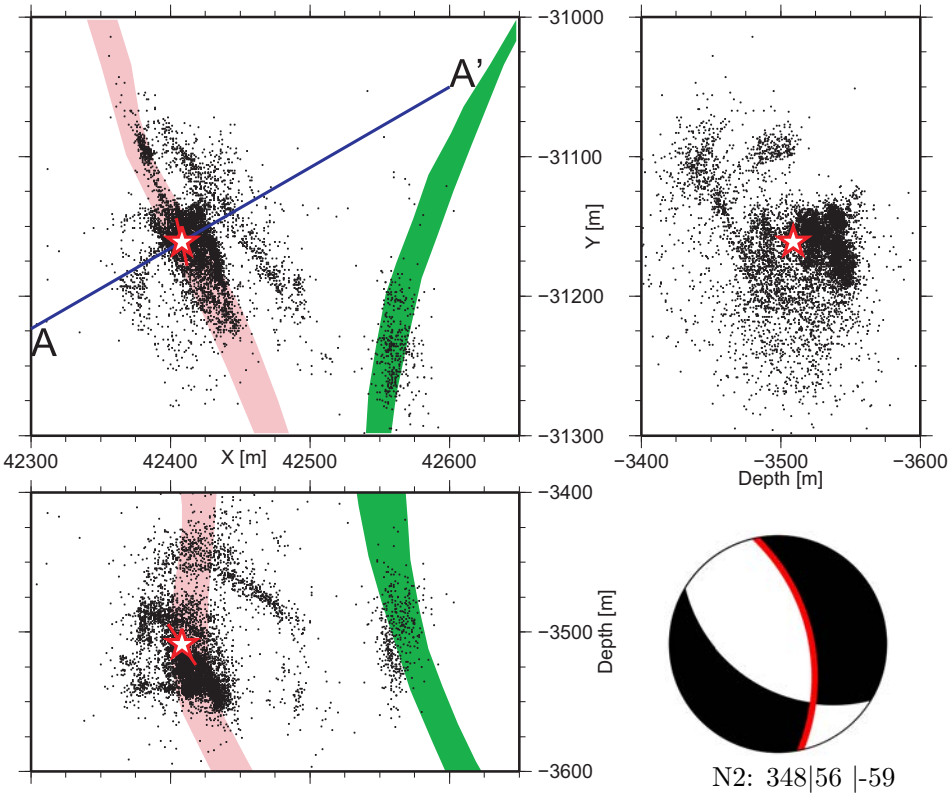

Figure 6.2: The distribution of aftershocks in map view (top left) and two depth sections (cumulative along the map area). The star marks the hypocentre of the M_w 1.9 main shock. The approximate extent (pink and green) of the two dykes at focal depth are displayed. The blue line A–A' indicates a transect (see Fig. 6.3) which is approximately perpendicular to the strike of the preferred nodal plane (red line, the rupture length (~35 m), derived from empirical relations (Leonard 2010)) Bottom right: Focal mechanism of the M_w main shock with the preferred nodal plane N2 in red (Naoi et al. 2011; Kwiatek and Ben-Zion 2013).

field (Lucier et al. 2009) and the general mechanisms of mining seismicity (Horner and Hasegawa 1978, in Hasegawa et al. 1989; Gay and Ortlepp 1979; Aswegen 2008).

6.3 Model description

To estimate the stress state and its changes due to the step-wise excavation of the gold reef immediately before the seismic event, we set up a 3D geomechanical-numerical model that simulates the excavation work of the mine and the consequent stress transfer. The resulting modelled induced stress changes are then inspected for their potential to cause the M_w 1.9 seismic event. In the following section the model assumptions, boundary conditions, properties and initial stress conditions are presented.

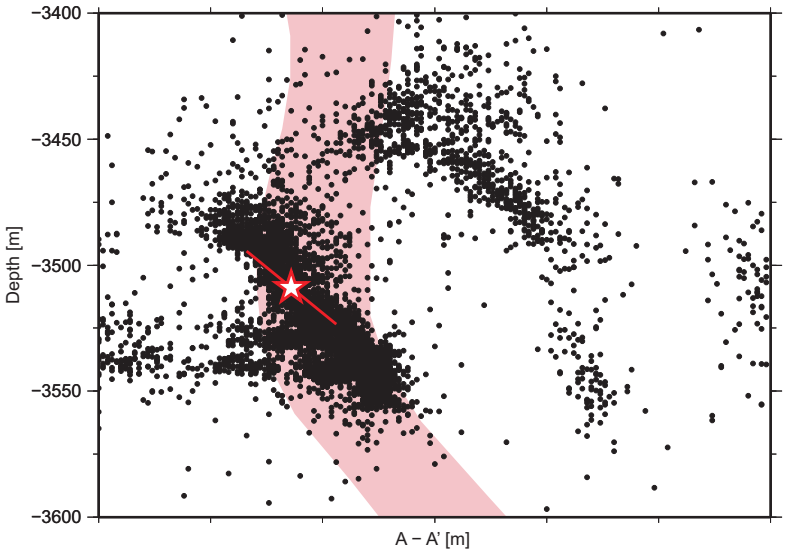

Figure 6.3: The aftershocks and the main shock (star) are projected onto the transect A–A' (blue line in Fig 6.2). The abscissa (A' is in direction of 70°) is approximately perpendicular to the strike direction of the nodal plane N2 (strike: 348°). An accumulation of aftershocks can be observed close to the hypocentre of the main shock on a plane dipping similar to the nodal plane N2 (dip: 56°, red line, the rupture length (~35 m), derived from empirical relations (Leonard 2010)).

6.3.1 Assumptions

In the process of model-building, we made the following assumptions concerning the model's properties and considered processes:

1. Dynamic triggering: No blasting was performed at the time and the days before the M_w 1.9 event due to the Christmas holidays (Hofmann et al. 2012; Plenkers et al. 2010). Thus, dynamic triggering can be ruled out.

2. Thermal stresses: The temperature at focal depth is ~60°C (Jones 1988). The air temperature in the mine is cooled down to about 35–40°C. The thermal stresses induced by the mentioned temperature change are at several magnitudes smaller than stress changes by mass removal and can be neglected.

3. Backfill and support pillars: Slurry of waste material is pumped into the mined out areas (Lucier et al. 2009). However, the rigidity of this backfill is rather low compared to the mined out rock and thus the impact of the backfilling it is not regarded. Also the impact of the pillars that support the roof of the mined out areas on the stress field is very local and small and thus can also be neglected.

4. Gravity acceleration: We assume gravitational body forces of $9.79\,m/s^2$ adapted to the depth and a local anomaly (Lindau 2007). Details on the implementation of the initial load due to gravity are presented in the following section 6.3.2.

5. Rheology: We assume linear elastic rock properties in each material block (gold reef, dykes and host rock) with the values stated in Tab. 6.2. To account for plastic processes in the

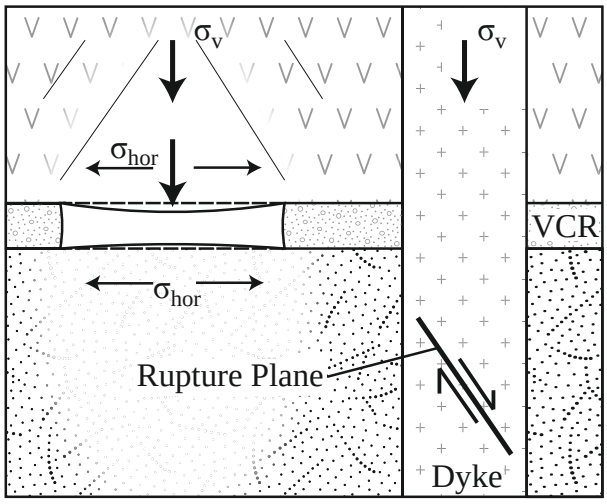

Figure 6.4: This sketch shows the response of the rock to excavation in a depth of ~3.5 km. The roof and floor of the excavated section bend inwards and thereby create tensile stresses in the horizontal. At the same time the stress due to the overburden in the mining horizon is redistributed to smaller unmined areas around the dyke. The vertical stress increases significantly in these areas and can ultimately lead to failure in a normal faulting event. Please note that the sketch is not to scale.

near-field of the excavation area, in particular the roof and the front of the mined out region (Malan 1999), we assume in one variant of the model result analysis that all horizontal stress components do not contribute to the stress changes in the dyke. Thus we consider two end member cases: The first assumes that stresses are transferred into the dyke by elastic response only. The second case assumes that all horizontal stresses are dissipated by local plastic processes (failure) in the excavation damage zone. The latter implies that only the change of the overburden (σ_v component in Fig. 6.4) controls the stress changes in the dyke.

6.3.2 Model formulation, parameters and solution

With the stated assumptions the problem can be formulated with the partial differential equation of the equilibrium of forces. The stress changes will result from the deformation that results from the excavation as indicated in the sketch of Fig. 6.4. These are equilibrated with the initial load due to gravity. Given the complexity of the 3D geometry and the inhomogeneous distribution of material properties, we use the Finite Element Method (FEM) to solve the problem numerically at discrete points. The FEM with its unstructured mesh allows the discretization of a volume with a high resolution in the area of interest and a coarse mesh further away (Fig. 6.5). This enables a beneficiary trade-off between spatial resolution and computation time. Furthermore, the FEM is capable to resemble the irregular shapes of the tunnel system, dykes and the thin gold reef. The different rock properties of each lithology (Tab. 6.2) are assigned to the corresponding elements.

6.3.3 Model geometry, discretization, boundary and initial conditions

The model volume of $450 \times 300 \times 310\,\mathrm{m}^3$ is only a small part of the mine and is located around the hypocentre of the M_w 1.9 seismic event. The geometrical and structural features, in particular the irregular shape of the dykes, were provided by the mining company. To ensure that the final discretization of the volume is sufficiently detailed and to avoid numerical errors, we performed

Table 6.2: Elastic material properties and density applied in the model.

Component	Lithology	Young's modulus [GPa]	Poisson ratio	Density [kg/m^3]
Dykes	Diorite^f/Gabbro^b	110^c	0.25^{d,e}	2900^{b,e}
Hanging Wall	Hard lava^a	88^a	0.26^a	2902^a
VCR (Gold reef)	Quartz pebble conglomerate^b	69^b	0.20^b	2600^c
Footwall	Quartzite^{a,f}	79^a	0.13^{a,e}	2710^{a,e}

^{a}Malan (1999), ^{b}Gay (1979), ^{c}MatWeb LLC (2013), ^{d}Gercek (2007),
^{e}S. Stanchits (pers. comm.), ^{f}Stanchits et al. (2010)

a series of 2D resolution test models (not shown in this paper). The final 3D mesh (Fig. 6.5) consists of ~10^6 finite elements (tetrahedra and hexahedra) with linear approximation functions.

The initial load due to the overburden and the tectonic stresses are implemented with appropriate kinematic boundary conditions. They are determined in such a way that they represent the in situ stress data from the neighbouring TauTona mine provided by Lucier et al. (2009) which we assume is comparable to the in situ stress state in Mponeng. Technically we apply on the top of the model a vertical stress of $S_{\mathrm{V}} = 92\,\mathrm{MPa}$ due to the 3380 m overburden. Within the model volume body forces due to gravity give an additional vertical stress component. To fit the magnitudes of the maximum and minimum horizontal stress S_{Hmax} and S_{hmin}, respectively, as reported by Lucier et al. (2009), we apply appropriate kinematic boundary conditions. The progress of mining excavation is simulated in monthly steps by the removal of material from the gold reef. The location, geometry and extent of these excavations were provided by the mining company. The removal of the rock material in the initial stress state results in deformations (Fig. 6.4) and consequent stress changes in the model volume. The solution of the resulting numerical problem is achieved with the commercial FEM software Abaqus v6.11.

6.4 Analysis of model results

To analyse whether the event was induced by stress changes, we use the change of Coulomb failure stress. The Coulomb failure stress (CFS) is defined as the stress state of a given plane and is expressed by

$$CFS = \tau - \mu\sigma_n \tag{6.1}$$

where τ is the shear stress, μ the friction coefficient which is usually assumed to be 0.6 (Byerlee 1978) and σ_n the normal stress (King et al. 1994; Jaeger et al. 2007). For the CFS calculation we use the rupture plane N2 of the M_w 1.9 event with an orientation of 348|56 (strike|dip)(Naoi et al. 2011; Kwiatek and Ben-Zion 2013). The changes in CFS (ΔCFS)

$$\Delta CFS = \Delta\tau - \mu\Delta\sigma_n \tag{6.2}$$

indicate whether a fault is brought closer to (positive ΔCFS value), or further away (negative ΔCFS value) from failure (King et al. 1994; Stein 1999). The ΔCFS is calculated by the subtraction of CFS of the unmined, initial stress state of the model from the CFS in December 2007, i.e. immediately before the event occurred, but after large amount of rock material was removed. We estimate two different values of ΔCFS; one with the shear stress component resolved in slip direction 348|56|-59 (ΔCFS_{slip}) and the other in direction of maximum shear stress on the rupture plane (ΔCFS_{max}). Furthermore, we calculate these two different ΔCFS values for both cases, the elastic response ($\Delta CFS_{slip,elastic}$, $\Delta CFS_{max,elastic}$) and the case where we implicitly assume in the analysis

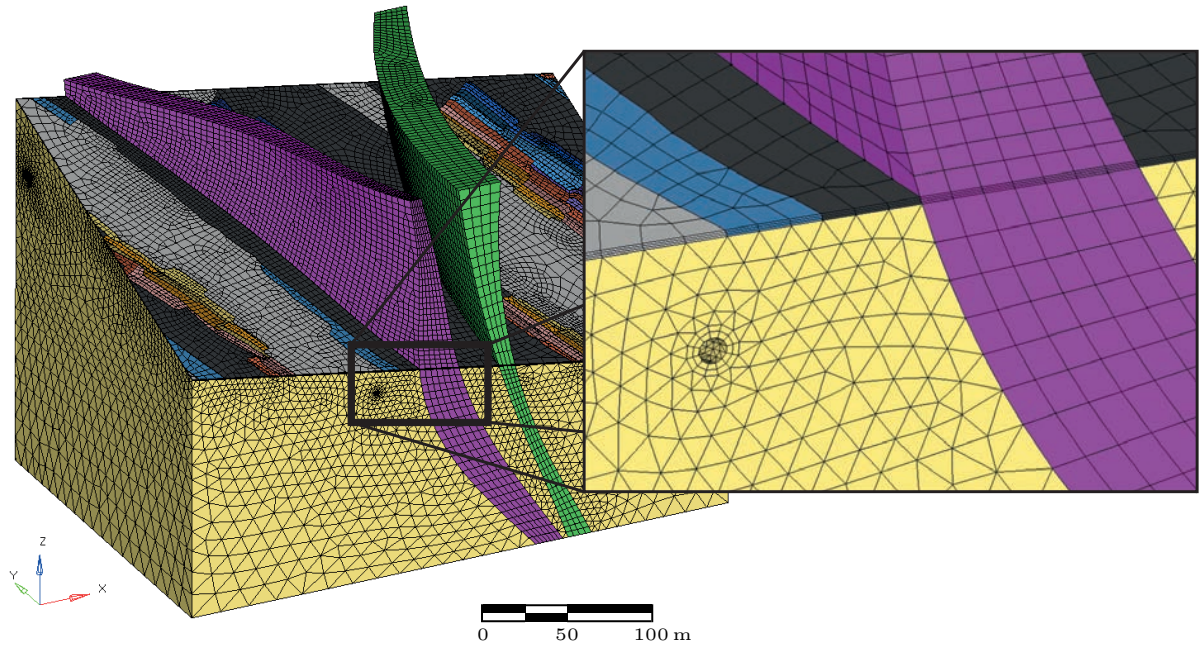

Figure 6.5: The discretised geometry of the gold mine. The gold reef (visible top layer) is colour-coded according to the monthly progress of the excavation work. The hanging wall is omitted here to facilitate viewing. Pink Green Dyke (purple) and Great Green Dyke (green) are displayed. The mesh contains ~10^6 hexahedron and tetrahedron elements. The close-up shows the Pink-Green dyke, the thin layered gold reef and the finer discretization around a mining tunnel. The gold reef is colour coded in grey (mined before 2007), blue (mined in 2007) and black (not mined as of 2009). Y axis points to the north.

that plastic deformation consumes all horizontal stress changes (pseudo-plastic, $\Delta CFS_{slip,plastic}$, $\Delta CFS_{max,plastic}$).

The results are displayed in 3D (Fig. 6.6) and cross sections (Fig. 6.7) for the ΔCFS_{slip} values of the elastic and the pseudo-plastic analysis case using the assumed rupture plane N2 of the focal mechanism solution. Both figures show that the event's hypocentre which is marked with a white star is located in an area of positive ΔCFS_{slip}. Tab. 6.3 summarizes all different ΔCFS values at the hypocentre for the two nodal planes. All values are positive regardless which ΔCFS value and plane is used and they range between 1.57 MPa for $\Delta CFS_{slip,plastic}$ on N1 and 14.77 MPa for $\Delta CFS_{slip,elastic}$ on N1. For the elastic case the difference between the ΔCFS_{max} and ΔCFS_{slip} is relatively small which indicates that the slip vector points in the overall direction of maximum shear stress. This is in agreement with the Bott hypothesis (Bott 1959) that slip occurs in the direction of maximum shear stress. Interestingly, the ΔCFS values for the elastic case are approximately 30% smaller for the rupture plane N2 compared to the auxiliary plane N1. In contrast to this, the ΔCFS values from the pseudo-plastic case are higher for the N2 plane, i.e. the rupture plane. The absolute numbers for the elastic case and the rupture plane N2 are in overall agreement with the ESS value of ~12 MPa estimated by Hofmann et al. (2012).

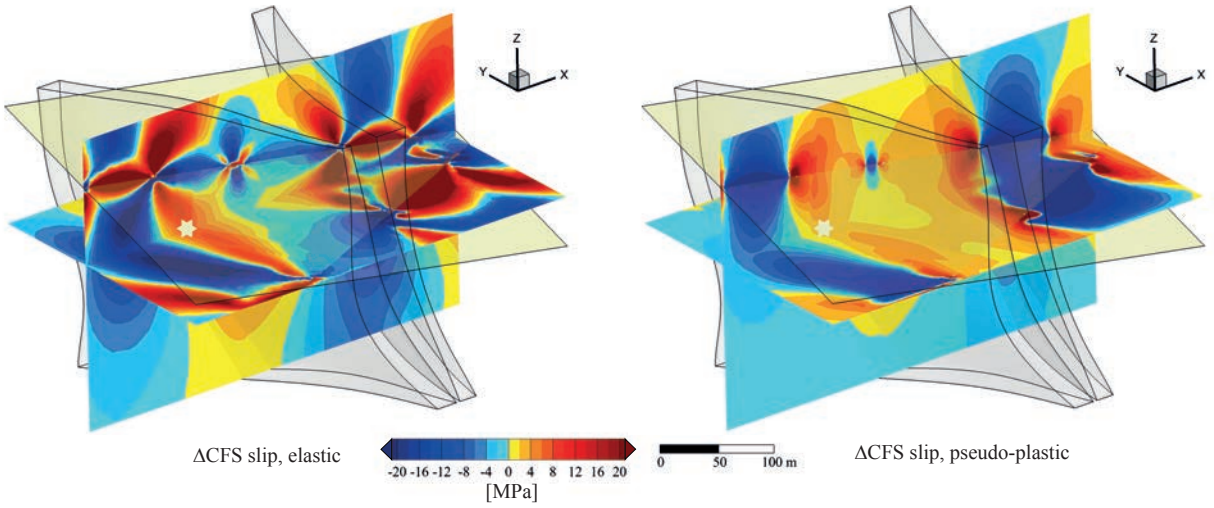

Figure 6.6: ΔCFS [MPa] in slip direction (ΔCFS_{slip}) at the time of the M_w 1.9 seismic event derived from the full stress tensor (left) and derived only from the vertical component (S_V) of the stress tensor, assuming a full dissipation of horizontal stresses (pseudo-plasticity) by local plastic deformation in the excavation damage zone (EDZ) (right). Displayed are two planes that intersect at the hypocentre of the seismic event. Event location is given by the white star. Dykes are the grey compounds and the gold reef is indicated by the yellow dipping plane. Y-axis points to the north. The two planes with ΔCFS are shown in more detail in Figure 6.7.

Table 6.3: The results of the different ΔCFS analysis at the hypocentre of the M_w 1.9 seismic event. The nodal plane N2: $(348|56| - 59)$(Naoi et al. 2011) is the rupture plane while N1 is the auxiliary plane. The shear stress in ΔCFS_{slip} is computed in direction of slip, while ΔCFS_{max} utilises the shear stress in the direction of maximum shear stress.

	Elastic		Pseudo-Plastic	
Receiver plane	ΔCFS_{slip}	ΔCFS_{max}	ΔCFS_{slip}	ΔCFS_{max}
N2: $(348\|56\| - 59)$	9.85 MPa	9.67 MPa	3.33 MPa	4.38 MPa
N1: $(125\|46\| - 129)$	14.77 MPa	14.74 MPa	1.57 MPa	3.33 MPa

6.5 Discussion

6.5.1 Discussion of the ΔCFS analysis results

The positive changes of all ΔCFS values indicate that the area around the hypocentre of the M_w 1.9 seismic event was brought closer to failure and that the event was most likely induced by the mining induced stress changes. For the elastic case the rupture plane N2 experienced a significantly smaller stress change compared to the auxiliary plane N1 even though N2 was clearly identified as the rupture plane by the distribution of aftershocks. However, this is not necessarily in contradiction with our findings when we consider the slip tendency (ST) value (Morris et al. 1996). ST is a an absolute measure of how close a fault is to failure and is defined after Morris et al. (1996) as:

$$ST = (\tau_{max}/\sigma_n) * \mu^{-1}. \tag{6.3}$$

Using a friction coefficient of $\mu = 0.6$ (Byerlee 1978) the ST value of the initial stress field for N1 is 0.39 and increases due to elastic stress transfer to 0.72. The ST value of the initial stress field

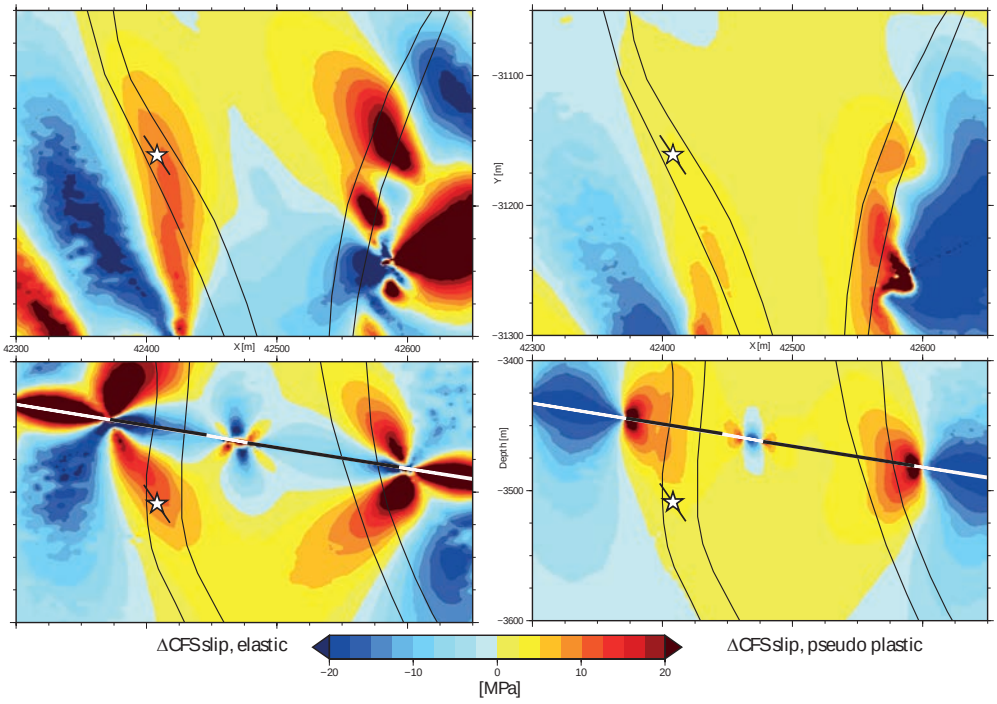

Figure 6.7: ΔCFS [MPa] in slip direction (ΔCFS_{slip}) at the time of the M_w 1.9 seismic event derived from the full stress tensor (left) and derived only from the vertical component (σ_v) of the stress tensor, assuming a pseudo-plasticity (right). Horizontal cross sections in depth of the hypocentre (top) and depth sections at Y=-31 160 m (bottom) of ΔCFS computed for the assumed rupture plane at depth of the hypocentre at the time of the M_w 1.9 seismic event (planes from Fig. 6.6). The event location is given by the white star; the strike (348°, top) and dip (56°, bottom) of the assumed fault plane is given by the black line (the rupture length of ~35 m is derived from empirical relations (Leonard 2010)); the dyke's extent is marked by the black lines. In the bottom figures, the state of excavation of the gold reef in December 2007 is indicated. Unmined areas are black and excavated areas white.

for N2 is 0.45 and increases due to the elastic stress transfer to 0.73. Thus, even though the stress transfer to N1 is in the elastic analysis larger than the one on N2, the absolute distance to failure is even slightly smaller for plane N2. Furthermore, the ST values indicate that even when cohesion is neglected the initial stress state in the dyke is still relatively far away from failure. However, the assumed initial stress field is calibrated against stress data that were not taken from a dyke but from the footwall (Lucier et al. 2009). Either in the dyke a pre-existing fault with a lower friction coefficient was reactivated ($\mu \approx 0.4$) or, which is more likely, the initial stress within the dyke are larger and closer to failure than intact rock due to its thermal history.

The main sources of uncertainty of the ΔCFS value is the orientation of the fault planes, but moderate deviations of the assumed fault plane in the order of 10–15° have no significant impact on the overall results of the model. Also the impact of uncertainties in the geometry of the gold reef, dyke and uncertainty of the material properties on this stress transfer simulation are of minor importance and do not change the general results of the model. Also the numerical error imposed by the linearisation of the problem has been tested and found to be insignificant. In summary this leads to an overall model uncertainty in the order of ±1 MPa.

6.5.2 Seismic hazard assessment

The previously presented results indicate a high probability that the M_w 1.9 event was induced by mining excavations. The hypocentre of the event was located in a dyke (Plenkers et al. 2010; Naoi et al. 2008) and dykes are generally known for an accumulation of seismicity with larger magnitude compared to the surrounding material (Gay and Ortlepp 1979; McGarr et al. 1975). Dykes are also known to bear higher compressive strength because they are stiffer than their surroundings (e.g. Zang and Stephansson 2010). Therefore it is of interest in which distance from the dyke mining is possible without significantly increasing the probability to induce an event in the dyke. We therefore apply a synthetic step-wise mining scenario, in which the excavation approaches the dyke from both sides until the dyke is reached; the actual mining compartments are not regarded here and in that sense the scenario is generic. To gain independence from a predefined slip direction, ΔCFS_{max} is applied for the elastic and the plastic analysis procedure. We use the orientation of nodal plane N2 as well as for six additional planes that are slightly deviated from N2 to account for uncertainties in the resulting ΔCFS values (maximum deviation in strike is 20° and 10° in dip direction).

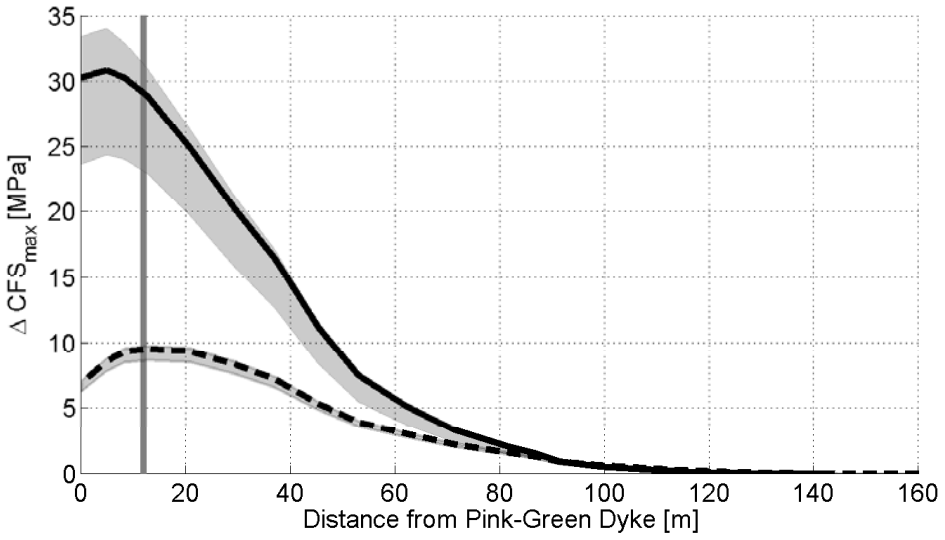

Figure 6.8: The *seismic hazard mitigation* at the hypocentre of the M_w 1.9 seismic event. The $\Delta CFS_{max,elastic}$ for the actual rupture plane (solid line) and for deviated planes (shaded area) are displayed. In addition the same is displayed for $\Delta CFS_{max,plastic}$ (dashed line) which is only computed from the vertical component of the stress tensor. Thereby a fully plastic dissipation of the horizontal stresses is assumed. The largest deviations of the plane's orientation from 348|56 in the strike are 20° and in the dip 10°. The vertical grey line indicates the approximate minimum distance of the mined out areas towards the dyke.

Fig. 6.8 displays the increase of ΔCFS_{max} with the advancing excavation towards the dyke. The curve for the elastic stress transfer (black solid line) indicates that mining up to a distance of ~120 m from the dyke is safe, since no changes in the ΔCFS_{max} are observed at the hypocentre of the seismic event. With decreasing distance to the dyke the ΔCFS_{max} value increases significantly up to a distance of ~10 m from the dyke where the maximum of 31 MPa is reached. Quantitatively, the pseudo-plastic stress transfer curve (dotted black line) shows a similar but less extreme behaviour; the maximum ΔCFS_{max} value of 9 MPa is also at ~10 m distance from the dyke.

Regardless the uncertainties and whether elastic or plastic analysis is used, this first-order assessment shows that small changes in the excavation distance with respect to the dyke change the

ΔCFS values significantly. However, at what level the ΔCFS value is critical is difficult to assess. This depends on (1) the stress state within the dyke before excavation, (2) the existence of pre-existing faults and their friction coefficient and (3) the rock strength of the intact rock. Furthermore, the real stress transfer is between the two end members of the elastic and the plastic case that we presented. Nevertheless, the definite increase clearly indicates that the hazard substantially increases within 50–10 m distance to the dyke.

6.6 Conclusion

In order to investigate the hypothesis that the M_w 1.9 seismic event on 27 December 2007 in the deep level Mponeng gold mine near Carletonville, South Africa, was induced by mining activity, a small scale (~0.05 km^3) 3-D geomechanical–numerical model of the gold mine was built. The ΔCFS analysis of the modelled stress state immediately before the seismic event strongly indicates that the stress changes by mining excavations induced this event. The rock was brought closer to failure on the derived rupture plane by stress changes of up to 1.5–15 MPa in dependence of the ΔCFS analysis type. The model uncertainties in the order of approximately ± 1 MPa do not change these principal findings. A forward modelling of a generic excavation scheme reveals that with decreasing distance to the dyke the ΔCFS values increase significantly. Hence even small changes in the mining progress can have a significant impact on the seismic hazard, i.e. the change of the occurrence probability to induce an event of economic concern.

Acknowledgement

The authors would like to thank AngloGold Ashanti for the kind permission to work and publish the data of the Mponeng gold mine, and the JAGUARS group for the provision of the data. Furthermore, the authors would like to thank Lanru Jing for his comments on an earlier version of the manuscript, which improved the manuscript. Figs. 6.1, 6.2, 6.3 and 6.7 were generated with the Generic Mapping Tool (GMT). In Fig. 6.1 SRTM3 V2 topographic data was used. The beachball plot in Fig. 6.2 was realised with the software MoPaD (http://www.mopad.org) by Krieger and Heimann (2012). Previously published preliminary results presented in a conference proceeding (Ziegler et al. 2014) contain some erroneous results and misinterpretations and should not further be used.

7 Discussion

Although the research areas of the four presented manuscripts vary on the spatial scale, they have two key issues in common: Firstly, they all provide an estimate of the contemporary or change of the in situ stress state in the crust, the spatial and magnitude variability of the stresses due to strength and density contrasts or the impact of faults and/or anthropogenic underground activities. Secondly, the manuscripts are related to applied geoscienes whether in the context of planning of deep geothermal wells in Alberta, examining a possible final nuclear waste repository site or explore the cause of seismic events in a deep gold mine. The presented manuscripts are discussed in the following, first individually and finally in synthesis.

7.1 A Revised Crustal Stress Orientation Database for Canada (Chapter 3)

This paper presents a revised and updated database for the Canadian stress map, where 514 new S_{Hmax} orientation data records are added to the World Stress Map (WSM) database with now 1667 entries in Canada and surrounding. A smoothing algorithm is applied to the new dataset to generate a smoothed stress map with the mean S_{Hmax} orientation on a regular grid. Furthermore, a measure of the wave-length of the stress pattern is applied for analysis. This confirmed that long spatial wavelength stress patterns ($\geq$1,000 km) exist in large areas of Canada.

There has not been a substantial revision or extension of the Canadian stress database for about two decades (Adams and Bell 1991; Bell et al. 1994). The data compilation of Chapter 3 increases the amount of available stress orientation data for Canada and surrounding by about 45%. A specific focus was on Alberta, to support the calibration of the intended crustal stress model of Alberta (Chapter 4). With 142 new data records in Alberta, the database entries have nearly doubled to now 297 stress orientation entries. Such data compilation provides deeper insight into the variation of the stress orientation; it is mainly a database for statistical analysis and serves geomechanical–numerical models, which can be calibrated using the data (cf. Chapter 4).

Statistical tests to determine the average S_{Hmax} orientation are applied in several studies (e.g. Bird and Li 1996; Coblentz and Richardson 1995; Hansen and Mount 1990; Heidbach and Ben-Avraham 2007; Müller et al. 2003; Rebaï et al. 1992). The algorithm of Heidbach et al. (2010) is further developed to eliminate the influence of data outliers on the smoothing result. First, the estimator of the mean S_{Hmax} orientation, the circular mean ($\widehat{S}_{Hmax}$) is replaced by the linear quasi circular median ($\widetilde{S}_{Hmax}$) of Ratanaruamkarn et al. (2009). Secondly, the former used deviation criteria of Heidbach et al. (2010) with a standard deviation of $\leq 25°$ is replaced by the here introduced quasi interquartile range on the circle (QIROC) of $\leq 20°$. This test is stricter and may exclude some of the data records, but it gives a more precise and robust estimation of average S_{Hmax} orientation.

The general trend of S_{Hmax} orientation eastwards of the Cordillera is northeast-southwest (Fig. 3.2), which is similarly observed for $\widetilde{S}_{Hmax}$ (Fig. 3.4). This correlates with North America's plate motion (Henton et al. 2006). The Alberta stress map (Fig. 3.3) shows a rather homogeneous stress pattern with only local deviations from the general trend. The S_{Hmax} orientation in Canada differs from the general trend only along the Canadian Cordillera, due to the North American–Pacific plate boundary. Other orientation differences are observed in the Mackenzie Mountains and along the St. Lawerence Platform up to the Gulf of St. Lawerence. Around the Hudson Bay, the centre of the Canadian Shield, some of the S_{Hmax} data are oriented towards the centre of the shield. Some of these orientations were previously interpreted to be caused by post-glacial isostatic rebound (Adams 1989; Adams and Bell 1991). However, constantly lower shear wave velocities (V_s) in the outer

rim of the Canadian Shield (Kao et al. 2013), in combination with an elastic thickness of 80 km in the centre of the shield (Kirby and Swain 2014), the structure and/or mechanical properties of the Canadian Shield could be responsible for the observed S_{Hmax} orientation.

Bell and Gough (1979) assumed that the stress orientation follows the convexly curvature of the Rocky Mountains topography, as observed for the Alpine Molasse Basin (Reinecker et al. 2010, Fig. 3.9). However, this curvature is not observed in the southern Alberta Basin, south of 50°N (Fig. 3.8). There are two potential reasons for this: (1) The Alberta Basin is more mature then the Alpine Molasse Basin as it is a result of Mesozoic deformation in contrast to Cenozoic ages. (2) The identified deviation of perpendicular S_{Hmax} orientations in the Alberta Basin in contrast to the Rocky Mountains trench are induced by basement features along the Bow Island Arch, it separates the Alberta Basin from the Wallistion Basin. The Bow Island Arch is a a north-eastward plunging Precambrian basement feature. Podruski (1988) speculated that it was activated during the Laramiden orogeny and that it might be associated with Eocene intrusions, a setting similar to that about 200 km to the south in Montana (USA). A similar deviation can be observed along the Peace River Arch in the new stress map of Alberta, already sufficiently discussed (e.g. Bell and Grasby 2012; Halchuk and Mereu 1990; Eaton et al. 1999; Dusseault and Yassir 1994).

7.2 3-D geomechanical–numerical model of the contemporary crustal stress state in the Alberta Basin (Canada) (Chapter 4)

This paper presents a large scale geomechanical–numerical model of the Alberta Basin, that quantifies the contemporary full 3-D stress tensor of the crust. The main aim was to examine the potential usage of safe and sustainable geothermal energy. The designed model contains the main structural features of the basin from the surface down to the lithospheric mantle, such as the Mohorovičić-discontinuity (Moho), the basement, the Rocky Mountains front, the foothill front as well as major faults. The main focus of the manuscript is on the calibration procedure. The general calibration workflow is similar to previous publications (e.g. Buchmann and Connolly 2007; Fischer and Henk 2013; Heidbach et al. 2013; Hergert and Heidbach 2011). A very large database with diverse data types of in situ stress data was available to calibrate the model step-wise to find the best-fit model. This model provides the full 3-D stress tensor and therefore allows the estimation of the stress orientation and magnitudes along any potential well path in advance of the first drilling.

The first step of the calibration was the determination of an ideal basin density using 981 vertical stress (S_V) magnitude data. Using the estimated whole basin density, the median difference between the model and the in situ S_V is close to zero (−0.09 MPa) with a standard deviation of 5.58 MPa and a correlation coefficient of r=0.935, which indicates a good data fit of the model (Fig. 4.14a). When plotting S_V deviation versus depth (not shown), no simple linear trend can be observed, like by an increasing density function into depth. Only a model with a considerable better stratigraphic resolution might be able to give a better data fit.

321 S_{Hmax} azimuth values are used to test the stress orientation within the model, mainly governed by the applied displacement boundary conditions along the model edges. The whole model median of the model deviation to the in situ stress orientation $\widetilde{\Delta S_{Hmax}}$ is −3.44°. The median histogram (Fig. 4.14b) displays a main cluster of ΔS_{Hmax} around zero; a second smaller cluster is around ±90°. This second cluster are probably misinterpreted data, e.g. drilling induced tensile fractures with spalling in S_{Hmax} orientation, in contrast to borehole breakouts with spalling in S_{hmin} orientation (e.g. Brudy and Kjø rholt 2001; Barton and Moos 2010). Therefore, the second cluster around ±90° rather confirms than disproves the good model fit with the in situ data. Two regions with a systematic deviation can be identified, the Peace River Arch and the Bow island Arch. This might be due to unclear basement structures, which are not represented appropriately in the model. Whereas the first region was known for stress orientation drift before (Bell and Babcock 1986;

Bell and McCallum 1990; Bell 1996b; Bell and Grasby 2012; Bouzidi et al. 2002; Dusseault and Yassir 1994; Eaton et al. 1999; Halchuk and Mereu 1990), the latter was identified by the studies in Chapter 3 and 4 for the first time.

To calibrate the magnitude of displacement boundary conditions, the n=1720 S_{hmin} and the 11 calculated and 2 measured S_{Hmax} magnitude values are used in combination. This parallel calibration can be justified by the used linear elastic material properties, given linear dependencies between push and pull on the model boundaries. Four models with different push vs. pull ratios are used to estimate the median deviation of S_{hmin} and S_{Hmax} between the in situ data and the model. Using bivariate linear regression based on the spatial distribution of the $\widetilde{\Delta S}_{hmin}$ and $\widetilde{\Delta S}_{Hmax}$, the intersection of the zero isolines are calculated (Fig. 4.15). This method allows calculating the best-fit push-pull ratio, based on only three model runs with variable magnitudes of boundary conditions. Eventually, $\widetilde{\Delta S}_{hmin}$ is -0.005 MPa and $\widetilde{\Delta S}_{Hmax}$ is 0.018 MPa, indicating a good fit. The found correlation coefficient of $r = 0.835$ is very similar to $r = 0.837$ when comparing with σ_3 from the model. Therefore, most of the S_{hmin} magnitude indicators represent S_{hmin}, which implies that nearly none of these magnitudes are from a thrust faulting regime.

The distribution of the normalized S_{hmin} (Fig. 4.14c) displays a positive screwness. The plot in Fig. 4.19 visualizes that the normalized S_{hmin} difference ($n\Delta S_{hmin}$) of the Leak-off test (LOT) magnitudes are not normally distributed in contrast to the other S_{hmin} indicators, derived from originally hydraulic fracturing. In situ LOT magnitudes are systematically higher at shallow depth (<500 m) and smaller at greater depth (>500 m). The reasons for the LOT data difference with depth are: (1.) a more significant influence of tensile rock strength on measured pressure at shallow depth (Bachu et al. 2008), (2.) preferred LOT measurements in shallow rocks which give higher S_{hmin} magnitudes like shales (Bell and Grasby 2012; Kry and Gronseth 1983), (3.) the possibility of man-made stress changes and (4.) merely numerical interpolation problems close to the free surface (topography). Small LOT magnitudes below 500 m are interpreted in two ways: First, some of these LOT data are rather formation integrity tests (FIT). These are used to determine whether the well-bore can be sustained during drilling or production (e.g. White et al. 2002). However, such tests deliver smaller magnitudes than real LOT. Second, LOT are preferred measurements in deep rocks which gives smaller S_{hmin} magnitudes, like sandstone (Bell and Grasby 2012; Kry and Gronseth 1983).

The crust-mantle interface (the Moho topography) was generated and included in the model geometry with much effort. However, a model with a flat Moho topography ($z = -50$ km) gave very similar results. Thus, stress orientation and magnitudes are only slightly influenced by the Moho topography in the Alberta Basin.

As the modelling intended to estimate the full stress tensor for possible geothermal projects, stress profiles for three virtual borehole sites are plotted. They are located below the towns of Hinton and Leduc (near Edmonton) and at the Hunt well site (near Fort McMurray). The virtual wells indicate a thrust faulting regime close to the Rocky Mountains (Hinton) up to a depth of ~1000 m. At a depth of ~4500 m the regime changes from strike-slip to normal faulting. Within the basin (Leduc) no thrust faulting is observed; the change from a strike-slip to a normal faulting regime occurs at a depth of ~3000 m. Further to the North-east, at the Hunt well site, where the foreland basin becomes thin (~500 m), the strike-slip to normal faulting regime change happens at a depth of ~2000 m. This confirms the general observations from Bell and Gough (1979); Bell et al. (1994); Bell and McLellan (1995); Bell and Babcock (1986); Bell and Bachu (2003); Bell and Grasby (2012); Woodland and Bell (1989); Fordjor et al. (1983); Jenkins and Kirkpatrick (1979). They found the same dependence of the stress regime on (1) the distance to the Rocky Mountains and (2) from surface to the depth. However, it remains unclear whether or not the basin structure or the lateral gravitational difference in the crust is the cause of the change.

Hydraulic fracturing in shallow depths close to the Rocky Mountains would create horizontal fractures. Horizontal wells, oriented parallel to S_{hmin} (southeast to northwest) (Bell and Grasby 2012), with multiple fractures, open in S_{Hmax} orientation. This would allow producing geothermal energy economical feasible (Hofmann et al. 2014) from low permeable rocks.

7.3 Stress field sensitivity analysis in a sedimentary sequence of the Alpine foreland, Northern Switzerland (Chapter 5)

The variability of stresses within a stratigraphic column due to variable geomechanical rock properties can be investigated using in situ data (Warpinski 1989) and/or generic models (Roche et al. 2013; Smart et al. 2014). However, the present-day knowledge of stress tensor variation within a sedimentary pile is limited. The influence of variable rock properties on the stress state within an argillaceous horizon is investigated using a semi-generic model, to examine a potential radioactive waste repository site in Northern Switzerland. The influence of topography, long-lasting tectonic shortening and stress release along (existing) faults on the stress state are modelled.

Topographic effects can mainly be observed close to the surface; but large-scale erosion, which can be expected during disposal life time would reduce S_V and therefore differential stresses would increase the more overburden is removed. Due to the south-north oriented tectonic shortening, stress ratios increase within the competent stratigraphic units such as the Upper Malm and the Upper Muschelkalk. Both formations shield the Opalinus clay, where the stress ratio change is low. This argues for the Opalinus Clay as the host rock for the repository. Furthermore, the tectonic shortening changes the tectonic regime to a compressional stress state where the S_{Hmax} and S_{hmin} are larger than S_V. Plastic failure under a compressional tectonic regime would lead to the formation of a thrust fault. Thrust faults tend to propagate towards the surface as the normal stress decreases close to the surface. Comparably low fracture potential values in the Upper Muschelkalk make the generation of a thrust fault propagating through the Opalinus Clay less likely, despite increased differential stress. Reactivation of already existing faults is a more likely scenario (e.g. Krantz 1991), as long the stress regime does not change (Sibson 1985).

Higher friction along the east-west striking faults would lead to higher S_{Hmax}/S_{hmin} ratio in the Mesozoic sediments. Slip along these faults releases tectonically derived stress accumulation. Fault related disturbance of the stresses are observed within ~1000 m distance to the faults.

The absence of stress magnitude data within the model area limits the model results; high-quality stress magnitudes from several formations within the model area would result in a more reliable estimation. A better structural understanding of the Permo-Carboniferous Trough below the model area as well as fault geometries would help to improve the model geometry.

7.4 Mining-induced stress transfer and its relation to a M_w 1.9 seismic event in an ultra-deep South African gold mine (Chapter 6)

This paper examines the static stress transfer within an ultra-deep South African gold mine and its relation to a M_w 1.9 seismic event in 2007 (Yabe et al. 2009; Plenkers et al. 2010; Naoi et al. 2011; Kwiatek et al. 2010; Kwiatek and Ben-Zion 2013). It occurred within the dyke, in agreement with the fact that dykes are known to attract seismicity (Gay and Ortlepp 1979; McGarr et al. 1975). The hypocentre was located just <50 m below the mining level. However, it is clear, that the event was initiated by static stress transfer only and not dynamically triggered by the mining activity because it happened during the Christmas holidays.

In addition to the mine's seismological network, several acoustic emission (AE) sensors were operating at the time of the event. As the AE network was set up very close to the event (~50 m), the location of aftershocks as low as to magnitude -4.4 could be detected and precisely located

(Kwiatek et al. 2010; Kwiatek and Ben-Zion 2013). Together with the main shock's focal mechanism derived from the mine's seismic network, the rupture plane could be identified. A high resolution 3-D geomechanical–numerical model which mimics the stepwise mining progress in detail was developed to investigate whether or not the event was induced by purely static stress changes.

To identify whether or not mining activity brought the area around the hypocentre closer to failure, the Coulomb failure stress change (ΔCFS) is estimated from the model results. The model indicates that the seismic event was induced by static stress changes. This result persists regardless of the different approaches to compute the ΔCFS or the assumption of reasonable uncertainties in the fault plane solution. However, the model cannot resolve why the seismic event happened in the dyke. There are several possible explanations: (1.) The dyke is more brittle than the country rock, therefore a failure within the dyke is more likely. (2.) The dyke contains pre-existing fractures which are reactivated. (3.) The dyke has a different stress state history due its cooling history. Additionally, the ΔCFS within the dyke in dependence to the distance to the mined gold reef is calculated. It shows that the event could have been avoided if the mining activity would have stopped at a larger distance to the dyke. To apply such a seismic hazard assessment in a quantitative way, detailed information about the material properties, orientation of possible pre-existing fractures and the stress state within the dyke are necessary.

7.5 Summarizing discussion and outlook

Estimation of crustal stress orientation and in particular the horizontal stress magnitudes are challenging. Numerous interpolation or smoothing algorithms have been applied in several studies (Bird and Li 1996; Hansen and Mount 1990; Müller et al. 2003; Rebaï et al. 1992). Coblentz and Richardson (1995) and later Heidbach et al. (2010) used statistic tests on a regular grid to analyse the stress pattern for a global dataset. However, such methods do not incorporate effects due to structural or rock property inhomogeneities, which have several effects (e.g. Bell and McLellan 1995; Röckel and Lempp 2003; Roth and Fleckenstein 2001; Yassir and Bell 1994; Warpinski 1989). In contrast, geomechanical–numerical models allow the incorporation of density and strength contrasts of formations and faults. Furthermore, past (or future) deformation by tectonic processes and other lateral stress sources (gravitational potential energy (GPE), remnant stresses, etc.) can be mimicked by those model's boundary conditions. The disadvantage of modelling is that stress data are needed to calibrate the models. An optimal calibration procedure is presented with the Alberta Model in Chapter 4. However, in situ data vary a lot, so that probably only statistic tests using different datasets with greater numbers of data are sufficient. In contrast to the Alberta model, the "Nördlich Lägern" Model (Chapter 5) and the Mponeng Model (Chapter 6) have no stress magnitude data within the model volume, needed for a reliable model calibration. These latter models can provide information about changing stresses or stress variability but not the contemporary stress tensor. The estimation of the best-fit model for Alberta also shows clearly that the stress orientation is sensitive to the orientation and the relative magnitude of the applied boundary conditions whereas the horizontal magnitudes are a function of the displacement along the model boundaries.

To take first-order stress sources and major regional structures into account and at the same time with a high resolution of local stratigraphy of a certain reservoir or target area is a major challenge for the future. Reiter et al. (2013) suggested to use regional stress models such as the Alberta Basin stress model (Chapter 4) to derive boundary conditions for local models on a size of the NL model (Chapter 5). The same approach can be used to transfer stresses from local model to reservoir model as boundary conditions, e.g. to the size of the Mponeng Model (Chapter 6). Analogue to that approach, the small model can be directly coupled with the larger model using contact surfaces. Such a model would provide results directly from one nested model. However, there is still no experience with such modelling approaches.

The Nördlich Lägern (NL) Model (Chapter 5) clearly displays, how much the stress varies within a sedimentary sequence, in agreement with previous studies (e.g. Warpinski 1989; Roche et al. 2013; Smart et al. 2014). The insufficient stratigraphic resolution in the Alberta Model might be one of the reasons for some of the differences between the model and the in situ data. A higher resolution model of an area of 1400 × 700 km^2 is difficult to realise in the near future, due to the limited computational power and limited knowledge of detailed crustal structures.

Models with a higher resolution may give better results. Figs. 4.18 and 4.19 shows the difference of S_{hmin} magnitudes between the model and the in situ data indicating a large variability. However, there is still no method to calculate S_{hmin} magnitudes from LOT magnitudes, which are comparable to classical hydraulic fracturing data. Furthermore, the accuracy of magnitudes derived from hydraulic fracturing are influenced by several variables. The new Quantitative World Stress Map database (Q-WSM, Zang et al. 2012) needs a similar quality ranking like the WSM (Heidbach et al. 2010), which would make the data comparable.

The use of the Moho topography within the Alberta Model (Chapter 4) did not change the results. However, this does not imply that other models on the same scale should not include the Mohorovičić-discontinuity. Local or reservoir models (e.g. Chapters 5 and 6) do not vary due to changing properties along the mantle-crust interface because this interface is several tenth of kilometres below the volume of interest.

The Alberta Basin stress model (Chapter 4) can give information about stress orientation and magnitude, necessary for the design of a potential geothermal production site. However, a detailed understanding of the target horizons (e.g. Weides et al. 2013, 2014a, b) is essential besides the precise estimation of temperatures in the chosen horizons (e.g. Gray et al. 2012; Majorowicz et al. 2012). Some of the target horizons reach the necessary permeabilities for the use of geothermal energy. Majorowicz and Moore (2008) and Hofmann et al. (2014) suggest that enhanced geothermal systems (EGS) would allow to enhance rock units with small effective porosities and make application of geothermal energy in Alberta competitive to other energy resources, especially considering the possibility to lower the greenhouse gas emission.

The NL paper (Chapter 5) is part of a series of geomechanical–numerical models, made for potential nuclear waste repository sites in Switzerland. The work is commissioned by the National Cooperative for the Disposal of Radioactive Waste (NAGRA), founded in 1972, which is responsible to propose an appropriate location for the construction of nuclear waste disposal sites. The scientific work is largely outsourced to external experts; quality is monitored by a multi-stage review process by external experts and a national supervisory authority, the Swiss Federal Nuclear Safety Inspectorate (ENSI). There is no official organisation or equivalent stage of development in Germany with respect to radioactive waste disposal sites. When transferring the findings of this thesis to Germany, the following suggestions can be made: Future tasks on the topic of crustal stresses in Germany are (1.) the search of a final repository site for high-level radioactive waste, (2.) the risks and advantages of hydraulic fracturing for geothermal energy or hydrocarbons. Up to now, there is no effort made to set-up a regional stress model of Germany, which would allow to get a better understanding of the stress pattern and stress sources, as well as it could be used to derive boundary conditions for local models.

Furthermore, results and experiences of the publications compiled in this thesis can provide a better understanding of geo-tectonically similar settings. For example, the Alpine Molasse Basin is slightly younger than the Alberta Basin, but the general setting is very similar. The same sedimentary pile as observed in the Swiss Molasse basin can be found in southern Germany. Therefore, the models of this thesis can give some implications for the usage of geothermal energy and potential repository sites, primarily in the federal states Bavaria and Baden-Württemberg.

8 Conclusions

From the summarizing discussion, I draw the following main conclusions:

1. The developed statistical method (IQROC) for the estimation of the mean S_{Hmax} orientation on a regular grid and the wave length of the stress pattern is more robust than previous methods and should be used for analysis of the next World Stress Map database release that is scheduled for 2016.

2. If there is a sufficient amount of stress data available, a step-wise model calibration using statistical measurement results in a reliable prediction of the 3-D contemporary stress magnitude. Without sufficient amount of stress magnitude data, the quality of the model calibration is limited and thus the reliability of the predicted stress field is low.

3. The results of the Nördlich Lägern model show the influence of the formation type and faults on the 3-D variability and sensitivity of the stress field. However, absolute stress values from the model shall not to be used due to the semi-generic character of the model set-up and the lack of stress magnitude data of the individual formations within the model area. In the next phase of the site selection process in Northern Switzerland, a number of boreholes are planned to gather more data of each remaining potential site for a nuclear waste repository. These future in-situ data and a better structural resolution could be used to improve the NL model.

4. The Mponeng stress model clearly shows that mining induced stress changes are the cause of the seismic event. However, the model cannot resolve why the seismic event occurred in the dyke. Different stress histories in combination with a higher Young's modulus are probably the major reasons. Thus, an in situ stress estimate of the stress magnitudes in the dyke would be essential to assess the hazard imposed by continued excavation towards the dyke.

References

Aadnø y, B. S. and Bell, J. S. (1998). Classification of Drilling-induced Fractures and Their Relationship o In-situ Stress Directions. *Log Analyst*, 39(December):27–42.

Adams, J. J. (1987). Canadian Crustal Stress Data: A Compilation to 1987. Technical report, Geological Survey of Canada.

Adams, J. J. (1989). Crustal stresses in eastern Canada. In Gregersen, S. r. and Basham, P. W., editors, *Earthquakes at North-Atlantic Passive Margins: Neotectonics and Postglacial Rebound*, volume 266, pages 289–297. Springer Netherlands.

Adams, J. J. and Bell, J. S. (1991). Crustal stresses in Canada. In Slemmons, D. B. and Engdahl, E. R., editors, *Neotectonics of North America, Decade of North American Neotectonics of North America*, chapter 20, pages 367–386. Geological Society of America.

Altmann, J. B., Müller, B. I., Müller, T. M., Heidbach, O., Tingay, M. R. P., and Weiß hardt, A. (2014). Pore pressure stress coupling in 3D and consequences for reservoir stress states and fault reactivation. *Geothermics*, 52:195–205.

Altmann, J. B., Müller, T. M., Müller, B. I., Tingay, M. R. P., and Heidbach, O. (2010). Poroelastic contribution to the reservoir stress path. *International Journal of Rock Mechanics and Mining Sciences*, 47(7):1104–1113.

Amadei, B. and Stephansson, O. (1997). *Rock Stress and Its Measurement*. Chapman & Hall, London.

Anderson, E. M. (1951). *The Dynamics of Faulting and Dyke Formation with Application to Britain*. 2nd ed. Oliver and Boyd, London and Edinburgh.

Angelier, J. (1979). Determination of the mean principal directions of stresses for a given fault population. *Tectonophysics*, 56(3-4):T17–T26.

Angelier, J. (1984). Tectonic analysis of fault slip data sets. *Journal of Geophysical Research*, 89(B7):5835–5848.

AngloGold Ashanti Limited (2013). *Online Sustainability Report*. Available from: www.aga-reports.com, Newtown, South Africa.

Armstrong, R., Compston, W., Retief, E., Williams, I., and Welke, H. (1991). Zircon ion microprobe studies bearing on the age and evolution of the Witwatersrand triad. *Precambrian Research*, 53(3-4):243–266.

Arnold, R. and Townend, J. (2007). A Bayesian approach to estimating tectonic stress from seismological data. *Geophysical Journal International*, 170(3):1336–1356.

Arnórsson, S. (1995). Geothermal systems in Iceland: Structure and conceptual models—I. High-temperature areas. *Geothermics*, 24(5-6):561–602.

Aswegen, G. V. (2008). Ortlepp Shears – dynamic brittle shears South African gold mines. In *1st Southern Hemisphere International Rock Mechanics Symposium SHIRMS 2008*.

Aulbach, S., Griffin, W., O'Reilly, S., and McCandless, T. E. (2004). Genesis and evolution of the lithospheric mantle beneath the Buffalo Head Terrane, Alberta (Canada). *Lithos*, 77(1-4):413–451.

Babcock, E. A. (1978). Measurement of subsurface fractures from dipmeter logs. *AAPG Bulletin*, 62(7):1111–1126.

Bachu, S., Haug, K., and Michael, K. (2008). Stress Regime at Acid-Gas Injection Operations in Western Canada. *Energy Resources Conservation Board, ERCB/AGS Special Report 094*, page 49.

Balfour, N. J., Cassidy, J. F., Dosso, S. E., and Mazzotti, S. (2011). Mapping crustal stress and strain in southwest British Columbia. *Journal of Geophysical Research*, 116(B3):B03314.

Baranova, V., Mustaqeem, A., and Bell, J. S. (1999). A model for induced seismicity caused by hydrocarbon production in the Western Canada Sedimentary Basin. *Canadian Journal of Earth Sciences*, 36(1):47–64.

Barton, C. A. and Moos, D. (2010). Geomechanical wellbore imaging: Key to managing the asset life cycle. Technical report, GeoMechanics International.

Barton, C. A. and Zoback, M. D. (1994). Stress perturbations associated with active faults penetrated by boreholes: Possible evidence for near-complete stress drop and a new technique for stress magnitude measurement. *Journal of Geophysical Research*, 99(B5):9373–9390.

Becker, T. W. and Faccenna, C. (2011). Mantle conveyor beneath the Tethyan collisional belt. *Earth and Planetary Science Letters*, 310(3-4):453–461.

Bell, J. S. (1985). Offset boreholes in the Rocky mountains of Alberta, Canada. *Geology*, 13(10):734–737.

Bell, J. S. (1993). Attached and detached in-situ stress regimes in sedimentary basins. In *55th EAEG Meeting*.

Bell, J. S. (1996a). In situ stresses in sedimentary rocks (part 1); Measurement techniques. *Geoscience Canada*, 23(2):85–100.

Bell, J. S. (1996b). In situ stresses in sedimentary rocks (part 2): Applications of stress measurements. *Geoscience Canada*, 23(3):135–153.

Bell, J. S. (2003). Practical methods for estimating in situ stresses for borehole stability applications in sedimentary basins. *Journal of Petroleum Science and Engineering*, 38(3-4):111–119.

Bell, J. S. and Babcock, E. A. (1986). The stress regime of the Western Canadian Basin and implications for hydrocarbon production. *Bulletin of Canadian Petroleum Geology*, 34(3):364–378.

Bell, J. S. and Bachu, S. (2003). In situ stress magnitude and orientation estimates for Cretaceous coal-bearing strata beneath the plains area of central and southern Alberta. *Bulletin of Canadian Petroleum Geology*, 51(1):1–28.

Bell, J. S. and Bachu, S. (2004). In-Situ Stress Magnitudes in the Alberta Basin-Regional Coverage for Petroleum Engineers. In *Proceedings of Canadian International Petroleum Conference*, pages 1–12, Calgary. Society of Petroleum Engineers.

Bell, J. S. and Gough, D. (1981). Intraplate stress orientations from Alberta oil-wells. *Geodynamics Series*, 5:96–104.

Bell, J. S. and Gough, D. I. (1979). Northeast-southwest compressive stress in Alberta evidence from oil wells. *Earth and Planetary Science Letters*, 45(2):475–482.

Bell, J. S. and Grasby, S. E. (2012). The stress regime of the Western Canadian Sedimentary Basin. *Geofluids*, 12(2):150–165.

Bell, J. S. and McCallum, R. (1990). In situ stress in the Peace River Arch area, Western Canada. *Bulletin of Canadian Petroleum Geology*, 38(1):270–281.

Bell, J. S. and McLellan, P. J. (1995). Exploration and production implications of subsurface rock stresses in western Canada. In *Proceedings of the Oil and Gas Forum*, page 5.

Bell, J. S., Price, R. A., and McLellan, P. J. (1994). In-situ stress in the Western Canada Sedimentary Basin. In Mossop, G. D. and Shetsen, I., editors, *Geological atlas of the Western Canada Sedimentary Basin*, chapter 29, pages 439–446. Canadian Society of Petroleum Geologists and Alberta Research Council, Alberta.

Bell, J. S. and Wu, P. (1997). High horizontal stresses in Hudson Bay, Canada. *Canadian Journal of Earth Sciences*, 34(7):949–957.

Bird, P. (2003). An updated digital model of plate boundaries. *Geochemistry, Geophysics, Geosystems*, 4(3):1027.

Bird, P. and Li, Y. (1996). Interpolation of principal stress directions by nonparametric statistics: Global maps with confidence limits. *Journal of Geophysical Research*, 101(B3):5435–5443.

Boerner, D., Kurtz, R., Craven, J., Ross, G., and Jones, F. (2000). A synthesis of electromagnetic studies in the Lithoprobe Alberta Basement Transect: constraints on Paleoproterozoic indentation tectonics. *Canadian Journal of Earth Sciences*, 37(11):1509–1534.

Bott, M. H. P. (1959). The Mechanics of Oblique Slip Faulting. *Geol. Mag.*, 96(02):109–117.

Bouzidi, Y., Schmitt, D. R., Burwash, R. A., and Kanasewich, E. R. (2002). Depth migration of deep seismic reflection profiles: crustal thickness variations in Alberta. *Canadian Journal of Earth Sciences*, 39(3):331–350.

Brady, B. H. G. and Brown, E. T. (2004). *Rock Mechanics for Underground Mining*. Kluwer Academic Publishers, Dodrecht Boston London, 3 edition.

Brooker, E. W. and Ireland, H. O. (1965). Earth Pressures at Rest Related to Stress History. *Canadian Geotechnical Journal*, 2(1):1–15.

Brown, D. W. (2009). Hot dry rock geothermal energy: important lessons from Fenton Hill. In *Thirty-Fourth Workshop on Geothermal Reservoir Engineering*, pages 3–6, Stanford.

Brown, E. and Hoek, E. (1978). Trends in relationships between measured in-situ stresses and depth. *Int. J. Rock Mech. Min. Sci. & Geomech. Abstr*, 15:211–215.

Brudy, M. and Kjø rholt, H. (2001). Stress orientation on the Norwegian continental shelf derived from borehole failures observed in high-resolution borehole imaging logs. *Tectonophysics*, 337(1-2):65–84.

Brudy, M., Zoback, M. D., Fuchs, K., Rummel, F., and Baumgärtner, J. (1997). Estimation of the complete stress tensor to 8 km depth in the KTB scientific drill holes: Implications for crustal strength. *Journal of Geophysical Research*, 102(B8):18,453–18,475.

Buchbinder, G. G. R. (1985). Shear-wave splitting and anisotropy in the Charlevoix Seismic Zone, Quebec. *Geophysical Research Letters*, 12(7):425–428.

Buchbinder, G. G. R. (1990). Shear wave splitting and anisotropy from the aftershocks of the Nahanni, Northwest Territories, Earthquakes. *Journal of Geophysical Research*, 95(B4):4777–4785.

Buchmann, T. J. and Connolly, P. T. (2007). Contemporary kinematics of the Upper Rhine Graben: A 3D finite element approach. *Global and Planetary Change*, 58(1-4):287–309.

Burianyk, M. J., Kanasewich, E. R., and Udey, N. (1997). Broadside wide-angle seismic studies and three-dimensional structure of the crust in the southeast Canadian Cordillera. *Canadian Journal of Earth Sciences*, 34(8):1156–1166.

Byerlee, J. (1978). Friction of rocks. *Pure and Applied Geophysics PAGEOPH*, 116(4-5):615–626.

Camelbeeck, T., de Viron, O., Van Camp, M., and Kusters, D. (2013). Local stress sources in Western Europe lithosphere from geoid anomalies. *Lithosphere*, 5(3):235–246.

Célérier, B., Etchecopar, A., Bergerat, F., Vergely, P., Arthaud, F., and Laurent, P. (2012). Inferring stress from faulting: From early concepts to inverse methods. *Tectonophysics*, 581:206–219.

Chacko, T., De, S. K., Creaser, R. A., and Muehlenbachs, K. (2000). Tectonic setting of the Taltson magmatic zone at 1.9-2.0 Ga: a granitoid-based perspective. *Canadian Journal of Earth Sciences*, 37(11):1597–1609.

Chamorro, C. R., Mondéjar, M. E., Ramos, R., Segovia, J. J., Martín, M. C., and Villamañán, M. a. (2012). World geothermal power production status: Energy, environmental and economic study of high enthalpy technologies. *Energy*, 42(1):10–18.

Chapman, N., McKinley, I., and Hill, M. (1987). *The geological disposal of nuclear waste*. John Wiley and Sons Inc; New York, NY (USA).

Clark, J. (1949). A Hydraulic Process for Increasing the Productivity of Wells. *Journal of Petroleum Technology*, 1(01):1–8.

Clough, R. W. (1960). The finite element method in plane stress analysis. In *2nd Conference on Electronic Computation, A.S.C.E. Structural Division*, Pittsburgh, Pennsylvania.

Clowes, R. M., Burianyk, M. J., Gorman, A. R., and Kanasewich, E. R. (2002). Crustal velocity structure from SAREX, the southern Alberta refraction experiment. *Canadian Journal of Earth Sciences*, 39(3):351–373.

Coblentz, D. D. and Richardson, R. M. (1995). Statistical trends in the intraplate stress field. *Journal of Geophysical Research*, 100(B10):20245–20255.

Coblentz, D. D. and Richardson, R. M. (1996). Analysis of the South American intraplate stress field. *Journal of Geophysical Research*, 101(B4):8643.

Coblentz, D. D. and Sandiford, M. (1994). Tectonic stresses in the African plate: Constraints on the ambient lithospheric stress state. *Geology*, 22(9):831.

Corrigan, D., Hajnal, Z., Németh, B., and Lucas, S. (2005). Tectonic framework of a Paleoproterozoic arc-continent to continent-continent collisional zone, Trans-Hudson Orogen, from geological and seismic reflection studies. *Canadian Journal of Earth Sciences*, 42(4):421–434.

Coward, M. P., Spencer, R. M., and Spencer, C. E. (1995). Development of the Witwatersrand Basin, South Africa. *Geological Society, London, Special Publications*, 95(1):243–269.

Cox, J. (1972). The High-Resolution Dipmeter Reveals Dip-Related Borehole And Formation Characteristics. *Journal of Canadian Petroleum Technology*, 11(1):46–57.

Dalton, C. A., Gaherty, J. B., and Courtier, A. M. (2011). Crustal Vs structure in northwestern Canada: Imaging the Cordillera-craton transition with ambient noise tomography. *Journal of Geophysical Research*, 116(B12):B12315.

Deichmann, N., Ballarin Dolfin, D., and Kastrup, U. (2000). Seismizität der Nord- und Zentralschweiz (NAGRA NTB 00-05). Technical report, Nationale Genossenschaft für die Lagerung radioaktiver Abfälle.

Deichmann, N. and Ernst, J. (2009). Earthquake focal mechanisms of the induced seismicity in 2006 and 2007 below Basel (Switzerland). *Swiss Journal of Geosciences*, 102(3):457–466.

Du, W.-x., Kim, W.-Y., and Sykes, L. R. (2003). Earthquake Source Parameters and State of Stress for the Northeastern United States and Southeastern Canada from Analysis of Regional Seismograms. *Bulletin of the Seismological Society of America*, 93(4):1633–1648.

Duchane, D. and Brown, D. (2002). Hot dry rock (HDR) geothermal energy research and development at Fenton Hill, New Mexico. *Geo-Heat Centre Quarterly Bulletin*, 23(3):13–19.

Dusseault, M. B. and Yassir, N. A. (1994). Effects of rock anisotropy and heterogeneity on stress distributions at selected sites in North America. *Engineering Geology*, 37(3-4):181–197.

Dyksterhuis, S., Albert, R., and Müller, R. D. (2005). Finite-element modelling of contemporary and palaeo-intraplate stress using ABAQUS (TM). *Computers & Geosciences*, 31(3):297–307.

Dziewonski, A. M. and Woodhouse, J. H. (1983). An experiment in systematic study of global seismicity: Centroid-moment tensor solutions for 201 moderate and large earthquakes of 1981. *Journal of Geophysical Research*, 88(B4):3247–3271.

Eaton, D. W., Ross, G. M., and Hope, J. (1999). The rise and fall of a cratonic arch: A regional seismic perspective on the Peace River Arch, Alberta. *Bulletin of Canadian Petroleum Geology*, 47(4):346–361.

Edwards, S., Meredith, P., and Murrell, S. (1998). An Investigation of Leak-off Test Data for Estimating In-situ Stress Magnitudes: Application to a Basinwide Study in the North Sea. In *Proceedings of SPE/ISRM Rock Mechanics in Petroleum Engineering*, pages 357–365, Trondheim. Society of Petroleum Engineers.

Eisbacher, G. H. and Bielenstein, H. U. (1971). Elastic strain recovery in Proterozoic rocks near Elliot Lake, Ontario. *Journal of Geophysical Research*, 76(8):2012–2021.

Ekstrom, M., Dahan, C., Chen, M., Lloyd, P., and Rossi, D. (1987). Formation imaging with microelectrical scanning arrays. *The Log Analyst*, 28(3):13.

England, T. and Bustin, R. (1986). Effect of thrust faulting on organic maturation in the southeastern Canadian Cordillera. *Organic Geochemistry*, 10(1-3):609–616.

English, J. M. and Johnston, S. T. (2004). The Laramide Orogeny: What Were the Driving Forces? *International Geology Review*, 46(9):833–838.

Eriksson, P., Hattingh, P., and Altermann, W. (1995). An overview of the geology of the Transvaal Sequence and Bushveld Complex, South Africa. *Mineralium Deposita*, 30(2):98–111.

Fairhurst, C. (1964). Measurement of in-situ rock stresses. With particular reference to hydraulic fracturing. *Rock Mech.;(United States)*, 2.

Fernández-Viejo, G. and Clowes, R. M. (2003). Lithospheric structure beneath the Archaean Slave Province and Proterozoic Wopmay orogen, northwestern Canada, from a lithoprobe refraction/wide-angle reflection survey. *Geophysical Journal International*, 153(1):1–19.

Fischer, K. and Henk, A. (2013). A workflow for building and calibrating 3-D geomechanical models &ndash a case study for a gas reservoir in the North German Basin. *Solid Earth*, 4(2):347–355.

Flesch, L. M., Holt, W. E., Haines, A. J., Wen, L., and Shen-Tu, B. (2007). The dynamics of western North America: stress magnitudes and the relative role of gravitational potential energy, plate interaction at the boundary and basal tractions. *Geophysical Journal International*, 169(3):866–896.

Flóvenz, O. G. and Saemundsson, K. (1993). Heat flow and geothermal processes in Iceland. *Tectonophysics*, 225(1-2):123–138.

Flowers, R. M., Ault, A. K., Kelley, S. A., Zhang, N., and Zhong, S. (2012). Epeirogeny or eustasy? Paleozoic–Mesozoic vertical motion of the North American continental interior from thermochronometry and implications for mantle dynamics. *Earth and Planetary Science Letters*, 317-318:436–445.

Fordjor, C. K., Bell, J. S., and Gough, D. I. (1983). Breakouts in Alberta and stress in the North American plate. *Canadian Journal of Earth Sciences*, 20(9):1445–1455.

Forsyth, D. W. and Uyedaf, S. (1975). On the Relative Importance of the Driving Forces of Plate Motion. *Geophysical Journal International*, 43(1):163–200.

Fossen, H. (2010). *Structural Geology*. Cambridge University Press.

Frimmel, H. E. and Minter, W. (2002). Recent developments concerning the geological history and genesis of the Witwatersrand gold deposits, South Africa. In Goldfarb, R. J. and Nielsen, R. L., editors, *Integr. Methods Discov. Glob. Explor. Twenty-First Century*, volume 9, chapter 2, pages 17–45. Society of Economic Geologists.

Fuchs, K. and Müller, B. (2001). World Stress Map of the Earth : a key to tectonic processes and technological applications. *Naturwissenschaften*, 88(9):357–371.

Gabrielse, H. and Yorath, C. (1989). The Cordilleran Orogen in Canada. *Geoscience Canada*, 16(2):67–83.

Ganz, B., Schellschmidt, R., Schulz, R., and Sanner, B. (2013). Geothermal Energy Use in Germany. In *European Geothermal Congress 2013*, pages 1–16, Pisa, Italy.

Gardner, J. and Dumanoir, J. (1980). Litho-density log interpretation. In *SPWLA 21st Annual Logging Symposium*, pages 1–23, Lafayette, Louisiana. Society of Petrophysicists and Well-Log Analysts.

Gay, N. C. (1975). In-situ stress measurements in Southern Africa. *Tectonophysics*, 29(1-4):447–459.

Gay, N. C. (1979). The state of stress in a large dyke on E.R.P.M., Boksburg, South Africa. *Int. J. Rock Mech. Min. Sci. Geomech. Abstr.*, 16(3):179–185.

Gay, N. C. and Ortlepp, W. D. (1979). Anatomy of a mining-induced fault zone. *Geol. Soc. Am. Bull.*, 90(1):47.

Gephart, J. W. and Forsyth, D. W. (1984). An improved method for determining the regional stress tensor using earthquake focal mechanism data: Application to the San Fernando Earthquake Sequence. *Journal of Geophysical Research*, 89(B11):9305.

Gercek, H. (2007). Poisson's ratio values for rocks. *International Journal of Rock Mechanics and Mining Sciences*, 44(1):1–13.

Ghosh, A., Holt, W. E., and Flesch, L. M. (2009). Contribution of gravitational potential energy differences to the global stress field. *Geophysical Journal International*, 179(2):787–812.

Ghosh, A., Holt, W. E., and Wen, L. (2013). Predicting the lithospheric stress field and plate motions by joint modeling of lithosphere and mantle dynamics. *Journal of Geophysical Research: Solid Earth*, 118(1):346–368.

Gough, D. I. (1984). Mantle upflow under North America and plate dynamics. *Nature*, 311(5985):428–433.

Gough, D. I., Fordjor, C. K., and Bell, J. S. (1983). A stress province boundary and tractions on the North American plate. *Nature*, 305(5935):619–621.

Gray, A. D., Majorowicz, J., and Unsworth, M. (2012). Investigation of the geothermal state of sedimentary basins using oil industry thermal data: case study from Northern Alberta exhibiting the need to systematically remove biased data. *Journal of Geophysics and Engineering*, 9(5):534–548.

Grobe, M. (2000). Distribution and thickness of salt within the Devonian Elk Point Group. Technical report, Alberta Energy and Utilities Board, Alberta Geological Survey, Edmonton.

Gronseth, J. and Kry, P. (1983). Instaneous Shut-In Pressure and Its Relationship to the Minimum In-Situ Stress. In Zoback, M. D. and Haimson, B., editors, *Hydraulic Fracturing Stress Measurements*, pages 55–60. US Nat. Comm. Rock Mechanics, Nat. Acad. Press,.

Gu, Y. J., Okeler, A., Shen, L., and Contenti, S. (2011). The Canadian Rockies and Alberta Network (CRANE): New Constraints on the Rockies and Western Canada Sedimentary Basin. *Seismological Research Letters*, 82(4):575–588.

Gunzburger, Y. and Magnenet, V. (2014). Stress inversion and basement-cover stress transmission across weak layers in the Paris basin, France. *Tectonophysics*, 617:44–57.

Haimson, B. C. and Cornet, F. (2003). ISRM Suggested Methods for rock stress estimation—Part 3: hydraulic fracturing (HF) and/or hydraulic testing of pre-existing fractures (HTPF). *International Journal of Rock Mechanics and Mining Sciences*, 40(7-8):1011–1020.

Haimson, B. C. and Fairhurst, C. (1969). In-situ stress determination at great depth by means of hydraulic fracturing. In *The 11th U.S. Symposium on Rock Mechanics (USRMS), 16-19 June, Berkeley, California*, pages 559–584. American Rock Mechanics Association.

Haimson, B. C. and Song, I. (1993). Laboratory study of borehole breakouts in Cordova Cream: a case of shear failure mechanism. *International Journal of Rock Mechanics and Mining Sciences & Geomechanics Abstracts*, 30(7):1047–1056.

Hajnal, Z., Lewry, J., White, D. J., Ashton, K. E., Clowes, R. M., Stauffer, M., Gyorfi, I., and Takacs, E. (2005). The Sask Craton and Hearne Province margin: seismic reflection studies in the western Trans-Hudson Orogen. *Canadian Journal of Earth Sciences*, 42(4):403–419.

Halchuk, S. and Mereu, R. (1990). A seismic investigation of the crust and Moho underlying the Peace River Arch, Canada. *Tectonophysics*, 185(1-2):1–19.

Hall, R., Els, B., and Mayer, J. (1997). The Ventersdorp contact reef; final phase of the Witwatersrand Basin, independent formation, or precursor to the Ventersdorp Supergroup? *South African Journal of Geology*, 100(3):213–222.

Hamid, O. (2008). *In-Situ Stress Analysis of Southwest Saskatchewan.* Master thesis, Saskatchewan.

Hamilton, W., Langenberg, C., Price, M., and Chao, D. (1999). Geological Map of Alberta. Technical report, Alberta Geological Survey, Edmonton.

Hancock, P. L. (1991). Determining Contemporary Stress Directions from Neotectonic Joint Systems [and Discussion]. *Philosophical Transactions of the Royal Society A: Mathematical, Physical and Engineering Sciences*, 337(1645):29–40.

Hancock, P. L. and Engelder, T. (1989). Neotectonic joints. *Geological Society of America Bulletin*, 101(10):1197–1208.

Hansen, K. M. and Mount, V. S. (1990). Smoothing and extrapolation of crustal stress orientation measurements. *Journal of Geophysical Research*, 95(B2):1155–1165.

Harris, R. A. (1998). Introduction to Special Section: Stress Triggers, Stress Shadows, and Implications for Seismic Hazard. *J. Geophys. Res.*, 103(B10):24347.

Harris, R. A. and Simpson, R. W. (1992). Changes in static stress on southern California faults after the 1992 Landers earthquake. *Nature*, 360:251–254.

Hasegawa, H. S., Wetmiller, R. J., and Gendzwill, D. J. (1989). Induced seismicity in mines in Canada - An overview. *Pure Appl. Geophys. PAGEOPH*, 129(3-4):423–453.

Hawkes, C. D., Bachu, S., Haug, K., and Thompson, A. W. (2005). Analysis of in-situ stress regime in the Alberta Basin, Canada, for performance assessment of CO2 geological sequestration sites. In *Proceedings of the fourth annual conference on carbon capture and sequestration DOE/NETL*, page 22.

Healy, J. H. and Zoback, M. D. (1988). Hydraulic fracturing in situ stress measurements to 2.1 km depth at Cajon Pass, California. *Geophysical Research Letters*, 15(9):1005–1008.

Heidbach, O. and Ben-Avraham, Z. (2007). Stress evolution and seismic hazard of the Dead Sea Fault System. *Earth and Planetary Science Letters*, 257(1-2):299–312.

Heidbach, O., Hergert, T., Reinecker, J., Reiter, K., Giger, S., Vietor, T., and Marschall, P. (2013). In Situ Stress in Switzerland – From Pointwise Field Data to a 3D Continuous Quantification. In *International Workshop on Geomechanics and Energy - The Ground as Energy Source and Storage*, pages 1–4, Lausanne. EAGE.

Heidbach, O. and Reinecker, J. (2013). Analyse des rezenten Spannungsfeldes der Nordschweiz. Technical report, National Cooperative for the Disposal of Radioactive Waste (NAGRA).

Heidbach, O., Reinecker, J., Tingay, M. R. P., Müller, B., Sperner, B., Fuchs, K., and Wenzel, F. (2007). Plate boundary forces are not enough: Second- and third-order stress patterns highlighted in the World Stress Map database. *Tectonics*, 26(6):1–19.

Heidbach, O., Tingay, M. R. P., Barth, A., Reinecker, J., Kurfeß, D., and Müller, B. (2009). The World Stress Map Based on the Database Release 2008, equatorial scale 1:46,000,000. Technical Report 3, Commission for the Geological Map of the World, Paris.

Heidbach, O., Tingay, M. R. P., Barth, A., Reinecker, J., Kurfeß, D., and Müller, B. (2010). Global crustal stress pattern based on the World Stress Map database release 2008. *Tectonophysics*, 482(1-4):3–15.

Heim, A. (1878). *Untersuchungen über den Mechanismus der Gebirgsbildung: im Anschluss an die geologische Monographie der Tödi-Windgällen-Gruppe*. Benno Schwabe Verlagsbuchhandlung, Basel.

Henk, A. (2005). Pre-drilling prediction of the tectonic stress field with geomechanical models. *First Break*, 23(1089):53–57.

Henk, A. (2009). Perspectives of Geomechanical Reservoir Models–Why Stress is Important. *Oil Gas: European Magazine*, 35(1):1–5.

Henton, J. A., Craymer, M. R., Ferland, R., Dragert, H., Mazzotti, S., and Forbes, D. L. (2006). Crustal motion and deformation monitoring of the Canadian landmass. *Geomatica*, 60(2):173–191.

Hergert, T. and Heidbach, O. (2006). New insights into the mechanism of postseismic stress relaxation exemplified by the 23 June 2001 M w = 8.4 earthquake in southern Peru. *Geophysical Research Letters*, 33(2):3–6.

Hergert, T. and Heidbach, O. (2011). Geomechanical model of the Marmara Sea region-II. 3-D contemporary background stress field. *Geophysical Journal International*, 185(3):1090–1102.

Hickman, S. and Zoback, M. D. (2004). Stress orientations and magnitudes in the SAFOD pilot hole. *Geophysical Research Letters*, 31(15):L15S12.

Hickman, S. H. and Zoback, M. D. (1983). The interpretation of hydraulic fracturing pressure-time data for in situ stress determination. In Hickman, S. H. and Zoback, M. D., editors, *Hydraulic Fracturing Stress Measurements*, chapter 1.4, pages 44–54. Office of Earthquakes, Volcanoes, and Engineering.

Hodges, J. L. and Lehmann, E. L. (1967). On Medians and Quasi Medians. *Journal of the American Statistical Association*, 62(319):926–931.

Hoffman, P. F. (1989). Precambrian geology and tectonic history of North America. In *The Geology of North America*, pages 447–512. The Geological Society of America.

Hofmann, G., Ogasawara, H., Katsura, T., and Roberts, D. (2012). An Attempt to constrain the Stress and Strength of a Dyke that accomodated a Ml 2.1 Seismic Event. In *South. Hemisph. Int. Rock Mech. Symp. SHIRMS 2012*, pages 1–15. The Southern African Institute of Mining and Metallurgy.

Hofmann, G., Scheepers, L., and Ogasawara, H. (2013). Loading conditions of geological faults in deep level tabular mines. In Ito, T., editor, *Proc. 6th Int. Symp. In-Situ Rock Stress*, pages 560–580. Tohoku University, Sendai.

Hofmann, H., Weides, S., Babadagli, T., Zimmermann, G., Moeck, I., Majorowicz, J., and Unsworth, M. (2014). Potential for enhanced geothermal systems in Alberta, Canada. *Energy*, 69:578–591.

Horner, R. B. and Hasegawa, H. S. (1978). The seismotectonics of southern Saskatchewan. *Can. J. Earth Sci.*, 15(8):1341–1355.

Hottman, C., Smith, J., and Purcell, W. (1979). Relationship Among Earth Stresses, Pore Pressure, and Drilling Problems Offshore Gulf of Alaska. *Journal of Petroleum Technology*, 31(11).

Huang, J. and Véronneau, M. (2005). Applications of downward-continuation in gravimetric geoid modeling: case studies in Western Canada. *Journal of Geodesy*, 79(1-3):135–145.

Hubbert, M. K. and Willis, D. G. (1957). Mechanics of hydraulic fracturing. *AIME Trans*, 210:153–168.

Huenges, E. (2010). *Geothermal Energy Systems*. WILEY-VCH Verlag GmbH & Co. KGaA, Weinheim.

Humphreys, E. D. and Coblentz, D. D. (2007). North American dynamics and western U.S. tectonics. *Reviews of Geophysics*, 45(3):30.

Hurd, O. and Zoback, M. D. (2012). Intraplate earthquakes, regional stress and fault mechanics in the Central and Eastern U.S. and Southeastern Canada. *Tectonophysics*, 581:182–192.

Hyndman, R. D., Currie, C. A., Mazzotti, S., and Frederiksen, A. (2009). Temperature control of continental lithosphere elastic thickness, Te vs Vs. *Earth and Planetary Science Letters*, 277(3-4):539–548.

Jaeger, J., Cook, N., and Zimmerman, R. (2009). *Fundamentals of rock mechanics*. John Wiley & Sons.

Jaeger, J. C., Cook, N. G. W., and Zimmerman, R. W. (2007). *Fundamentals of Rock Mechanics*. Blackwell Publishing Ltd., Malden Oxford Carlton, 4th edition.

Jáky, J. (1944). The coefficient of earth pressure at rest. *Journal of the Society of Hungarian Architects and Engineers*, 78(22):355–358.

Jarosinski, M., Beekman, F., Bada, G., and Cloetingh, S. (2006). Redistribution of recent collision push and ridge push in Central Europe: insights from FEM modelling. *Geophysical Journal International*, 167(2):860–880.

Jenkins, G. and Kirkpatrick, J. (1979). Mbustion Project. *Journal of Canadian Petroleum Technology*, 18(2):85–94.

Jolley, S. J., Freeman, S., Barnicoat, A. C., Phillips, G., Knipe, R., Pather, A., Fox, N. P. C., Strydom, D., Birch, M., Henderson, I. H. C., and Rowland, T. (2004). Structural controls on Witwatersrand gold mineralisation. *Journal of Structural Geology*, 26(6-7):1067–1086.

Jones, M. Q. W. (1988). Heat flow in the Witwatersrand Basin and environs and its significance for the South African Shield Geotherm and lithosphere thickness. *J. Geophys. Res.*, 93(B4):3243–3260.

Kaiser, P., Mackay, C., and Morgenstern, N. (1982). Performance Of A Shaft In Weak Rock (Bearpa W Shale). In *ISRM International Symposium, 26-28 May, Aachen, Germany*, pages 613–622.

Kanamori, H. and Brodsky, E. E. (2004). The physics of earthquakes. *Reports on Progress in Physics*, 67(8):1429–1496.

Kao, H., Behr, Y., Currie, C. a., Hyndman, R. D., Townend, J., Lin, F.-C., Ritzwoller, M. H., Shan, S.-J., and He, J. (2013). Ambient seismic noise tomography of Canada and adjacent regions: Part I. Crustal structures. *Journal of Geophysical Research: Solid Earth*, 118(11):5865–5887.

Kim, W.-Y. (2003). The 18 June 2002 Caborn, Indiana, Earthquake: Reactivation of Ancient Rift in the Wabash Valley Seismic Zone? *Bulletin of the Seismological Society of America*, 93(5):2201–2211.

Kim, W.-Y., Dineva, S., Ma, S., and Eaton, D. W. (2006). The 4 August 2004, Lake Ontario, Earthquake. *Seismological Research Letters*, 77(1):65–73.

King, G. C. P., Stein, R. S., and Lin, J. (1994). Static stress changes and the triggering of earthquakes. *Bull. Seismol. Soc. Am.*, 84(3):935–953.

King, M. (1983). Static and dynamic elastic properties of rocks from the Canadian Shield. *International Journal of Rock Mechanics and Mining Sciences & Geomechanics Abstracts*, 20(5):237–241.

Kirby, J. F. and Swain, C. J. (2014). The long wavelength admittance and effective elastic thickness of the Canadian shield. *Journal of Geophysical Research: Solid Earth*, 119:28.

Klee, G. (2012). Geothermal borehole Schlattingen 1 - Hydraulic fracturing stress measurements -NPB 12-08. Technical report, Nationale Genossenschaft für die Lagerung radioaktiver Abfälle, Wettingen.

Konstantinovskaya, E., Malo, M., and Castillo, D. (2012). Present-day stress analysis of the St. Lawrence Lowlands sedimentary basin (Canada) and implications for caprock integrity during CO2 injection operations. *Tectonophysics*, 518-521:119–137.

Krantz, R. W. (1991). Measurements of friction coefficients and cohesion for faulting and fault reactivation in laboratory models using sand and sand mixtures. *Tectonophysics*, 188(1-2):203–207.

Krieger, L. and Heimann, S. (2012). MoPaD—moment tensor plotting and decomposition: a tool for graphical and numerical analysis of seismic moment tensors. *Seismol. Res. Lett.*, 83(3):589–595.

Kry, P. and Gronseth, J. (1983). In-situ Stresses And Hydraulic Fracturing In the Deep Basin. *Journal of Canadian Petroleum Technology*, 22(6):31–35.

Kwiatek, G. and Ben-Zion, Y. (2013). Assessment of P and S wave energy radiated from very small shear-tensile seismic events in a deep South African mine. *Journal of Geophysical Research: Solid Earth*, 118(7):3630–3641.

Kwiatek, G., Plenkers, K., Nakatani, M., Yabe, Y., and Dresen, G. (2010). Frequency-Magnitude Characteristics Down to Magnitude -4.4 for Induced Seismicity Recorded at Mponeng Gold Mine, South Africa. *Bull. Seismol. Soc. Am.*, 100(3):1165–1173.

Lam, H. and Jones, F. (1984). Geothermal gradients of Alberta in Western Canada. *Geothermics*, 13(3):181–192.

Laubscher, H. (1992). Jura kinematics and the Molasse Bassin. *Eclogae Geologicae Helvetiae*, 85(3):653–675.

Leckie, D. A. and Smith, D. G. (1992). Regional setting, evolution, and depositional cycles of the Western Canada Foreland Basin. In Macqueen, R. W. and Leckie, D. A., editors, *Foreland Basins and Fold Belts*, volume A136, chapter 1, pages 9–46. American Association of Petroleum Geologists.

Legarth, B., Huenges, E., and Zimmermann, G. (2005). Hydraulic fracturing in a sedimentary geothermal reservoir: Results and implications. *International Journal of Rock Mechanics and Mining Sciences*, 42(7-8):1028–1041.

Leonard, M. (2010). Earthquake Fault Scaling: Self-Consistent Relating of Rupture Length, Width, Average Displacement, and Moment Release. *Bull. Seismol. Soc. Am.*, 100(5A):1971–1988.

Li, G., Lorwongngam, A., and Roegiers, J. (2009). Critical Review Of Leak-Off Test As A Practice For Determination Of In-Situ Stresses. In *43rd US Rock Mechanics Symposium and 4th U.S.-Canada Rock Mechanics Symposium*, page 5, Asheville. American Rock Mechanics Association.

Li, Y. G., Leary, P. C., and Henyey, T. L. (1988). Stress orientation inferred from shear wave splitting in basement rock at Cajon Pass. *Geophysical Research Letters*, 15(9):997–1000.

Lindau, A. (2007). Gravity Information System. www.ptb.de/cartoweb3/SISproject.php. Online. Last accessed: 24 May 2013.

Lindner, E. N. and Halpern, J. A. (1978). In-situ stress in north America: A compilation. *International Journal of Rock Mechanics and Mining Sciences & Geomechanics Abstracts*, 15:183–203.

Ljunggren, C., Chang, Y., Janson, T., and Christiansson, R. (2003). An overview of rock stress measurement methods. *International Journal of Rock Mechanics and Mining Sciences*, 40(7-8):975–989.

Lucier, A. M., Zoback, M. D., Heesakkers, V., Reches, Z., and Murphy, S. K. (2009). Constraining the far-field in situ stress state near a deep South African gold mine. *Int. J. Rock Mech. Min. Sci.*, 46(3):555–567.

Ma, S., Eaton, D. W., and Adams, J. J. (2008). Intraplate Seismicity of a Recently Deglaciated Shield Terrane: A Case Study from Northern Ontario, Canada. *Bulletin of the Seismological Society of America*, 98(6):2828–2848.

Majer, E. L., Baria, R., Stark, M., Oates, S., Bommer, J., Smith, B., and Asanuma, H. (2007). Induced seismicity associated with Enhanced Geothermal Systems. *Geothermics*, 36(3):185–222.

Majorowicz, J., Chan, J., Crowell, J., Gosnold, W., Heaman, L. M., Kuck, J., Nieuwenhuis, G., Schmitt, D. R., Unsworth, M. J., Walsh, N., and Weides, S. (2014). The first deep heat flow determination in crystalline basement rocks beneath the Western Canadian Sedimentary Basin. *Geophysical Journal International*, 197(2):731–747.

Majorowicz, J., Gosnold, W., Gray, A. D., Safanda, J., Klenner, R., and Unsworth, M. J. (2012). Implications of post-glacial warming for Northern Alberta heat flow-correcting for the underestimate of the geothermal potential. *Geothermal Resources Council Transactions*, 36:693–698.

Majorowicz, J. and Grasby, S. E. (2010a). Heat flow, depth–temperature variations and stored thermal energy for enhanced geothermal systems in Canada. *Journal of Geophysics and Engineering*, 7(3):232–241.

Majorowicz, J. and Grasby, S. E. (2010b). High Potential Regions for Enhanced Geothermal Systems in Canada. *Natural Resources Research*, 19(3):177–188.

Majorowicz, J. and Grasby, S. E. (2010c). High Potential Regions for Enhanced Geothermal Systems in Canada. *Natural Resources Research*, 19(3):177–188.

Majorowicz, J. and Moore, M. (2008). Enhanced Geothermal Systems (EGS) potential in the Alberta Basin. Technical Report July, The Institute for Sustainable Energy, Environment and Economy (ISEEE), Calgary.

Malan, D. F. (1999). Time-dependent Behaviour of Deep Level Tabular Excavations in Hard Rock. *Rock Mechanics and Rock Engineering*, 32(2):123–155.

Mallet, J.-L. (1992). Discrete smooth interpolation in geometric modelling. *Computer-Aided Design*, 24(4):178–191.

Mallet, J.-L. (2002). *Geomodeling*. Oxford University Press, Inc. New York, NY, USA.

Mardia, K. (1972). *Statistics of directional data*. Academic Press (London and New York).

MatWeb LLC (2013). MatWeb - Material property data. http://www.matweb.com. Online. Last accessed: 10 April 2013.

Mavko, G., Mukerji, T., and Dvorkin, J. (2009). *The rock physics handbook: Tools for seismic analysis of porous media*. Cambridge University Press, Cambridge.

Mayne, P. W. and Kulhawy, F. H. (1982). Ko - OCR Relationships in Soil. *Journal of the Geotechnical Engineering Division*, 108(6):851–872.

Mazurek, M., Hurford, A. J., and Leu, W. (2006). Unravelling the multi-stage burial history of the Swiss Molasse Basin: integration of apatite fission track, vitrinite reflectance and biomarker isomerisation analysis. *Basin Research*, 18(1):27–50.

Mazzotti, S. and Hyndman, R. D. (2002). Yakutat collision and strain transfer across the northern Canadian Cordillera. *Geology*, 30(6):495.

Mazzotti, S., Leonard, L. J., Cassidy, J. F., Rogers, G. C., and Halchuk, S. (2011). Seismic hazard in western Canada from GPS strain rates versus earthquake catalog. *Journal of Geophysical Research*, 116(B12):B12310.

Mazzotti, S. and Townend, J. (2010). State of stress in central and eastern North American seismic zones. *Lithosphere*, 2(2):76–83.

McCloskey, J., Nalbant, S. S., and Steacy, S. (2005). Earthquake risk from co-seismic stress. *Nature*, 434(17. March 2005):291–291.

McGarr, A. (1971). Violent deformation of rock near deep-level, tabular excavations—seismic events. *Bull. Seismol. Soc. Am.*, 61(5):1453–1466.

McGarr, A. (1982). Analysis of states of stress between provinces of constant stress. *Journal of Geophysical Research*, 87(B11):9279.

McGarr, A. and Gay, N. C. (1978). State of stress in the earth's crust. *Annual Review of Earth and Planetary Sciences*, 6:405–436.

McGarr, A., Spottiswoode, S. M., and Gay, N. C. (1975). Relationship of mine tremors to induced stresses and to rock properties in the focal region. *Bull. Seismol. Soc. Am.*, 65(4):981–993.

McKenzie, D. (1969). The relation between fault plane solutions for earthquakes and the directions of the principal stresses. *Bulletin of the Seismological Society of America*, 2:591–601.

McLellan, P. (1987). In-Situ Stress Prediction And Measurement By Hydraulic Fracturing, Wapiti, Alberta. In *Proceedings of Annual Technical Meeting*, pages 967–933, Calgary. Society of Petroleum Engineers.

McMechan, M. E. and Price, R. A. (1982). Transverse folding and superposed deformation, Mount Fisher area, southern Canadian Rocky Mountain thrust and fold belt. *Canadian Journal of Earth Sciences*, 19(5):1011–1024.

Meijer Drees, N. C. (1994). Devonian Elk Point Group of the Western Canada Sedimentary Basin. In Mossop, G. D. and Shetsen, I., editors, *Geological atlas of the Western Canada Sedimentary Basin*, chapter 10, pages 129–147. Canadian Society of Petroleum Geologists and Alberta Research Council, Alberta.

Michael, A. J. (1987). Use of focal mechanisms to determine stress: A control study. *Journal of Geophysical Research*, 92(B1):357–368.

Michael, K. and Buschkuehle, M. (2008). Subsurface characterization of acid-gas injection operations in the Peace River Arch Area. *Energy Resources Conservation Board, ERCB/AGS Special Report 090*, pages 1–186.

Miller, W., Alexander, R., Chapman, N., McKinley, J. C., and Smellie, J. (2000). *Geological Disposal of Radioactive Wastes and Natural Analogues*. Elsevier Science Ltd.

Moeck, I. and Backers, T. (2011). Fault reactivation potential as a critical factor during reservoir stimulation. *First Break*, 29(1789):73 – 80.

Moeck, I., Kwiatek, G., and Zimmermann, G. (2009). Slip tendency analysis, fault reactivation potential and induced seismicity in a deep geothermal reservoir. *Journal of Structural Geology*, 31(10):1174–1182.

Moeck, I. S. (2014). Catalog of geothermal play types based on geologic controls. *Renewable and Sustainable Energy Reviews*, 37:867–882.

Monger, J. and Price, R. A. (2002). The Canadian Cordillera: geology and tectonic evolution. *CSEG Recorder*, 27:17–36.

Monger, J., Souther, J., and Gabrielse, H. (1972). Evolution of the Canadian Cordillera; a plate-tectonic model. *American Journal of Science*, 272(7):577–602.

Morris, A., Ferrill, D. A., and Henderson, D. B. (1996). Slip-tendency analysis and fault reactivation. *Geology*, 24(3):275.

Mossop, G. D. and Shetsen, I., editors (1994a). *Geological atlas of the Western Canada Sedimentary Basin*. Canadian Society of Petroleum Geologists and Alberta Research Council.

Mossop, G. D. and Shetsen, I. (1994b). Introduction to the Geological Atlas of the western canada sedimentary basin. In Mossop, G. D. and Shetsen, I., editors, *Geological atlas of the Western Canada Sedimentary Basin*, chapter 1, pages 1–11. Canadian Society of Petroleum Geologists and Alberta Research Council, Alberta.

Müller, B., Wehrle, V., Hettel, S., Sperner, B., and Fuchs, K. (2003). A new method for smoothing orientated data and its application to stress data. *Geological Society, London, Special Publications*, 209(1):107–126.

Müller, B., Wehrle, V., Zeyen, H., and Fuchs, K. (1997). Short-scale variations of tectonic regimes in the western European stress province north of the Alps and Pyrenees. *Tectonophysics*, 275(1-3):199–219.

NAGRA (2001). Sondierbohrung Benken Untersuchungsbericht (NAGRA NTB 00-01). Technical report, Nationale Genossenschaft für die Lagerung radioaktiver Abfälle.

NAGRA (2008). Vorschlag geologischer Standortgebiete für das SMA- und das HAA-Lager. Geologische Grundlagen - NTB 08-04. Technical report, Nationale Genossenschaft für die Lagerung radioaktiver Abfälle, Wettingen.

Nakamura, K. (1977). Volcanoes as possible indicators of tectonic stress orientation — principle and proposal. *Journal of Volcanology and Geothermal Research*, 2(1):1–16.

Nakamura, K., Jacob, K. H., and Davies, J. N. (1977). Volcanoes as possible indicators of tectonic stress orientation — Aleutians and Alaska. *Pure and Applied Geophysics*, 115(1-2):87–112.

Nakatani, M., Yabe, Y., Philipp, J., Morema, M., Stanchits, S., Dresen, G., and JAGUARS Research Group (2008). Acoustic emission measurements in a deep gold mine in South Africa: Project overview and some typical waveforms. *Seismol. Res. Lett.*, 79(2):311.

Naliboff, J., Lithgow-Bertelloni, C., Ruff, L., and de Koker, N. (2012). The effects of lithospheric thickness and density structure on Earth's stress field. *Geophysical Journal International*, 188(1):1–17.

Naoi, M., Nakatani, M., Yabe, Y., Kwiatek, G., Igarashi, T., and Plenkers, K. (2011). Twenty Thousand Aftershocks of a Very Small (M 2) Earthquake and Their Relation to the Mainshock Rupture and Geological Structures. *Bull. Seismol. Soc. Am.*, 101(5):2399–2407.

Naoi, M., Nakatani, M., Yabe, Y., and Philipp, J. (2008). Very high frequency AE (up to 200 kHz) and microseismicity observation in a deep South African gold mine-evaluation of the acoustic properties of the site by in-situ test -. *Seism. Res. Lett.*, 79(2):330.

Németh, B., Clowes, R. M., and Hajnal, Z. (2005). Lithospheric structure of the Trans-Hudson Orogen from seismic refraction - wide-angle reflection studies. *Canadian Journal of Earth Sciences*, 42(4):435–456.

Németh, B., Hajnal, Z., and Lucas, S. (1996). Moho signature from wide-angle reflections: preliminary results of the 1993 Trans-Hudson Orogen refraction experiment. *Tectonophysics*, 264(1-4):111–121.

Norris, A. (1986). Review of Hudson Platform Paleozoic stratigraphy and biostratigraphy. In Martini, I. P., editor, *Canadian Inland Seas*, pages 494–503. Elsevier Science Publishing Company INC.

NRCan (2009). Atlas of Canada 6th Edition — Geological Provinces.

Nurkowski, J. R. (1984). Coal Quality, Coal Rank Variation and its Relation to Reconstructed Overburden, Upper Cretaceous and Tertiary Plains Coals, Alberta, Canada. *AAPG Bulletin*, 68(3):285–295.

Oakey, G. N. and Stephenson, R. (2008). Crustal structure of the Innuitian region of Arctic Canada and Greenland from gravity modelling: implications for the Palaeogene Eurekan orogen. *Geophysical Journal International*, 173(3):1039–1063.

Obert, L. (1962). In situ determination of stress in rock. *Mining Engineer*, 14:51–58.

Okrusch, M. and Matthes, S. (2005). *Mineralogie*. Springer-Lehrbuch. Springer-Verlag, Berlin/Heidelberg.

Orlecka-Sikora, B., Lasocki, S., Lizurek, G., and Rudziński, u. (2012). Response of seismic activity in mines to the stress changes due to mining induced strong seismic events. *International Journal of Rock Mechanics and Mining Sciences*, 53:151–158.

Orlic, B. and Wassing, B. B. T. (2012). A Study of Stress Change and Fault Slip in Producing Gas Reservoirs Overlain by Elastic and Viscoelastic Caprocks. *Rock Mechanics and Rock Engineering*, 46(3):421–435.

Ortlepp, W. D. (1992). Note on fault-slip motion inferred from a study of micro-cataclastic particles from an underground shear rupture. *Pure Appl. Geophys. PAGEOPH*, 139(3-4):677–695.

Ortlepp, W. D. (2001). Thoughts on the rockburst source mechanism based on observations of the mine-induced shear rupture. In *Proc. 5th Int. Symp. Rockbursts Seism. Mines*. South African Institute of Mining and Metallurgy.

Parsons, T. (2006). Tectonic stressing in California modeled from GPS observations. *Journal of Geophysical Research*, 111(B3):1–16.

Paschen, H., Oertel, D., and Grünwald, R. (2003). Möglichkeiten geothermischer Stromerzeugung in Deutschland. Technical Report 84, Büro für Technikfolgen-Abschätzung beim Deutschen Bundestag (TAB).

Pathak, V., Babadagli, T., Majorowicz, J. a., and Unsworth, M. J. (2013). Evaluation of Engineered Geothermal Systems as a Heat Source for Oil Sands Production in Northern Alberta. *Natural Resources Research*, 23(2):247–265.

Peska, P. and Zoback, M. D. (1995). Compressive and tensile failure of inclined well bores and determination of in situ stress and rock strength. *Journal of Geophysical Research*, 100(B7):12791–12811.

Plenkers, K., Kwiatek, G., Nakatani, M., and Dresen, G. (2010). Observation of Seismic Events with Frequencies f $>$ 25 kHz at Mponeng Deep Gold Mine, South Africa. *Seismological Research Letters*, 81(3):467–479.

Plumb, R. A. and Hickman, S. H. (1985). Stress-induced borehole elongation: A comparison between the four-arm dipmeter and the borehole televiewer in the Auburn Geothermal Well. *Journal of Geophysical Research*, 90(B7):5513–5521.

Podruski, J. (1988). Contrasting character of the Peace River and Sweetgrass Arches, Western Canada Sedimentary Basin. *Geoscience Canada*, 15(2):94–97.

Pollock, J. C., Hibbard, J. P., and Staal, C. R. V. (2012). A paleogeographical review of the peri-Gondwanan realm of the Appalachian orogen. *Canadian Journal of Earth Sciences*, 288(1):259–288.

Porter, J. W., Price, R. A., and McCrossan, R. G. (1982). The Western Canada Sedimentary Basin. *Philosophical Transactions of the Royal Society of London*, 305(1489):169–192.

Poujol, M., Robb, L. J., and Respaut, J. (1999). U–Pb and Pb–Pb isotopic studies relating to the origin of gold mineralization in the Evander Goldfield, Witwatersrand Basin, South Africa. *Precambrian Research*, 95(3-4):167–185.

Poulton, T., Christopher, J., Hays, B., Losert, J., Tittemore, J., and Gilchrist, R. (1994). Jurassic and Lowermost Cretaceous Strata of the Western Canada Sedimentary Basin. In Mossop, G. D. and Shetsen, I., editors, *Geological atlas of the Western Canada Sedimentary Basin*, chapter 18, pages 297–316. Canadian Society of Petroleum Geologists and Alberta Research Council, Alberta.

Pretorius, D. A. (1976). The nature of Witwatersrand gold-uranium deposits. In Wolf, K. H., editor, *Handb. Strat. Stratif. ore Depos. - Au, U, Fe, Mn, Hg, Sb, W P Depos. - Vol. 7*, chapter 2, page 656. Elsevier Scientific Publishing Company, Amsterdam Oxford New York.

Price, R. (1981a). The Cordilleran foreland thrust and fold belt in the southern Canadian Rocky Mountains. In McClay, K. R. and Price, R. A., editors, *Thrust and Nappe Tectonics*, pages 427–448. The Geological Society of London.

Price, R. A. (1981b). The Cordilleran foreland thrust and fold belt in the southern Canadian Rocky Mountains. *Geological Society, London, Special Publications*, 9(1):427–448.

Price, R. A. (1986). The southeastern Canadian Cordillera: Thrust faulting, tectonic wedging, and delamination of the lithosphere. *Journal of Structural Geology*, 8(3-4):239–254.

Price, R. A. (1994). Cordilleran Tectonics and the Evolution of the Western Canada Sedimentary Basin. In Mossop, G. D. and Shetsen, I., editors, *Geological atlas of the Western Canada Sedimentary Basin*, chapter 2, pages 13–24. Canadian Society of Petroleum Geologists and Alberta Research Council.

Prinsloo, L. (2011). South African mine deaths down 24 % in 2010. *Min. Wkly.*, 27(January 2011).

Pytel, W. (2003). Rock mass—mine workings interaction model for Polish copper mine conditions. *Int. J. Rock Mech. Min. Sci.*, 40(4):497–526.

Raleigh, C. B., Healy, J. H., and Bredehoeft, J. D. (1972). Faulting and Crustal Stress at Rangely , Colorado. In Heard, H. C., Borg, I. Y., Carter, N. L., and Raleigh, C. B., editors, *Flow and Fracture of Rocks*, volume 16, pages 275–284. U.S. Geological Survey.

Ratanaruamkarn, S., Niewiadomska-Bugaj, M., and Wang, J.-C. (2009). A New Estimator of a Circular Median. *Communications in Statistics - Simulation and Computation*, 38(6):1269–1291.

Rebaï, S., Philip, H., and Taboada, A. (1992). Modern tectonic stress field in the Mediterranean region: evidence for variation in stress directions at different scales. *Geophysical Journal International*, 110(1):106–140.

Reinecker, J., Tingay, M. R. P., and Müller, B. (2003). Borehole breakout analysis from four-arm caliper logs. Technical report, World Stress Map Project.

Reinecker, J., Tingay, M. R. P., Müller, B., and Heidbach, O. (2010). Present-day stress orientation in the Molasse Basin. *Tectonophysics*, 482(1-4):129–138.

Reiter, K. and Heidbach, O. (2014). 3-D geomechanical–numerical model of the contemporary crustal stress state in the Alberta Basin (Canada). *Solid Earth*, 5(2):1123–1149.

Reiter, K., Heidbach, O., and Moeck, I. (2013). Stress Field Modelling in the Alberta Basin, Canada. In *International Workshop on Geomechanics and Energy - The Ground as Energy Source and Storage*, pages 26–28, Lausanne. EAGE.

Reiter, K., Heidbach, O., Schmitt, D., Haug, K., Ziegler, M., and Moeck, I. (2014). A revised crustal stress orientation database for Canada. *Tectonophysics*, 636:111–124.

Renner, J., Hettkamp, T., and Rummel, F. (2000). Rock Mechanical Characterization of an Argillaceous Host Rock of a Potential Radioactive Waste Repository. *Rock Mechanics and Rock Engineering*, 33(3):153–178.

Richardson, R. M. (1992). Ridge forces, absolute plate motions, and the intraplate stress field. *Journal of Geophysical Research*, 97(B8):11739–11748.

Richardson, R. M. and Reding, L. M. (1991). North American Plate Dynamics. *Journal of Geophysical Research*, 96(B7):12201–12223.

Richardson, R. M., Solomon, S. C., and Sleep, N. H. (1976). Intraplate stress as an indicator of plate tectonic driving forces. *Journal of Geophysical Research*, 81(11):1847–1856.

Ristau, J., Rogers, G. C., and Cassidy, J. F. (2007). Stress in western Canada from regional moment tensor analysis. *Canadian Journal of Earth Sciences*, 44(2):127–148.

Robb, L. J., Davis, D. W., Kamo, S. L., and Meyer, F. (1992). Ages of altered granites adjoining the Witwatersrand Basin with implications for the origin of gold and uranium. *Nature*, 357(6380):677–680.

Roberts, M. and Schweitzer, J. (1999). Geotechnical areas associated with the Ventersdorp Contact Reef, Witwatersrand Basin, South Africa. *Journal of the South African Institute of Mining and Metallurgy*, 99(3):157–166.

Roche, V., Homberg, C., and Rocher, M. (2013). Fault nucleation, restriction, and aspect ratio in layered sections: Quantification of the strength and stiffness roles using numerical modeling. *Journal of Geophysical Research: Solid Earth*, 118(8):4446–4460.

Röckel, T. and Lempp, C. (2003). Der Spannungszustand im Norddeutschen Becken. *Erdöl Erdgas Kohle*, 119(2):73–80.

Ross, G. M., Broome, J., and Miles, W. (1994). Potential Fields and Basement Structure - Western Canada Sedimentary Basin. In Mossop, G. D. and Shetsen, I., editors, *Geological atlas of the Western Canada Sedimentary Basin*, chapter 4, pages 41–47. Canadian Society of Petroleum Geologists and Alberta Research Council, Alberta.

Ross, G. M., Eaton, D. W., Boerner, D. E., and Miles, W. (2000). Tectonic entrapment and its role in the evolution of continental lithosphere: An example from the Precambrian of western Canada. *Tectonics*, 19(1):116–134.

Ross, M., Parent, M., and Lefebvre, R. (2004). 3D geologic framework models for regional hydrogeology and land-use management: a case study from a Quaternary basin of southwestern Quebec, Canada. *Hydrogeology Journal*, 13(5-6):690–707.

Roth, F. and Fleckenstein, P. (2001). Stress orientations found in north-east Germany differ from the West European trend. *Terra Nova*, 13(4):289–296.

Ruppert, N. A. (2008). Stress Map for Alaska From Earthquake Focal Mechanisms. *Geophysical monograph*, 179:351–367.

Rutqvist, J., Tsang, C.-F., and Stephansson, O. (2000). Uncertainty in the maximum principal stress estimated from hydraulic fracturing measurements due to the presence of the induced fracture. *International Journal of Rock Mechanics and Mining Sciences*, 37(1-2):107–120.

Ryder, J. A. (1988). Excess shear stress in the assessment of geologically hazardous situations. *J. South African Inst. Min. Metall.*, 88(1):27–39.

Sami, T. T. and James, N. P. (1993). Evolution of an early Proterozoic foreland basin carbonate platform, lower Pethei Group, Great Slave Lake, north-west Canada. *Sedimentology*, 40(3):403–430.

Saucier, F., Humphreys, E., and Weldon, R. (1992). Stress near geometrically complex strike-slip faults: Application to the San Andreas Fault at Cajon Pass, southern California. *Journal of Geophysical Research*, 97(B4):5081–5094.

Savage, W. Z. and Morin, R. H. (2002). Topographic stress perturbations in southern Davis Mountains, west Texas 1. Polarity reversal of principal stresses. *Journal of Geophysical Research*, 107(B12):2339.

Sbar, M. L. and Sykes, L. R. (1973). Contemporary Compressive Stress and Seismicity in Eastern North America: An Example of Intra-Plate Tectonics. *Geological Society of America Bulletin*, 84(6):1861–1882.

Scheidegger, A. (1962). Stresses in the earth's crust as determined from hydraulic fracturing data. *Geologie und Bauwesen*, 27(2).

Schellschmidt, R., Sanner, B., Pester, S., and Schulz, R. (2010). Geothermal Energy Use in Germany. In *Proceedings World Geothermal Congress. 2010*, pages 25–29, Bali, Indonesia.

Schmitt, D. R., Currie, C. A., and Zhang, L. (2012). Crustal stress determination from boreholes and rock cores: Fundamental principles. *Tectonophysics*, 580:1–26.

Schultz, R., Stern, V., and Gu, Y. J. (2014). An investigation of seismicity clustered near the Cordel Field, west-central Alberta and its relation to a nearby disposal well. *Journal of Geophysical Research: Solid Earth*, 119:1–14.

Scoates, J. S. and Friedman, R. M. (2008). Precise age of the platiniferous Merensky Reef, Bushveld Complex, South Africa, by the U-Pb zircon chemical abrasion ID-TIMS technique. *Economic Geology*, 103(3):465–471.

Segall, P. (1989). Earthquakes triggered by fluid extraction. *Geology*, 17(10):942–946.

Sheorey, P. (1994). A theory for In Situ stresses in isotropic and transverseley isotropic rock. *International Journal of Rock Mechanics and Mining Sciences & Geomechanics Abstracts*, 31(1):23–34.

Shragge, J., Bostock, M. G., Bank, C.-G., and Ellis, R. M. (2002). Integrated teleseismic studies of the southern Alberta upper mantle. *Canadian Journal of Earth Sciences*, 39(3):399–411.

Sibson, R. H. (1985). A note on fault reactivation. *Journal of Structural Geology*, 7(6):751–754.

Sigloch, K. and Mihalynuk, M. G. (2013). Intra-oceanic subduction shaped the assembly of Cordilleran North America. *Nature*, 496(7443):50–56.

Sikaneta, S. and Evans, K. (2012). Stress heterogeneity and natural fractures in the Basel EGS granite reservoir inferred from an acoustic televiewer log of the Basel-1 well. In *37th Workshop on Geothermal Reservoir Engineering Stanford University*, page 12.

Simpson, R. W. (1997). Quantifying Anderson's fault types. *Journal of Geophysical Research*, 102(B8):17909–17919.

Smart, K. J., Ofoegbu, G. I., Morris, A. P., McGinnis, R. N., and Ferrill, D. A. (2014). Geomechanical modeling of hydraulic fracturing: Why mechanical stratigraphy, stress state, and pre-existing structure matter. *AAPG Bulletin*, 98(11):2237–2261.

Smith, D. (1994). Paleogeographic Evolution of the Western Canada Foreland Basin. In Mossop, G. D. and Shetsen, I., editors, *Geological atlas of the Western Canada Sedimentary Basin*, chapter 17, pages 227–296. Canadian Society of Petroleum Geologists and Alberta Research Council, Alberta.

Spence, G. D. and McLean, N. a. (1998). Crustal seismic velocity and density structure of the Intermontane and Coast belts, southwestern Cordillera. *Canadian Journal of Earth Sciences*, 35(12):1362–1379.

Sperner, B., Müller, B., Heidbach, O., Delvaux, D., Reinecker, J., and Fuchs, K. (2003). Tectonic stress in the Earth's crust: advances in the World Stress Map project. *Geological Society Special Publication*, 212:101–116.

Stacey, T. and Wesseloo, J. (2002). Application of indirect stress measurement techniques (non strain gauge based technology) to quantify stress environments in mines. Technical Report March, The University of the Witwatersrand & SRK Consulting.

Stanchits, S., Dresen, G., and JAGUARS Research Group (2010). Formation of Faults in Diorite and Quartzite Samples Extracted From a Deep Gold Mine (South Africa). In *Geophys. Res. Abstr.*, volume 12, page 5605.

Steffen, R., Eaton, D. W., and Wu, P. (2012). Moment tensors, state of stress and their relation to post-glacial rebound in northeastern Canada. *Geophysical Journal International*, 189(3):1741–1752.

Stein, R. S. (1999). The role of stress transfer in earthquake occurrence. *Nature*, 402(6762):605–609.

Stephansson, O. and Berner, H. (1971). The finite element method in tectonic processes. *Physics of the Earth and Planetary Interiors*, 4(4):301–321.

StLouisEQcenter (2010). St. Louis University Earthquake Center.

Stock, J. M., Healy, J. H., Hickman, S. H., and Zoback, M. D. (1985). Hydraulic Fracturing Stress Measurements at Yucca Mountain, Nevada, and Relationship to the Regional Stress Field. *Journal of Geophysical Research*, 90(B10):8691–8706.

Tester, J. W., Anderson, B. J., Batchelor, A. S., Blackwell, D. D., DiPippo, R., Drake, E. M., Garnish, J., Livesay, B., Moore, M. C., Nichols, K., Petty, S., Toksöz, M. N., and Veatch Jr., R. W. (2006). The Future of Geothermal Energy. Technical Report November, Idaho National Laboratory.

Thompson, A. (2010). Geothermal Development in Canada: Country Update. In *World Geothermal Congress 2010*, pages 1–3, Bali, Indonesia.

Tingay, M. R. P., Hillis, R. R., Morley, C. K., Swarbrick, R. E., and Drake, S. J. (2005a). Present-day stress orientation in Brunei: a snapshot of 'prograding tectonics' in a Tertiary delta. *Journal of the Geological Society, London*, 162:39–49.

Tingay, M. R. P., Müller, B., Reinecker, J., Heidbach, O., Wenzel, F., and Fleckenstein, P. (2005b). Understanding tectonic stress in the oil patch: The World Stress Map Project. *The Leading Edge*, 24(12):1276–1282.

Tingay, M. R. P., Reinecker, J., and Müller, B. (2008). Borehole breakout and drilling-induced fracture analysis from image logs. Technical report, World Stress Map Project.

Turcotte, D. L. and Schubert, G. (2002). *Geodynamics*. Cambridge University Press.

Turner, M., Clough, R., Martin, H., and Topp, L. (1956). Stiffness and Deflection Analysis of Complex Structures. *Journal of the Aeronautical Sciences*, 23(9):805–823.

Upton, G. and Cook, I. T. (1996). *Understanding statistics*. Oxford University Press.

USGS (2008). GTOPO30 - Global Land Survey Digital Elevation Model (GLSDEM).

Van der Westhuizen, W., De Bruiyn, H., and Meintjes, P. G. (1991). The Ventersdorp supergroup: an overview. *J. African Earth Sci. (and Middle East)*, 13(1):83–105.

Van Wees, J. D., Orlic, B., Van Eijs, R., Zijl, W., Jongerius, P., Schreppers, G. J., Hendriks, M., and Cornu, T. (2003). Integrated 3D geomechanical modelling for deep subsurface deformation: a case study of tectonic and human-induced deformation in the eastern Netherlands. *Geological Society, London, Special Publications*, 212(1):313–328.

Véronneau, M. (1997). The GSD95 geoid model for Canada. Technical report, Geodetic Survey Division, Dept. of Natural Resources, Ottawa.

Wahlstrom, R. (1987). The North Gower, Ontario, Earthquake of 11 October 1983: Focal Mechanism and Aftershocks. *Seismological Research Letters*, 58(3):65–72.

Waldhauser, F., Lippitsch, R., Kissling, E., and Ansorge, J. (2002). High-resolution teleseismic tomography of upper-mantle structure using an a priori three-dimensional crustal model. *Geophysical Journal International*, 150(2):403–414.

Wang, Z., Nur, A., and Ebrom, D. (2000). Seismic and Acoustic Velocities in Reservoir Rocks: Volume 3, Recent Developments. *Expl. Geophys*, 3.

Warpinski, N. (1989). Determining the minimum in situ stress from hydraulic fracturing through perforations. *International Journal of Rock Mechanics and Mining Sciences & Geomechanics Abstracts*, 26(6):523–531.

Warren, W. E. and Smith, C. W. (1985). In situ stress estimates from hydraulic fracturing and direct observation of crack orientation. *Journal of Geophysical Research*, 90(B8):6829.

Weides, S. and Majorowicz, J. (2014). Implications of Spatial Variability in Heat Flow for Geothermal Resource Evaluation in Large Foreland Basins: The Case of the Western Canada Sedimentary Basin. *Energies*, 7(4):2573–2594.

Weides, S., Moeck, I., Majorowicz, J., and Grobe, M. (2014a). The Cambrian Basal Sandstone Unit in central Alberta – an investigation of temperature distribution, petrography and hydraulic and geomechanical properties of a deep saline aquifer. *Canadian Journal of Earth Sciences*, 51(8):783–796.

Weides, S., Moeck, I., Majorowicz, J., Palombi, D., Grobe, M., and Mareschal, J.-C. (2013). Geothermal exploration of Paleozoic formations in Central Alberta. *Canadian Journal of Earth Sciences*, 50(5):519–534.

Weides, S. N., Moeck, I. S., Schmitt, D. R., and Majorowicz, J. a. (2014b). An integrative geothermal resource assessment study for the siliciclastic Granite Wash Unit, northwestern Alberta (Canada). *Environmental Earth Sciences*.

Welford, J. K., Clowes, R. M., Ellis, R. M., Spence, G. D., Asudeh, I., and Hajnal, Z. (2001). Lithospheric structure across the craton-Cordilleran transition of northeastern British Columbia. *Canadian Journal of Earth Sciences*, 38:1169–1189.

Wessel, P., Smith, W. H. F., Scharroo, R., Luis, J., and Wobbe, F. (2013). Generic Mapping Tools: Improved Version Released. *Eos, Transactions American Geophysical Union*, 94(45):409–410.

Wessling, S., Junker, R., Rutqvist, J., Silin, D., Sulzbacher, H., Tischner, T., and Tsang, C.-F. (2009). Pressure analysis of the hydromechanical fracture behaviour in stimulated tight sedimentary geothermal reservoirs. *Geothermics*, 38(2):211–226.

White, A. J., Traugott, M. O., and Swarbrick, R. E. (2002). The use of leak-off tests as means of predicting minimum in-situ stress. *Petroleum Geoscience*, 8(2):189–193.

White, D. J., Thomas, M., Jones, A., Hope, J., Németh, B., and Hajnal, Z. (2005). Geophysical transect across a Paleoproterozoic continent continent collision zone: The Trans-Hudson Orogen. *Canadian Journal of Earth Sciences*, 42(4):385–402.

Woodland, D. and Bell, J. S. (1989). In Situ Stress Magnitudes From Mini-Frac Records In Western Canada. *Journal of Canadian Petroleum Technology*, 28(5):22–31.

Wright, G., McMechan, M., and Potter, D. (1994). Structure and Architecture of the Western Canada Sedimentary Basin. In Mossop, G. D. and Shetsen, I., editors, *Geological atlas of the Western Canada Sedimentary Basin*, chapter 3, pages 25–40. Canadian Society of Petroleum Geologists and Alberta Research Council.

Yabe, Y., Philipp, J., Nakatani, M., Morema, G., Naoi, M., and Kawakata, H. (2009). Observation of numerous aftershocks of an Mw 1.9 earthquake with an AE network installed in a deep gold mine in South Africa. *Earth Planets Space*, 61(10):49–52.

Yale, D. P. (2003). Fault and stress magnitude controls on variations in the orientation of in situ stress. *Geological Society, London, Special Publications*, 209(1):55–64.

Yassir, N. A. and Bell, J. S. (1994). Relationships between pore pressure, stresses, and present-day geodynamics in the Scotian Shelf, offshore eastern Canada. *AAPG bulletin*, 78(12):1863–1880.

Yassir, N. A. and Dusseault, M. B. (1992). Stress trajectory determinations in southwestern Ontario from borehole logs. *Geological Society, London, Special Publications*, 65(1):169–177.

Zakharova, N. V. and Goldberg, D. S. (2014). In situ stress analysis in the northern Newark Basin: Implications for induced seismicity from CO2 injection. *Journal of Geophysical Research: Solid Earth*, 119(3):2362–2374.

Zang, A. and Stephansson, O. (2010). *Stress Field of the Earth's Crust*. Springer Netherlands, Dordrecht.

Zang, A., Stephansson, O., Heidbach, O., and Janouschkowetz, S. (2012). World Stress Map Database as a Resource for Rock Mechanics and Rock Engineering. *Geotechnical and Geological Engineering*, 30(3):625–646.

Zelt, C. A. and White, D. J. (1995). Crustal structure and tectonics of the southeastern Canadian Cordillera. *Journal of Geophysical Research*, 100(B12):24255.

Zemanek, J., Caldwell, R., Glenn, E. E., Holcomb, S., Norton, L. J., and Straus, A. (1969). The borehole televiewer — a new logging concept for fracture location and other types of borehole inspection. *Journal of Petroleum Technology*, 21(6).

Zemanek, J., Glenn, E. E., Norton, L. J., and Caldwell, R. L. (1970). Formation evaluation by inspection with the borehole televiewer. *Geophysics*, 35(2):254–269.

Zhou, S. (1997). A method of estimating horizontal principal stress magnitudes from stress-induced wellbore breakout and leak-off tests and its application to petroleum engineering. *Petroleum Geoscience*, 3:57–64.

Ziegler, M., Reiter, K., Heidbach, O., Zang, A., Kwiatek, G., Dahm, T., Dresen, G., and Hofmann, G. (2014). Mining induced static stress transfer and its relation to a high-precision located M w = 1 . 9 seismic event in a South African gold mine. In Alejano, Perucho, Olalla, and Jiménez, editors, *Rock Engineering and Rock Mechanics: Structures in and on Rock Masses*, pages 603–608, London. Taylor & Francis Group.

Zoback, M. (2010). *Reservoir geomechanics*. Cambridge University Press.

Zoback, M. D. (2007). *Reservoir geomechanics: Earth stress and rock mechanics applied to exploration, production and wellbore stability*. Cambridge Press.

Zoback, M. D., Barton, C. A., Brudy, M., Castillo, D., Finkbeiner, T., Grollimund, B., Moos, D., Peska, P., Ward, C., and Wiprut, D. (2003). Determination of stress orientation and magnitude in deep wells. *International Journal of Rock Mechanics and Mining Sciences*, 40(7-8):1049–1076.

Zoback, M. D., Moos, D., Mastin, L., and Anderson, R. N. (1985). Well bore breakouts and in situ stress. *Journal of Geophysical Research*, 90(B7):5523.

Zoback, M. D. and Zoback, M. L. (1981). State of stress and intraplate earthquakes in the United States. *Science (New York, N.Y.)*, 213(4503):96–104.

Zoback, M. D. and Zoback, M. L. (1991). Tectonic stress field of North America and relative plate motions. In Slemmons, D. B. and Engdahl, E. R., editors, *Neotectonics of North America*, pages 339–366. Geological Society of America.

Zoback, M. L. (1992). First- and second-order patterns of stress in the lithosphere: The World Stress Map Project. *Journal of Geophysical Research*, 97(B8):11703–11728.

Zoback, M. L. and Mooney, W. D. (2003). Lithospheric Buoyancy and Continental Intraplate Stresses. *International Geology Review*, 45(2):95–118.

Zoback, M. L. and Zoback, M. D. (1980). State of stress in the conterminous United States. *Journal of Geophysical Research*, 85(B11):6113–6156.

Zoback, M. L. and Zoback, M. D. (1989). Tectonic stress field of the continental United States. In Pakiser, L. and Mooney, W. D., editors, *Geophysical Framework of the Continental United States*, volume 172, chapter 24, pages 523–540. Geological Society of America, geological edition.

Zoback, M. L., Zoback, M. D., Adams, J. J., Assumpção, M., Bell, J. S., Bergman, E. A., Blümling, P., Brereton, N. R., Denham, D., Ding, J., Fuchs, K., Gay, N., Gregersen, S., Gupta, H. K., Gvishiani, A., Jacob, K., Klein, R., Knoll, P., Magee, M., Mercier, J. L., Müller, B. C., Paquin, C., Rajendran, K., Stephansson, O., Suarez, G., Suter, M., Udias, A., Xu, Z. H., and Zhizhin, M. (1989). Global patterns of tectonic stress. *Nature*, 341(6240):291–298.

Notation (List of Symbols)

$\boldsymbol{\epsilon}$	Strain
φ	Friction angle
ν	Poisson's ratio
μ'	Friction coefficient
ρ	Density
$\boldsymbol{\sigma}$	Stress at a point
$\hat{\boldsymbol{\sigma}}$	Principal stress
$\sigma_1, \sigma_2, \sigma_3$	Largest, middle and least principal stress
σ_d	Differential stress ($\sigma_1 - \sigma_3$)
σ_{dcrit}	critical differential stress at which the failure envelope is reached
ΔCFS	Coulomb failure stress change
ΔCFS_{slip}	Shear stress in direction of the slip
ΔCFS_{max}	Maximum shear stress
C	Cohesion
E	Young's modulus
k, K	k-ratio ($\mathrm{S_{Hmean}}$/ $\mathrm{S_V}$)
M_w	Earthquake moment magnitude
OCR	Overconsolidation ratio
P_c	Fracture breakdown pressure
P_p	Pore water pressure
$\mathrm{S_V}$	Vertical (overburden) stress
S_{VC}	maximum ever achieved vertical stress
$\mathrm{S_{Hmax}}$	Maximum horizontal stress
$\mathrm{S_{hmin}}$	Minimum horizontal stress
$\mathrm{S_{Hmean}}$	Mean horizontal stress
$\Delta\mathrm{S}$	Deviation between $\mathrm{S}_{measured}$ and S_{model}
$n\Delta\mathrm{S}$	ΔS normalized by S_{model}
$\widetilde{\Delta\mathrm{S}}$	Whole model median of ΔS
$\overline{\Delta\mathrm{S}}$	Whole model mean of ΔS
T_0	Tensile strength of the rock
V_S	Shear wave velocity
x, y, z	Cartesian coordinates

List of Figures

List of Tables

Acknowledgement

I have to thank all the people who gave me support during the work on this thesis:

First of all, I have to thank my colleague and technical supervisor Oliver Heidbach, who gave me the fullest support, motivation and freedom to get the best out of me. I also thank my university supervisor Michael Weber. I have to thank Moritz Ziegler, Konrad Schellbach, Dietrich Stromeyer, Johannes Altmann, Gottfried Grünthal, Arno Zang, Fabrice Cotton and all other colleagues of Section 2.6, for the inspiring and pleasant working atmosphere.

The Helmholtz-Alberta-Initiative (HAI) founded my work for most of the time; I have to thank the colleagues from the HAI project such as Simon Weides, Hannes Hofman, Mareike Noah, Steffi Genderjan, Nathaniel Walsh, Douglas R. Schmitt, Inga Moeck, Kristine Haug, Michael Lappé, Martyn J. Unsworth and Ernst Huenges for the fruitful collaboration as well as the nice time, we spent together. I thank the people, which are involved in World Stress Map working group for the interesting discussions and fruitful collaboration, such as Oliver Heidbach, Tobias Hergert, Mojtaba Rajabi, Mark Tingay, Birgit Müller and John Reinecker. Furthermore, I thank all the co-authors of the papers, talks and posters.

I thank Sections 3.1 and 4.4 at GFZ Potsdam in which I could work in the time, before I started my PhD work. I have to thank my supervisors of my Diploma work and my Diploma Mapping, Nina Kukowski, Lothar Ratschbacher, Bernhard Schulz as well all the other teachers from the Freiberg University of Mining and Technology, who taught me geology and scientific working. I thank Ulrich Sebastian for planting the seeds for fascination on geology.

Finally, I thank my girlfriend Betty, my brother Hendrik, my flat mates in Potsdam e.g. Lutz, Krister, Helen, Ev3, Stefan and Anne, the friends from Potsdam such as Kira and Matze as well as all the other unnamed, who accompanied me through the highs and lows of the last three and a half years since I started my PhD thesis. Thanks to all those who found several typos or grammar errors in parts of this thesis, such as Oliver, Dough, Kristin, Nate, Betty, Anne, Dietrich, Kira and Moritz.

"If we knew what it was we were doing, it would not be called research, would it?" (Albert Einstein)

Declaration

Ich versichere, dass ich die von mir vorgelegte Arbeit selbstständig verfasst habe, dass ich die verwendeten Quellen, Internet-Quellen und Hilfsmittel vollständig angegeben habe und dass ich die Stellen der Arbeit - einschließlich Tabellen, Karten und Abbildungen -, die anderen Werken oder dem Internet im Wortlaut oder dem Sinn nach entnommen sind, in jedem Fall unter Angabe der Quelle als Entlehnung kenntlich gemacht habe.

Potsdam, den 26. November 2014

.....

(Unterschrift des Kandidaten)